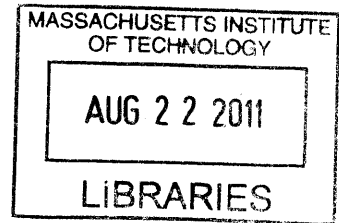


Estimation of Cardiovascular Indices by Analysis of the Arterial Blood Pressure Signal

by
Tatsuya Arai

Master of Science
The University of Tokyo, 2005



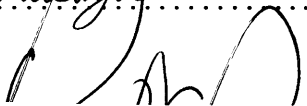
Submitted to the Department of Aeronautics and Astronautics
in Partial Fulfillment of the Requirements for the Degree of
Doctor of Philosophy at the
MASSACHUSETTS INSTITUTE OF TECHNOLOGY


ARCHIVES

May 2011

[June 2011]

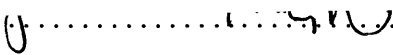
© 2011 Massachusetts Institute of Technology. All rights reserved.


Author

Department of Aeronautics and Astronautics
May 11, 2011

Certified by

Laurence R. Young
Apollo Program Professor of Aeronautics and
Professor of Health Sciences and Technology
Committee Chair

Certified by

Richard J. Cohen
Whitaker Professor in Biomedical Engineering
Thesis Supervisor

Certified by

Roger G. Mark
Distinguished Professor in Health Sciences and Technology and
Electrical Engineering and Computer Science

Accepted by

Eytan H. Modiano
Associate Professor of Aeronautics and Astronautics
Chair, Graduate Program Committee

Estimation of Cardiovascular Indices by Analysis of the Arterial Blood Pressure Signal

by
Tatsuya Arai

Submitted to the Department of Aeronautics and Astronautics
on May 11, 2011, in Partial Fulfillment of the
Requirements for the Degree of
Doctor of Philosophy

Abstract

This thesis introduces novel mathematical algorithms that track changes in stroke volume (SV), cardiac output (CO), and total peripheral resistance (TPR) by analysis of the arterial blood pressure (ABP) signal. The algorithms incorporate cardiovascular physiology within the framework of a generalized Windkessel model, which is a widely accepted cardiovascular model. Algorithms to identify end systole were also developed and implemented in the new and existing SV, CO, and TPR estimation algorithms.

The algorithms were validated by applying them to previously recorded Yorkshire swine data sets that include directly measured aortic blood flow (ABF), SV, CO, as well as central and peripheral ABP. Among the algorithms using the end systole identification algorithms, Parabolic Method, Modified Herd's Method, Kouchoukos Correction Method, and Corrected Impedance Method achieved low root normalized mean squared errors (RNMSEs).

This thesis also introduces and validates a novel algorithm to reconstruct instantaneous ABF waveforms from the ABP signal. The algorithm utilizes an auto-regressive with exogenous input (ARX) model to describe the filter between ABF and ABP. Because ABF (the exogenous input to the peripheral circulation) is approximately zero during diastole, the diastolic ABP waveforms can be regarded as auto-regressive (AR). By the AR analysis of multiple diastolic ABP waveforms, the AR parameters are obtained. The AR parameters were applied to the ABP waveforms (both systolic and diastolic) to compute beat-to-beat ABF waveforms. The errors of skewness and kurtosis of the estimated ABF waveforms were statistically smaller than those estimated by the standard Windkessel model. The estimated ABF waveforms were further processed to estimate SV, CO, and TPR. The algorithm achieved RNMSEs of 15.3, 19.6, and 21.8% in SV estimation; 12.7, 15.2, and 15.8% in CO estimation; and 14.3, 20.9, and 19.4 % in TPR estimation derived from central, femoral, and radial ABP, respectively.

Thesis supervisor: Richard J. Cohen

Title: Whitaker Professor in Biomedical Engineering

To my parents

Acknowledgements

I would like to thank Professor Richard Cohen for the opportunity and support to work in his laboratory. This thesis work could not have been accomplished without his insight and guidance. His optimistic outlook for innovation provided continual motivation for this work. I would like to thank Professor Laurence Young for his academic advice and for chairing my thesis committee. His arrangement of the summer internship at the Johnson Space Center further enriched my experience in this doctoral program. I would like to thank Professor Roger Mark for his research advice in and outside the committee meetings. His strict and encouraging research advice helped me to improve my thesis work. I would also like to thank Professor George Verghese and Dr. Thomas Heldt for their advice on my thesis.

I would like to thank the members of this laboratory. Dr. Kichang Lee let me become involved in experiments and gave me the opportunity to assist in hands-on work in the laboratory. Danilo Sčepanović always inspired me by his rigorous signal processing and mathematical modeling skills as well as his craftsmanship in the hobby shop. Wener Lü gave me many insights on mathematical modeling in the lab meetings and his experiments. Our lab administrator Candance (Candy) Weaver's great initiative and administrative support helped me get through the program. Dr. Robert Marini, Alison Hayward, Catrina Wong, Professor Antonis Armoundas, and Dr. Conor Barrett were wonderful colleagues. From them, I learned hands-on laboratory and surgical skills as well as the application of engineering to life science. I would also like to thank the previous lab members, Dr. Tamara Rosbury, Dr. Maya Barley, Dr. Evgeny Ter-Ovanesyan, and Amy Donovan for their help and feedback.

I had a great time with the MIT CADLAB group. I would like to thank my minor program advisor Professor David Wallace for his fantastic courses and advice on the product design projects. I would also like to thank the Gordon-MIT Engineering Leadership Program for the financial support.

The summer internship at the NASA Johnson Space Center (JSC) was one of the highlights in my doctoral program. I would like to thank Dr. Steven Platts, Dr. Michael Stenger, and the Cardiovascular Laboratory members for their mentoring, research guidance, and willingness to escort me on the JSC

campus. I would also like to thank the MIT Man Vehicle Laboratory and Baylor College of Medicine for organizing and supporting the wonderful opportunity.

I also had a great time with my friends at MIT, especially in playing tennis and organizing cultural festivals with the Japanese Association of MIT. Through the activities, I could rediscover the culture of my home country.

I could not accomplish this thesis work without support from my parents and my brother. Their continuous encouragement from Japan was the major dynamo of my thesis work.

Finally, my deepest thanks and love to my wife Sarah, who went through the rough waters at MIT with me. Sarah, I'm the luckiest man to share the time here and the rest of my life with you.

April 14, 2011

Houston, TX

Table of Contents

1.	Introduction.....	12
1.1.	Background.....	12
1.2.	Previous Methods	19
1.2.1.	Pulse Contour Methods.....	19
1.2.2.	Alternative Methods.....	21
1.3.	Specific Aims.....	24
1.4.	Thesis Organization.....	24
2.	Previous Work.....	26
2.1.	Ohm's Law in the Cardiovascular System.....	27
2.2.	Windkessel Model	27
2.3.	Windkessel SV.....	29
2.4.	Pulse Pressure.....	29
2.5.	Liljestrand-Zander's Method	30
2.6.	Herd's Pulse Pressure	31
2.7.	Beat-to-Beat Averaged Model	31
2.8.	Systolic Area.....	33
2.9.	Corrected Impedance.....	34
2.10.	Systolic Area with a Kouchoukos Correction.....	34
2.11.	AC Power	34
2.12.	Auto-Regressive and Moving-Average Model.....	35
2.13.	Summary.....	37
3.	Estimation of Stroke Volume and Cardiac Output.....	38
3.1.	Minimum Variance Method.....	38
3.2.	Modified Herd's Method	43
3.3.	Parabolic Aortic Blood Flow Model.....	44
3.4.	Pressure Ratio Method.....	47
3.5.	Hybrid Model	49
3.5.1.	Basic Model (<i>Model 1</i>).....	50
3.5.2.	Reduced Parameter Models (<i>Model 2 and 3</i>).....	52
3.5.3.	Hybrid Model.....	53
3.5.4.	Implementation	56
4.	Estimation of Aortic Blood Flow Waveforms.....	58
4.1.	Algorithm	59
4.1.1.	Model Description	59
4.1.2.	Criterion for Selecting AR Parameter Length.....	62
4.2.	Conditioning of Arterial Blood Pressure Data.....	66
4.3.	Model Validation	67
4.3.1.	Validation Steps	67
4.3.2.	Error Criteria.....	68
5.	Labeling Characteristic Points	71
5.1.	Identification of Peak Systole.....	71
5.2.	Identification of End Diastole.....	73
5.3.	Renewal of Gaussian Convolution Based on RR interval	74
5.4.	Identification of End Diastole.....	74
5.4.1.	Exponential Model.....	75
5.4.2.	Partial Pulse Pressure	76
6.	Results.....	77
6.1.	End Systole Estimation.....	78
6.2.	SV, CO, and TPR Estimation.....	79

6.2.1.	Windkessel Model.....	79
6.2.2.	Pulse Pressure	82
6.2.3.	Liljestrand-Zander's Method	85
6.2.4.	Herd's Pulse Pressure.....	88
6.2.5.	Beat-to-Beat Averaged Method.....	91
6.2.6.	Systolic Area	94
6.2.7.	Corrected Impedance	97
6.2.8.	Systolic Area with Kouchoukos Correction.....	100
6.2.9.	AC Power.....	103
6.2.10.	ARMA Model	106
6.2.11.	Minimum Variance Method	108
6.2.12.	Modified Herd's Method.....	111
6.2.13.	Parabolic ABF Model	114
6.2.14.	Pressure Ratio Method.....	117
6.2.15.	Hybrid Method Results	120
6.3.	Summary of the SV, CO, and TPR Estimation	125
6.4.	ABF Estimation	130
6.4.1.	Comparison with the Windkessel model.....	130
6.4.2.	Comparison with Standard Waveforms.....	138
6.4.3.	Exponential Model for End Systole Detection.....	144
6.5.	Summary.....	145
7.	Discussion.....	149
7.1.	CO, SV, and TPR estimation	149
7.2.	ABF Estimation	151
7.2.1.	Overview.....	151
7.2.2.	Sensitivity Analysis Regarding the Onset of Diastole	155
7.2.3.	Summary.....	159
8.	Conclusions and Future Work.....	161
8.1.	Summary.....	161
8.2.	Contributions	162
8.3.	Suggestions for Further Research	163
Appendix A: Derivation of High-Order Hybrid Model		166
A.1.	Quadratic Model	166
A.2.	General Model	170
Appendix B: Conference Posters		173
B.1.	The 59th International Astronautical Congress	173
B.2.	The 18th IAA Humans in Space Symposium.....	174
Bibliography		175

List of Figures

Fig. 1.1	Schematic diagram of the parallel and series arrangement of the vessels composing the circulatory system.	12
Fig. 1.2.	Typical ABF and ABP waveforms simultaneously recorded in swine.....	15
Fig. 1.3.	Illustration of cardiac cycle.	16
Fig. 1.4.	Fainting episode induced by venesection.	16
Fig. 1.5.	Ultrasonic flow probe.	17
Fig. 1.6.	Schematic drawing of the thermodilution catheter position during measurement.....	18
Fig. 1.7.	Arterial blood pressure curves recorded simultaneously in a wombat.....	20
Fig. 1.8.	Insensitivity of MAP and DBP to distortion.....	21

Fig. 1.9. Impedance Cardiography.....	22
Fig. 2.1. Two-parameter Windkessel model.....	28
Fig. 2.2. Qualitative illustration of a pressure-volume curve.....	30
Fig. 2.3. Systolic Area under the ABP curve.....	33
Fig. 2.4. The auto-regressive and moving average model	36
Fig. 2.5. Impulse response in ARMA model.....	36
Fig. 3.1. Typical ABF waveform and its integral from the onset of systole to time t	39
Fig. 3.2. Beats with a normal and abnormal diastolic interval.....	44
Fig. 3.3. Waveform of the measured femoral ABP and the theoretical Windkessel model ABP.....	50
Fig. 3.4. Model 2 and 3 of the Hybrid Model.	56
Fig. 4.1. Auto-regressive model with exogenous input.....	59
Fig. 4.2. Typical AR parameters and impulse response of the ARX model.	61
Fig. 4.3. ABF determination parameters as functions of AR parameter length L	64
Fig. 4.4. Histogram of the difference of the selected AR parameter lengths.	65
Fig. 4.5. Illustration of original (a) and modified (b) ABP waveforms.....	66
Fig. 4.6 Original and modified femoral ABP waveforms in Swine #5.	66
Fig. 4.7. Skewness and Kurtosis.	69
Fig. 5.1. Radial ABP data recorded from Yorkshire swine.	72
Fig. 5.2. Gaussian distribution (normalized).....	72
Fig. 5.3. Labeling systolic peaks.....	73
Fig. 5.4. Normal and abnormal radial ABP data recorded from Yorkshire swine.....	74
Fig. 5.5. A current systolic interval as a function of a preceding RR interval.....	75
Fig. 5.6. End systole defined by means of the partial pulse pressure.....	76
Fig. 6.1. SV estimation by the Windkessel model.	79
Fig. 6.2. CO estimation by the Windkessel model.....	80
Fig. 6.3. CO estimation by the Windkessel model.....	81
Fig. 6.4. SV estimation by the Pulse Pressure method.....	82
Fig. 6.5. CO estimation by the Pulse Pressure method.	83
Fig. 6.6. TPR estimation by the Pulse Pressure method.	84
Fig. 6.7. SV estimation by Liljestrand-Zander's method.	85
Fig. 6.8. CO estimation by Liljestrand-Zander's method.	86
Fig. 6.9. TPR estimation by Liljestrand-Zander's method.....	87
Fig. 6.10. SV estimation by Herd's method.	88
Fig. 6.11. CO estimation by Herd's method.....	89
Fig. 6.12. TPR estimation by Herd's method.....	90
Fig. 6.13. SV estimation by the Beat-to-Beat Averaged method.	91
Fig. 6.14. CO estimation by the Beat-to-Beat Averaged method.....	92
Fig. 6.15. TPR estimation by the Beat-to-Beat Averaged method.	93
Fig. 6.16. SV estimation by the Systolic Area method.	94
Fig. 6.17. CO estimation by the Systolic Area method.....	95
Fig. 6.18. TPR estimation by the Systolic Area method.	96
Fig. 6.19. SV estimation by the Corrected Impedance method.....	97
Fig. 6.20. CO estimation by the Corrected Impedance method.....	98
Fig. 6.21. TPR estimation by the Corrected Impedance method.	99
Fig. 6.22. SV estimation by the Kouchoukos method.....	100
Fig. 6.23. CO estimation by the Kouchoukos method.....	101
Fig. 6.24. TPR estimation by the Kouchoukos method.	102
Fig. 6.25. SV estimation by the AC Power method.	103
Fig. 6.26. CO estimation by the AC Power method.....	104
Fig. 6.27. TPR estimation by the AC Power method.	105
Fig. 6.28. CO estimation by the ARMA method.....	106
Fig. 6.29. TPR estimation by the ARMA method.....	107
Fig. 6.30. SV estimation by the Minimum Variance method.....	108

Fig. 6.31. CO estimation by the Minimum Variance method.	109
Fig. 6.32. TPR estimation by the Minimum Variance method.....	110
Fig. 6.33. SV estimation by the Modified Herd’s method.	111
Fig. 6.34. CO estimation by the Modified Herd method.	112
Fig. 6.35. TPR estimation by the Modified Herd method.....	113
Fig. 6.36. SV estimation by the Parabolic ABF method.	114
Fig. 6.37. CO estimation by the Parabolic ABF method.....	115
Fig. 6.38. TPR estimation by the Parabolic ABF method.....	116
Fig. 6.39. SV estimation by the Pressure Ratio method.....	117
Fig. 6.40. CO estimation by the Pressure Ratio method.....	118
Fig. 6.41. TPR estimation by the Pressure Ratio method.	119
Fig. 6.42. Agreement of the measured and estimated cardiac output and stroke volume.	122
Fig. 6.43. Bland-Altman plots of the CO and SV estimates using the new method.	123
Fig. 6.44. Measured ABF and estimated ABF by the Windkessel model using CAP (applied to Swine #8 data).	131
Fig. 6.45. Measured ABF and estimated ABF by the Windkessel model using FAP (applied to Swine #8 data).	132
Fig. 6.46. Measured ABF and estimated ABF by the Windkessel model using RAP (applied to Swine #8 data).	133
Fig. 6.47. Calculation process of SD differences.....	134
Fig. 6.48. Histograms of the SD errors by the ARX algorithm and the Windkessel model.....	135
Fig. 6.49. Histograms of the skewness and kurtosis errors by the ARX algorithm and the Windkessel model.	136
Fig. 6.50. Agreement of the measured and estimated stroke volume and cardiac output from central, femoral, and radial arterial blood pressure using the ARX method.	137
Fig. 6.51. Standard systolic ABF waveforms.....	139
Fig. 6.52. Histograms of the SD errors by the ARX algorithm and the first beat in each animal.	140
Fig. 6.53. Histograms of the skewness and kurtosis errors by the ARX algorithm and the first beat in each animal.....	141
Fig. 6.54. Histograms of the SD errors by the ARX algorithm and the median of all the true ABF waveforms.	142
Fig. 6.55. Histograms of the skewness and kurtosis errors of the ARX algorithm and the median of all the true ABF waveforms.	143
Fig. 6.56. Histograms of the waveform errors using ARX with true and estimated intervals.	144
Fig. 6.57. Summary of SV, CO, and TPR estimation using CAP.....	146
Fig. 6.58. Summary of SV, CO, and TPR estimation using FAP.....	147
Fig. 6.59. Summary of SV, CO, and TPR estimation using RAP.....	148
Fig. 7.1. Cyclic patterns of the measured and estimated ABF signals.	153
Fig. 7.2. Increased and decreased diastolic interval.....	156
Fig. 7.3. Histograms of the standard deviation, skewness, and kurtosis errors of ABF waveforms with a +10% diastolic interval offset.	157
Fig. 7.4. Histograms of the standard deviation, skewness, and kurtosis errors of ABF waveforms with a -10% diastolic interval offset.....	158
Fig. 7.5. Sensitivity of the new algorithm to the error of the identified diastolic interval.	159
Fig. 8.1. Bi-ventricular pacing.	164
Fig. 8.2. Schematic drawing of the Integrated Cardiovascular Investigation in the Columbus Laboratory onboard the International Space Station.	165

List of Tables

Table 6.1. Summary of cardiovascular parameters of the six swine data sets.	77
Table 6.2. Summary of diastolic interval errors \pm standard deviation (SD).....	78
Table 6.3. RNMSLEs of SV (CO) estimation by the Hybrid algorithm.	124
Table 6.4. RNMSLEs in SV estimation using the new and existing estimation methods.	127
Table 6.5. RNMSLEs in CO estimation using the new and existing estimation methods.....	128
Table 6.6. RNMSLEs in TPR estimation using the new and existing estimation methods.	129
Table 6.7. Correlation coefficients of skewness and kurtosis of measured and estimated ABF.....	133
Table 6.8. SV, CO, and TPR estimation results by the ARX method.....	134
Table 6.9. Results of SV estimations using different evaluation functions to determine L	134
Table 6.10. SV and CO estimation results by the ARX method with the estimated diastolic intervals.	144
Table 7.1. SV and CO estimation results with the identified diastolic intervals increased by 10%.....	156
Table 7.2. SV and CO estimation results with the identified diastolic interval decreased by 10%.....	158

1. Introduction

1.1. Background

The cardiovascular system is the primary mechanism within the body for maintaining homeostasis by delivering oxygen and nutrition, as well as removing wastes. As the average life expectancy lengthens, age-induced cardiovascular risk is a major concern. Cardiovascular monitoring during clinical, surgical, and research procedures is an important aspect of modern medicine, serving the function of monitoring and maintaining the blood flow and pressure in the major organs such as the brain, the heart itself, and the lungs (Fig. 1.1).

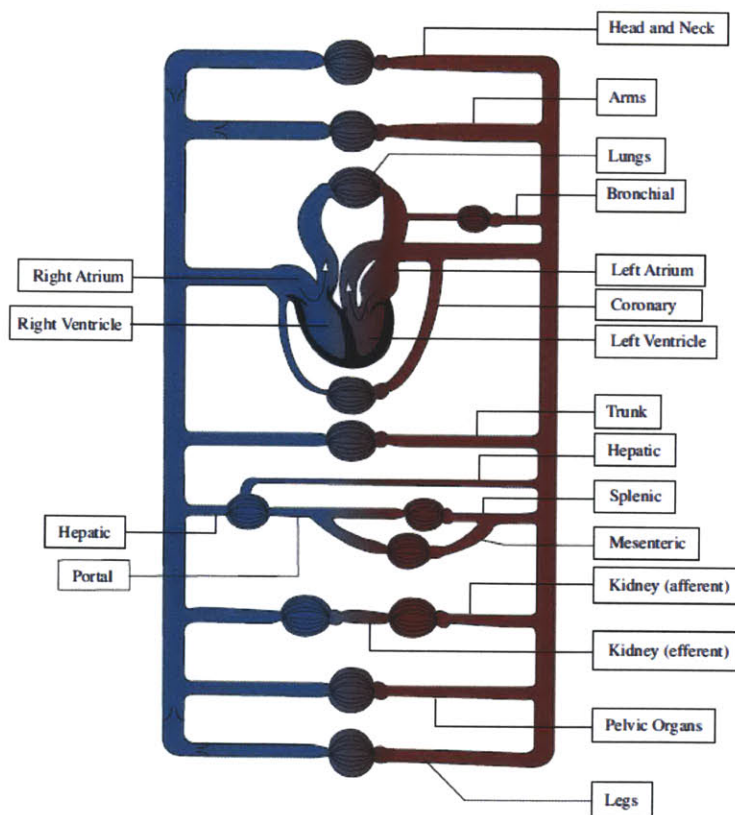


Fig. 1.1 Schematic diagram of the parallel and series arrangement of the vessels composing the circulatory system. The capillary beds are represented by thin lines connecting the arteries (red) with the veins (blue). The crescent-shaped thickenings proximal to the capillary beds represent the arterioles (resistance vessels). (Redrawn from Green, H. D.: In Glasser, OI, editor: Medical Physics, vol. 1, Chicago, 1944, Year Book Medical Publishers, Inc.) Figure by MIT OCW, obtained from the lecture notes of 6.522 Quantitative Physiology II, MIT.

Over the last 100 years, researchers have developed techniques for minimally- or non-invasive cardiovascular monitoring. This concept dates back many centuries to a time when legendary doctors diagnosed patients by feeling their arterial pulses [1]. In modern medicine, the concept is augmented by mathematical modeling as well as signal recording and processing techniques. Such techniques include cardiovascular system identification (CSI) [2-6], which describes cardiovascular physiology as nesting transfer functions relating cardiovascular variables. The complexity of the cardiovascular models that have been developed varies from a one-to-one relationship of the cardiovascular readings [7-30] to more complicated multi-variable models [2, 4-6, 31-33].

In emergency and clinical care, the major cardiovascular indices to be monitored are:

1. Arterial blood pressure (ABP; Fig. 1.2b-d)

ABP is the periodic fluctuation caused by the heart beat and occurs at the same frequency as the heart beat [1]. ABP is usually monitored clinically by means of a radial artery catheter; it may also be monitored non-invasively by using a finger-tip plethysmograph or radial artery tonometer.

2. Stroke volume (SV)

SV is the volume of blood ejected by the ventricles during each cardiac cycle [34]. In this thesis, SV represents a beat-to-beat bolus of blood ejected from the left ventricle. Increases in left ventricular relaxation and contraction lead to increased SV.

3. Cardiac output (CO)

CO is the average volume of blood pumped into the aorta by the heart per unit time [34]. CO is a key hemodynamic parameter to be monitored and assessed in patients. CO can also be an indicator of the exercise level as well as an early indicator of hemorrhage. CO is a flow rate [L/min] determined as a function of SV and heart rate (HR):

$$CO = SV \cdot HR \quad (1.1)$$

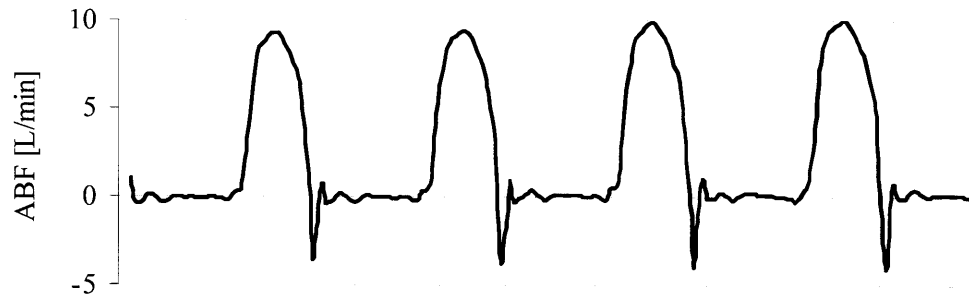
4. Total peripheral resistance (TPR)

TPR is the sum of arterial vascular resistances, mostly of arterioles. The smooth muscle tone modulates the diameters of the vessels to increase or decrease the resistance and controls systemic/local blood pressure and flow. In this thesis, the measured TPR represents the value calculated by the measured CO and mean arterial pressure (MAP) using Ohm's law as described in Eq. (2.1).

5. Aortic blood flow (ABF; Fig. 1.2a)

ABF is the instantaneous blood flow in the aorta. The waveforms can be characterized by systole (forward flow into the aorta from the left ventricle through the aortic valve), negative flow due to the negative pressure generated by the prompt aortic valve closure, and diastole (approximately zero flow, with aortic valve closed, as shown in Fig. 1.3). By integrating the beat-to-beat systolic ABF over time, one can obtain the SV. Time-averaging of SV values yields the CO.

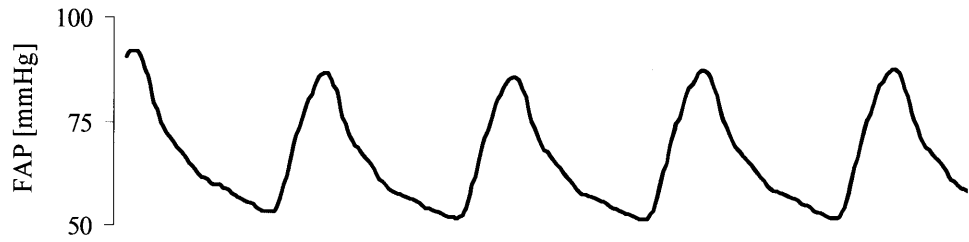
Currently, hemodynamic monitoring of patients in critical care settings depends heavily on the monitoring of ABP. ABP is usually monitored clinically by means of a radial artery catheter. However, ABP is a late indicator of hemodynamic decompensation. For example, Fig. 1.4 shows a hemorrhage study by Barcroft et al [35] demonstrating that during the hemorrhage caused by venesection, the CO continued to decrease while the blood pressure was maintained until the subject fainted. Multiple physiologic feedback systems maintain ABP until the patient is on the verge of hemodynamic collapse. CO and SV monitoring enables earlier identification of hemodynamic decompensation, but CO and SV are difficult to measure and monitor.



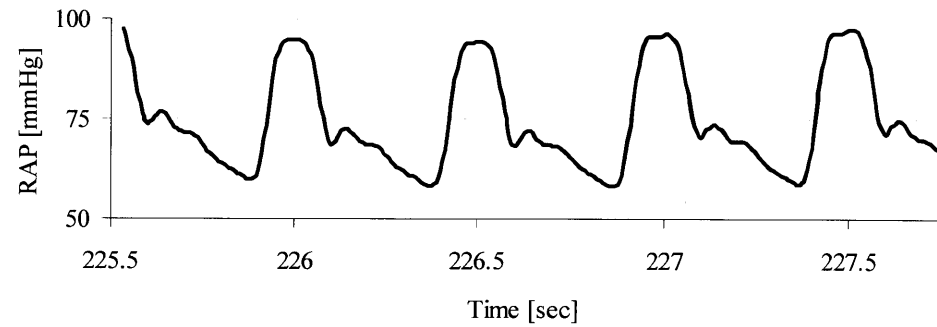
(a) Aortic blood flow (ABF)



(b) Central arterial pressure (CAP)



(b) Femoral arterial pressure (FAP)



(d) Radial arterial pressure (RAP)

Fig. 1.2. Typical ABF and ABP waveforms simultaneously recorded in swine. CAP, FAP, and RAP represent central, femoral, and radial arterial blood pressure, respectively.

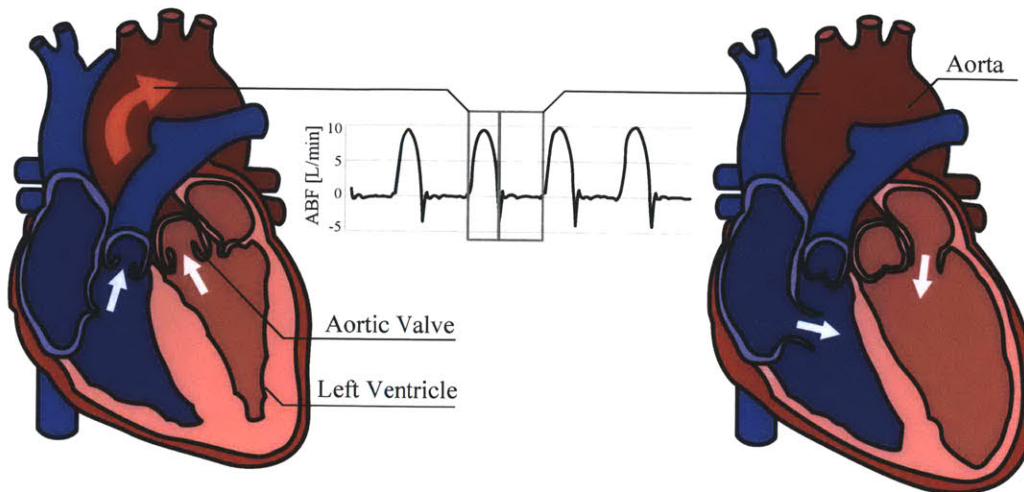


Fig. 1.3. Illustration of cardiac cycle.

Systolic contraction of the left ventricle generates positive blood flow that opens the aortic valve and rushes into the aorta. During diastole, the aortic valve is closed and there is no flow into the aorta.

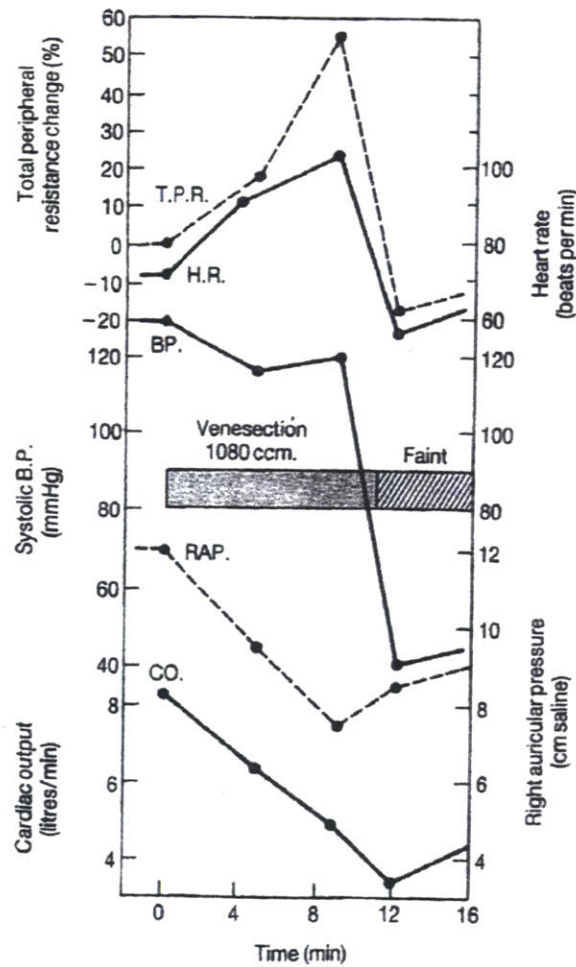


Fig. 1.4. Fainting episode induced by venesection.

In this instance, there is a slight further reduction in cardiac output during the fainting episode, but the total peripheral resistance undergoes a much more profound decrease (1944 Barcroft *et al.*, [35].)

The most accurate method for measuring SV and CO involves the surgical placement of a blood flow probe around the aorta. The drawback of the flow probe is that this method requires a highly invasive thoracotomy procedure [20]. For the monitoring of CO, thermodilution [36] is a commonly used method. Thermodilution involves injecting cold saline through a central venous catheter into right atrium and measuring the temperature change in the pulmonary artery (Fig. 1.6). CO is then calculated using the Stewart-Hamilton equation [37]. However, thermodilution requires a pulmonary artery catheterization, which is associated with cardiovascular risks such as carotid artery puncture (when accessing an intrajugular vein), cardiac arrhythmia, bleeding, embolism, clotting, and infection [38, 39]. Moreover, thermodilution cannot continuously measure SV on a beat-to-beat basis, and its accuracy is limited. For example, Boreto *et al.* compared a continuous thermodilution method with an ultrasonic flow probe and reported a 0.36 L/min bias and a 1.96 L/min standard deviation (SD) [40]. Therefore, many studies have been devoted to developing minimally- or non-invasive methods to monitor the cardiovascular indices (SV, CO, and TPR).

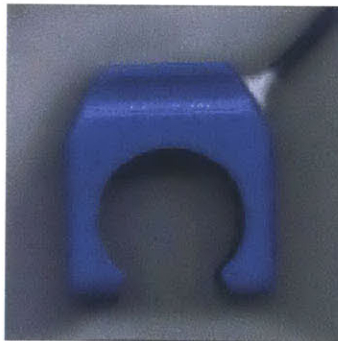


Fig. 1.5. Ultrasonic flow probe.
Developed by Transonic Systems. Image obtained from <http://www.emkabiotech.com/> on March 4, 2011.

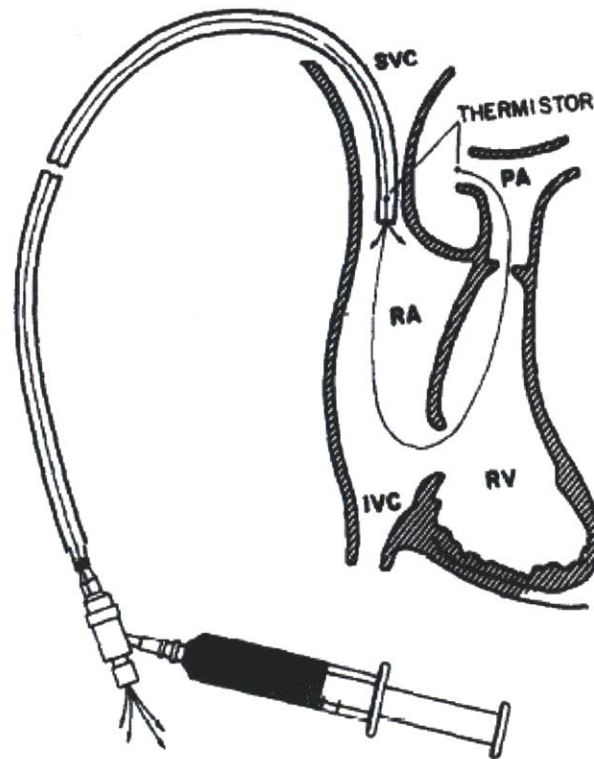


Fig. 1.6. Schematic drawing of the thermodilution catheter position during measurement. The injection catheter is in the superior vena cava (SVC). The thermometers are placed 1 to 2 cm from the tip and in the main branch of the pulmonary artery (PA). RA, RV, and IVC represent the right atrium, right ventricle, and inferior vena cava, respectively. Image and caption obtained from Ganz *et al.* [36].

Arterial pulse has been used by researchers to estimate the cardiovascular indices because the arterial pulse is readily accessible in general. In particular, analyses of arterial pressure waveforms (rather than directly measurable simple mean, systolic, and diastolic pressure) have been conducted over the last few decades to extract essential information that can be a better indicator of cardiovascular indices than directly measurable ABP values. Along the line of such pulse contour analyses, this thesis aims to develop novel algorithms to estimate SV, CO, TPR, and ABF by analyzing ABP waveforms and to compare the performance of these algorithms with that of existing methods.

1.2. Previous Methods

This section describes an overview of minimally- or non-invasive cardiovascular index estimation.

1.2.1. Pulse Contour Methods

Pulse contour methods (PCMs) have been extensively studied [4, 10-32] over the last 100 years as a means of estimating cardiovascular indices from the continuous mathematical analysis of peripheral ABP waveforms. PCMs, in general, utilize characteristic points or portions of ABP waveforms. Researchers have selected, processed, and combined several characteristic points or continuous portions of ABP waveforms to formulate SV, CO, and TPR estimation methods.

One of the major challenges in developing PCMs is determining how to handle ABP distortion. As arterial pulsation propagates from the aorta to the peripheral arterial tree, it experiences a tapered elastic network, bifurcation, and reflection from the peripheral arterial lines. These perturbations cause ABP waveform distortion (Fig. 1.7). The systolic peak values (systolic blood pressure, SBP) become higher in the peripheral arteries than the central artery. This notion was confirmed by the analysis of central and peripheral (femoral and radial) ABP waveforms recorded from swine (Fig. 1.8). The characteristic values (MAP, end-diastolic pressure or DBP, and SBP) in the peripheral (femoral and radial) and central ABP recorded from six Yorkshire swine data sets were compared. The vertical axes of Fig. 1.8 represent the

pressure value changes defined as

$$\frac{Peripheral - Central}{Central} \times 100 \quad (1.2)$$

where *Central* and *Peripheral* represent the central and peripheral ABP values, respectively. For instance, the leftmost bar in Fig. 1.8a shows the change of central MAP and peripheral MAP:

$$\frac{MAP_{peripheral} - MAP_{central}}{MAP_{central}} \times 100 \quad (1.2a)$$

As can be seen, SBP values tend to increase more compared to DBP and MAP values.

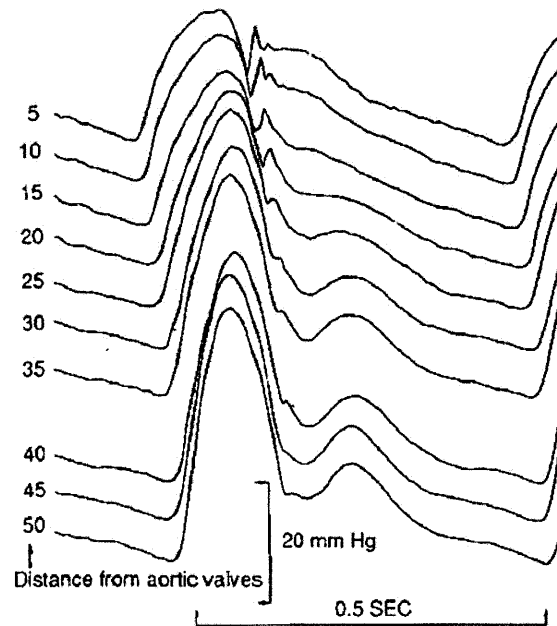
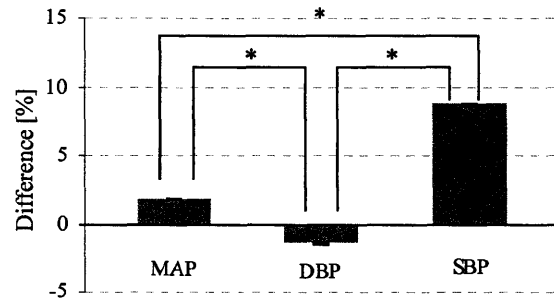


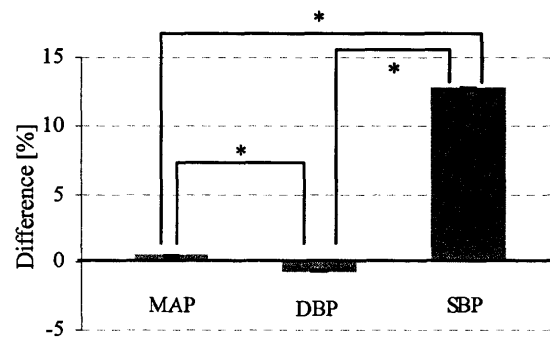
Fig. 1.7. Arterial blood pressure curves recorded simultaneously in a wombat. The top and bottom waveforms correspond to the proximal aorta (top) and peripheral arteries (below). From “Arterial Pulse” by O’Rourke *et al.* [1].

To overcome the influence of waveform distortion, researchers have taken unique approaches. Herd *et al.* and Parlikar *et al.* utilized ABP descriptors that are insensitive to distortion. Specifically, DBP and MAP are used in their model to calculate CO. The advantage of the method is that it does not use the systolic ABP that is subject to the distortion of ABP as it propagates through the arterial tree. Mukkamala

et al. took an approach inspired by transmission line theory, which predicts that the confounding effects of wave reflections diminish over an increasing time scale. The wave reflections significantly corrupt peripheral ABP waveforms over short time scales (high frequencies) without complicating them over longer time scales (low frequencies) [41]. Further details of the existing methods are introduced in Chapter 2.



(a) Femoral vs. Central ABP



(b) Radial vs. Central ABP

Fig. 1.8. Insensitivity of MAP and DBP to distortion.

As ABP waveforms propagate from central to peripheral (femoral and radial) arteries, the waveforms get distorted. MAP and DBP values do not change between central and peripheral arteries, whereas SBP values increase. The bars represent the mean, and black lines represent the standard error from the mean.

1.2.2. Alternative Methods

Although not explored in this thesis, there are other non-invasive or minimally invasive CO and SV estimation methods.

Impedance Cardiography

One of the commercially available methods other than the PCMs is bio-impedance or impedance cardiography [34, 35]. This method involves the passing of a low-amperage ($< 4 \text{ mA}$), high-frequency (50 – 100 Hz) current through the limb, thorax, or forehead to the limb using a pair of electrodes (Fig. 1.9). A second pair of electrodes is also placed to the aforementioned locations to measure the impedance Z and its derivative dZ/dt . These variables are used with a conversion factor to calculate the stroke volume and cardiac output. It is difficult to determine what regions or organs contribute to the impedance change recorded from the thoracic surface [42]. Although it shows remarkably good correlation with other cardiac output measurement systems if applied to a select relatively healthy population, the results in hospitalized patients are not satisfactory [43].

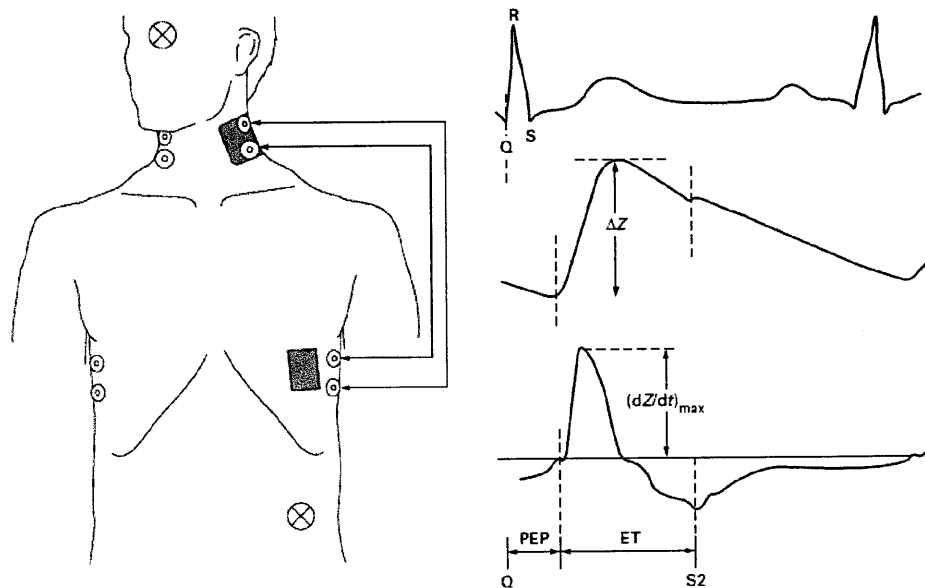


Fig. 1.9. Impedance Cardiography.

Figures obtained from Critchley, 1998 [44]. The thorax-limb configuration of the current injection and sensing electrodes is shown on the left. The graphs on the right illustrate the measured ECG (top), impedance (middle), and the first derivative of impedance (bottom).

Fick's principle

By analyzing airway gas measurement (carbon dioxide, CO₂), Fick's principle can be used to estimate cardiac output:

$$CO = \frac{\dot{V}CO_2}{CvCO_2 - CaCO_2} \quad (1.3)$$

where $\dot{V}CO_2$ is the CO₂ excreted by the lungs and $CaCO_2$ and $CvCO_2$ are the arterial and venous CO₂ contents, respectively. The CO₂ contents in the blood are estimated from end-tidal CO₂. Although the mixed venous blood contents including $CvCO_2$ are difficult to measure, one can obtain CO by using a re-breathing technique [45]. Assuming that CO does not change between time 1 and time 2,

$$CO = \frac{\dot{V}CO_{2,1}}{Cv_1CO_2 - Ca_1CO_2} = \frac{\dot{V}CO_{2,2}}{Cv_2CO_2 - Ca_2CO_2} \quad (1.4)$$

where subscripts 1 and 2 indicate values at time 1 and 2 respectively. Utilizing the algebra: $X = A/B = C/D = (A-C)/(B-D)$,

$$\begin{aligned} CO &= \frac{\dot{V}CO_{2,1} - \dot{V}CO_{2,2}}{(Cv_1CO_2 - Ca_1CO_2) - (Cv_2CO_2 - Ca_2CO_2)} \\ &= \frac{\dot{V}CO_{2,1} - \dot{V}CO_{2,2}}{(Cv_1CO_2 - Cv_2CO_2) - (Ca_1CO_2 - Ca_2CO_2)} \\ &\approx \frac{\dot{V}CO_{2,1} - \dot{V}CO_{2,2}}{Ca_2CO_2 - Ca_1CO_2} \end{aligned} \quad (1.5)$$

assuming that the mixed venous CO₂ content does not change during a brief change in effective ventilation ($Cv_1CO_2 = Cv_2CO_2$). Thus, one can obtain CO by measuring the end-tidal CO₂ and arterial CO₂ contents. The effects of unknown ventilation/perfusion inequality in patients may explain why the performance of this method shows a lack of agreement with results obtained by the thermodilution method [46].

1.3. Specific Aims

The primary goal of this thesis was to develop novel algorithms to continuously monitor SV, CO, TPR, and ABF waveforms by the analysis of ABP waveforms. The specific aims are two-fold:

Aim 1. Develop novel algorithms to estimate SV, CO, and TPR by the analysis of ABP waveforms and compare the results with those of existing methods.

Using modeling techniques based on cardiovascular physiology and the Windkessel Model, several SV, CO, and TPR estimation methods were developed. The estimation results were comprehensively compared with those of the existing methods.

Aim 2. Develop a novel algorithm to estimate the aortic blood flow waveform by the analysis of arterial blood pressure waveforms.

The second aim was to develop a novel algorithm to estimate instantaneous ABF waveforms. In addition to the traditional ABP analysis, ABF analysis would enable further cardiovascular assessment such as evaluation of the left ventricular contractility.

1.4. Thesis Organization

In this chapter, an overview of the monitoring of cardiovascular indices was introduced, and the specific aims of the thesis were described. Chapter 2 introduces existing cardiovascular modeling techniques. The chapter covers a variety of major methods including empirical and theoretical models.

Chapter 3 is dedicated to the introduction of novel algorithms developed to estimate SV, CO, TPR by the analysis of ABP waveforms. The algorithms incorporate mathematical models based on the Windkessel model and cardiovascular physiology.

Chapter 4 introduces a novel algorithm to estimate instantaneous ABF by the analysis of ABP. An auto-regressive model with exogenous input is adopted to describe the relationship between ABF and ABP.

Chapter 5 provides details of the pre-processing of the ABP data sets. The methods to identify end systole, peak systole, and end diastole on a beat-to-beat basis are described, as end systole time stamps are not available in general from ABP signals. In particular, Section 5.4 introduces a series of methods to identify end systole that could advance the new and existing cardiovascular index estimation algorithms.

The estimation results of the existing and novel methods are reported and summarized in Chapter 6. Root normalized mean square errors (RNMSEs) and Bland-Altman's plots [47] are used for the comparison of CO, SV, and TPR estimation performance. For the reconstruction of ABF waveforms, standard deviation, skewness, and kurtosis were also used to quantitatively evaluate the shapes of the estimated waveforms compared to the measured waveforms.

Chapter 7 discusses the SV, CO, and TPR estimation results as well as a series of sensitivity studies for the ABF estimation algorithm. The contributions of the present work and suggestion for future work are summarized in Chapter 8.

Appendix A describes the derivation of the Hybrid Model, one of the novel algorithms developed in this thesis work (introduced in Section 3.5). Appendix B shows conference posters describing the new algorithms to estimate cardiovascular indices.

2. Previous Work

The aim of pulse contour analysis is to extract essential hemodynamic information (e.g., ABF, SV, CO, and TPR) from the peripheral data (i.e., peripheral ABP). Researchers have developed several models and algorithms to estimate SV, CO, and TPR by the analysis of central and/or peripheral ABP waveforms. Their approaches can be categorized into two groups: empirical (data-driven) and model-based (theoretical cardiovascular physiology).

Empirical models utilize characteristic cardiovascular descriptors such as HR, area under the ABP curves, pulse pressure (PP), and MAP to find linear or non-linear coefficients for the descriptors to construct a SV estimation formula. In finding coefficients, measured CO data (mostly recorded from the thermodilution method) are used to calibrate the models. Other than selecting the physiological descriptors (i.e., HR, PP, MAP), the model can be highly data-driven, and cardiovascular physiology in terms of the relationship between descriptors is not necessarily taken into account. Thus, these models may work for a nominal cardiovascular system in the healthy population but not for people who are de-conditioned and have premature ABP beats and/or heart failure.

On the other hand, model-based approaches adopt cardiovascular physiology and mechanical principles in modeling, and in many cases, simplify the arterial system to obtain SV, CO, and/or TPR. Therefore, model-based approaches are expected to work for off-nominal conditioned cardiovascular systems as well as deconditioned systems. Nonetheless, any method has to make assumptions in processing ABP data. One cannot model the entire cardiovascular system in complete detail from the observation of ABP signals. One has to assume, for example, that ABP reflection is negligible, ABP waveform distortion in peripheral arterial branches is not considerably large, or that the MAP is approximately equal in central and peripheral ABP signals. Note that what differentiates one PCM from another is its assumptions in modeling the relevant cardiovascular physiology.

Before introducing the existing PCMs and discussing their pros and cons, the first two sections

describe the most widely accepted common-ground frameworks of each PCM: Ohm's Law as used in electrical circuits and the Windkessel model named after the German fire extinguisher that involves a buffering system.

2.1. Ohm's Law in the Cardiovascular System

The steady-state pressure and flow relationship in the cardiovascular system can be described as the Ohm's law of an electrical circuit:

$$\bar{P} = \bar{F} \cdot TPR \quad \text{or} \quad MAP = CO \cdot TPR \quad (2.1)$$

where \bar{P} is the MAP, and \bar{F} is the mean flow or CO.

2.2. Windkessel Model

“Windkessel” literally means “air chamber” or “elastic reservoir” in German. The vessels can be modeled as elastic tubes that store blood volume, build up pressure in systole, and recoil and discharge blood flow during diastole in each cardiac cycle. In quantifying the elastic reservoir, the mathematical foundation was developed by Otto Frank [48]. The two-parameter Windkessel model (Fig. 2.1) is the widely accepted electrical circuit (RC circuit) analog of the cardiovascular system [8, 10, 20, 49-52]. The elements (battery, capacitor, and resistor) represent the heart, aortic or arterial compliance (C_a), and total peripheral resistance (TPR) or systemic resistance, respectively. The current and voltage are equivalent to blood flow and blood pressure, respectively. The current source provides a train of impulses. The voltage then shows exponential decay curves that mimic diastolic ABP waveforms. The characteristic time constant τ can be described as the product of arterial compliance (C_a) and TPR.

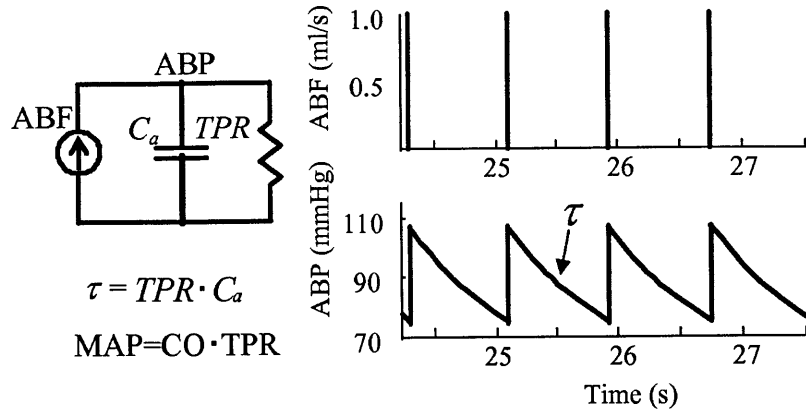


Fig. 2.1. Two-parameter Windkessel model.

Systole is modeled as an impulse ejection of blood from the flow source (the heart) into the RC circuit representing the vasculature. The resistance, capacitance, and voltage are represented by total peripheral resistance (TPR), arterial compliance (C_a), and arterial blood pressure (ABP), respectively. The equations describe the time constant (τ) of the exponential decay of the ABP waveform and Ohm's law. The figure was obtained from Mukkamala *et al.* [20].

The principal equation of the two-parameter Windkessel model is:

$$\frac{F}{C_a} = \frac{dP}{dt} + \frac{P}{\tau} \quad (2.2)$$

The impulse response of the system is ideally an exponential decay with the characteristic time constant τ .

Ohm's law and the Windkessel model have provided researchers with a fundamental framework with which to model the cardiovascular system that involves ABP, TPR, CO, SV, and ABF. For instance, Bourgeois *et al.* [9] was one of the first researchers to analyze the exponential decay constant of the diastolic ABP waveforms to obtain τ . This method worked for applications related to the estimation of central ABP (CAP). SV and CO were also successfully estimated using these methods in applications related to the analysis of the CAP waveform in both dogs and humans [9, 13, 27]. However, such exponential decay curves are generally not apparent in peripheral ABP waveforms. To overcome this problem, further models have been developed by researchers to analyze the pulse contour of ABP and extract characteristic descriptors within the ABP waveforms.

The following sections describe existing PCMs that analyze peripheral ABP to estimate proportional CO, TPR, and SV.

2.3. Windkessel SV

As mentioned in section 2.2, the two-parameter Windkessel model

$$\frac{F}{C_a} = \frac{dP}{dt} + \frac{P}{\tau} \quad (2.2)$$

has been widely used by researchers to model the cardiovascular physiology as an electrical circuit equivalent. By fitting the diastolic ABP signal to an exponential decay curve, one can obtain the characteristic time constant τ .

The integral of the proportional ABF (F/C_a) in time provides a proportional SV estimate:

$$\begin{aligned} \int_1^2 \frac{F}{C_a} dt &= \int_1^2 \left(\frac{dP}{dt} + \frac{P}{\tau} \right) dt \\ &= P_2 - P_1 + \frac{1}{\tau} \int_1^2 P dt \end{aligned} \quad (2.3)$$

where 1 and 2 are the start and end points of the integral, respectively. The time average of the SV estimate is the CO estimate. In this thesis, end diastole of the preceding beat and the current end systole are the points 1 and 2, respectively.

Some of the following methods use this Windkessel model SV with different assumptions for P_1 , P_2 , and τ .

2.4. Pulse Pressure

This method takes the capacitor equation into account.

$$\begin{aligned} \Delta Q &= C \cdot \Delta V \\ \Rightarrow SV &= C_a \cdot \Delta PP \end{aligned} \quad (2.4)$$

Pulse pressure (PP), i.e., the difference between SBP and DBP of the preceding beat is regarded as a proportional SV [12]. Because it is easy to find SBP and DBP in ABP signals by using devices such as a

sphygmomanometer, this method is widely used as an estimation method to track changes in SV.

The drawback of this method is that SBP values can be distorted as ABP waveforms propagate from the aorta through the arterial tree to the peripheral ABP measurement locations, as can be seen in Fig. 1.8. In the meantime, DBP stays relatively constant. Thus, the proportional SV could be overestimated.

2.5. Liljestrand-Zander's Method

Liljestrand and Zander [17] modeled the arterial compliance C_a as a function of pressure. As ABP rises, C_a decreases, as shown in Fig. 2.2. The figure also shows two different operating pressures. Both have equal PP while SBP and DBP are different, and when the mean of SBP and DBP is high, C_a becomes small. Therefore, by considering the inversely proportional relationship between ABP and C_a , C_a can be described approximately as

$$C_a \propto \frac{1}{SBP + DBP} \quad (2.5)$$

Then, the proportional SV can be obtained by:

$$SV = C_a \times PP \propto \frac{SBP - DBP}{SBP + DBP} \quad (2.6)$$

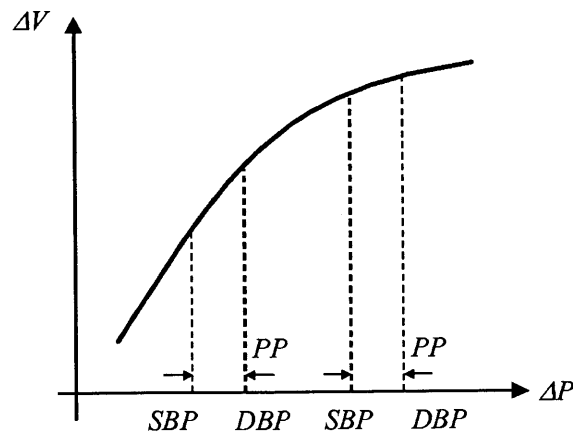


Fig. 2.2. Qualitative illustration of a pressure-volume curve. The slope of the solid line (pressure-volume curve) represents arterial compliance C_a . The dotted line shows SBP and DBP under different operating pressures.

This method was reported to have resulted in the best CO estimation (reference method: thermodilution) when applied to the data sets recorded from ICU patients [53].

2.6. Herd's Pulse Pressure

This method was developed by Herd [14] *et al.* and re-discovered by Sun [53] and Parlikar [23]. Instead of SBP, MAP is used in the pulse pressure method. Both MAP and DBP are robust against distortion, and this method provides reasonably robust SV estimation.

$$SV \propto (MAP - DBP) \quad (2.7)$$

The drawback of Herd's method becomes apparent when the diastolic interval becomes longer than regular beats (e.g., asystole); regardless of the systolic pulsation, as diastole continues, the current MAP value continues decreasing. Consequently, the estimated proportional SV ends up in underestimating the SV. To overcome this problem, a new method is introduced in section 3.2.

2.7. Beat-to-Beat Averaged Model

Parlikar *et al.* [23] developed a new beat-to-beat CO estimation method based on the Windkessel model.

$$\begin{aligned} \int_1^2 \frac{F(t)}{C_a} dt &= \frac{SV}{C_a} \\ &= P_2 - P_1 + \frac{1}{\tau} \int_1^2 P dt \end{aligned} \quad (2.8)$$

$$\begin{aligned}
&\Rightarrow \frac{CO}{C_a} = \frac{SV \cdot HR}{C_a} \\
&= \frac{SV}{C_a} \cdot \frac{1}{T} \\
&= \frac{1}{T} \left(P_2 - P_1 + \frac{1}{\tau} \int_1^2 P dt \right) \\
&= \frac{P_2 - P_1}{T} + \frac{MAP}{\tau}
\end{aligned}$$

where F represents ABF, P is ABP, C_a is arterial compliance, subscripts 1 and 2 indicate the onset of diastole and an arbitrary time point after the end systole of the beat, respectively. To obtain τ , instead of diastolic exponential curve fitting, they utilized the pulse pressure method (2.7):

$$\begin{aligned}
SV &= 2(MAP - DBP) \cdot C_a \\
\Rightarrow \frac{CO}{C_a} &= \frac{2(MAP - DBP)}{T} \tag{2.9}
\end{aligned}$$

The coefficient 2 in front of $(MAP-DBP)$ was empirically found by Parlikar *et al.* [23] to provide the lowest CO estimation errors. Thus, from (2.8) and (2.9), one can obtain τ by solving

$$\frac{MAP}{\tau} = \frac{2(MAP - DBP) - (P_2 - P_1)}{T} \tag{2.10}$$

or by using multiple beats to solve the following equation:

$$\begin{bmatrix} MAP_i \\ MAP_{i+1} \\ \vdots \\ MAP_{i+N} \end{bmatrix} \frac{1}{\tau} = \begin{bmatrix} \frac{2(MAP_i - DBP_i) - (P_2 - P_1)_i}{T_i} \\ \frac{2(MAP_{i+1} - DBP_{i+1}) - (P_2 - P_1)_{i+1}}{T_{i+1}} \\ \vdots \\ \frac{2(MAP_{i+N} - DBP_{i+N}) - (P_2 - P_1)_{i+N}}{T_{i+N}} \end{bmatrix} \tag{2.11}$$

The obtained τ was used in (2.8) to calculate the proportional CO.

2.8. Systolic Area

One intuitive way to estimate SV, the time integral of instantaneous blood flow, is the integration of the ABP signal [27, 50].

$$SV \propto \int_{t^{ED}}^{t^{ES}} P(t) dt \quad (2.12)$$

where t^{ED} and t^{ES} are the time stamps for the end-diastole of the preceding beat and current end systole, respectively, and P is the ABP signal. This model can be re-described as the integral of the instantaneous aortic blood flow in the Windkessel model with a constant TPR and equal preceding and current end diastolic pressures. A variant of the method subtracts DBP from the ABP signal:

$$SV \propto \int_{t^{ED}}^{t^{ES}} (P(t) - DBP) dt \quad (2.13)$$

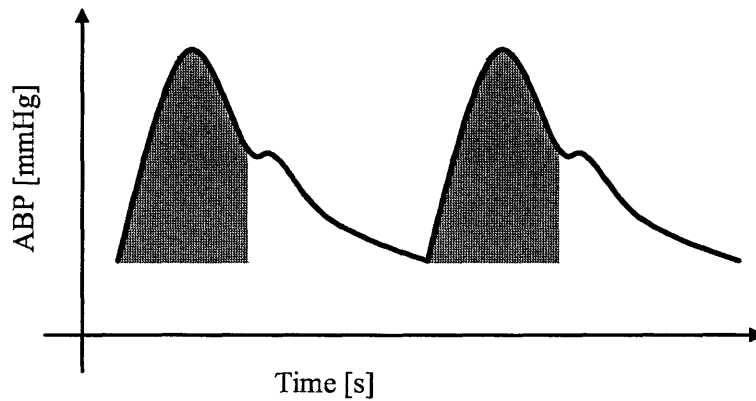


Fig. 2.3. Systolic Area under the ABP curve.

2.9. Corrected Impedance

Wesseling *et al.* [29] developed a SV estimation method based on the Systolic Area method. They obtained impedance as a function of MAP and HR.

$$SV \propto (163 + HR - 0.48 \cdot MAP) \int_{t^{ED}}^{t^{ES}} (P(t) - DBP) dt \quad (2.14)$$

The coefficients in the impedance (scaling factor) were empirically obtained from healthy male subjects in their 20s. Thus, this method can be described as a model-based method (systolic area) scaled by empirical coefficients.

2.10. Systolic Area with a Kouchoukos Correction

Kouchoukos *et al.* developed a different algorithm based on the Systolic Area method:

$$SV \propto \left(1 + \frac{T_S}{T_D}\right) \int_{t^{ED}}^{t^{ES}} (P(t) - DBP) dt \quad (2.15)$$

where T is the beat interval, and T_D and T_S are diastolic and systolic durations, respectively [15]. The correction factor $1 + T_S/T_D$ comes from the work by Warner *et al.* [28]. The correction factor takes into account the run-off aortic flow into the arterial tree bed during systole.

2.11. AC Power

This method calculates

$$SV \propto \sqrt{\frac{1}{T} \int_T (P(t) - MAP)^2 dt} \quad (2.16)$$

where T is the beat interval [53].

2.12. Auto-Regressive and Moving-Average Model

Mukkamala *et al.* [20] introduced system identification techniques into the cardiovascular parameter estimation. They modeled the impulse response of the cardiovascular system as an exponential decay curve with the characteristic time constant τ . In the model, the current ABP signal can be described by the preceding ABP signals with weighting coefficients, and the arterial pulse. The arterial pulse was approximated as the PP values.

$$P[i] = \sum_{j=1}^p a[j]P[i-j] + \sum_{k=1}^q b[k]PP[i-k] \quad (2.17)$$

or

$$\begin{bmatrix} P[i] \\ P[i+1] \\ \vdots \\ P[i+N] \end{bmatrix} = \begin{bmatrix} P[i-1] & P[i-2] & \cdots & P[i-p] \\ P[i] & P[i-1] & \cdots & P[i-p+1] \\ \vdots & \vdots & \ddots & \vdots \\ P[i-1+N] & P[i-2+N] & \cdots & P[i-p+N] \end{bmatrix} \begin{bmatrix} a[1] \\ a[2] \\ \vdots \\ a[p] \end{bmatrix} + \begin{bmatrix} PP[i-1] & PP[i-2] & \cdots & PP[i-q] \\ PP[i] & PP[i-1] & \cdots & PP[i-q+1] \\ \vdots & \vdots & \ddots & \vdots \\ PP[i-1+N] & PP[i-2+N] & \cdots & PP[i-q+N] \end{bmatrix} \begin{bmatrix} b[1] \\ b[2] \\ \vdots \\ b[q] \end{bmatrix} \quad (2.18)$$

where a and b are auto-regressive (AR) and moving-average (MA) weighting coefficients (parameters), and p and q are the parameter lengths. N is the number of data points in six minutes (sampling rate: 90 Hz). An interval of six minutes was selected by Mukkamala *et al.* Note that P represents the ABP signal and PP is a train of intermittent PP spikes at the onset of systole (Fig. 2.4). By utilizing the minimum description length (MDL) technique [54], Mukkamala *et al.* found that p and q were smaller than 20 for an ABP recorded at 90 Hz.

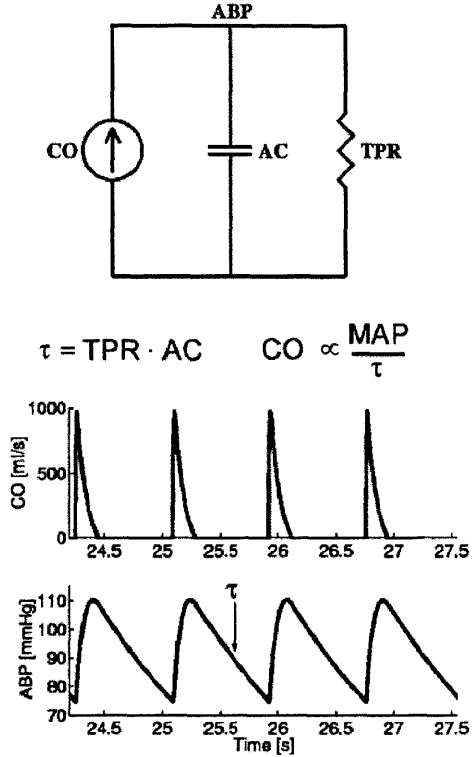


Fig. 2.4. The auto-regressive and moving average model
 CO is modeled as a train of PP aligned at the onset of systoles. Obtained from Mukkamala *et al.* (2006) [20].

The impulse response of the system $h[n]$ can be obtained from the AR and MA parameters:

$$h[n] = \sum_{j=1}^{p1} a[j]h[n-j] + \sum_{k=1}^{p2} b[k]\delta[n-k] \quad (2.19)$$

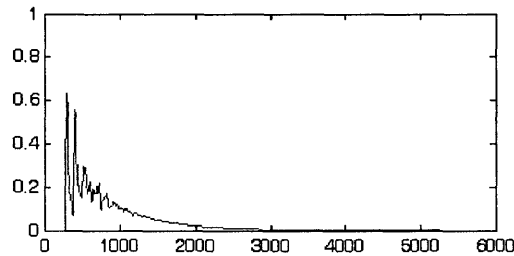


Fig. 2.5. Impulse response in ARMA model

A typical impulse response is shown in Fig. 2.5. The characteristic time constant τ is obtained by the decaying slope. The proportional time constant τ and MAP are used to calculate a proportional CO estimate:

$$CO = \frac{MAP}{TPR} \propto \frac{MAP}{\tau} \quad (2.20)$$

2.13. Summary

In this chapter, several cardiovascular indices estimation methods were introduced. If the cardiovascular system to monitor is ideally compliant with their assumptions, i.e., central ABP, no reflection from the peripheral circulation, no distortion, no large perturbation in ABP signals, and no external disturbance such as respiration, all the methods should work and provide low-error SV and CO estimates. However, that is not the case for measurements taken in clinical, surgery, and research settings.

The current challenge is to develop a robust model that is insensitive to disturbances external to the model in the way it processes, removes, or filters the recorded ABP signals. In the following chapters, other novel algorithms to estimate CO, SV, and ABF are introduced and validated.

3. Estimation of Stroke Volume and Cardiac Output

This chapter introduces new algorithms to continuously estimate SV, CO, and TPR. The algorithms are based on quantitative cardiovascular physiology. Each method utilizes a different assumption in calculating the characteristic time constant τ .

3.1. Minimum Variance Method

The ideal two-parameter Windkessel model is

$$\frac{F(t)}{C_a} = \frac{dP(t)}{dt} + \frac{P(t)}{\tau} \quad (2.2)$$

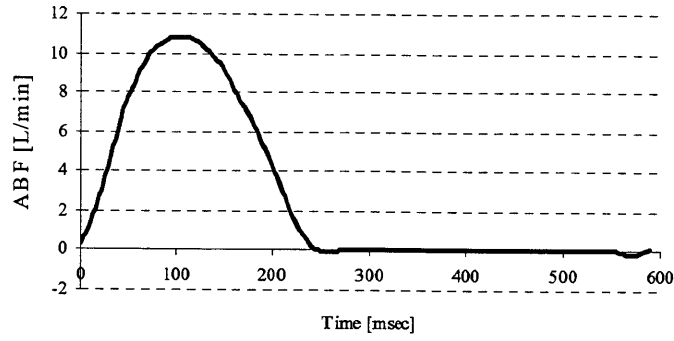
where τ is the characteristic time constant. Let β be the inverse of τ for convenience:

$$\beta \equiv \frac{1}{\tau} \quad (3.1)$$

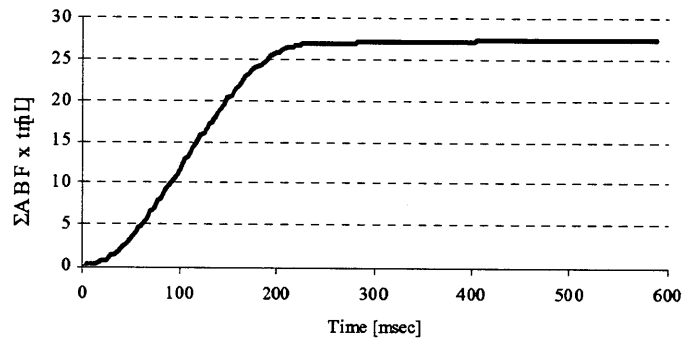
The integral of the beat is taken to obtain the proportional stroke volume of the beat:

$$\begin{aligned} \frac{SV}{C_a} &= \int_{t_D}^t \frac{F(t)}{C_a} dt \\ &= \int_{t_D}^t \left(\frac{dP(t)}{dt} + \beta P(t) \right) dt \\ &= P(t) - P(t_D) + \beta \int_{t_D}^t P(t) dt \end{aligned} \quad (3.2)$$

where t_D is the time of the end diastole of the preceding beat. SV is given by integrating systolic ABF; the integral of diastolic ABF ($t_S < t < T$) does not contribute to SV (Fig. 3.1). Therefore, the left item of (3.2) should be the same for all t that satisfy $t_S < t < T$. Therefore,



(a) ABF (t)



(a) $\Sigma ABF(t) \times t$

Fig. 3.1. Typical ABF waveform and its integral from the onset of systole to time t . With t in diastole, the integral of $ABF(t)$ (i.e., SV) does not change because $ABF(t)$ is approximately zero during diastole.

$$\begin{aligned}
 P(t_s) - P(t_D) + \beta \int_{t_D}^{t_s} P(t) dt &= P(t_s + \Delta t) - P(t_D) + \beta \int_{t_D}^{t_s + \Delta t} P(t) dt \\
 &= \dots \\
 &= P(T) - P(t_D) + \beta \int_{t_D}^{t_D + T} P(t) dt
 \end{aligned} \tag{3.3}$$

where Δt represents the time increment. Thus, one can find the β that provides the least variation of proportional stroke volume.

$$\text{Var}\left(\frac{SV_i}{C_a}\right) = E\left[\left(\frac{SV_i}{C_a}\right)^2\right] - \left(E\left[\frac{SV_i}{C_a}\right]\right)^2 \quad (3.4)$$

where $E[X]$ represents the expected value of X and i is the beat number. In this case, the expected value is the mean of X over the single beat T . The optimal value of β would satisfy Eq. (3.3) and provide the least variance in (3.4). The following steps provide an analytical solution for β .

The expected value of X is defined as

$$E[X] = \frac{1}{T} \int_{t_D}^{t_D+T} (X) dt \quad (3.5)$$

Therefore,

$$\begin{aligned} E\left[\left(\frac{SV_i}{C_a}\right)^2\right] &= E\left[\left(P(t) - P(t_D) + \beta \int_{t_D}^t P(t') dt'\right)^2\right] \\ &= \frac{1}{T} \int_{t_D}^{t_D+T} \left(P(t) - P(t_D) + \beta \int_{t_D}^t P(t') dt'\right)^2 dt \end{aligned} \quad (3.6)$$

and

$$\begin{aligned} E\left[\frac{SV_i}{C_a}\right] &= E\left[P(t) - P(t_D) + \beta \int_{t_D}^t P(t') dt'\right] \\ &= \frac{1}{T} \int_{t_D}^{t_D+T} \left(P(t) - P(t_D) + \beta \int_{t_D}^t P(t') dt'\right) dt \end{aligned} \quad (3.7)$$

The variance is defined as

$$\begin{aligned}
V &= \text{Var}\left(\frac{SV_i}{C_a}\right) \\
&= E\left[\left(\frac{SV_i}{C_a}\right)^2\right] - \left(E\left[\frac{SV_i}{C_a}\right]\right)^2 \\
&= \frac{1}{T} \int_{t_D}^{t_D+T} (P(t) - P(t_D) + \beta I(t))^2 dt - \left(\frac{1}{T} \int_{t_D}^{t_D+T} (P(t) - P(t_D) + \beta I(t)) dt\right)^2
\end{aligned} \tag{3.8}$$

where

$$I(t) = \int_{t_D}^t P(t') dt' \tag{3.9}$$

to describe V as

$$V = \frac{1}{T} \int_{t_D}^{t_D+T} (P(t) - P(t_D) + \beta I(t))^2 dt - \left(\frac{1}{T} \int_{t_D}^{t_D+T} (P(t) - P(t_D) + \beta I(t)) dt\right)^2 \tag{3.10}$$

To find β that minimizes the variance V ,

$$\begin{aligned}
\frac{\partial V}{\partial \beta} &= \frac{\partial}{\partial \beta} \frac{1}{T} \int_{t_D}^{t_D+T} (P(t) - P(t_D) + \beta I(t))^2 dt \\
&\quad - \frac{\partial}{\partial \beta} \frac{1}{T^2} \left(\int_{t_D}^{t_D+T} (P(t) - P(t_D) + \beta I(t)) dt \right)^2 \\
&= 0
\end{aligned} \tag{3.11}$$

Further process the equation to obtain an analytical solution:

$$\begin{aligned}
0 &= \frac{1}{T} \int_{t_D}^{t_D+T} \frac{\partial}{\partial \beta} (P(t) - P(t_D) + \beta I(t))^2 dt \\
&\quad - \frac{1}{T^2} \frac{\partial}{\partial \beta} \left(\int_{t_D}^{t_D+T} (P(t) - P(t_D) + \beta I(t)) dt \right)^2 \\
&= \frac{2}{T} \int_{t_D}^{t_D+T} (P(t) - P(t_D) + \beta I(t)) \cdot I(t) dt \\
&\quad - \frac{2}{T^2} \left(\int_{t_D}^{t_D+T} (P(t) - P(t_D) + \beta I(t)) dt \right) \frac{\partial}{\partial \beta} \left(\int_{t_D}^{t_D+T} (P(t) - P(t_D) + \beta I(t)) dt \right) \\
&= \frac{2}{T} \int_{t_D}^{t_D+T} (P(t) - P(t_D) + \beta I(t)) \cdot I(t) dt \\
&\quad - \frac{2}{T^2} \left(\int_{t_D}^{t_D+T} (P(t) - P(t_D) + \beta I(t)) dt \right) \int_{t_D}^{t_D+T} I(t) dt
\end{aligned} \tag{3.12}$$

Thus,

$$\int_{t_D}^{t_D+T} (P(t) - P(t_D) + \beta I(t)) \cdot I(t) dt = \frac{1}{T} \left(\int_{t_D}^{t_D+T} (P(t) - P(t_D) + \beta I(t)) dt \right) \int_{t_D}^{t_D+T} I(t) dt \tag{3.13}$$

Sort the equation in terms of β ,

$$\begin{aligned}
&\int_{t_D}^{t_D+T} (P(t) - P(t_D)) \cdot I(t) dt + \beta \int_{t_D}^{t_D+T} I(t)^2 dt \\
&= \frac{1}{T} \left(\int_{t_D}^{t_D+T} (P(t) - P(t_D)) dt \right) \int_{t_D}^{t_D+T} I(t) dt + \frac{\beta}{T} \left(\int_{t_D}^{t_D+T} I(t) dt \right)^2
\end{aligned} \tag{3.14}$$

Thus,

$$\begin{aligned}
\beta \int_{t_D}^{t_D+T} I(t)^2 dt - \frac{\beta}{T} \left(\int_{t_D}^{t_D+T} I(t) dt \right)^2 &= \frac{1}{T} \left(\int_{t_D}^{t_D+T} (P(t) - P(t_D)) dt \right) \int_{t_D}^{t_D+T} I(t) dt \\
&\quad - \int_{t_D}^{t_D+T} (P(t) - P(t_D)) \cdot I(t) dt
\end{aligned} \tag{3.15}$$

Therefore, the analytical solution of τ (inverse of β) is given by

$$\begin{aligned}
\tau &= \frac{1}{\beta} \\
&= \frac{\int_{t_D}^{t_D+T} I(t)^2 dt - \frac{1}{T} \left(\int_{t_D}^{t_D+T} I(t) dt \right)^2}{\frac{1}{T} \left(\int_{t_D}^{t_D+T} (P(t) - P(t_D)) dt \right) \int_{t_D}^{t_D+T} I(t) dt - \int_{t_D}^{t_D+T} (P(t) - P(t_D)) \cdot I(t) dt} \\
&= \frac{T \int_{t_D}^{t_D+T} I(t)^2 dt - \left(\int_{t_D}^{t_D+T} I(t) dt \right)^2}{\left(\int_{t_D}^{t_D+T} (P(t) - P(t_D)) dt \right) \int_{t_D}^{t_D+T} I(t) dt - T \int_{t_D}^{t_D+T} (P(t) - P(t_D)) \cdot I(t) dt}
\end{aligned} \tag{3.16}$$

The value of τ is used in (3.2) to calculate the proportional SV, and the time average of SV values over six minutes gives CO. In obtaining β , multiple beats ($M = 17$) were used to obtain a stable value of β and the value of β was applied to the central beat in the 17-beat moving window.

$$\begin{aligned}
\tau &= \frac{\sum_{m=1}^M T \int_{t_D}^{t_{D,m}+T_m} I_m(t)^2 dt - \sum_{m=1}^M \left(\int_{t_D}^{t_{D,m}+T_m} I_m(t) dt \right)^2}{\sum_{m=1}^M \left(\int_{t_{D,m}}^{t_{D,m}+T_m} (P_m(t) - P_m(t_D)) dt \right) \int_{t_{D,m}}^{t_{D,m}+T_m} I_m(t) dt - \sum_{m=1}^M T_m \int_{t_{D,m}}^{t_{D,m}+T_m} (P_m(t) - P_m(t_D)) \cdot I_m(t) dt}
\end{aligned} \tag{3.16a}$$

where m is the beat number.

3.2. Modified Herd's Method

This method stems from the notion that MAP and DBP are insensitive to distortion (Fig. 1.8 and [14]).

The hypothesis was that the pulse pressure method to estimate SV based on the Windkessel model [18]:

$$\frac{SV}{C} = SBP - DBP \quad (3.17)$$

can be improved by introducing MAP instead of SBP that is sensitive to distortion (Herd's work):

$$\frac{SV}{C} = MAP - DBP \quad (3.18)$$

The disadvantage of the method is that MAP takes a diastolic interval into consideration. Suppose the diastolic duration was extended after the aortic valve closure. For this beat, DBP remains almost the same as the preceding beats, but MAP becomes lower than the preceding beats. As a result, the algorithm underestimates the proportional SV using (3.18).

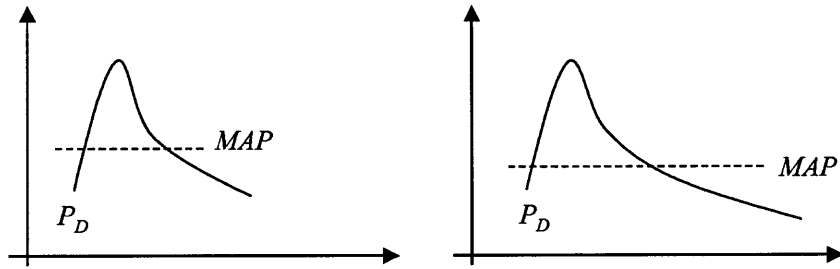


Fig. 3.2. Beats with a normal and abnormal diastolic interval.

An increased diastolic interval lowers the calculated MAP of the beat, and its stroke volume would be underestimated using Herd's method.

In this section, a modified Herd's method is proposed. MAP is regarded as a mean pressure value over the systolic interval.

$$\frac{SV}{C_a} = \int_{Systole} P(t) dt - DBP \quad (3.19)$$

This method requires the identification of end systole. In validating the method, a series of methods to identify end systole (section 5.4) are used.

3.3. Parabolic Aortic Blood Flow Model

This model approximates the Windkessel aortic blood flow as a parabolic flow curve:

$$F = At(T_s - t) \quad (3.20)$$

where A is a scaling factor, T_s is the time stamp of the end systole of the current beat, and t is time. SV of the beat is an integral of the flow from end diastole to end systole:

$$\begin{aligned} SV &= \int_0^{T_s} F(t) dt \\ &= A \int_0^{T_s} t(T_s - t) dt \\ &= \frac{AT_s^3}{6} \\ \therefore A &= \frac{6SV}{T_s^3} \end{aligned} \quad (3.21)$$

The ABP can be described as a sum of static ($P_0 \exp(-t/\tau)$, decaying end diastole from the preceding beat) and dynamic (decaying external input, i.e., ABF) components:

$$\begin{aligned} P(t) &= P_0 e^{-\frac{t}{\tau}} + \frac{1}{C_a} \int_0^t e^{-\frac{t-t'}{\tau}} F(t') dt' \\ &= P_0 e^{-\beta t} + \frac{6SV e^{-\beta t}}{C_a T_s^3} \int_0^t e^{\beta t'} (T_s - t') t' dt' \\ &= e^{-\beta t} \left\{ P_0 + \frac{6SV}{C_a T_s^3} \left(\frac{T_s}{\beta^2} + \frac{2}{\beta^3} \right) \right\} + \frac{6SV}{C_a T_s^3} \left\{ \frac{t^2}{\beta} + \left(\frac{T_s}{\beta} + \frac{2}{\beta^2} \right) t - \frac{T_s}{\beta^2} - \frac{2}{\beta^3} \right\} \end{aligned} \quad (3.22)$$

where

$$\beta \equiv \frac{1}{\tau} \quad (3.23)$$

Taking the average of both items in (3.22) over the systolic interval T_s ,

$$\begin{aligned}
\bar{P}_{systole} &\equiv \frac{1}{T_s} \int_0^{T_s} P(t) dt \\
&= \frac{1}{T_s} \int_0^{T_s} e^{-\beta t} \left\{ P_0 + \frac{6SV}{C_a T_s^3} \left(\frac{T_s}{\beta^2} + \frac{2}{\beta^3} \right) \right\} \\
&\quad + \frac{6SV}{C_a T_s^3} \left\{ \frac{t^2}{\beta} + \left(\frac{T_s}{\beta} + \frac{2}{\beta^2} \right) t - \frac{T_s}{\beta^2} - \frac{2}{\beta^3} \right\} dt \\
&= \frac{1-e^{-\gamma}}{\gamma} P_0 + \frac{6SV}{C_a \gamma^3} \left\{ \frac{1-e^{-\gamma}}{\gamma} \cdot \left(\frac{1}{\gamma^2} + \frac{2}{\gamma^3} \right) + \left(\frac{1}{6\gamma} - \frac{2}{\gamma^3} \right) \right\}
\end{aligned} \tag{3.24}$$

Therefore, the proportional $SV (Q/Ca)$ can be calculated as

$$\frac{SV}{C_a} = \gamma^3 \frac{\frac{1}{T_s} \int_0^{T_s} P(t) dt - \frac{1-e^{-\gamma}}{\gamma} P_0}{6 \left\{ \frac{1-e^{-\gamma}}{\gamma} \cdot \left(\frac{1}{\gamma^2} + \frac{2}{\gamma^3} \right) + \left(\frac{1}{6\gamma} - \frac{2}{\gamma^3} \right) \right\}} \tag{3.25}$$

where

$$\gamma \equiv \beta T_s \tag{3.26}$$

Here, by introducing Ohm's law:

$$\begin{aligned}
MAP &= CO \cdot TPR \\
&= CO \cdot \frac{\tau}{C_a}
\end{aligned} \tag{2.1}$$

a beat-to-beat CO can be calculated as

$$CO = \frac{SV}{T} \tag{3.27}$$

where T is the beat interval. Plugging (3.26) and (3.27) into (2.1),

$$\begin{aligned}
MAP &= \frac{SV}{C_a} \frac{\tau}{T} \\
&= \frac{SV}{C_a} \frac{1}{T\beta} \\
&= \frac{SV}{C_a} \frac{T_s}{T\gamma}
\end{aligned}
\tag{3.28}$$

Using multiple beats to in obtain stable value of τ ,

$$\begin{aligned}
\frac{1}{\sum T_i} \int_0^{\sum T_i} P(t) dt &= \tau \sum \frac{SV}{C_a} / \sum T_i \\
\Rightarrow \tau &= \frac{\frac{1}{\sum T_i} \int_0^{\sum T_i} P(t) dt}{\tau \sum \frac{SV}{C_a} / \sum T_i}
\end{aligned}
\tag{3.29}$$

Therefore, by plugging (3.26) and (3.29) into (3.25), one can obtain proportional SV. The proportional CO can be also calculated time-averaging the SV values.

3.4. Pressure Ratio Method

As can be seen in the Minimum Variance Method (Section 3.1), the Pressure Ratio Method takes into account the two-parameter Windkessel model and the fact that aortic blood flow is approximately zero during diastole. Starting from the Windkessel model:

$$\frac{SV}{C_a} = P(t) - P(t_D) + \beta \int_{t_D}^t P(t) dt
\tag{3.2}$$

Now, select two different ends of the integral: end systole t^{ES} and end diastole t^{ED} . Because the flow integral from end diastole t_D of the preceding beat to the end systole t^{ES} should be the same as that from end diastole of the preceding beat t_D to the current end diastole t^{ED} ,

$$\begin{aligned}
\frac{SV}{C_a} &= \int_{t_{i-1}^{ED}}^{t_i^{ES}} \frac{F(t)}{C_a} dt = P_i^{ES} - P_{i-1}^{ED} + \beta \cdot PSI_i \\
&= \int_{t_{i-1}^{ED}}^{t_i^{ED}} \frac{F(t)}{C_a} dt = P_i^{ED} - P_{i-1}^{ED} + \beta \cdot PI_i
\end{aligned} \tag{3.30}$$

where

$$PSI_i \equiv \int_{t_{i-1}^{ED}}^{t_i^{ES}} P(t) dt \tag{3.31}$$

and

$$PI_i \equiv \int_{t_{i-1}^{ED}}^{t_i^{ED}} P(t) dt \tag{3.32}$$

Therefore, one can calculate τ (inverse of β) and proportional SV by

$$\tau = \frac{1}{\beta} = \frac{PI_i - PSI_i}{P_i^{ES} - P_i^{ED}} \tag{3.33}$$

and the proportional SV of the beat can be calculated as

$$\begin{aligned}
\frac{SV_i}{C_a} &= \int_{t_{i-1}^{ED}}^{t_i^{ES}} \frac{F(t)}{C_a} dt = P_i^{ES} - P_{i-1}^{ED} + \frac{P_i^{ES} - P_i^{ED}}{PI_i - PSI_i} \cdot PSI_i \\
&= \int_{t_{i-1}^{ED}}^{t_i^{ED}} \frac{F(t)}{C_a} dt = P_i^{ED} - P_{i-1}^{ED} + \frac{P_i^{ES} - P_i^{ED}}{PI_i - PSI_i} \cdot PI_i
\end{aligned} \tag{3.34}$$

Furthermore, using multiple beats to obtain a stable value of $\beta=1/\tau$,

$$\begin{aligned}
\sum_{i=1}^N \frac{SV}{C_a} &= \sum_{i=1}^N (P_i^{ES} - P_{i-1}^{ED}) + \beta \cdot PSI_{i-1}^N \\
&= \sum_{i=1}^N (P_i^{ED} - P_{i-1}^{ED}) + \beta \cdot PI_{i-1}^N = P_N^{ED} - P_0^{ED} + \beta \cdot PI_{i-1}^N
\end{aligned} \tag{3.30a}$$

where

$$PSI_i^N \equiv \int_{t_{i-1}^{ED}}^{t_{i+N}^{ES}} P(t)dt = \sum_{i=1}^N PSI_i \quad (3.31a)$$

and

$$PI_i^N \equiv \int_{t_{i-1}^{ED}}^{t_{i+N}^{ED}} P(t)dt = \left(\sum_{i=1}^N T_i \right) \bar{P} \quad (3.32a)$$

Therefore, one can calculate τ (inverse of β) by

$$\tau = \frac{1}{\beta} = \frac{\left(\sum_{i=1}^N T_i \right) \bar{P} - \sum_{i=1}^N PSI_i}{\sum_{i=1}^N (P_i^{ES} - P_{i-1}^{ED}) - (P_N^{ED} - P_0^{ED})} \quad (3.33a)$$

The obtained β is used to calculate SV from (3.30).

3.5. Hybrid Model

This algorithm utilizes end-diastolic blood pressure (end-DBP) values, beat-MAP (MAP_i - MAP of a single beat), inter-beat interval (T_i), and the time interval from the onset of SBP to peak SBP (T_i^S) in the peripheral ABP waveform. These variables are selected for the CO and SV estimations because they are known to be relatively insensitive descriptors to the distortion of the ABP waveform in the arterial tree [1]. This notion was confirmed by analyzing the previously recorded Yorkshire swine data sets (Fig. 1.8). This new algorithm takes an approach to reconstruct ideal or theoretical Windkessel ABP waveforms by using the aforementioned descriptors.

3.5.1. Basic Model (*Model 1*)

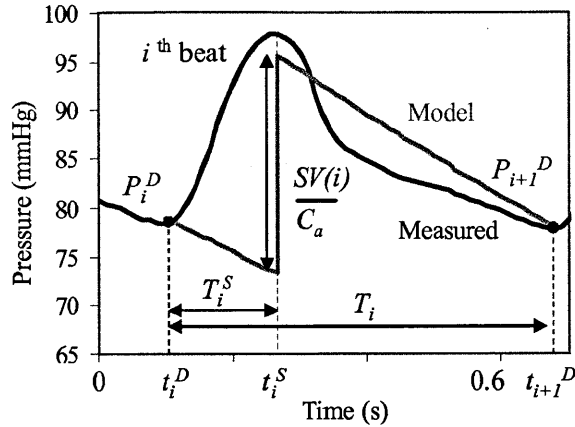


Fig. 3.3. Waveform of the measured femoral ABP and the theoretical Windkessel model ABP. Each systolic peak time (T_i^S) in the Windkessel ABP (gray) is aligned to that of the measured ABP (black). On a beat-to-beat basis, the Windkessel time constant (τ) is computed so that the beat-MAPs of the measured and calculated Windkessel waveforms are equal.

The new algorithm estimates SV using the end-DBP immediately preceding the current beat (P_i^D), the end-DBP at the end of the current beat (P_{i+1}^D), MAP_i , T_i , and T_i^S . In the two-parameter Windkessel model, proportional SV can be obtained from these variables as $SV(i)/C_a$.

Fig. 3.3 illustrates the measured ABP and the theoretical Windkessel model ABP. Although C_a declines with age [55], C_a is nearly constant on the time scale of months over a wide pressure range [45, 46]; thus, C_a was assumed to be constant throughout this relatively short experimental period. For each cardiac cycle, the two end-DBP values (P_i^D , P_{i+1}^D) were obtained.

Then, the theoretical Windkessel ABP waveform was generated using the following equations:

$$P(t) = P_i^D \exp\left(-\frac{(t-t_i^D)}{\tau_i}\right) \quad \text{for } t_i^D < t < t_i^S \quad (3.35)$$

$$P(t) = \left(P_i^D \exp\left(-\frac{T_i^S}{\tau_i}\right) + \frac{SV(i)}{C_a} \right) \exp\left(-\frac{(t-t_i^S)}{\tau_i}\right) \quad \text{for } t_i^S < t < t_{i+1}^D \quad (3.36)$$

where t_i^D and t_i^S are time stamps of the end of diastole (onset of systole) and the peak systolic point of the i^{th} ABP waveform, respectively. P_i^D is the end-DBP immediately preceding the i^{th} beat of the measured ABP. T_i^S and T_i are the intervals from the onset of systole to the peak systolic point and inter-beat interval of the i^{th} ABP waveform (onset of systole to onset of next systole), respectively. $SV(i)$ is the SV of the i^{th} beat. The step in the theoretical ABP waveform is aligned to the peak of the measured systolic ABP. The Windkessel time constant (τ) is adjusted so that for each beat, the MAP of the measured ABP equaled the MAP of the Windkessel ABP.

Taking the average of the ABP over the i^{th} beat using the above equations (3.35, 3.36), the MAP can be expressed in terms of T_i , P_i^D , P_{i+1}^D , $SV(i)$, τ_i , and C_a as follows:

$$MAP_i = \frac{1}{T_i} \int_{t_i^D}^{t_{i+1}^D} P_i(t) dt = \frac{\tau_i}{T_i} (P_i^D + \frac{SV(i)}{C_a} - P_{i+1}^D) \quad (3.37)$$

As shown in Fig. 3.3, the i^{th} -beat PP of the ideal Windkessel ABP from (3.35, 3.36) can be calculated by subtracting the two ABP values at T_i^S , yielding:

$$\frac{SV(i)}{C_a} = P_{i+1}^D \exp\left(\frac{(T_i - T_i^S)}{\tau_i}\right) - P_i^D \exp\left(-\frac{T_i^S}{\tau_i}\right) \quad (3.38)$$

Substituting (3.38) into (3.37),

$$MAP_i = \frac{\tau_i}{T_i} \left\{ P_{i+1}^D \left(\exp\left(\frac{(T_i - T_i^S)}{\tau_i}\right) - 1 \right) + P_i^D \left(1 - \exp\left(-\frac{T_i^S}{\tau_i}\right) \right) \right\} \quad (3.39)$$

Equation (3.39) can be numerically solved for τ_i . $SV(i)/C_a$ thus may be estimated from the values of P_i^D , P_{i+1}^D , MAP_i , T_i , and T_i^S . The value of the peak systolic blood pressure, which is more prone to distortion than end-DBP, is not used.

The new method can estimate τ on a beat-by-beat basis. In actual implementation, the median value of τ is calculated after applying (3.39) over a 20-second moving window; this median value is regarded as the τ of the beat in the middle of the 20-second moving window. The SV of each beat is calculated by shifting the 20-second moving window on a beat-to-beat basis. The 20-second window was empirically found by the

authors to provide the smallest estimation errors over a wide range of physiological conditions.

τ equals the product of TPR and C_a . C_a is assumed to be constant. TPR varies with changes in vasomotor tone, which generally occur slowly on a time scale not faster than 20 seconds. However, SV which depends on other factors (such as changes in filling pressure, filling time, and contractility) can vary on a beat-by-beat basis (e.g., consider a premature ventricular beat). Thus, estimating the tau parameter as the median of a 20-second window reduces the noise in this estimation without compromising our ability to estimate beat-to-beat changes in SV.

3.5.2. Reduced Parameter Models (*Model 2 and 3*)

Models 2 and 3

Model 1 is a five-parameter model:

$$SV_{prop1}(i) \equiv \frac{SV(i)}{C_a} = f(MAP_i, P_i^D, P_{i+1}^D, T_i, T_i^S) \quad (3.40)$$

Here, SV_{prop} is proportional to SV with a proportionality constant of $1/C_a$.

In addition to *Model 1*, four- and three-parameter versions of the model were introduced. In *Model 2*, T_i^S is set to zero and the step in the theoretical ABP is set to coincide with the end of diastole/onset of systole.

$$SV_{prop2}(i) = f(MAP_i, P_i^D, P_{i+1}^D, T_i) \quad (3.41)$$

Model 3 is the same as *Model 2* except that it is assumed that $P_i^D = P_{i+1}^D$:

$$SV_{prop3}(i) = f(MAP_i, P_i^D, T_i) \quad (3.42)$$

Each model is illustrated in Fig. 3.4.

3.5.3. Hybrid Model

Of the five measured parameters, there are three dimensionless variables (T_i^S/T_b , P_i^D/MAP_b , and P_{i+1}^D/MAP_i) that characterize the ABP waveform. Thus, combining the three models for estimating SV_{prop} should span the space covered by the three dimensionless parameters. Thus, one can think of the three proportional estimates of SV generated by the models as a generalized vector of estimates that span the parameter space. A hybrid model can be used to combine the three estimates of SV_{prop} to form a specific estimate of SV_{prop} .

One hybrid model for estimating the SV of the i^{th} beat SV_i is given by:

$$SV_i = C_a SV_{prop1}(i) \cdot \left(\frac{SV_{prop2}(i)}{SV_{prop1}(i)} \right)^{a_1} \cdot \left(\frac{SV_{prop3}(i)}{SV_{prop1}(i)} \right)^{a_2} \quad (3.43)$$

Note that the equation estimates SV_i in terms of geometrically weighted estimates of SV_{prop} from *Models 1-3* using exponents a_1 and a_2 . For example, if $a_1=0$ and $a_2=1$, then $SV=C_a SV_3$ and (3.42) is adopted. The coefficients allow non-discrete switching between the three models. By taking the natural logarithm of (3.43), the equation becomes linear

$$y(i, j) = D(j) + y_1(i, j) + a_1 X_1(i, j) + a_2 X_2(i, j) \quad (3.44)$$

where i is the beat number, j is the subject number, $y=\ln(SV_i)$, $D(j)=\ln(C_a)$, $y_1=\ln(SV_{prop1})$, $X_1=\ln(SV_{prop2}/SV_{prop1})$, and $X_2=\ln(SV_{prop3}/SV_{prop1})$. Linear regression and least mean square error analysis yield arterial compliances $C_a(j)$, a_1 , and a_2 . The parameters a_1 and a_2 are common among all the subjects, and each compliance $C_a(j)$ is unique to the subject j .

Redefine $y - y_1$ as Y :

$$Y(i, j) = D(j) + a_1 X_1(i, j) + a_2 X_2(i, j) \quad (3.45)$$

Define

$$E(i, j) \equiv Y(i, j) - D(j) - a_1 X_1(i, j) - a_2 X_2(i, j) \quad (3.46)$$

and

$$E \equiv \sum_{j=1}^L \sum_{i=1}^{N(j)} \{Y(i, j) - D(j) - a_1 X_1(i, j) - a_2 X_2(i, j)\}^2 \quad (3.47)$$

where $N(j)$ is the number of beats recorded from animal/subject j .

To minimize E with a 's,

$$\frac{\partial E}{\partial a_m} = 2 \sum_{j=1}^L \sum_{i=1}^{N(j)} \{Y(i, j) - D(j) - a_1 X_1(i, j) - a_2 X_2(i, j)\} (-X_m(i, j)) = 0 \quad (3.48)$$

$$\Rightarrow \sum_{j=1}^L \sum_{i=1}^{N(j)} Y(i, j) X_m(i, j) = \sum_{j=1}^L \sum_{i=1}^{N(j)} D(j) X_m(i, j) + \sum_{k=1}^2 a_k \sum_{j=1}^L \sum_{i=1}^{N(j)} X_k(i, j) X_m(i, j) \quad (3.49)$$

or

$$\begin{aligned} & \sum_{j=1}^L \sum_{i=1}^{N(j)} Y(i, j) X_1(i, j) \\ &= \sum_{j=1}^L D(j) \sum_{i=1}^{N(j)} X_1(i, j) + a_1 \sum_{j=1}^L \sum_{i=1}^{N(j)} X_1(i, j) X_1(i, j) + a_2 \sum_{j=1}^L \sum_{i=1}^{N(j)} X_2(i, j) X_1(i, j) \\ & \sum_{j=1}^L \sum_{i=1}^{N(j)} Y(i, j) X_2(i, j) \\ &= \sum_{j=1}^L D(j) \sum_{i=1}^{N(j)} X_2(i, j) + a_1 \sum_{j=1}^L \sum_{i=1}^{N(j)} X_1(i, j) X_2(i, j) + a_2 \sum_{j=1}^L \sum_{i=1}^{N(j)} X_2(i, j) X_2(i, j) \end{aligned} \quad (3.50)$$

Also, change the D 's to minimize E

$$\begin{aligned} \frac{\partial E}{\partial D_n} &= -2 \sum_{i=1}^{N(j)} \{Y(i, n) - D(n) - a_1 X_1(i, n) - a_2 X_2(i, n)\} \\ &= 0 \end{aligned} \quad (3.51)$$

$$\Rightarrow \sum_{i=1}^{N(n)} Y(i, n) = \sum_{i=1}^{N(n)} Y(i, n) + a_1 \sum_{i=1}^{N(n)} X_1(i, n) + a_2 \sum_{i=1}^{N(n)} X_2(i, n) \quad (3.52)$$

Therefore,

$$\begin{aligned} \sum_{i=1}^{N(1)} Y(i, 1) &= \sum_{i=1}^{N(1)} Y(i, 1) + a_1 \sum_{i=1}^{N(1)} X_1(i, 1) + a_2 \sum_{i=1}^{N(1)} X_2(i, 1) \\ \dots \\ \sum_{i=1}^{N(L)} Y(i, L) &= \sum_{i=1}^{N(L)} Y(i, 1) + a_1 \sum_{i=1}^{N(L)} X_1(i, L) + a_2 \sum_{i=1}^{N(L)} X_2(i, L) \end{aligned} \quad (3.53)$$

Combining them, the following matrix can be obtained:

$$\begin{pmatrix} \sum_{i=1}^{N(1)} Y(i, 1) \\ \vdots \\ \sum_{i=1}^{N(L)} Y(i, L) \\ \sum_{j=1}^L \sum_{i=1}^{N(j)} Y(i, j) X_1(i, j) \\ \sum_{j=1}^L \sum_{i=1}^{N(j)} Y(i, j) X_2(i, j) \end{pmatrix} = \begin{pmatrix} N_1 & \dots & \dots & 0 & \sum_{i=1}^{N(1)} X_1(i, 1) & \sum_{i=1}^{N(1)} X_2(i, 1) \\ \vdots & N_2 & \dots & 0 & \sum_{i=1}^{N(2)} X_1(i, 2) & \sum_{i=1}^{N(2)} X_2(i, 2) \\ 0 & \dots & \ddots & 0 & \vdots & \vdots \\ 0 & 0 & \dots & N_L & \sum_{i=1}^{N(L)} X_1(i, L) & \sum_{i=1}^{N(L)} X_2(i, L) \\ \sum_{i=1}^{N(1)} X_1(i, 1) & \dots & \dots & \sum_{i=1}^{N(L)} X_1(i, L) & \sum_{j=1}^L \sum_{i=1}^{N(j)} X_1(i, j) X_1(i, j) & \sum_{j=1}^L \sum_{i=1}^{N(j)} X_2(i, j) X_1(i, j) \\ \sum_{i=1}^{N(1)} X_2(i, 1) & \dots & \dots & \sum_{i=1}^{N(L)} X_2(i, L) & \sum_{j=1}^L \sum_{i=1}^{N(j)} X_1(i, j) X_2(i, j) & \sum_{j=1}^L \sum_{i=1}^{N(j)} X_2(i, j) X_2(i, j) \end{pmatrix} \begin{pmatrix} D_1 \\ \vdots \\ D_L \\ a_1 \\ a_2 \end{pmatrix} \quad (3.54)$$

The parameters a_1 and a_2 are common among all the animals, and each compliance $C_a(j)$ is unique to the animal j .

Although (3.45) is a first-order equation, it is possible to generalize the hybrid model by introducing X_1 and X_2 raised to higher powers. Equation (3.45) can be generalized as

$$y(i, j) = D(j) + y_0(i, j) + \sum_{M=1}^{M_{\max}} \sum_{q=0}^M {}_M C_q \cdot a_{Mq} \cdot (X_1(i, j))^{M-q} (X_2(i, j))^q \quad (3.55)$$

where M_{\max} is the model order and ${}_M C_q$ is the binomial coefficient, while a_{Mq} are the parameters to be found by the linear regression analysis. For the derivation and implementation of (3.55), see Appendix A.

Once the parameters are obtained, SV is calculated as

$$SV = \exp(y) \quad (3.56)$$

CO is calculated by averaging SV over the six-minute window that overlaps every three minutes.

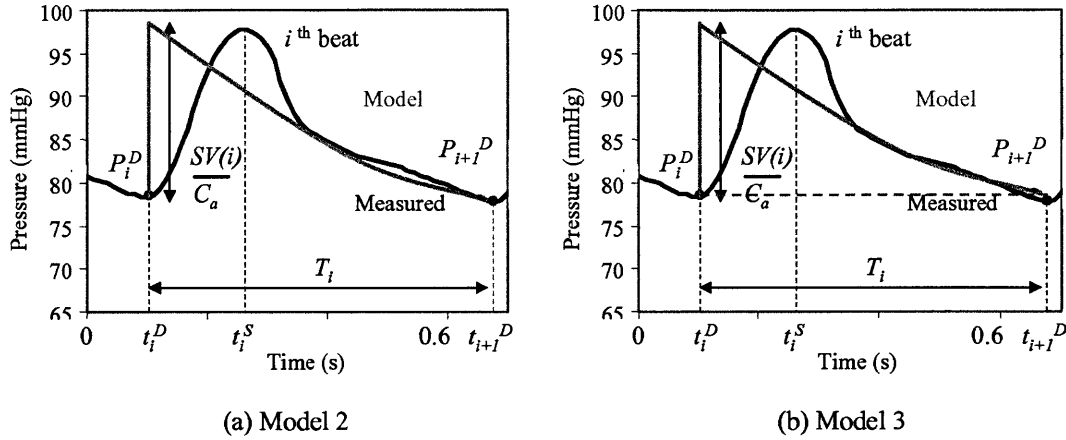


Fig. 3.4. Model 2 and 3 of the Hybrid Model.

3.5.4. Implementation

The algorithms were implemented in the following steps. First, all the characteristic points in the ABF and ABP waveforms were labeled using a labeling algorithm described in Chapter 5. The ABF characteristic points are the onset of systole, peak systole, the first dip after the peak of systole (valve closure point), and end of diastole. The ABP characteristic points are the onset of systole, peak systole, onset of diastole mapped from the ABF characteristic point, and end of diastole. Secondly, reference CO and SV were calculated from the measured aortic blood flow by the flow probe. The following sections describe the implementation of each method.

End-DBP (P^D), time interval (T), time to systolic peak (T^S), and MAP were defined by the analysis of femoral and radial ABP and applied to (3.39) to obtain the Windkessel time constant (τ). The median values of τ and T^S over a 20-second moving window were used to minimize the error due to outliers. The values of τ were applied to (3.40 - 3.42) to estimate the proportional SV (SV_{prop1} , SV_{prop2} , and SV_{prop3}) on a

beat-to-beat basis in each model. The measured SV and SV_{prop1} , SV_{prop2} , SV_{prop3} were used to calculate the C_a of each animal subject and the parameters a_{Mq} in (3.54) using linear regression and least mean square error analysis. The obtained parameters a_{Mq} and C_a were applied to (3.55), and the final SV was estimated. To compare with other CO estimation methods, the beat-to-beat SV estimates were averaged every six minutes. The order M_{max} in (3.55) was determined by a minimum description length (MDL) criterion [54, 56].

In the implementation above, all the SV data were used as pilot data to obtain parameters using (3.54). Another way to calculate parameters is to use half of the SV values in the data sets as pilot data to obtain parameters and apply the parameters to the latter half of the data. These results are also reported in Chapter 6.

4. Estimation of Aortic Blood Flow Waveforms

Aortic blood flow (ABF) is the instantaneous blood flow in the aorta and one of the most important cardiovascular indices. Currently, ABF is not clinically available in general. The availability of ABF will be clinically useful to: (1) calculate SV and CO by beat-to-beat integration of the ABF waveform and time-averaging, respectively; (2) evaluate contractile function of the left ventricle during normal and abnormal beats; and (4) adjust the timing delay of bi-ventricular pacing. In particular, SV and CO are direct indicators of hemodynamic abnormality and are useful in clinical and surgical settings.

The most accurate method to continuously measure ABF is an ultrasonic flow probe surgically placed around the aortic root. The drawback of the flow probe is again that it involves a highly invasive open-chest surgical procedure [20]. Non-invasive methods include echocardiography that require skilled technician to hold the probe at the correct angle on the patient's body. Thus, long-term continuous measurement is not feasible. PCM is also a promising approach for continuous, non-invasive or minimally invasive ABF monitoring because ABP is accessible, and it is easy to implement in the existing continuous ABP measurement systems.

In this chapter, a new algorithm to estimate ABF waveforms by the analysis of ABP is introduced and validated. The arterial tree is modeled as a system with ABF input and ABP output. The key step of the procedure is to obtain a set of auto-regressive parameters and impulse responses from ABP to ABF by the analysis of the diastolic ABP waveforms; because ABF input to the peripheral circulation is approximately zero during diastole [57], diastolic ABP waveform analysis provides auto-regressive parameters of the model. The parameters are obtained on a beat-to-beat basis and are applied to each ABP waveform to estimate the ABF waveform.

4.1. Algorithm

4.1.1. Model Description

Over a short time interval, the cardiovascular system can be described as a time-invariant system with an input of ABF ($F[n]$) and output of ABP ($P[n]$), as illustrated in Fig. 4.1.

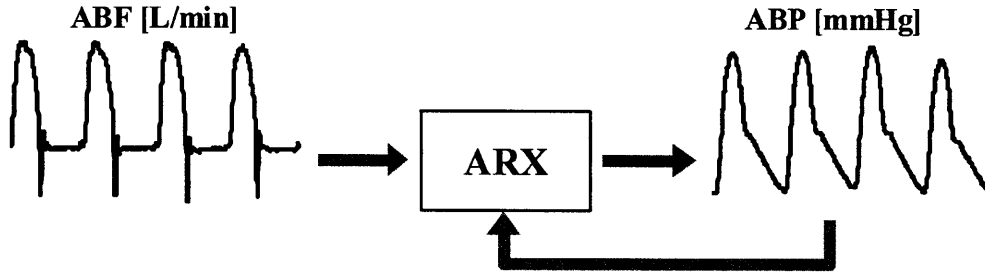


Fig. 4.1. Auto-regressive model with exogenous input.

The ABP value $P[n]$ in the interval can be described in an auto-regressive exogenous (ARX) model:

$$P[n] = \sum_{j=1}^L a[j]P[n-j] + \alpha F[n] \quad (4.1)$$

where $a[j]$ are weighting coefficients, L is the parameter length, and α is a scaling factor (i.e., coefficient for the exogenous input $F[n]$). The ARX model can be re-described as

$$\alpha F[n] = P[n] - \sum_{j=1}^L a[j]P[n-j] \quad (4.2)$$

As shown in Fig. 1.3, there is no input to the system during diastole:

$$0 = P[n] - \sum_{j=1}^L a[j]P[n-j] \quad (4.3)$$

Therefore, the weighting coefficients $a[j]$ are auto-regressive (AR) parameters. The AR parameters $a[j]$ can be obtained by solving the matrix equation (least square error method) derived from multiple beats:

$$\begin{bmatrix} P_1[n] \\ P_1[n+1] \\ \vdots \\ P_1[n+N_1-1] \\ \vdots \\ P_{17}[n] \\ P_{17}[n+1] \\ \vdots \\ P_{17}[n+N_{17}-1] \end{bmatrix} = \begin{bmatrix} P_1[n-1] & \cdots & P_1[n-L] \\ P_1[n] & \cdots & P_1[n-L-1] \\ \vdots & \ddots & \vdots \\ P_1[n+N_1-2] & \cdots & P_1[n-L+N_1-1] \\ \vdots & & \vdots \\ P_{17}[n-1] & \cdots & P_{17}[n-L] \\ P_{17}[n] & \cdots & P_{17}[n-L-1] \\ \vdots & \ddots & \vdots \\ P_{17}[n+N_{17}-2] & \cdots & P_{17}[n-L+N_{17}-1] \end{bmatrix} \begin{bmatrix} a[1] \\ a[2] \\ \vdots \\ a[L] \end{bmatrix} \quad (4.4)$$

where $P[n]$ are the ABP values in the i^{th} beat and N_i is the number of diastolic samples in the i^{th} beat ($1 < i < M$) where M is the number of the beats in the moving window. An $M = 17$ moving window size was empirically found to be optimal and adopted. Typical $a[j]$ are shown in Fig. 4.2(a).

The scaling factor α can be obtained by the following procedure. By taking the average of both sides of (4.2):

$$\alpha = \frac{\left(1 - \sum_{j=1}^L a[j]\right) \cdot MAP}{CO} \quad (4.5)$$

where MAP is the mean arterial pressure. Ohm's law gives

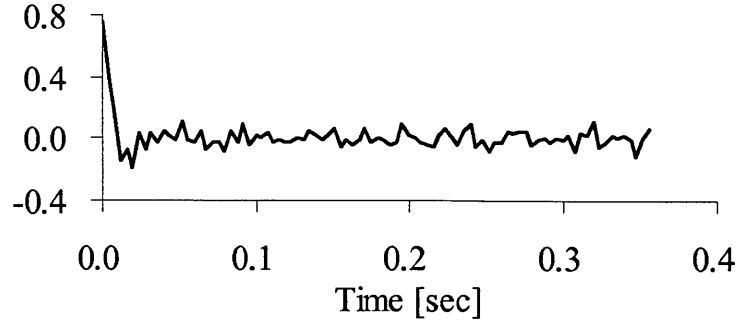
$$MAP = CO \cdot TPR \quad (4.6)$$

The characteristic time constant of the system can be described by the product of C_a and TPR :

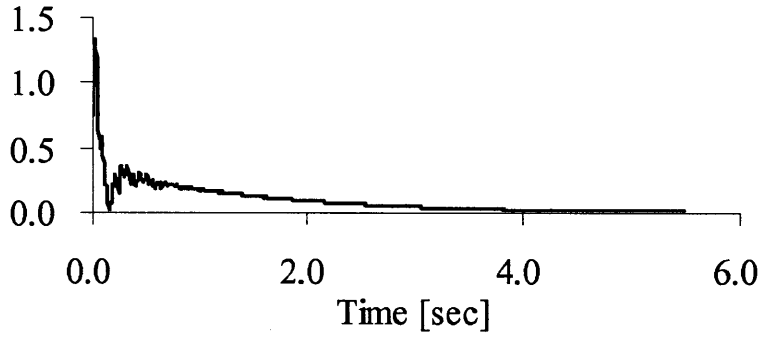
$$\tau = C_a \times TPR \quad (4.7)$$

where τ can be obtained by investigating the exponentially decaying curve of the impulse response of the system $h[n]$ shown in Fig. 4.2(b):

$$h[n] = \sum_{j=1}^L a[j]h[n-j] + \delta[n] \quad (4.8)$$



(a) AR parameters



(b) Impulse response

Fig. 4.2. Typical AR parameters and impulse response of the ARX model. Obtained from radial ABP data in Swine #4.

The equations (4.5) – (4.7) can re-describe the scaling factor α as

$$\alpha = \frac{\tau}{C_a} \left(1 - \sum_{j=1}^L a[j] \right) \quad (4.9)$$

Therefore, the instantaneous ABF can be calculated as

$$F[n] = \frac{C_a}{\tau \cdot \left(1 - \sum_{j=1}^L a[j] \right)} \left(P[n] - \sum_{j=1}^L a[j] P[n-j] \right) \quad (4.10)$$

Assuming C_a is constant, the proportional ABF can be obtained as

$$\begin{aligned}
F_{calc}[n] &= \frac{F[n]}{C_a} \\
&= \frac{\left(P[n] - \sum_{j=1}^L a[j]P[n-j] \right)}{\tau \cdot \left(1 - \sum_{j=1}^L a[j] \right)}
\end{aligned} \tag{4.11}$$

In the following subsection, the method for obtaining the AR parameter length L is presented.

4.1.2. Criterion for Selecting AR Parameter Length

In obtaining the proportional instantaneous flow $F[n]$ in equation (4.11), the determination of the AR parameter length L (i.e., model order) is the key step because L influences all the other parameters; L determines the size of the matrix equation (4.4) and the length of $a[j]$. The values of $a[j]$ determine the shape of the impulse response (i.e., time constant τ) as well as the summation of $\Sigma a[j]$. Finally, the scaling factor α is determined by τ and $a[j]$, which both depend on L . The author attempted a fixed length or fixed ratio of $L/RRinterval$. However, the fixed L or fixed ratio of $L/RRinterval$ failed to provide reasonable ABF waveforms as well as consistent scaling factors. An adaptive algorithm to update L was needed.

As mentioned earlier, L determines the other parameter values in (4.11). Different L values provide different sets of parameter values. Fig. 4.3 shows the parameter values $\Sigma a[j]$, τ , and α as evaluation functions of L . For each model order L , equation (4.4) was solved to obtain $a[j]$ and consequently the other parameters. As can be seen, there are local minima and maxima in each graph. The L value that provides local minima/maxima of the evaluation function could be the correct AR parameter length. In addition, the proportional ABF (within a scaling factor of C_a) was also calculated by (4.11) for each L and was investigated in the following evaluation functions:

- Smoothness of calculated systolic ABF

$$Smoothness = \sum_{systole} (\hat{F}_{calc}[i] - \hat{F}_{calc}[i-1]) \quad (4.12)$$

where \hat{F} is a normalized instantaneous blood flow waveform.

- Flatness of calculated diastolic ABF (errors in the diastolic ABF signal)

$$MDL = 1 + \frac{L \cdot \ln(N_d)}{N_d} \cdot \sum_{diastole} F_{calc}[i]^2 \quad (4.13)$$

$$AIC = \frac{\sum_{diastole} F_{calc}[i]^2}{N_d} \cdot \frac{1 + L/N_d}{1 - L/N_d} \quad (4.14)$$

where N_d is the total length of diastolic durations within the 17-beat moving window.

- Standard deviation of diastolic ABF signal
- Standard deviation of systolic ABF signal
- Area of negative values in the calculated ABF

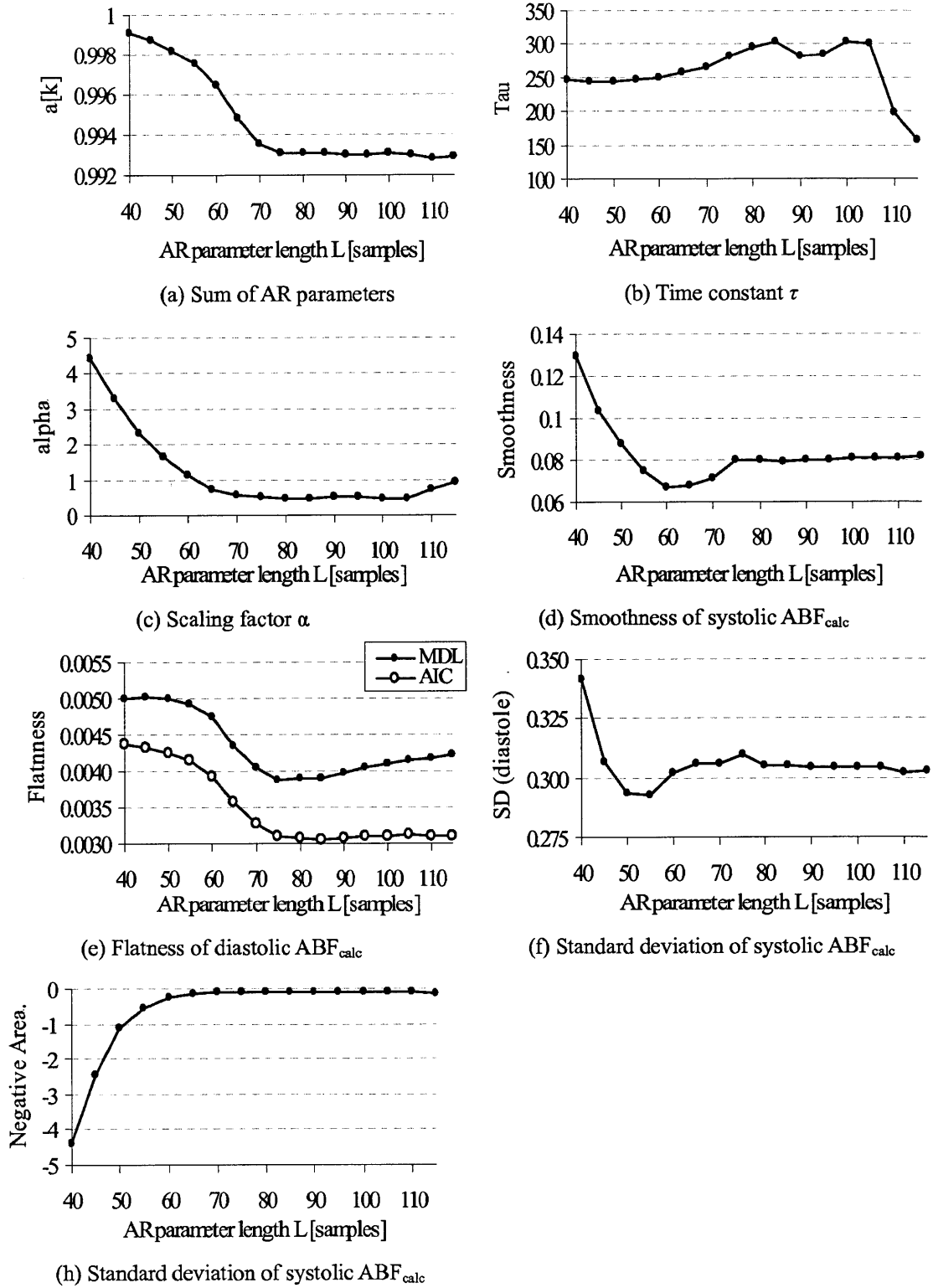


Fig. 4.3. ABF determination parameters as functions of AR parameter length L .

Among these evaluation functions, $\Sigma a[j]$ provided the best SV estimation and ABF waveforms (reported in the following section, Table 6.9). Therefore, an AR parameter length $L[i]$ of the i^{th} beat that minimized $\Sigma a[j]$ was adopted.

The author also found that the changes in L (defined as $L[i] - L[i-1]$) occur mostly within five samples (~ 20 [msec]) as shown in Fig. 4.4. Therefore, the numerical search for L was limited to within $L[i-1]-5 < L[i] < L[i-1]+5$ (at 250-Hz sampling frequency) to speed up computation time. The initial L value was arbitrarily set as 75 samples (=300 [msec]).

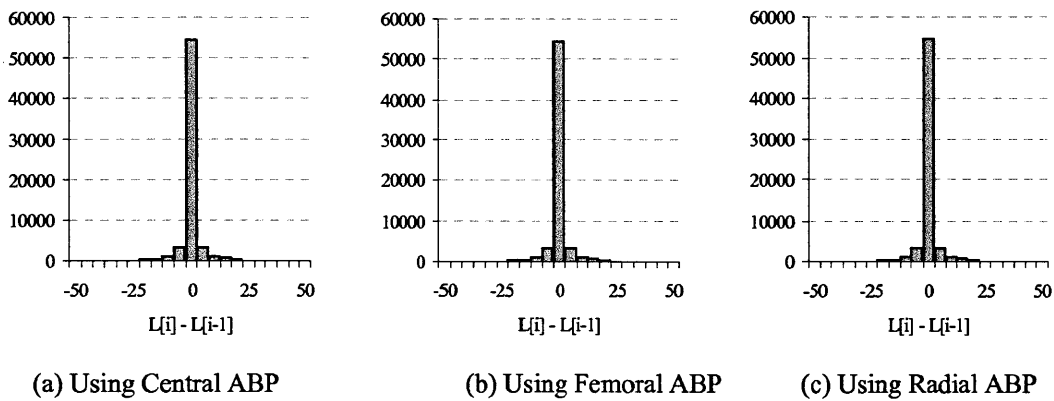


Fig. 4.4. Histogram of the difference of the selected AR parameter lengths. The difference is defined as $L[i] - L[i-1]$. The standard deviations are 4.8, 5.2, and 5.7, and over 92.9, 93.8, and 92.7% of the data reside within ± 5 samples, respectively.

The integrals of $F[n]$ were calculated on a beat-to-beat basis to obtain SV estimates, and the time averages of SV were calculated to obtain CO estimates.

The onset of diastole in each beat was identified by using the measured ABF, and the diastolic duration N was given in each ABF estimation procedure. In practical settings, there would be cases where one cannot identify onsets of diastoles. To investigate such cases, sensitivity analyses were conducted to test the impact of error in determining the onset of diastole (section 7.2.2).

4.2. Conditioning of Arterial Blood Pressure Data

For the sake of easing the parameter computation, the raw ABP data were horizontally and vertically scaled (Fig. 4.5(b), Fig. 4.6) so that all the beats in the 17-beat window had the same systolic and diastolic ABP values, RR interval, and diastolic duration as those of the middle beat in the window (i.e., ninth beat). Note that this data conditioning was done solely for parameter acquisition. Once AR parameters were obtained, they were applied to the raw ABP waveforms. Then, only the estimated ninth ABF waveform in the window was adopted. This procedure was applied to the moving 17-beat window throughout the ABP data.

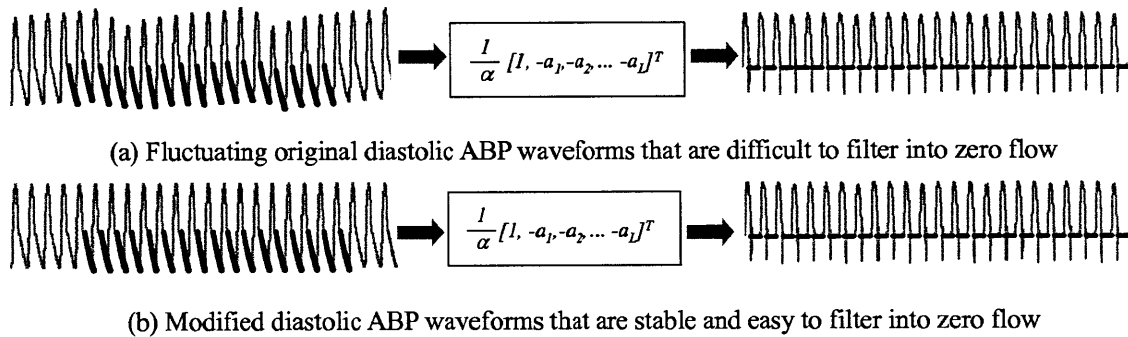


Fig. 4.5. Illustration of original (a) and modified (b) ABP waveforms.

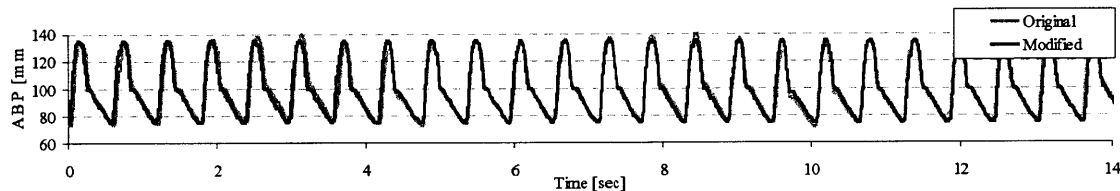


Fig. 4.6 Original and modified femoral ABP waveforms in Swine #5.

The original beat-to-beat instantaneous ABP waveforms (gray) are scaled horizontally and vertically so that all the SBP, DBP, PP and RR intervals of the beats in the window are equal (black).

The conditioning of the data to synthesize the systolic and diastolic ABP within the moving window was a key necessary process. Ideally, the system does not receive any perturbation other than ABF and

ABP and is not time-invariant within the moving window. Then, one can use a long window to include all the modes excited within the window to conduct system identification. However, without conditioning, one often observes divergence in the impulse response, and estimated ABF before scaling had noisy waveforms. The cause of the instability was varying ABP data that incur computational challenges in obtaining the AR parameters. For example, beat-to-beat MAP values are, in general cases, rapidly changing on a beat-to-beat basis due to respiration or a physiological feedback system in response to vaso-active drugs; thus, the range of diastolic ABP values varies from one beat to another within a window. Such time-variant data force the algorithm (4.4) to find a compromised single set of AR parameters that can filter multiple diastolic ABP waveforms to reduce the diastolic signal amplitude down to zero. Also, if the length of the RR interval and diastolic duration vary among 17 beats in the window, it is difficult to find a single AR parameter length L that satisfies all beats. Thus, the data-conditioning was conducted to relax the computational challenge in AR parameter acquisition. Although the beats in the moving window are rescaled horizontally (resampling) and vertically (rescaling) for the aforementioned purpose, this procedure was only used to obtain AR parameters of the window. The AR parameters were applied to the original ABP waveforms to obtain ABF. Therefore, the physiological changes occurring within a shorter interval than the window size (e.g., respiration) can be seen in the estimated ABF.

4.3. Model Validation

4.3.1. Validation Steps

The algorithm was implemented in the following steps. First, all the characteristic points in the ABF and ABP waveforms were labeled using a labeling algorithm described in Chapter 5. The ABF characteristic points are the onset of systole, peak systole, and the first dip after the peak of systole (valve closure point). The ABP characteristic points are the onset of systole, peak of systole, onset of diastole mapped from the ABF characteristic point, and end of diastole.

For determining the AR parameter order L , $\Sigma a[j]$, smoothness of systolic F_{calc} , and negative area of F_{calc} are used and compared. Because MDL, AIC, and other evaluation functions provided high SV errors as well as unreasonable ABF waveforms during initial investigations, only $\Sigma a[j]$, smoothness of systolic F_{calc} , and negative area of F_{calc} are reported.

4.3.2. Error Criteria

SV, CO, TPR waveform analysis

The estimation errors are defined in this thesis as RNMSEs:

$$RNMSE = 100 \sqrt{\frac{\sum_{n=1}^N \left(\frac{Meas - Est}{Meas} \right)^2}{N - N_f}} \quad (4.15)$$

where $MEAS$ and EST are measured and estimated values, N is the number of data points, and N_f is the number of free parameters.

For statistical analysis, one-way ANOVA was conducted to find statistical significance among the SV, CO, and TPR estimation methods in conjunction with the end systole identification methods. If a significance difference(s) was found, Scheffé's test was conducted. Statistical significance was defined as $p < 0.05$.

ABF waveform analysis

All the signal processing and analyses were conducted by MATLAB R2009a (The Mathworks Inc., Natick, MA). The standard deviation (SD), skewness, and kurtosis of the estimated systolic ABF waveforms were compared to those of the measured waveforms on a beat-to-beat basis. Take the SD comparison, for example. First, SD values of the measured and estimated systolic ABF were calculated on a beat-to-beat basis (steps shown in Fig. 6.47). Then, the differences of each SD ($SD_{ABFmeas} - SD_{ABFcalc}$) were calculated and plotted on a histogram. In the same manner, the differences (errors) of the skewness and kurtosis of the calculated ABF waveforms were investigated as well. The skewness (s) and kurtosis

(k) were given by

$$s = \frac{E(F_s - \mu)^3}{\sigma^3} \quad (4.16)$$

$$k = \frac{E(F_s - \mu)^4}{\sigma^4} \quad (4.17)$$

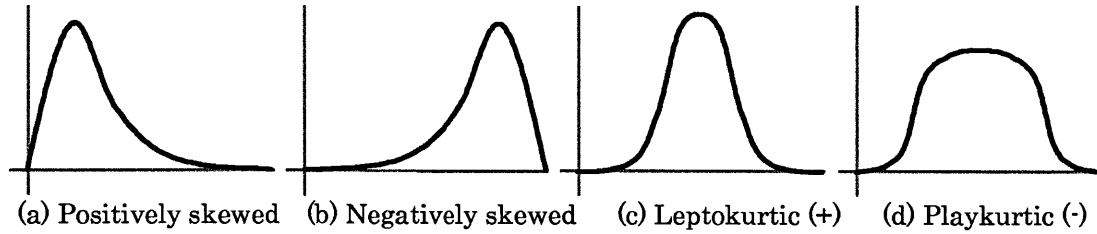


Fig. 4.7. Skewness and Kurtosis.

Example waveforms of positive and negative skewness (a-b) and positive and negative kurtosis (c-d).

where F_s is the ABF (measured or estimated); μ and σ are the mean and standard deviation of F_s , respectively; and $E[.]$ represents the expected value. Positive s values represent early peaks and elongated tails at the right, and positive k values represent sharp peaks compared to a normal distribution (Fig. 4.7). The skewness and kurtosis errors were defined as the difference between the measured and estimated values. The error of the algorithm was compared with the error of the standard Windkessel model that provides ABF as

$$\frac{F}{C_a} = \frac{dP}{dt} + \frac{P}{\tau} \quad (2.2)$$

where τ was adopted from an exponential decay fitted to a diastolic ABP waveform.

SV, CO, and TPR analysis

For comparison, C_a in each animal was calculated by

$$C_a = \frac{\text{mean}(\text{meas})}{\text{mean}(\text{estimated})} \quad (4.18)$$

where *meas* and *estimated* are the measured and estimated proportional SV, CO, or TPR (proportional τ),

for instance. Although C_a declines with age [55], C_a is nearly constant on the time scale of months over a wide pressure range [45, 46]; thus, C_a was assumed to be constant (mean measured CO divided by mean estimated CO) throughout the experimental period in each animal (blind compliance), and the proportional SV, CO, and τ estimates were scaled by the constant to compare results with the measured SV, CO, and TPR.

5. Labeling Characteristic Points

In preparation for developing novel PCMs, this chapter describes an algorithm to label characteristic points in ABF and ABP data. The characteristic points of interest are: onset of systole (end of diastole), peak systole, and onset of diastole (end of systole). The following sections describe a step-by-step procedure to identify these points in ABF and ABP data. In summary, peak systoles are first identified. Secondly, an evaluation function is introduced to identify the onset of systole between two peak systoles. Thirdly, another evaluation function is introduced to identify the onset of diastole between two peak systoles.

5.1. Identification of Peak Systole

Peak systole is an inter-beat local maximum. The challenge is that there can be multiple peaks in a single beat (as shown in Fig. 5.1 in gray). Because there can be two peaks in ABP waveforms and the baseline can change in a short period of time by respiration, for instance, sometimes a simple threshold is not enough to detect peaks. To extract only the peak systole among the peaks in a single beat, convolution of a Gaussian distribution (5.1) with the original ABP data is introduced:

$$f(x) = \frac{1}{\sqrt{2\pi\sigma^2}} \exp\left(-\frac{(x-\mu)^2}{2\sigma^2}\right) \quad (5.1)$$

where the standard deviation of the distribution is arbitrarily set initially. The Gaussian distribution (Fig. 5.2) is then convoluted with the ABF or ABP data. The outcome is shown in Fig. 5.1 (black). Note that the output curve (convolution of the Gaussian and ABP) has a single peak in each beat. The second peak near the dicrotic notch is smeared out in the output curve and is not counted as a peak. The key of this method is to set a right standard deviation (wide enough) so that one can extract the single beat and identify only one local maximum. The time stamp of the local maximum in the convolution outcome in a single beat is

now mapped onto the original ABF/ABP waveform. Then, the local maximum around the point is regarded as the systolic peak of the beat (Fig. 5.3).

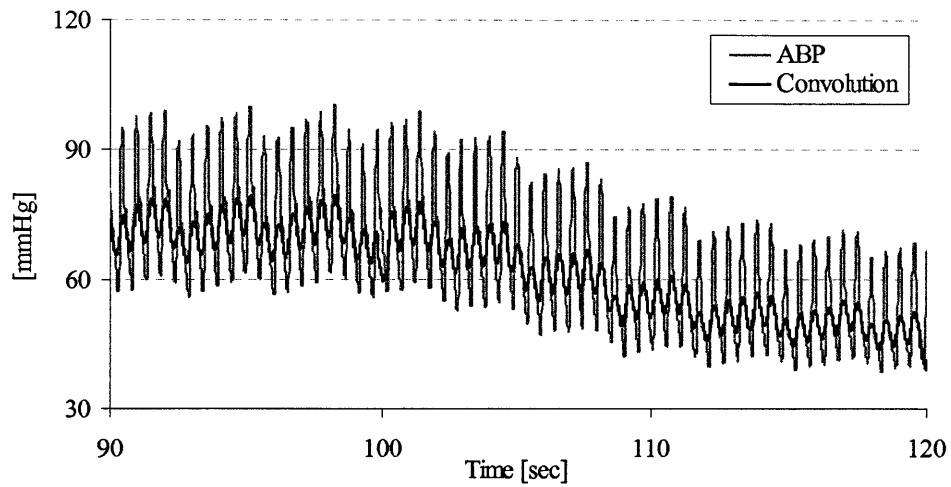


Fig. 5.1. Radial ABP data recorded from Yorkshire swine. Recorded from Swine #7. The baseline changed over a short interval.

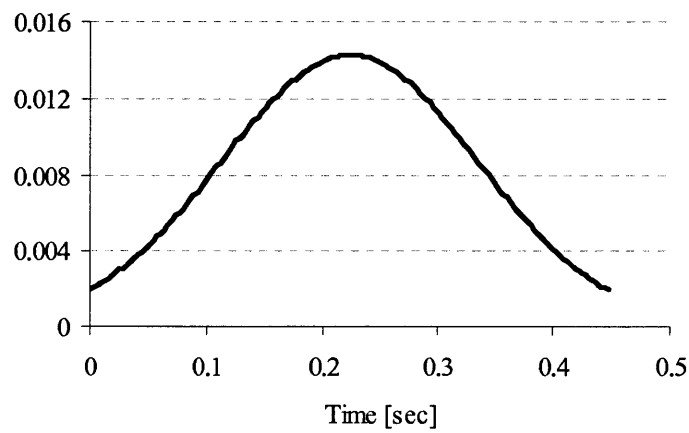


Fig. 5.2. Gaussian distribution (normalized). The width is set to the median R-R interval of the preceding beats. The interval is updated on a beat-to-beat basis.

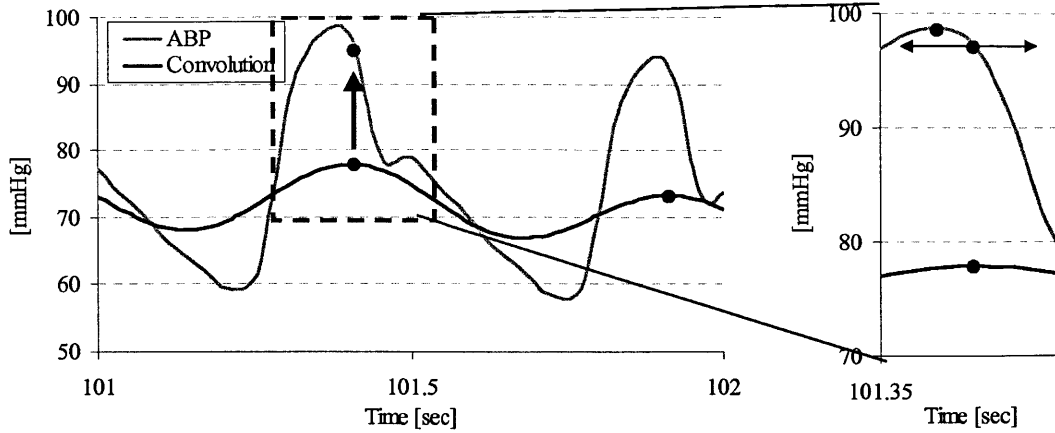


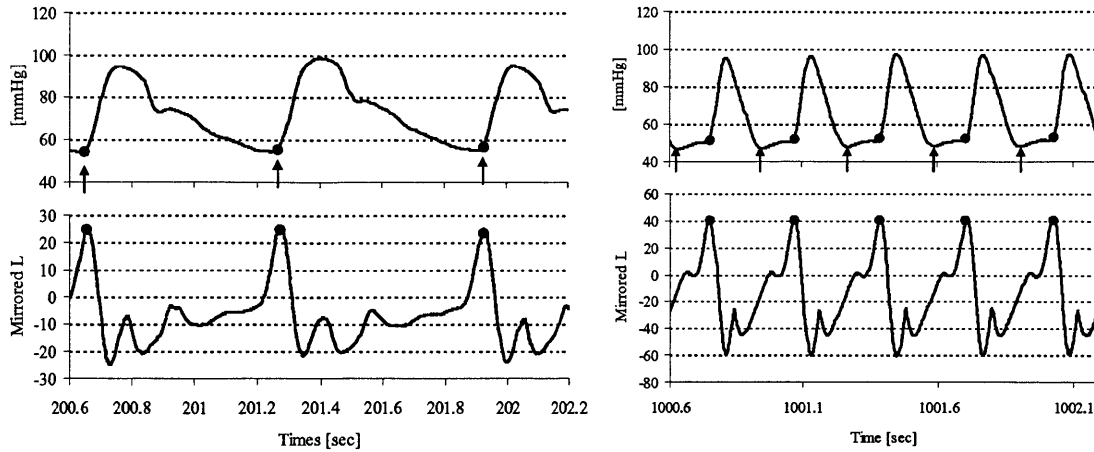
Fig. 5.3. Labeling systolic peaks

5.2. Identification of End Diastole

The challenge in detecting end diastole (i.e., onset of systole) is that the local minimum right before a peak systole is not necessarily an end diastole. Examples are shown in Fig. 5.4b. For a robust detection algorithm, the following evaluation function was introduced.

$$mirroredL = (x[i] - x[i - d]) - |x[i] - x[i + d]| \quad (5.2)$$

Equation (5.2) detects a waveform in the shape of a mirrored “L”. The function *mirroredL* becomes large when the point $x[i]$ is the bending point (or elbow) of the mirrored “L”. Fig. 5.4 shows examples of ABP waveforms $x[i]$ and corresponding $mirroredL[i]$ in normal and abnormal beats. The local maximum of *mirroredL* between two peak systoles was regarded as an end diastole. Note that the mapped black circles in the ABP waveforms are more robust indicators of the onsets of diastoles than the inter-beat local minima (arrows.)



(a) Normal ABP waveforms

(b) Abnormal ABP waveforms

Fig. 5.4. Normal and abnormal radial ABP data recorded from Yorkshire swine. Recorded from Swine #5. The corresponding mirrored L is shown below each ABP. The peaks in the mirrored L (black circles) are mapped onto the ABP waveform. Note that the mapped black circles in the ABP waveforms correspond to the end-diastoles for both normal and abnormal beats. The mirrored L is a more robust indicator of onsets of diastoles than the inter-beat local minima (arrows).

5.3. Renewal of Gaussian Convolution Based on RR interval

The standard deviation of the normal distribution for convolution is updated based on the preceding RR interval (inverse of HR) for the next ten-second moving window.

For the validation of the algorithms described in the following sections, the aforementioned steps were repeated to label all the characteristic points in the ABF, central ABP (CAP), femoral ABP (FAP), and radial ABP (RAP) signals.

5.4. Identification of End Diastole

A number of methods introduced and validated in the following chapters utilize end systole (onset of diastole). For practical applications in clinical settings, ABF is not available. Therefore, an estimation method for the determination of diastolic onset in each beat is needed. Several estimation methods are

introduced here.

5.4.1. Exponential Model

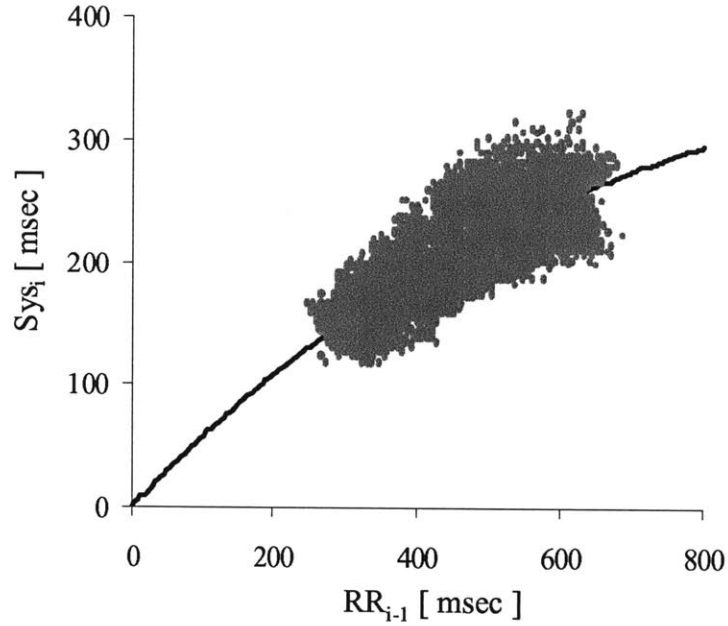


Fig. 5.5. A current systolic interval as a function of a preceding RR interval.

The duration of systole (Sys) can be described as a function of the preceding RR interval [58].

Using six Yorkshire swine data sets that include measured (true) systolic durations and RR intervals on a beat-to-beat basis, the relation between Sys and RR was found as

$$Sys_i = 436 \left(1 - \exp \left(-0.0057 RR_{i-1}^{measured} \right) \right) \quad (5.3)$$

where i is the beat number, and the diastolic duration Dia_i can be described as

$$\begin{aligned} Dia_i &= RR_i^{measured} - Sys_i \\ &= RR_i^{measured} - 436 \left(1 - \exp \left(-0.0057 RR_{i-1}^{measured} \right) \right) \end{aligned} \quad (5.4)$$

Using the Yorkshire swine data sets (>60,000 beats), the calculated diastolic duration Dia was compared

with the measured diastolic duration $Dia^{measured}$.

5.4.2. Partial Pulse Pressure

An end diastole always comes after a systolic peak. At the end systole, the pressure value is equal or lower than SBP. When the pressure drops from SBP to $\alpha\%$ pulse pressure (PP),

$$P_{ES} = P_D + \alpha(P_S - P_D) \quad (5.5)$$

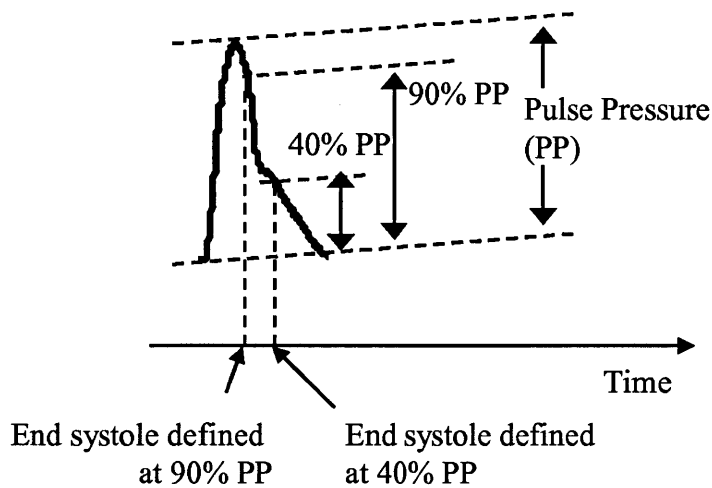


Fig. 5.6. End systole defined by means of the partial pulse pressure.

As examples, end systoles identified by the 40% PP and 90% PP are shown in Fig. 5.6. The time stamp of P_{ES} can be regarded as the time of an estimated end systole.

6. Results

The aforementioned SV, CO, TPR, and ABF estimation methods as well as existing methods were applied to the previously recorded Yorkshire swine data sets [20]. The summary of the data is shown on Table 6.1.

ANIMAL	Length (min)	CO (L/min)	SV (mL)	Femoral MAP (mmHg)	Radial MAP (mmHg)	HR (bpm)
1	113	3.6 +/- 1.0	28.4 +/- 5.8	63 +/- 19	61 +/- 19	129 +/- 29
2	97	3.2 +/- 0.6	25.0 +/- 5.0	83 +/- 21	73 +/- 20	135 +/- 38
3	88	4.0 +/- 0.7	31.7 +/- 7.1	83 +/- 16	87 +/- 15	133 +/- 32
4	106	3.2 +/- 0.6	25.2 +/- 4.3	89 +/- 19	79 +/- 18	129 +/- 34
5	90	3.3 +/- 0.5	26.7 +/- 6.4	80 +/- 21	85 +/- 19	130 +/- 32
6	68	3.4 +/- 1.2	28.5 +/- 8.1	72 +/- 19	75 +/- 20	130 +/- 26
MEAN	94	3.5 +/- 0.8	27.5 +/- 6.7	79 +/- 21	76 +/- 21	131 +/- 32

Table 6.1. Summary of cardiovascular parameters of the six swine data sets.

Wide physiological ranges (mean \pm SD) of cardiac output (CO), stroke volume (SV), femoral and radial mean arterial blood pressure (MAP), and heart rate (HR) were obtained in the six swine data sets.

Each section of this Chapter contains the RNMSE and plots of the measured and estimated indices, as well as the Bland-Altman plot [47]. It plots difference of two groups against the mean of two groups. The plots aid in the visualization of the agreement of the two groups; for a good agreement, there should not be any trend, and the majority of the plots should stay within ± 1.96 SD, which is drawn as dotted horizontal lines.

Some of the SV, CO, TPR, and ABF estimation methods require the use of end-systole timestamps. Because this information is not available in clinical care, the following methods are used: (1) true end systole obtained from the measured ABF, (2) end systole estimated from the RR interval of the preceding beat (exponential model, described in Section 5.4.1), and (3) partial pressure as end systole (described in Section 5.4.2).

To validate the algorithm described in the following chapters and sections, previously reported [20] data from six Yorkshire swine (30–34 kg) recorded under a protocol approved by the MIT Committee on Animal Care were processed and analyzed offline. Table 6.2 summarizes the physiological ranges of the

data sets. Aortic blood flow was recorded using an ultrasonic flow probe (T206 with A-series probes, Transonic Systems, Ithaca, NY) placed around the aortic root. Radial and femoral ABP were measured using a micromanometer-tipped catheter (SPC350, Millar Instruments, Houston, TX) and an external fluid-filled pressure transducer (TSD104A, Biopac Systems, Santa Barbara, CA). Aortic blood flow, ECG, and blood pressures were recorded using an A/D conversion system (MP150WSW, Biopac Systems) at a sampling rate of 250 Hz. For more details, please refer to Mukkamala *et al.* [20].

6.1. End Systole Estimation

Using the exponential model (5.4), the mean error of the diastolic duration was 6.56 %, and the standard deviation from the mean was 5.86 %. The formula (5.4) was used to determine the diastolic duration in each beat in the algorithms reported in the following sections. Also, the partial pressure method (5.5) was investigated. Table 6.2 summarizes the errors of diastolic intervals estimated by the partial PP method. 60%, 50%, and 50% PP would be good indicators of end systoles for CAP, FAP, and RAP, respectively.

	CAP	FAP	RAP
40% PP	17.1 ± 11.6	5.9 ± 8.0	6.0 ± 14.2
50% PP	10.1 ± 9.0	-3.3 ± 5.5	-1.4 ± 12.5
60% PP	1.8 ± 6.9	-7.4 ± 4.1	-10.8 ± 6.8
70% PP	-4.7 ± 4.3	-10.0 ± 3.9	-13.8 ± 7.1
80% PP	-8.2 ± 3.5	-12.8 ± 3.9	-17.1 ± 8.2
90% PP	-11.3 ± 3.8	-16.3 ± 4.3	-23.8 ± 11.3
100% PP	-29.0 ± 21.1	-31.9 ± 16.9	-36.4 ± 17.1

Table 6.2. Summary of diastolic interval errors ± standard deviation (SD).

In the following sections, the true end systole, end systole estimated by the exponential model, and partial PP method are used to identify end systoles and calculate ABF, SV, CO, and TPR.

6.2. SV, CO, and TPR Estimation

6.2.1. Windkessel Model

The Windkessel method achieved 23.7% (CAP), 18.8% (FAP), and 37.7% (RAP) RNMSEs in SV estimation.

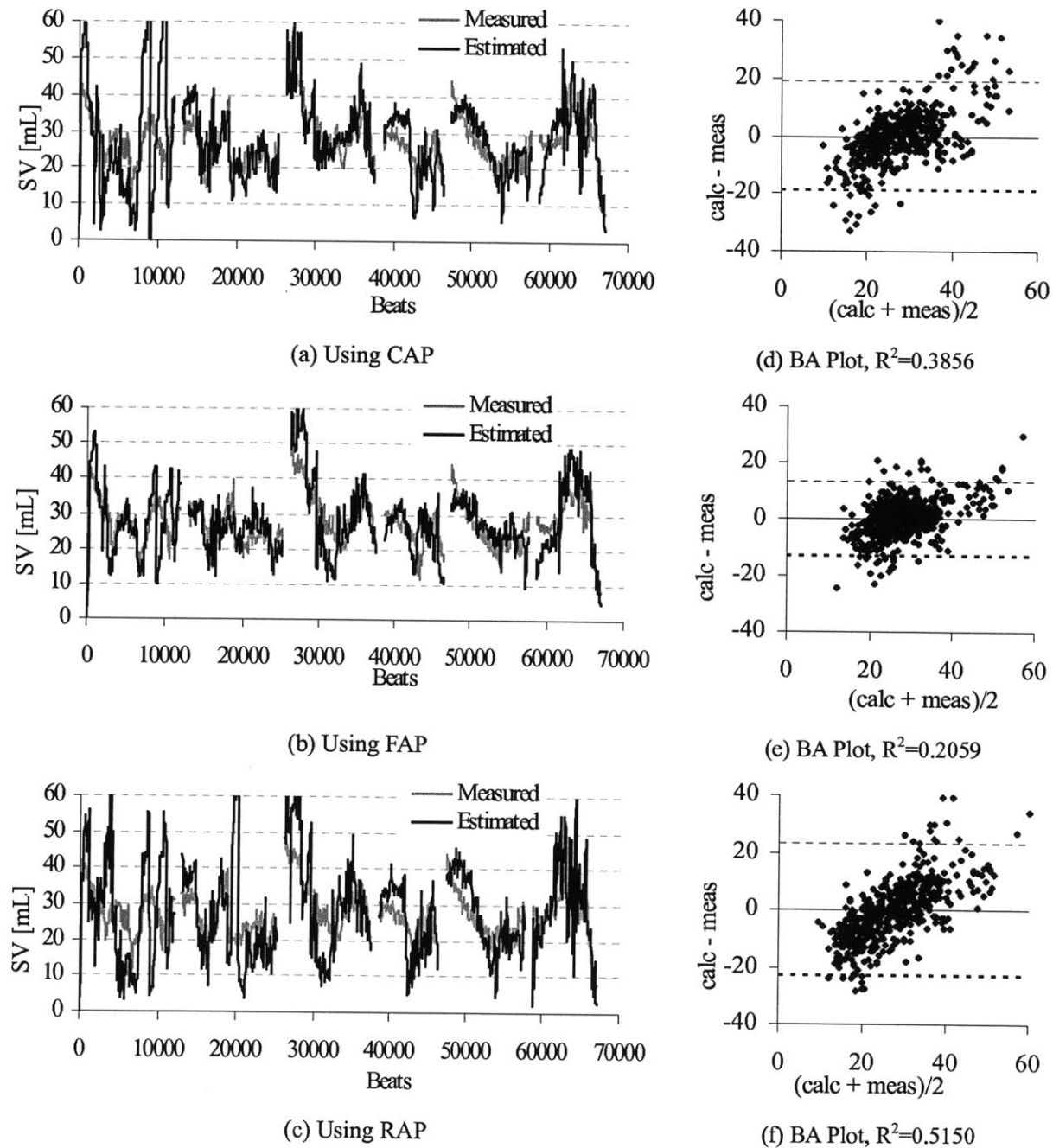
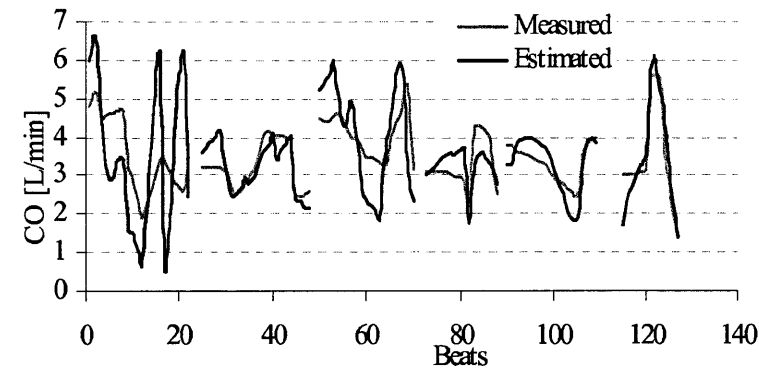
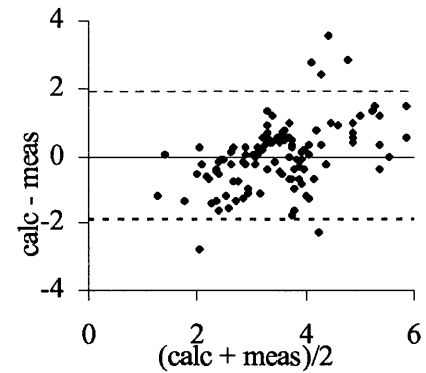


Fig. 6.1. SV estimation by the Windkessel model.

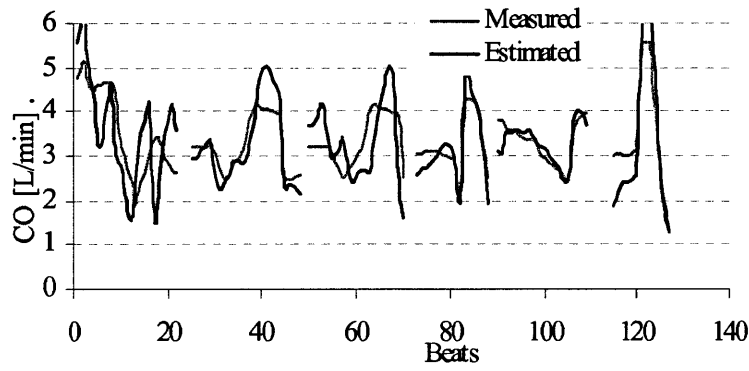
Using CAP, FAP, and RAP waveforms, the Windkessel method achieved 17.0, 16.6, and 44.8% RNMSEs in CO estimation, respectively.



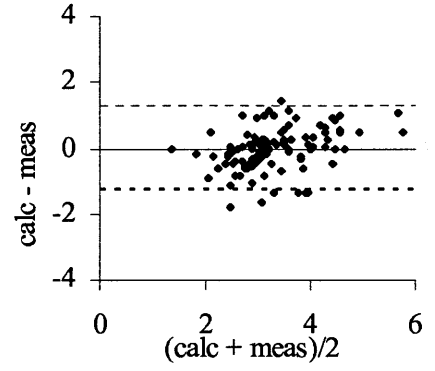
(a) Using CAP



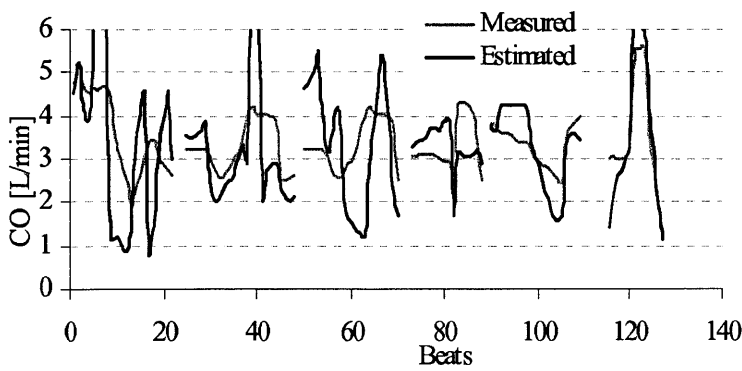
(d) BA Plot, $R^2=0.2247$



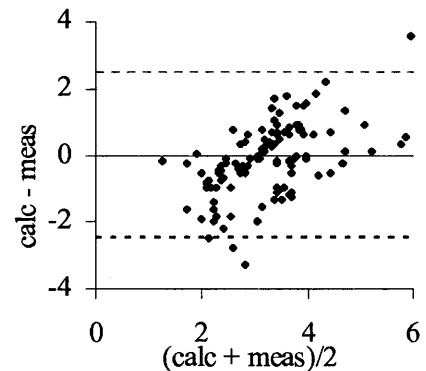
(b) Using FAP



(e) BA Plot, $R^2=0.2428$



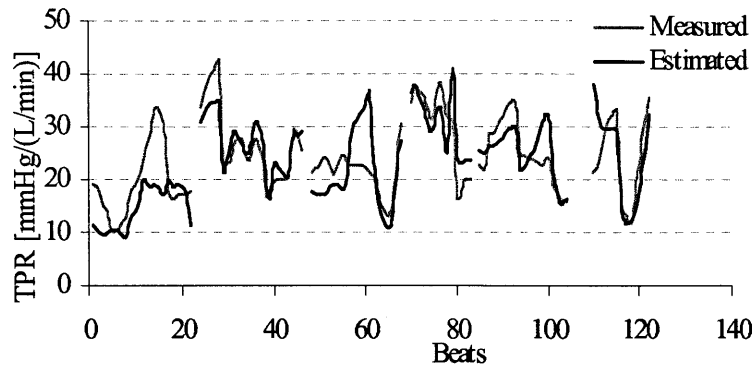
(c) Using RAP



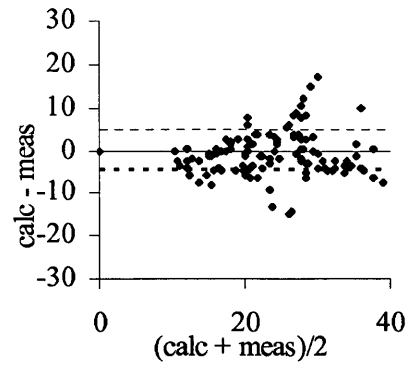
(f) BA Plot, $R^2=0.4416$

Fig. 6.2. CO estimation by the Windkessel model.

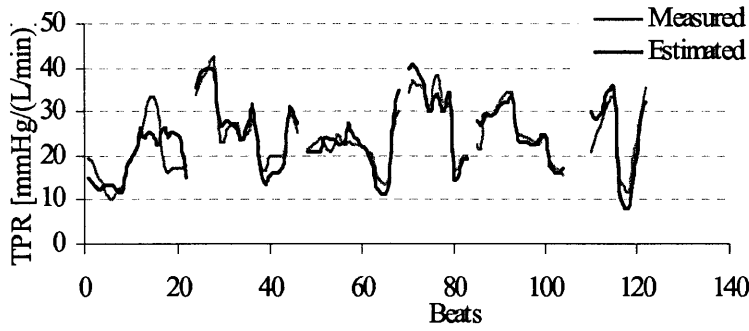
Using CAP, FAP, and RAP waveforms, the Windkessel method achieved 21.3, 17.3, and 36.4% RNMSEs in TPR estimation, respectively.



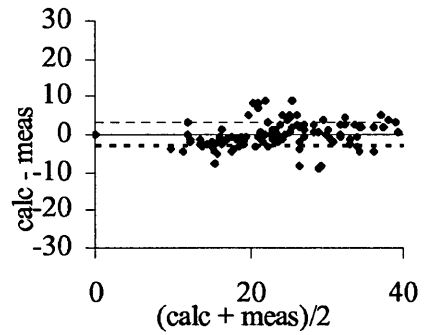
(a) Using CAP



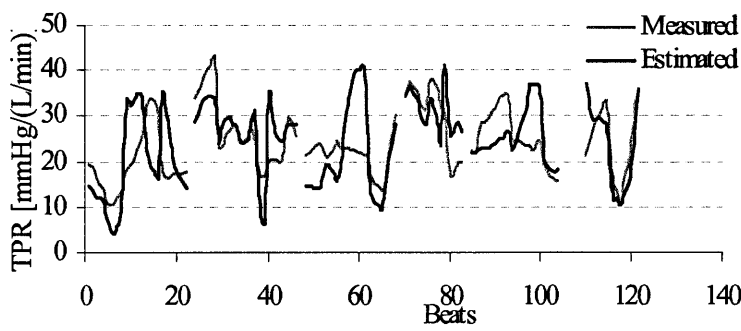
(d) BA Plot, $R^2=0.0011$



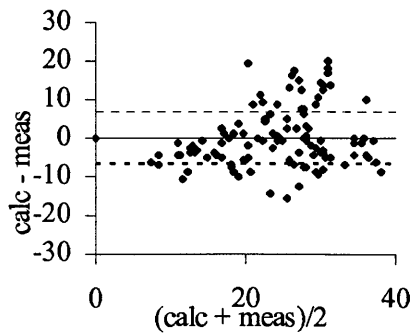
(b) Using FAP



(e) BA Plot, $R^2=0.0031$



(c) Using RAP

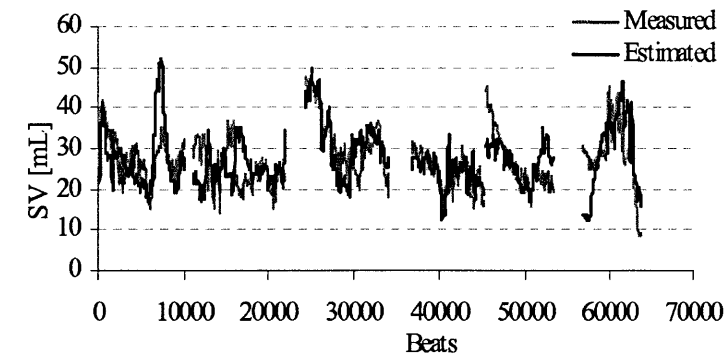


(f) BA Plot, $R^2=0.0011$

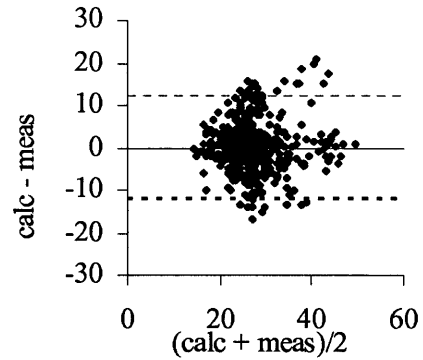
Fig. 6.3. TPR estimation by the Windkessel model.

6.2.2. Pulse Pressure

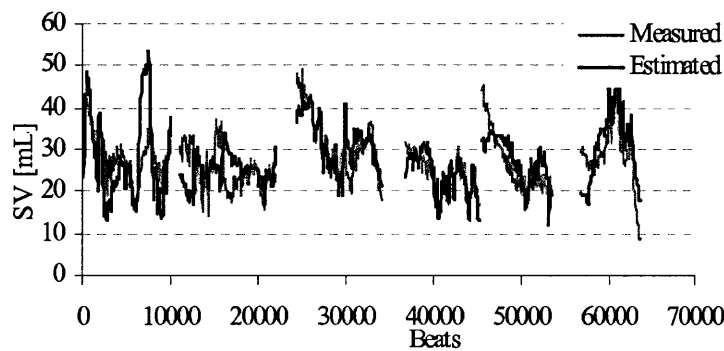
The Pulse Pressure method achieved 20.5% (CAP), 20.7% (FAP), and 22.0% (RAP) RNMSEs in SV estimation.



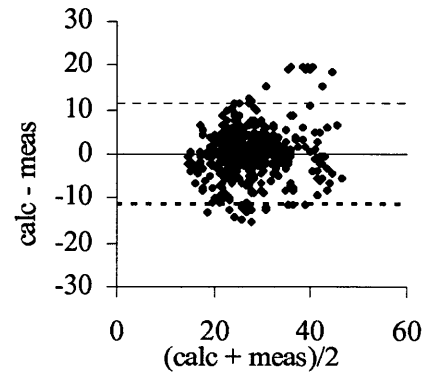
(a) Using CAP



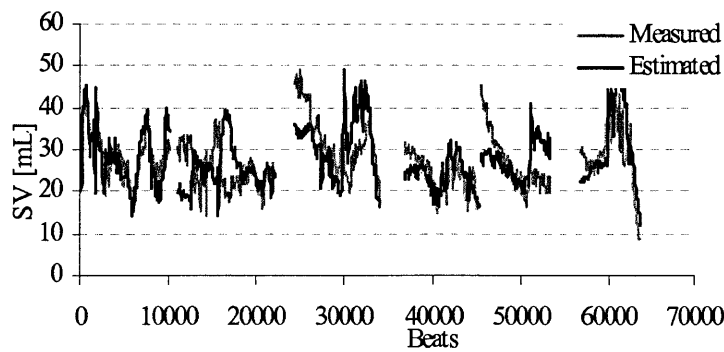
(d) BA Plot, $R^2=0.0006$



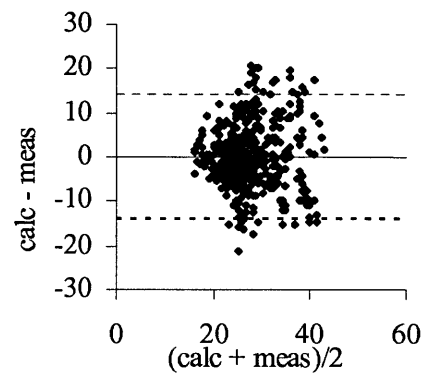
(b) Using FAP



(e) BA Plot, $R^2=0.0193$



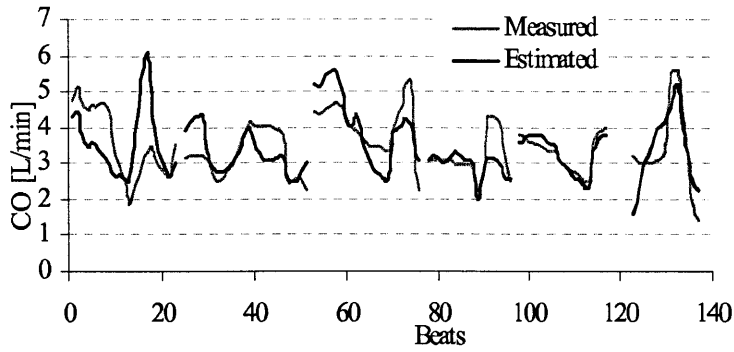
(c) Using RAP



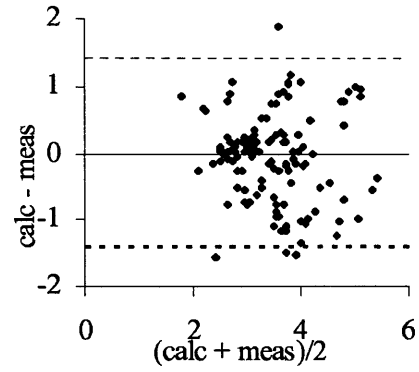
(f) BA Plot, $R^2=0.0003$

Fig. 6.4. SV estimation by the Pulse Pressure method.

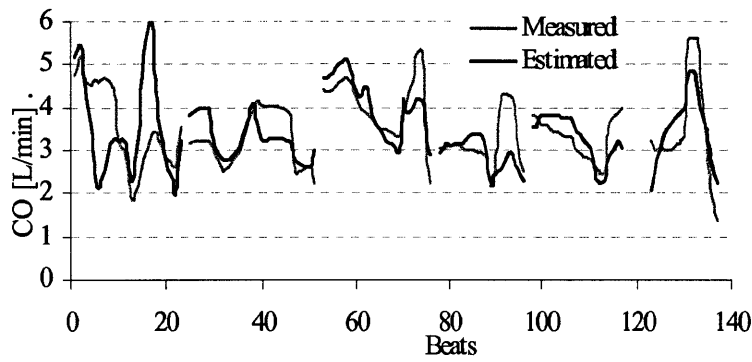
Using CAP, FAP, and RAP waveforms, the Pulse Pressure method achieved 20.1, 22.7, and 11.5% RNMSEs in CO estimation, respectively.



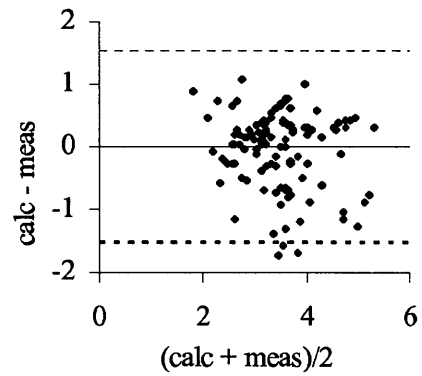
(a) Using CAP



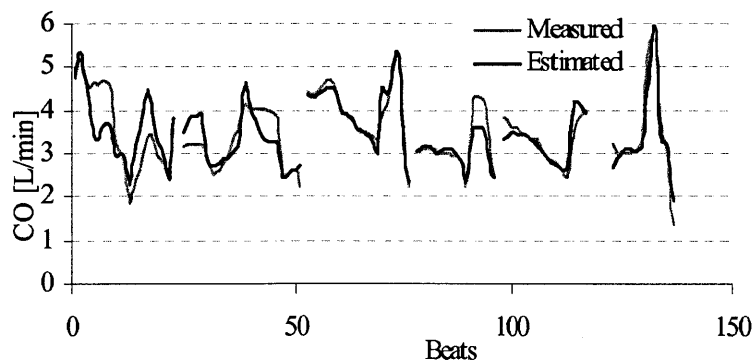
(d) BA Plot, $R^2=0.0002$



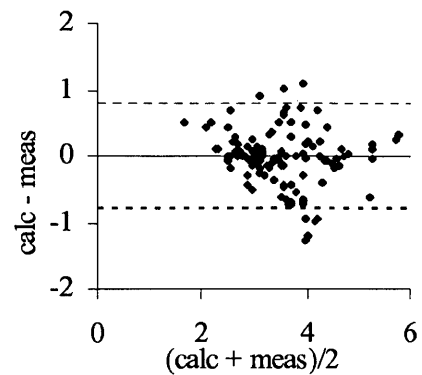
(b) Using FAP



(e) BA Plot, $R^2=0.0015$



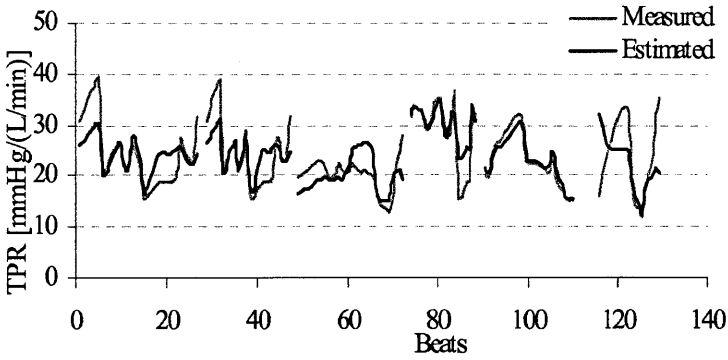
(c) Using RAP



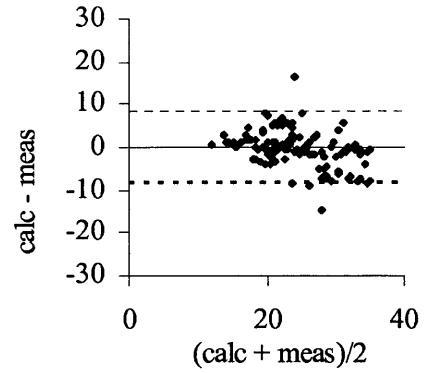
(f) BA Plot, $R^2=0.025$

Fig. 6.5. CO estimation by the Pulse Pressure method.

Using CAP, FAP, and RAP waveforms, the Pulse Pressure method achieved 44.4, 38.4, and 22.0% RNMSEs in TPR estimation, respectively.



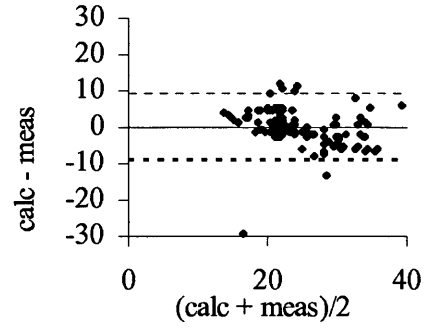
(a) Using CAP



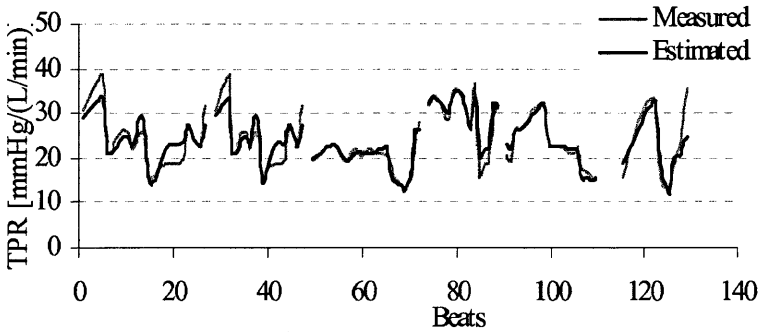
(d) BA Plot, $R^2=0.1581$



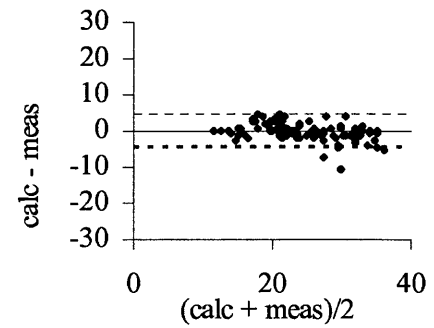
(b) Using FAP



(e) BA Plot, $R^2=0.0793$



(c) Using RAP

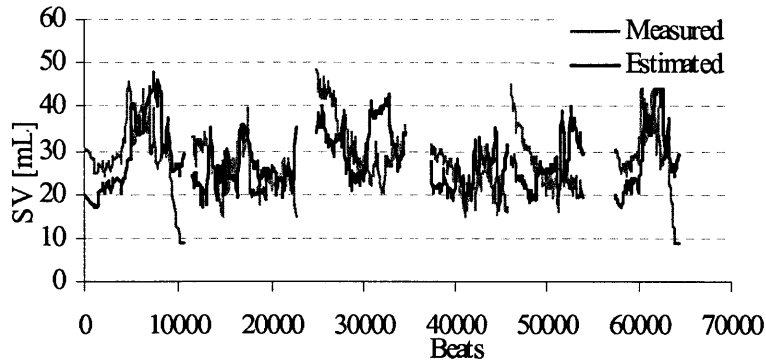


(f) BA Plot, $R^2=0.1544$

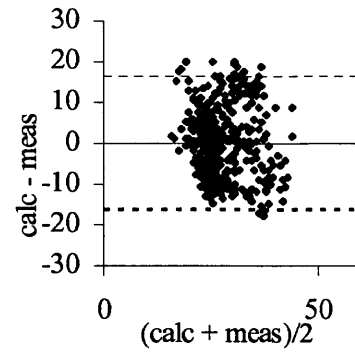
Fig. 6.6. TPR estimation by the Pulse Pressure method.

6.2.3. Liljestrand-Zander's Method

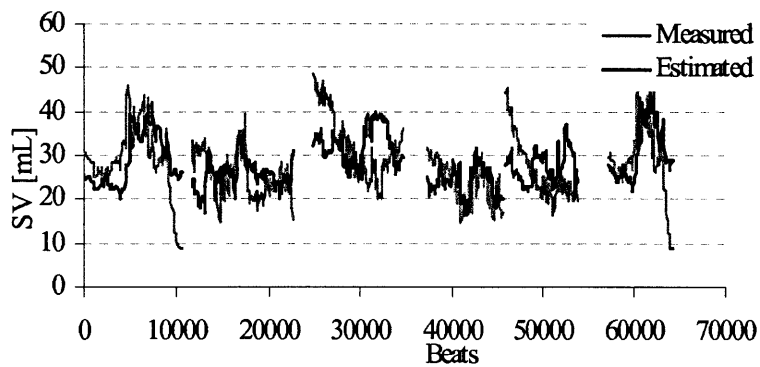
Using CAP, FAP, and RAP waveforms, the Liljestrand-Zander's method achieved 34.9, 31.2, and 34.2% RNMSEs in SV estimation, respectively.



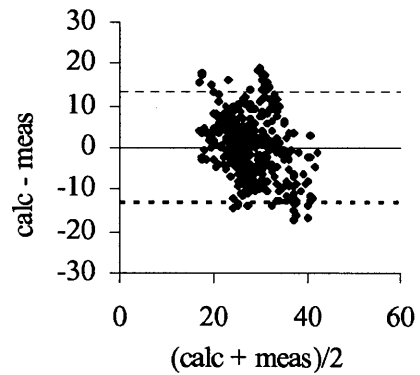
(a) Using CAP



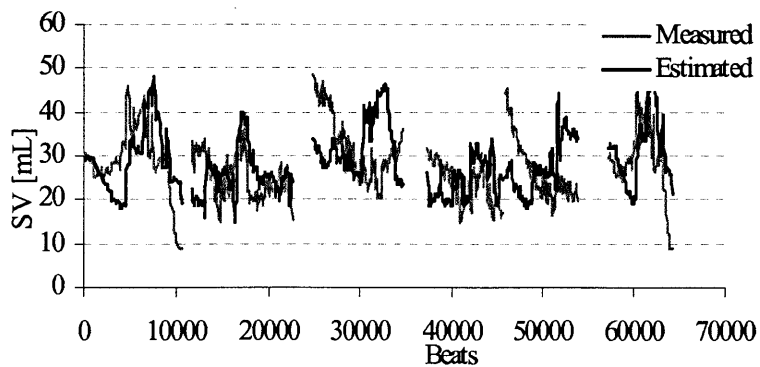
(d) BA Plot, $R^2=0.011$



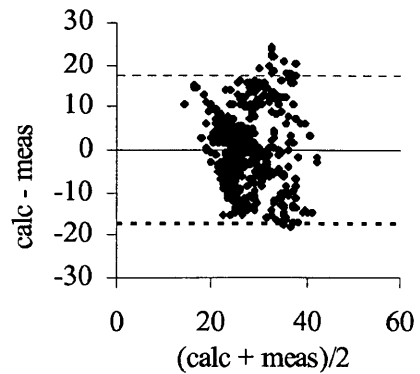
(b) Using FAP



(e) BA Plot, $R^2=0.1038$



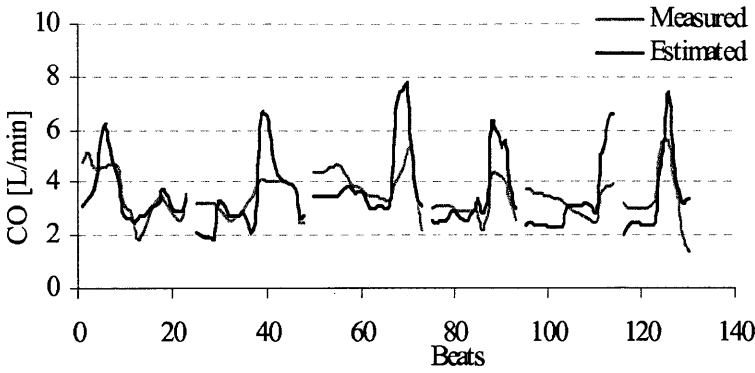
(c) Using RAP



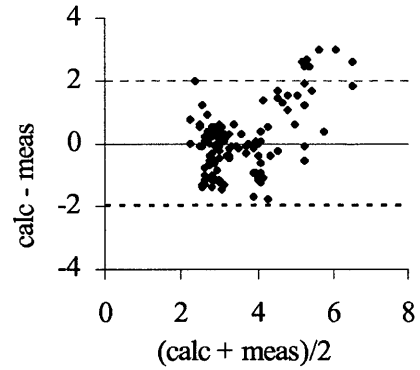
(f) BA Plot, $R^2=0.0026$

Fig. 6.7. SV estimation by Liljestrand-Zander's method.

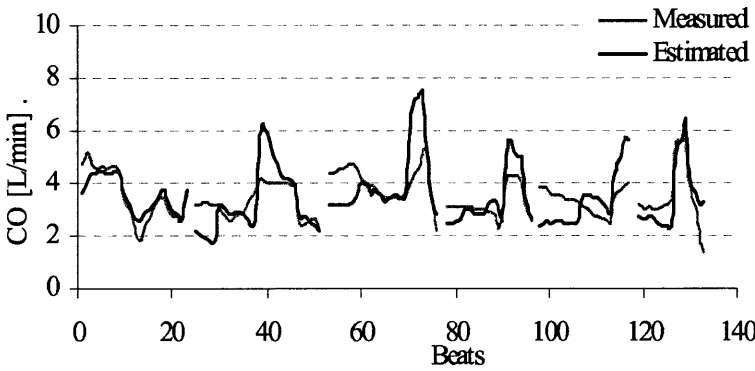
Using CAP, FAP, and RAP waveforms, Liljestrand-Zander's method achieved 29.7, 24.5, and 29.7% RNMSEs in CO estimation, respectively.



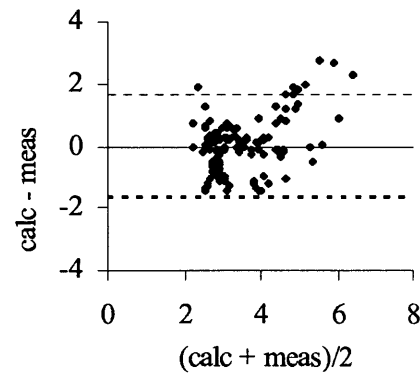
(a) Using CAP



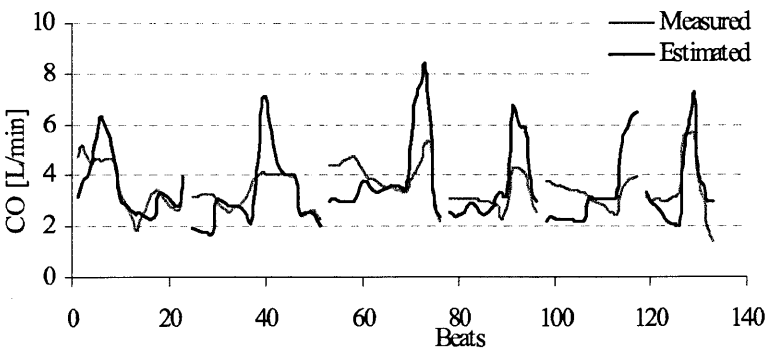
(d) BA Plot, $R^2=0.2981$



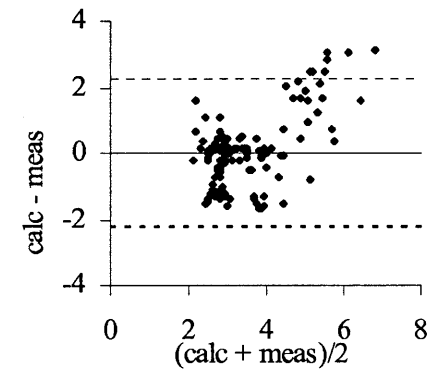
(b) Using FAP



(e) BA Plot, $R^2=0.173$



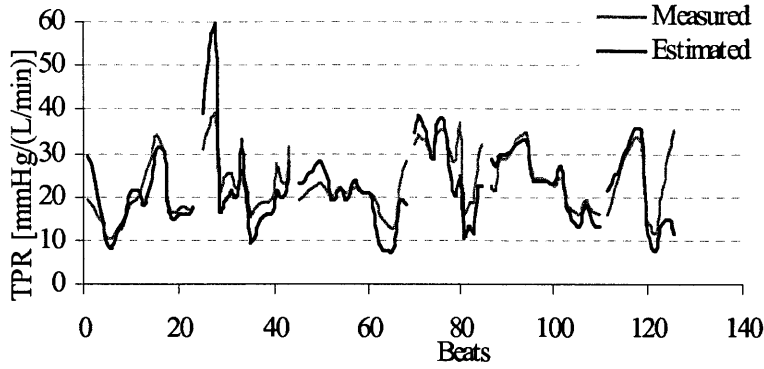
(c) Using RAP



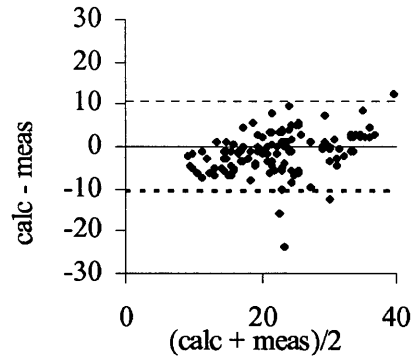
(f) BA Plot, $R^2=0.3797$

Fig. 6.8. CO estimation by Liljestrand-Zander's method.

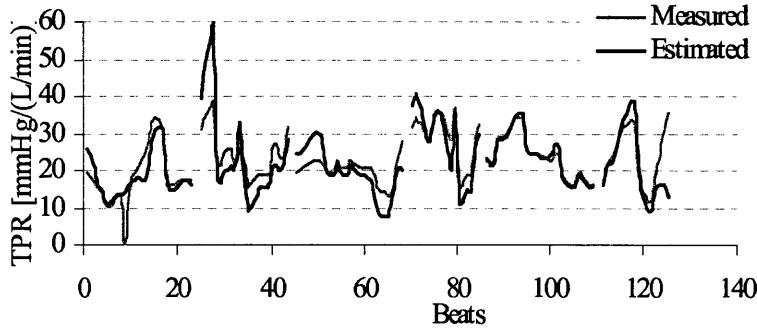
Using CAP, FAP, and RAP waveforms, Liljestrand-Zander's method achieved 29.9, 26.7, and 31.1% RNMSEs in TPR estimation, respectively.



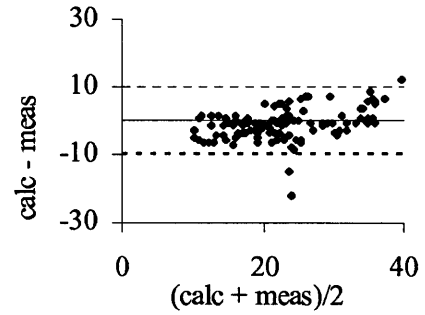
(a) Using CAP



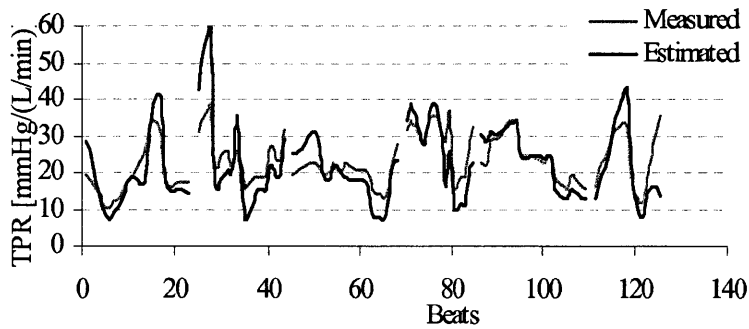
(d) BA Plot, $R^2=0.2525$



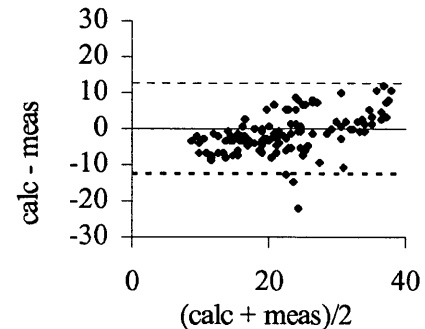
(b) Using FAP



(e) BA Plot, $R^2=0.2901$



(c) Using RAP

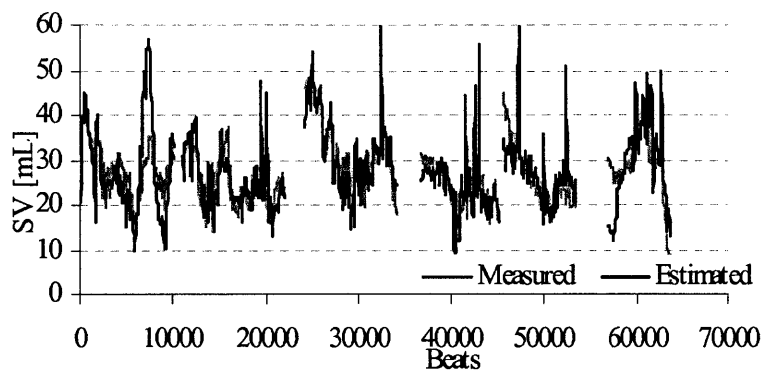


(f) BA Plot, $R^2=0.4116$

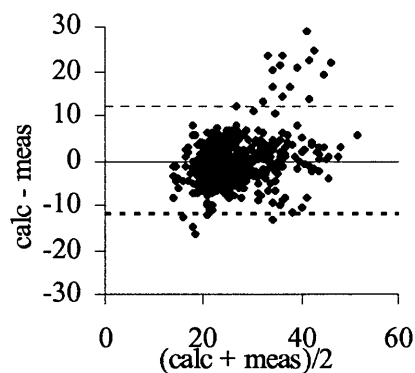
Fig. 6.9. TPR estimation by Liljestrand-Zander's method.

6.2.4. Herd's Pulse Pressure

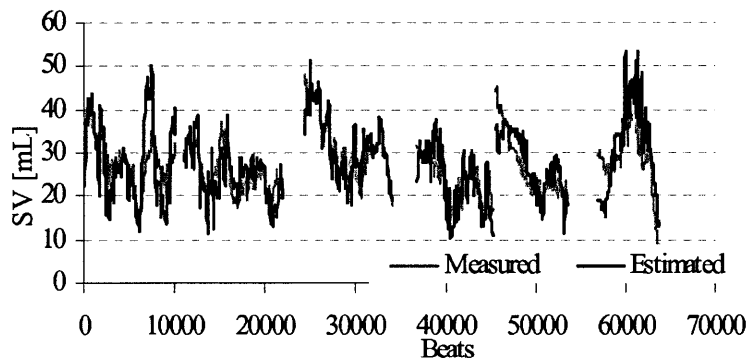
Using CAP, FAP, and RAP waveforms, Herd's Pulse Pressure method achieved 14.9, 17.2, and 18.6% RNMSEs in SV estimation, respectively.



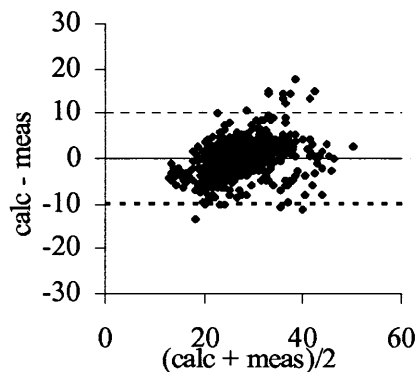
(a) Using CAP



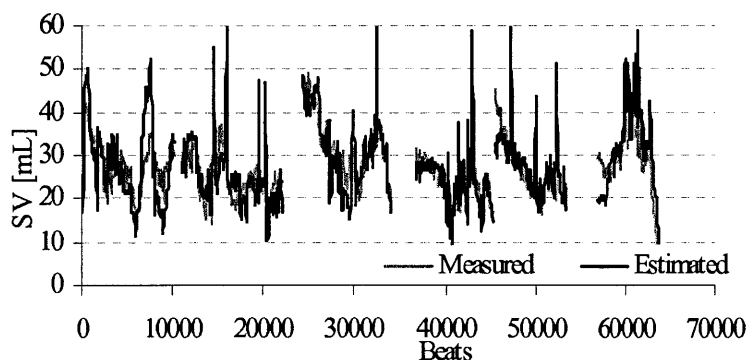
(d) BA Plot, $R^2=0.1263$



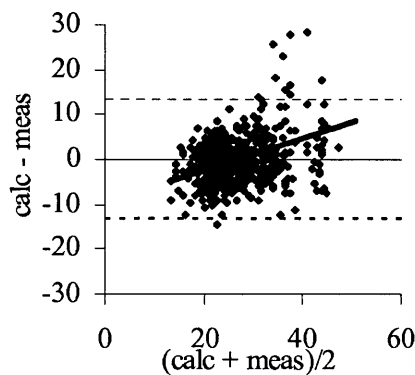
(b) Using FAP



(e) BA Plot, $R^2=0.111$



(c) Using RAP



(f) BA Plot, $R^2=0.1465$

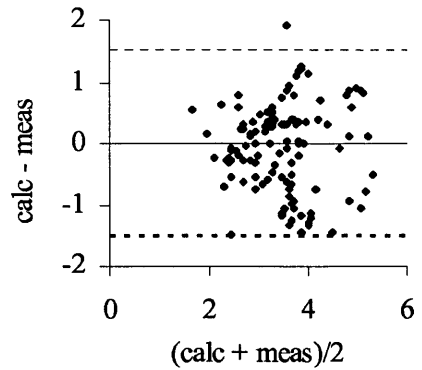
Fig. 6.10. SV estimation by Herd's method.

Using CAP, FAP, and RAP waveforms, Herd's Pulse Pressure method achieved 21.1, 21.0, and 18.7%

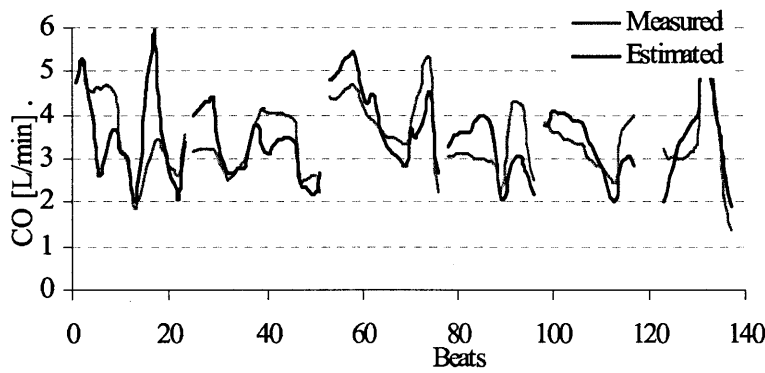
RNMSEs in CO estimation, respectively.



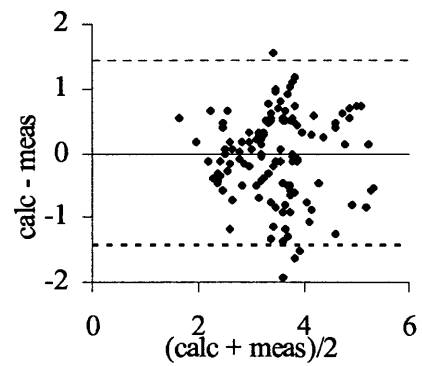
(a) Using CAP



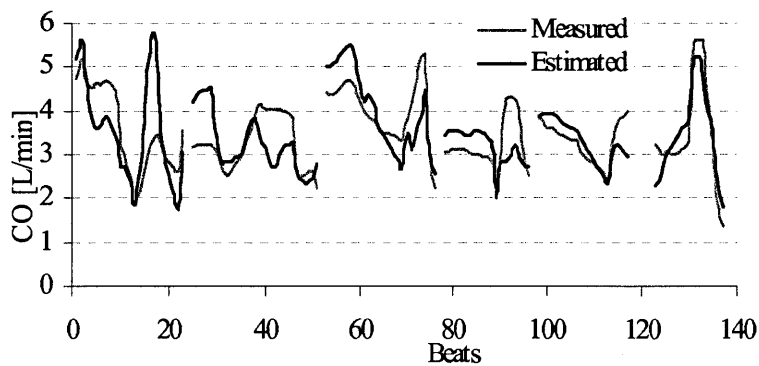
(d) BA Plot, $R^2=0.0099$



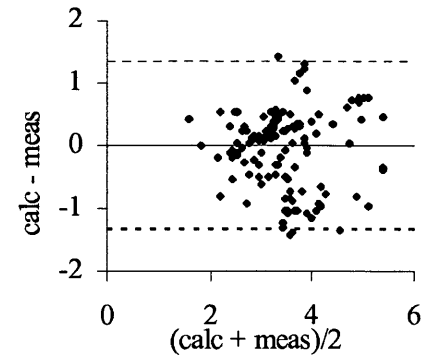
(b) Using FAP



(e) BA Plot, $R^2=0.0023$



(c) Using RAP

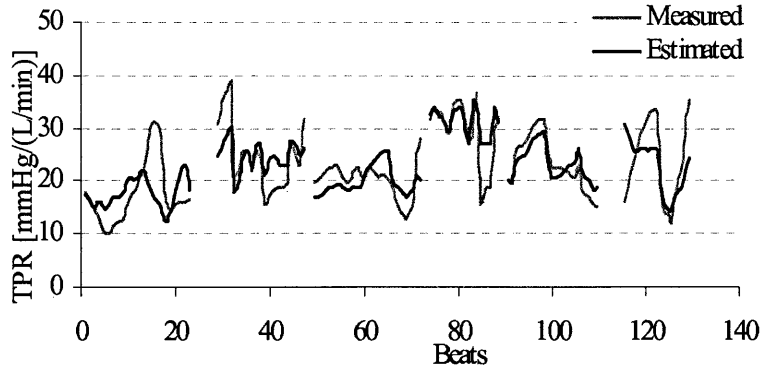


(f) BA Plot, $R^2=0.0046$

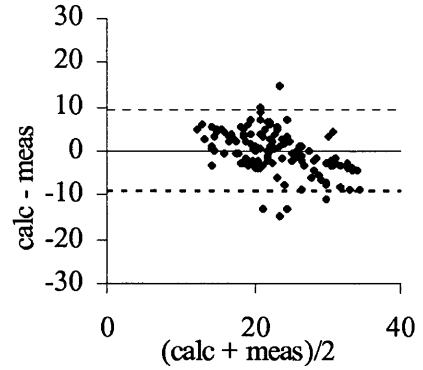
Fig. 6.11. CO estimation by Herd's method.

Using CAP, FAP, and RAP waveforms, Herd's Pulse Pressure method achieved 23.0, 22.7, and 21.5%

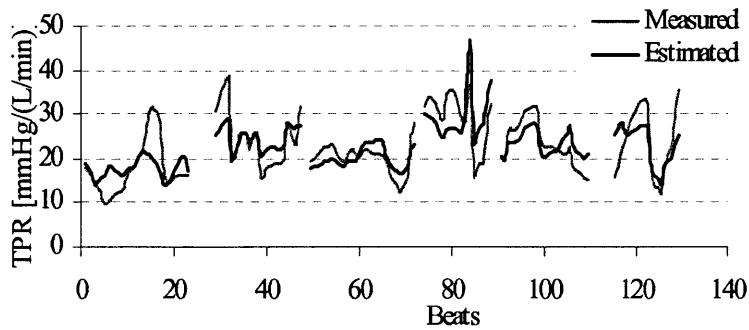
RNMSEs in TPR estimation, respectively.



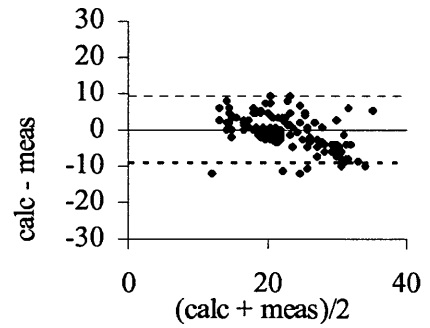
(a) Using CAP



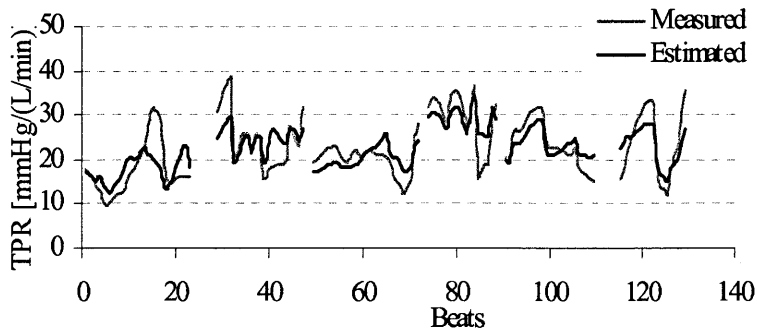
(d) BA Plot, $R^2=0.2247$



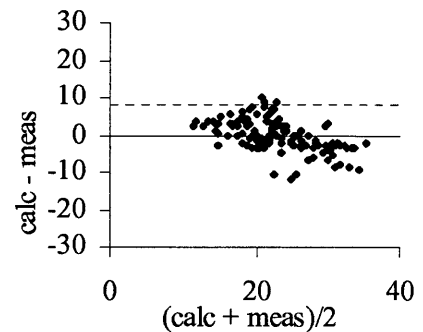
(b) Using FAP



(e) BA Plot, $R^2=0.1534$



(c) Using RAP

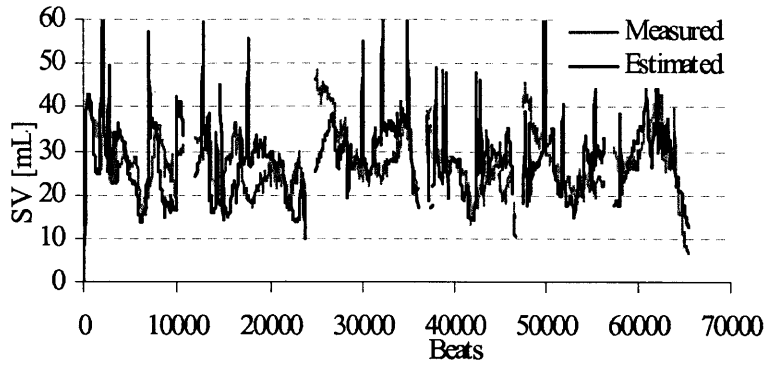


(f) BA Plot, $R^2=0.3012$

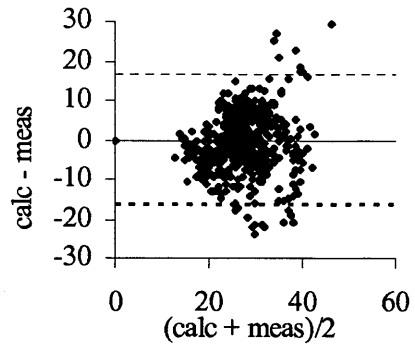
Fig. 6.12. TPR estimation by Herd's method.

6.2.5. Beat-to-Beat Averaged Method

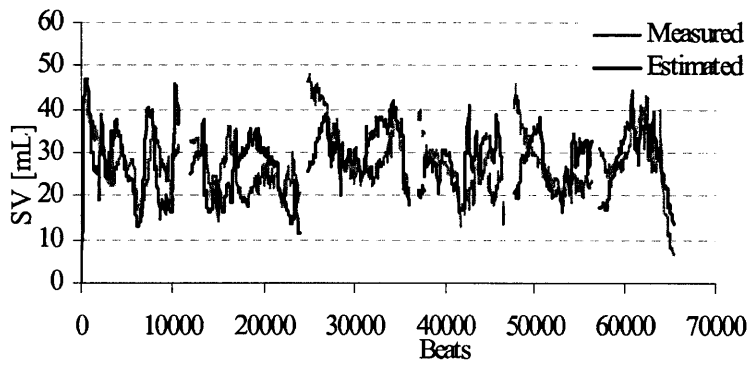
Using CAP, FAP, and RAP waveforms, the Beat-to-Beat Averaged method achieved 18.7, 20.7, and 20.9% RNMSEs in SV estimation, respectively.



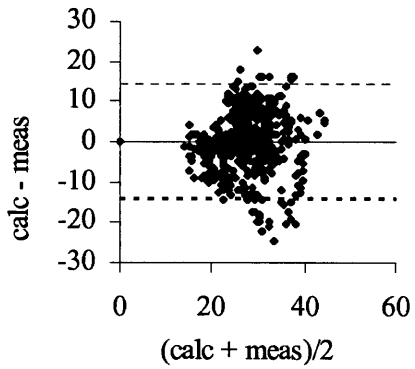
(a) Using CAP



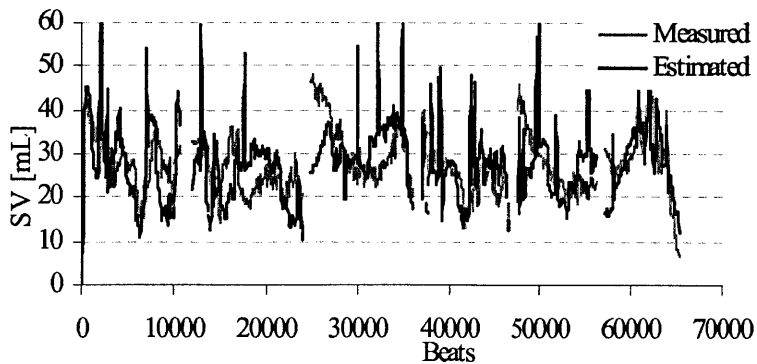
(d) BA Plot, $R^2=0.0842$



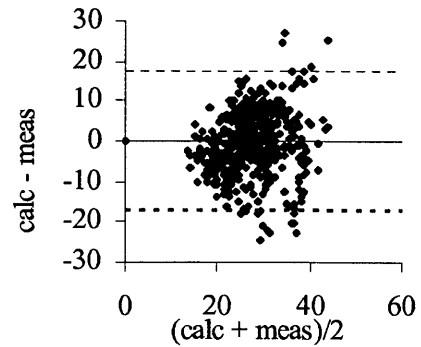
(b) Using FAP



(e) BA Plot, $R^2=0.0068$



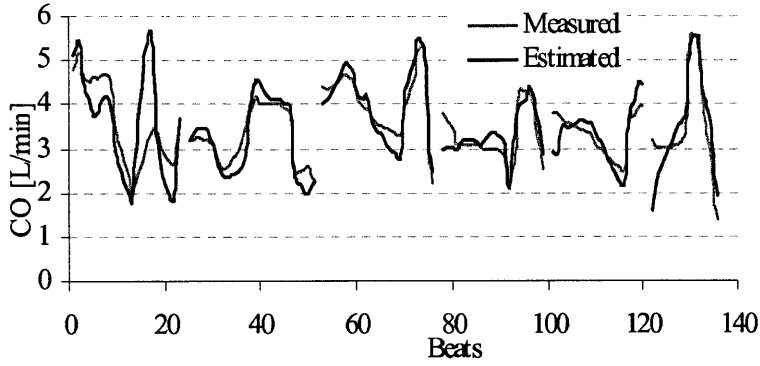
(c) Using RAP



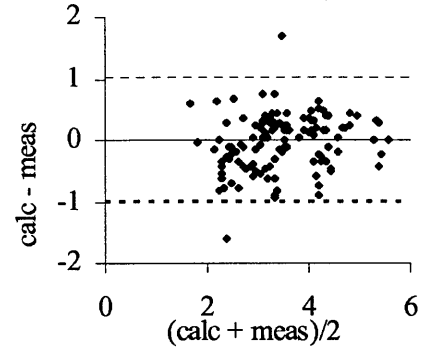
(f) BA Plot, $R^2=0.0863$

Fig. 6.13. SV estimation by the Beat-to-Beat Averaged method.

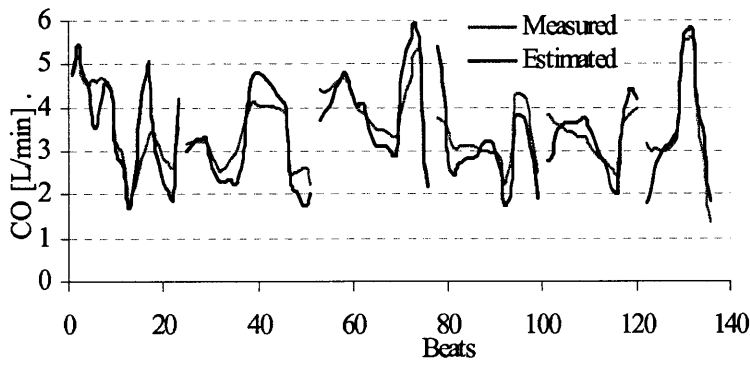
Using CAP, FAP, and RAP waveforms, the Beat-to-Beat Averaged method achieved 17.0, 16.6, and 13.7% RNMSEs in CO estimation, respectively.



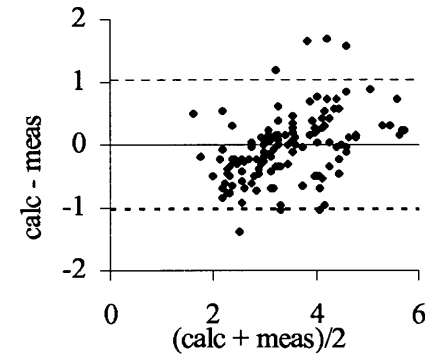
(a) Using CAP



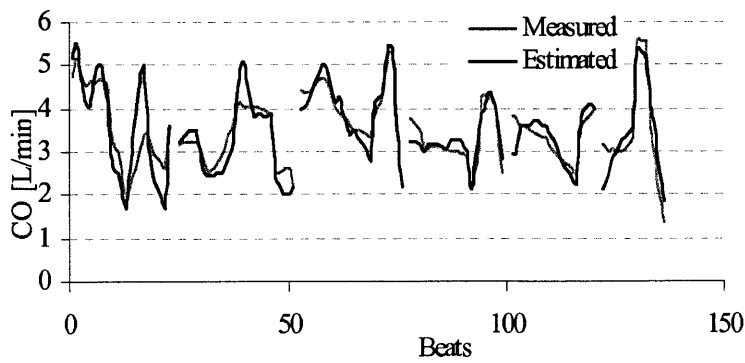
(d) BA Plot, $R^2=0.0558$



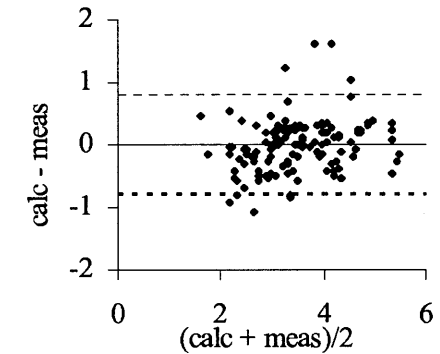
(b) Using FAP



(e) BA Plot, $R^2=0.1941$



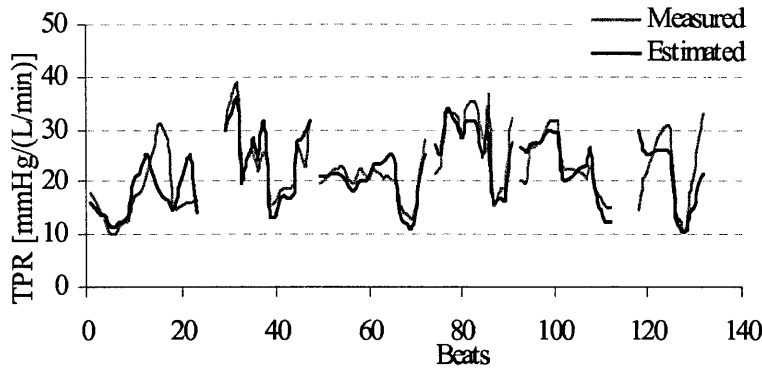
(c) Using RAP



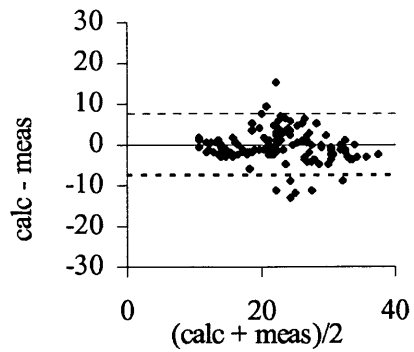
(f) BA Plot, $R^2=0.0611$

Fig. 6.14. CO estimation by the Beat-to-Beat Averaged method.

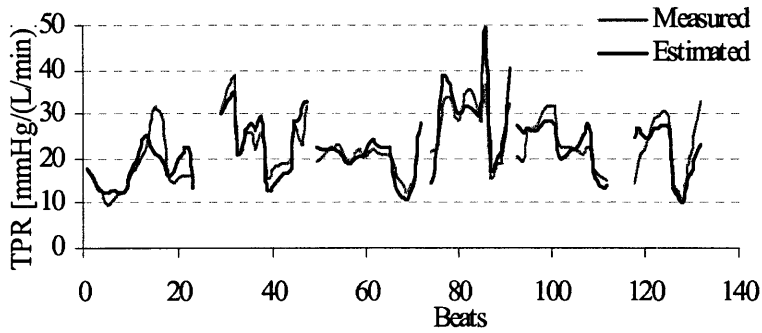
Using CAP, FAP, and RAP waveforms, the Beat-to-Beat Averaged method achieved 16.5, 16.5, and 16.0% RNMSEs in TPR estimation, respectively.



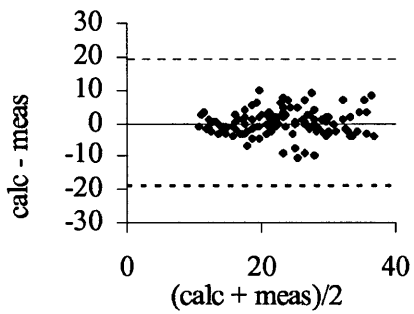
(a) Using CAP



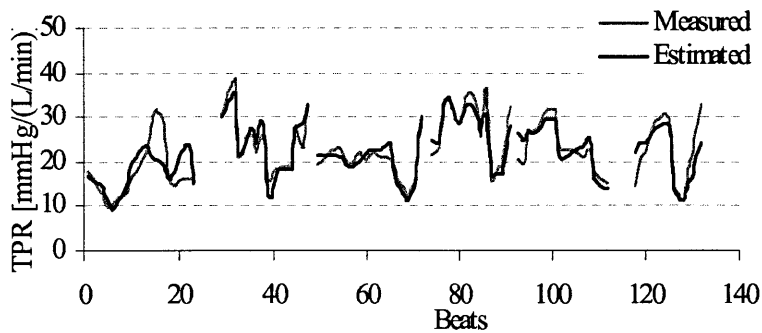
(d) BA Plot, $R^2=0.0087$



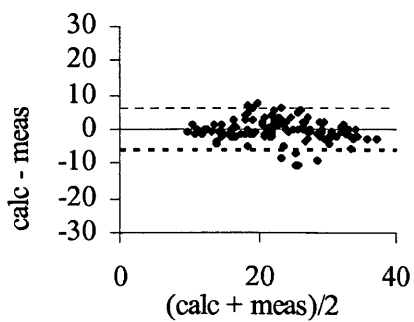
(b) Using FAP



(e) BA Plot, $R^2=0.2725$



(c) Using RAP

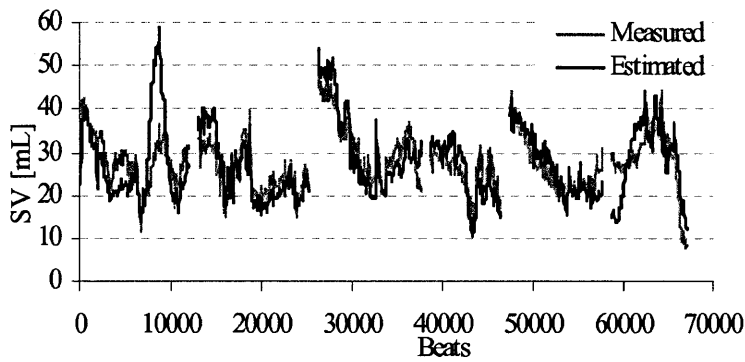


(f) BA Plot, $R^2=0.0278$

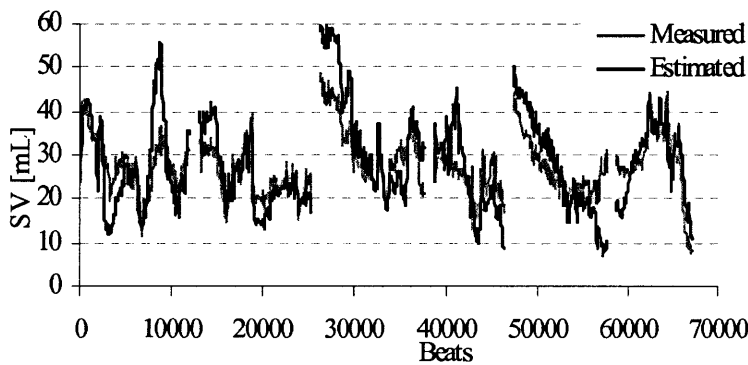
Fig. 6.15. TPR estimation by the Beat-to-Beat Averaged method.

6.2.6. Systolic Area

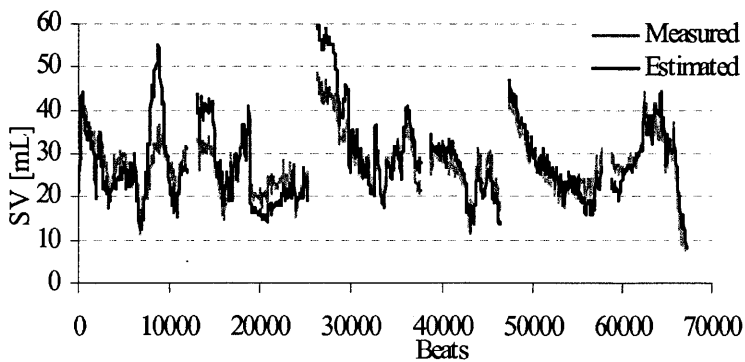
Using CAP, FAP, and RAP waveforms, the Systolic Area method achieved 16.5% (exponential model for end systole), 21.6% (50% PP for end systole), and 19.1% (60% PP for end systole) RNMSEs in SV estimation, respectively.



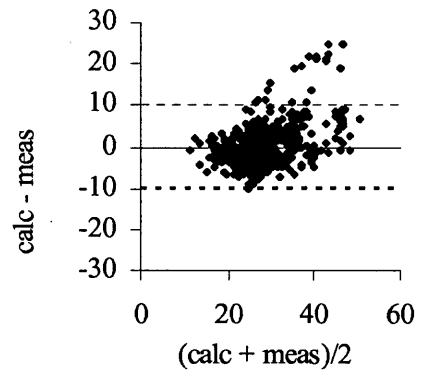
(a) Using CAP



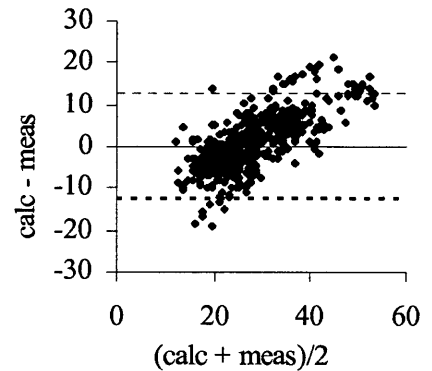
(b) Using FAP



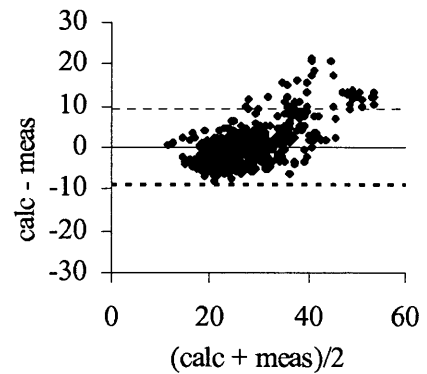
(c) Using RAP



(d) BA Plot, $R^2=0.2194$



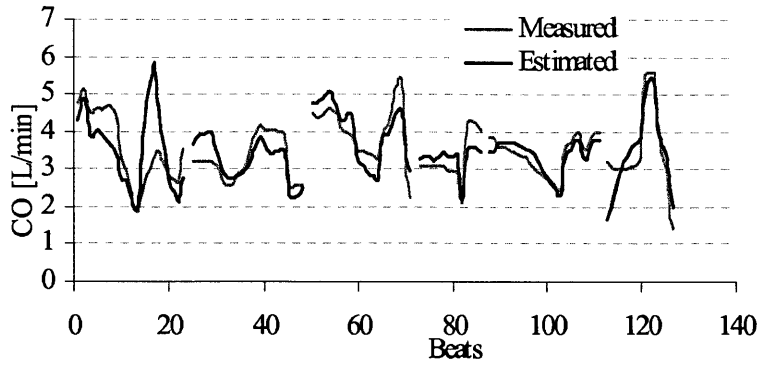
(e) BA Plot, $R^2=0.5298$



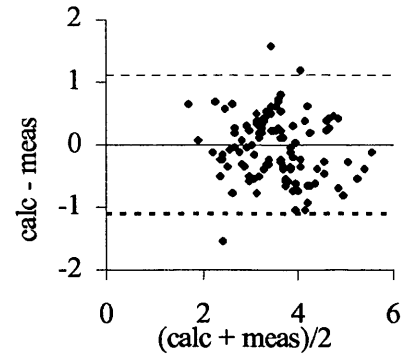
(f) BA Plot, $R^2=0.4702$

Fig. 6.16. SV estimation by the Systolic Area method.

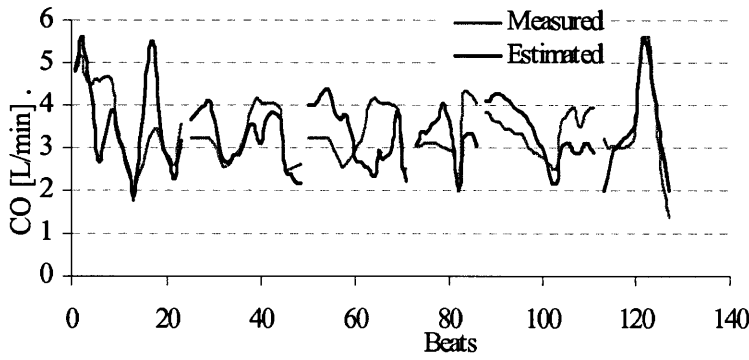
Using CAP, FAP, and RAP waveforms, the Systolic Area method achieved 14.3% (exponential model for end systole), 19.1% (50% PP for end systole), and 13.5% (true end systole) RNMSEs in CO estimation, respectively.



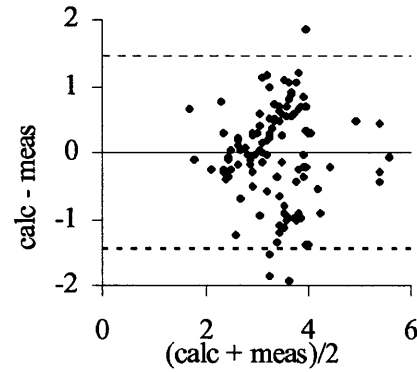
(a) Using CAP



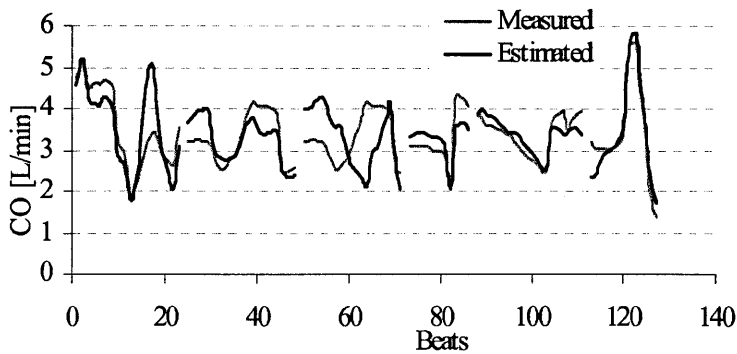
(d) BA Plot, $R^2=0.001$



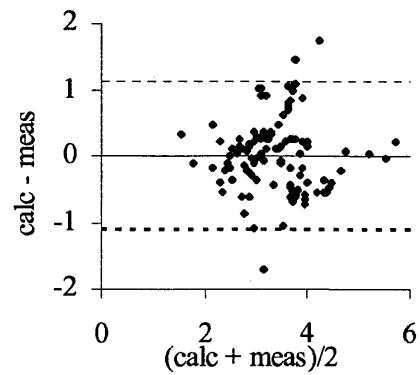
(b) Using FAP



(e) BA Plot, $R^2=0.0002$



(c) Using RAP



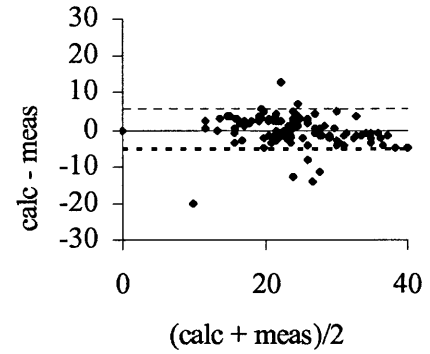
(f) BA Plot, $R^2=0.0003$

Fig. 6.17. CO estimation by the Systolic Area method.

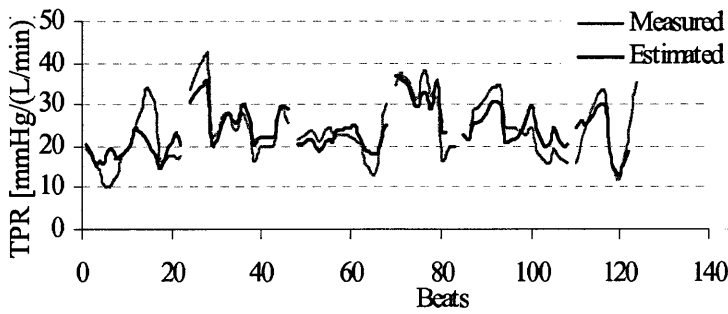
Using CAP, FAP, and RAP waveforms, the Systolic Area method achieved 16.5% (true end systole), 20.7% (true end systole), and 13.5% (true end systole) RNMSEs in TPR estimation, respectively.



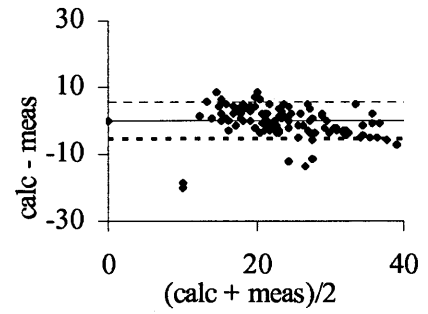
(a) Using CAP



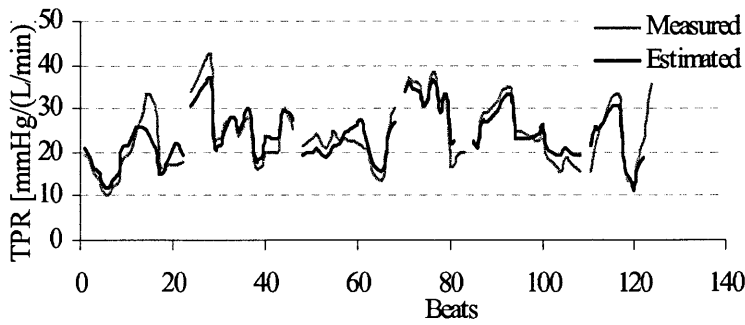
(d) BA Plot, R²=0.0139



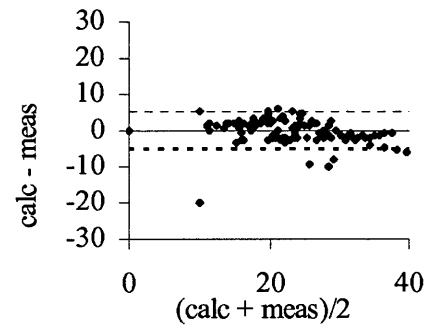
(b) Using FAP



(e) BA Plot, R²=0.0184



(c) Using RAP

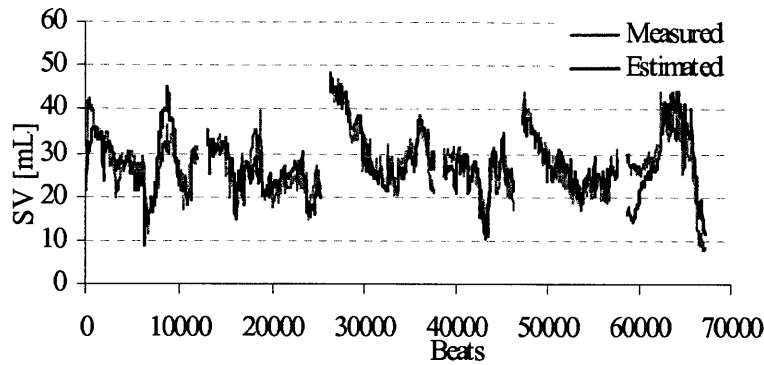


(f) BA Plot, R²=0.0011

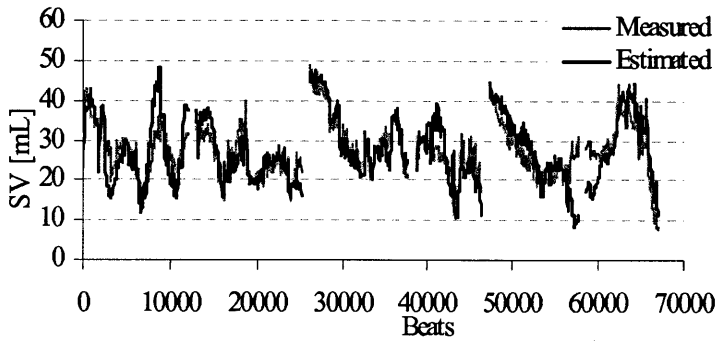
Fig. 6.18. TPR estimation by the Systolic Area method.

6.2.7. Corrected Impedance

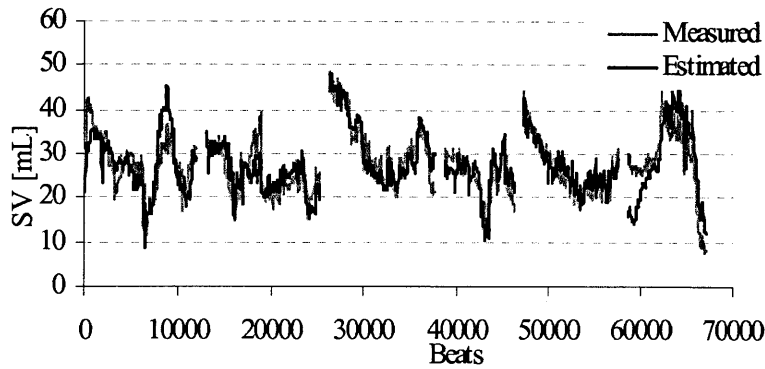
Using CAP, FAP, and RAP waveforms, the Corrected Impedance method achieved 13.9% (70% PP for end systole), 16.4% (40% PP for end systole), and 14.9% (70% PP for end systole) RNMSEs in SV estimation, respectively.



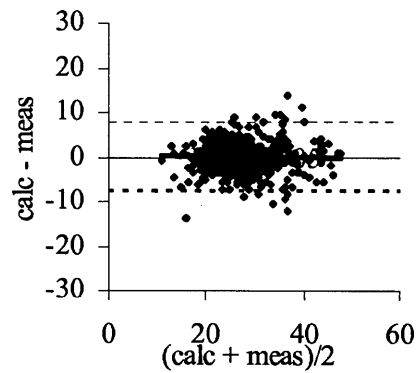
(a) Using CAP



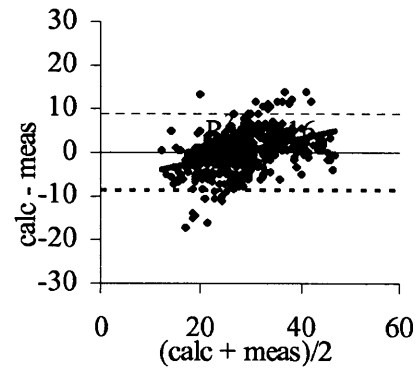
(b) Using FAP



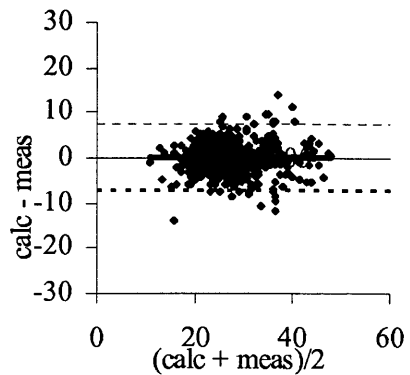
(c) Using RAP



(d) BA Plot, $R^2=0.0000$



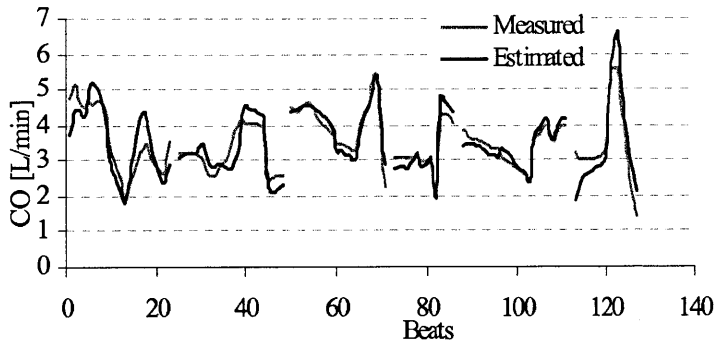
(e) BA Plot, $R^2=0.1600$



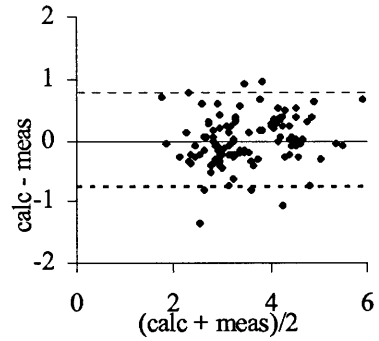
(f) BA Plot, $R^2=0.0000$

Fig. 6.19. SV estimation by the Corrected Impedance method.

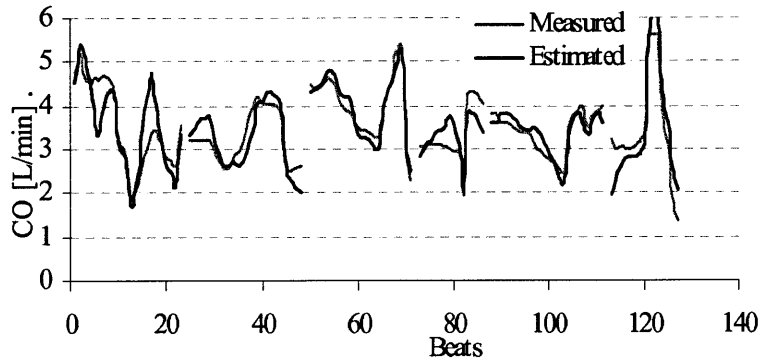
Using CAP, FAP, and RAP waveforms, the Corrected Impedance method achieved 12.7% (70% PP for end systole), 13.6% (50% PP for end systole), and 10.5% (true end systole) RNMSEs in CO estimation, respectively.



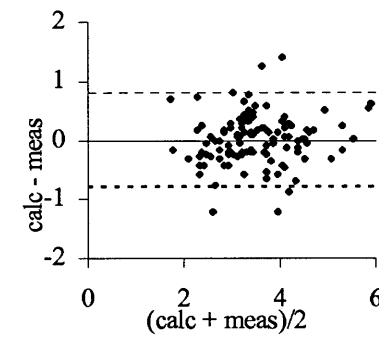
(a) Using CAP



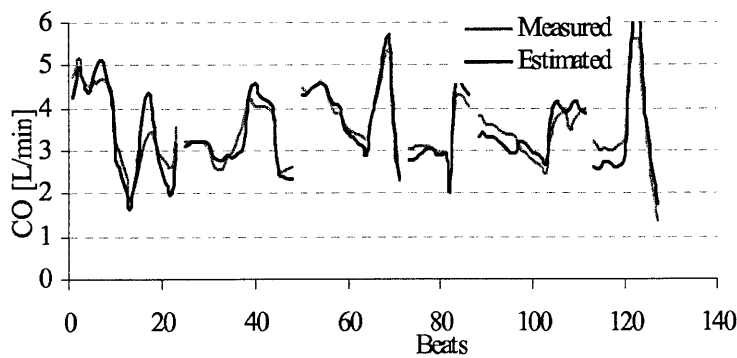
(d) BA Plot, $R^2=0.0685$



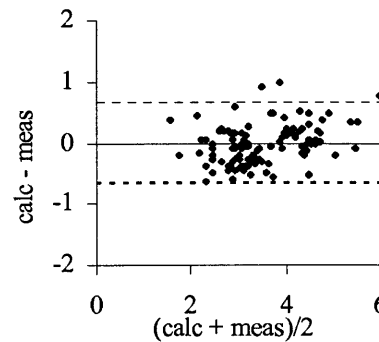
(b) Using FAP



(e) BA Plot, $R^2=0.0025$



(c) Using RAP



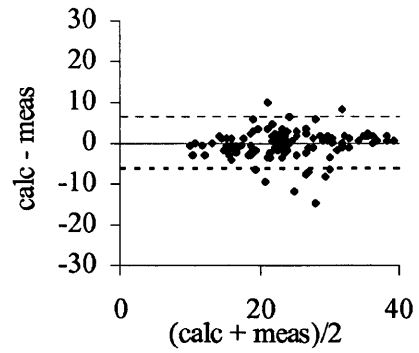
(f) BA Plot, $R^2=0.1662$

Fig. 6.20. CO estimation by the Corrected Impedance method.

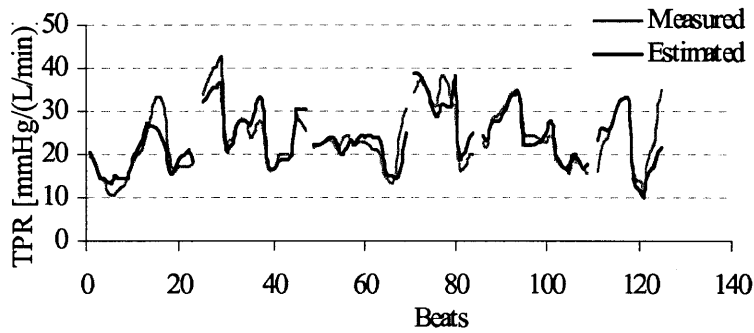
Using CAP, FAP, and RAP waveforms, the Corrected Impedance method achieved 13.7% (70% PP for end systole), 13.8% (40% PP for end systole), and 10.6% (true end systole) RNMSEs in TPR estimation, respectively.



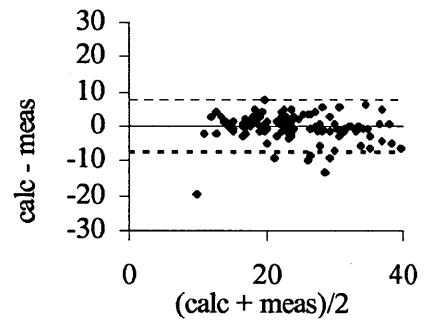
(a) Using CAP



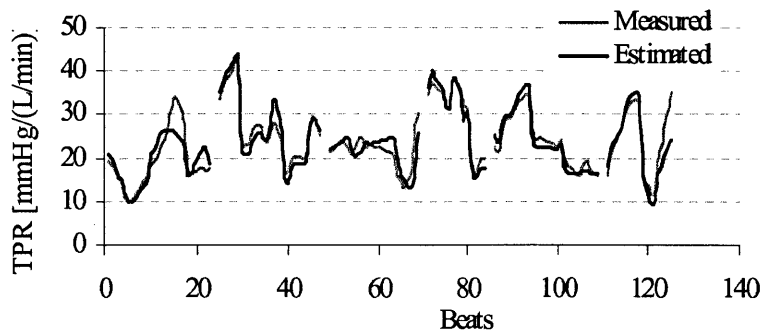
(d) BA Plot, $R^2=0.0127$



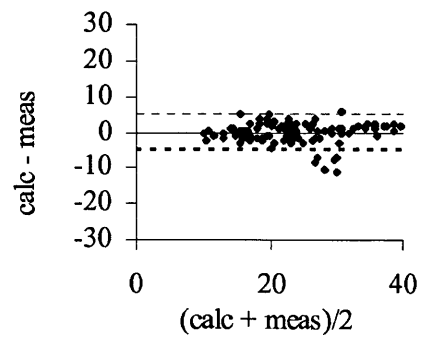
(b) Using FAP



(e) BA Plot, $R^2=0.0134$



(c) Using RAP

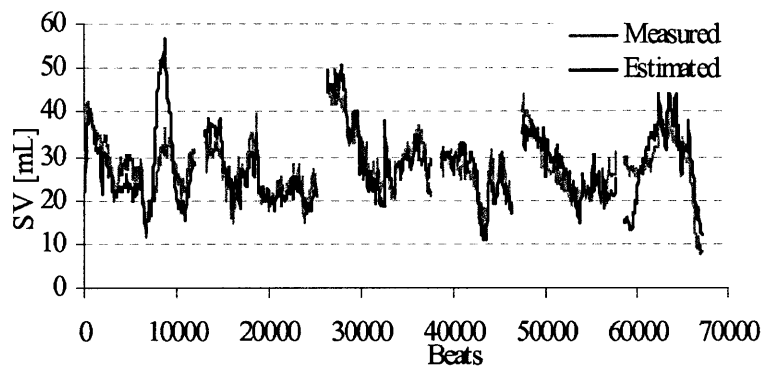


(f) BA Plot, $R^2=0.0062$

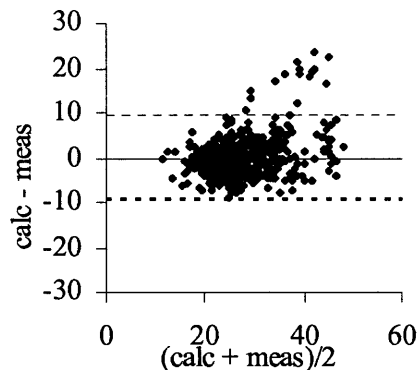
Fig. 6.21. TPR estimation by the Corrected Impedance method.

6.2.8. Systolic Area with Kouchoukos Correction

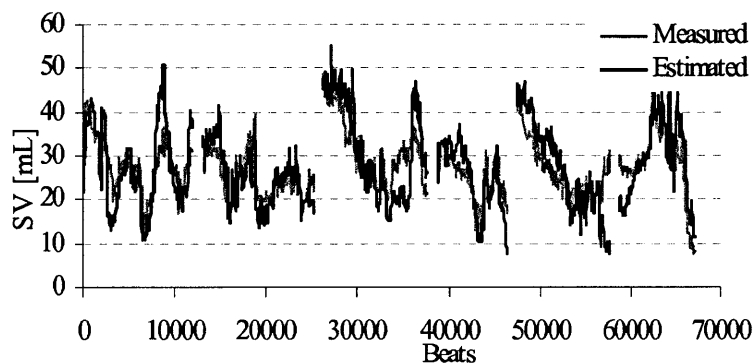
Using CAP, FAP, and RAP waveforms, the Kouchoukos Correction method achieved 14.8% (exponential model for end systole), 19.7% (50% PP for end systole), and 13.1% (exponential model for end systole) RNMSEs in SV estimation, respectively.



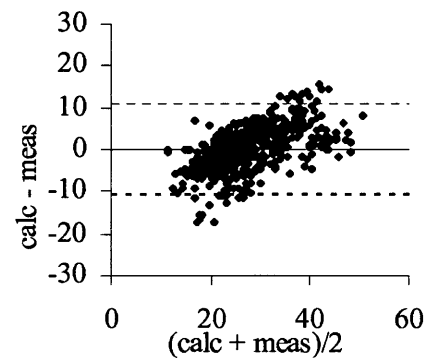
(a) Using CAP



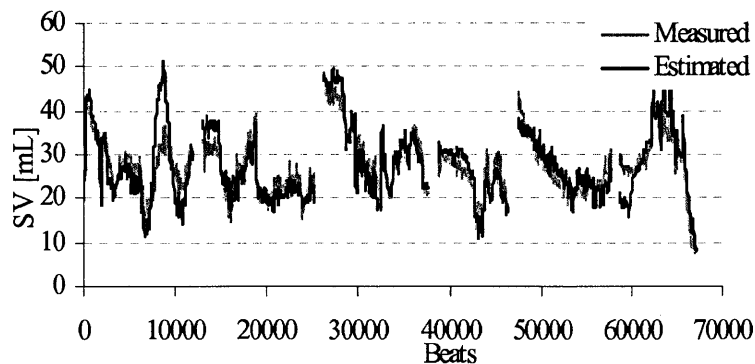
(d) BA Plot, $R^2=0.1049$



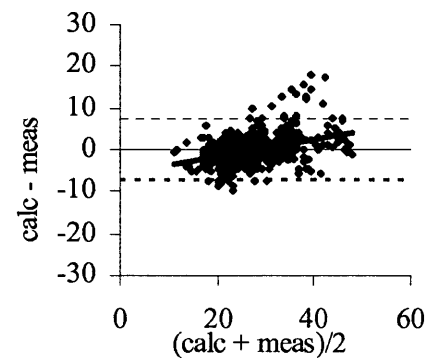
(b) Using FAP



(e) BA Plot, $R^2=0.3393$



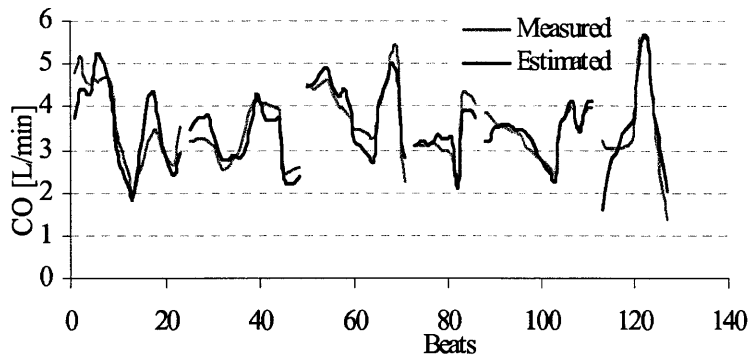
(c) Using RAP



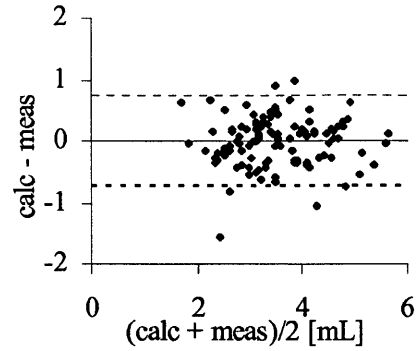
(f) BA Plot, $R^2=0.1486$

Fig. 6.22. SV estimation by the Kouchoukos method.

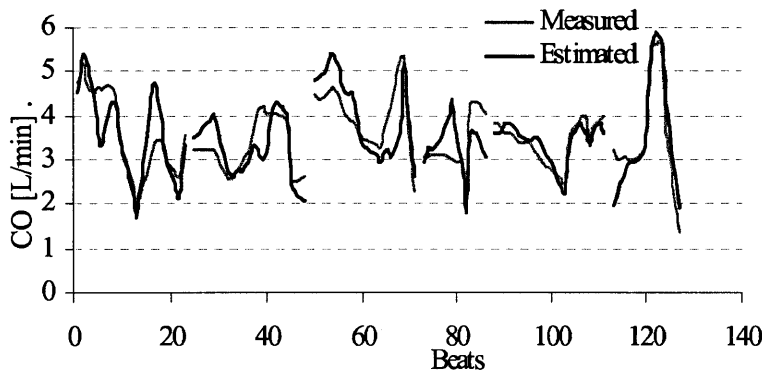
Using CAP, FAP, and RAP waveforms, the Kouchoukos Correction method achieved 12.2% (exponential model for end systole), 16.9% (50% PP for end systole), and 11.5% (exponential model for end systole) RNMSEs in CO estimation, respectively.



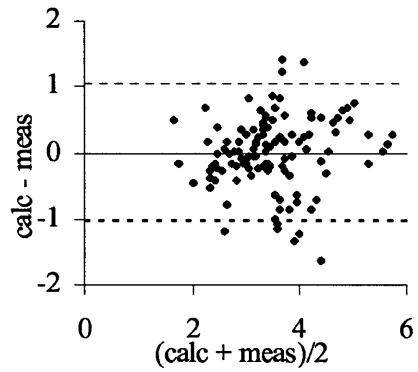
(a) Using CAP



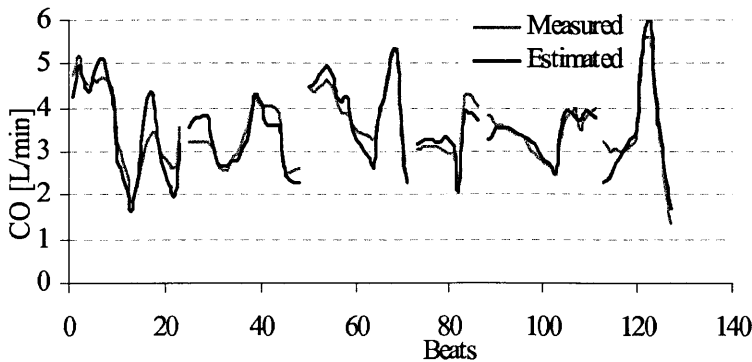
(d) BA Plot, $R^2=0.0012$



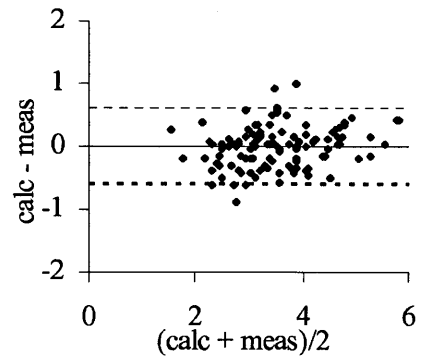
(b) Using FAP



(e) BA Plot, $R^2=0.0014$



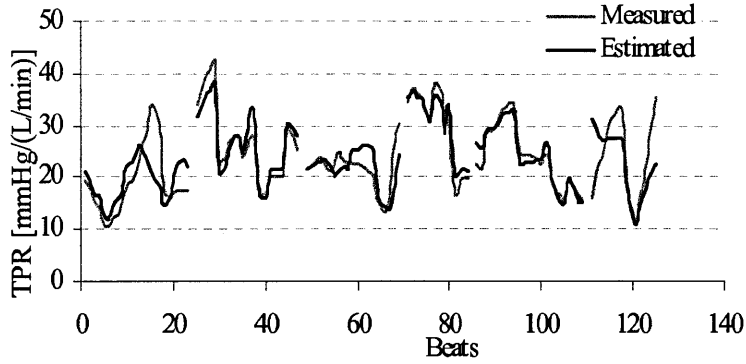
(c) Using RAP



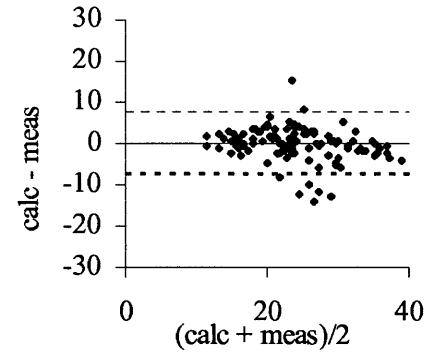
(f) BA Plot, $R^2=0.0453$

Fig. 6.23. CO estimation by the Kouchoukos method.

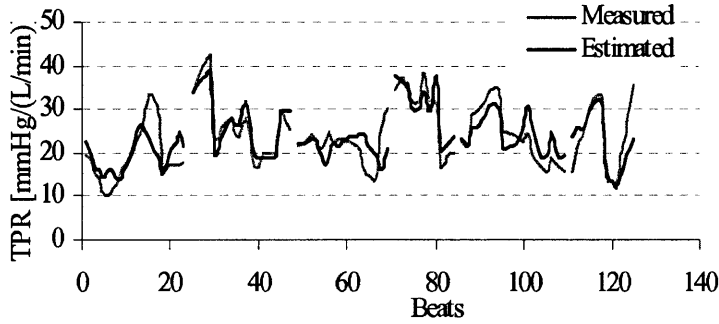
Using CAP, FAP, and RAP waveforms, the Kouchoukos Correction method achieved 15.2% (exponential model for end systole), 18.4% (true end systole), and 11.3% (exponential model for end systole) RNMSEs in TPR estimation, respectively.



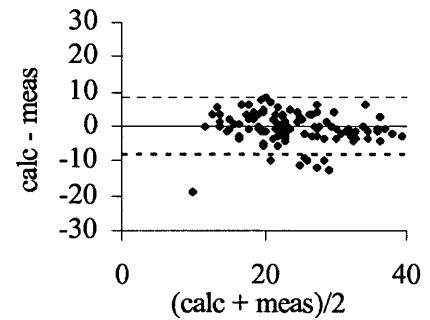
(a) Using CAP



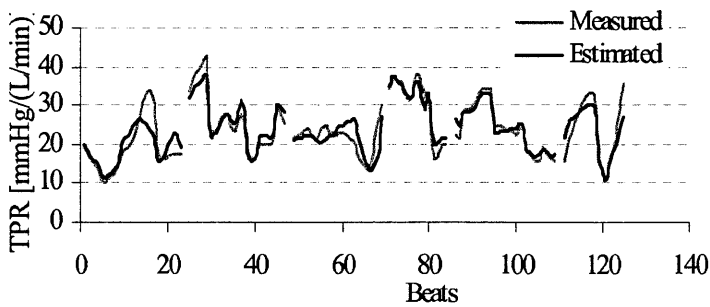
(d) BA Plot, $R^2=0.0815$



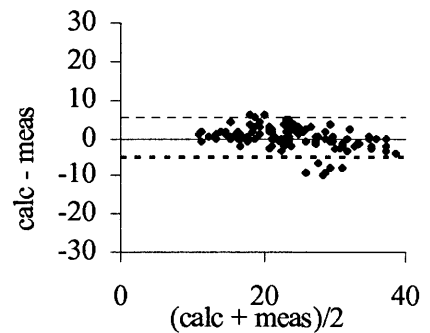
(b) Using FAP



(e) BA Plot, $R^2=0.0575$



(c) Using RAP

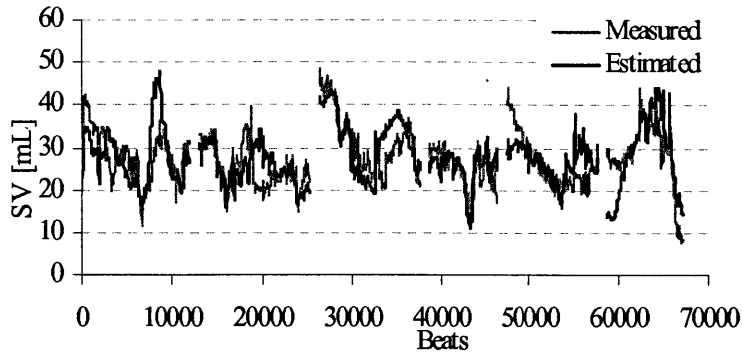


(f) BA Plot, $R^2=0.1916$

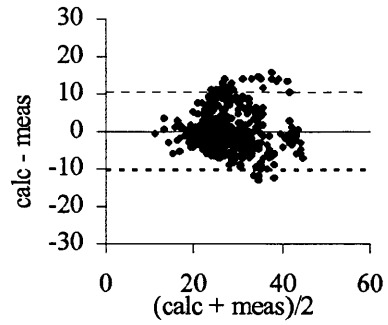
Fig. 6.24. TPR estimation by the Kouchoukos method.

6.2.9. AC Power

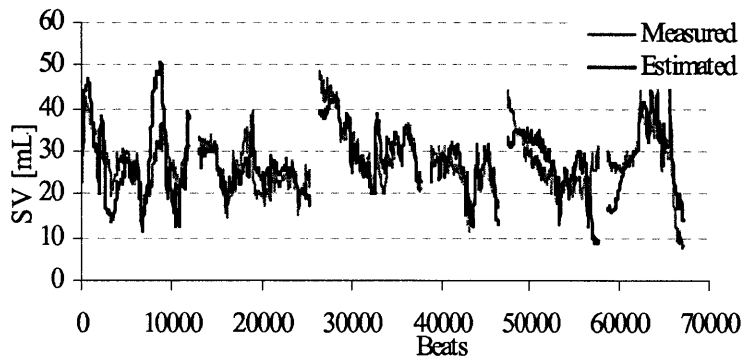
Using CAP, FAP, and RAP waveforms, the AC Power method achieved 20.6, 20.8, and 22.1% RNMSEs in SV estimation, respectively.



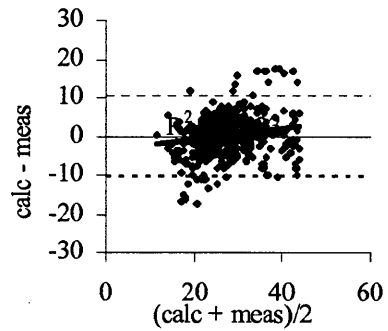
(a) Using CAP



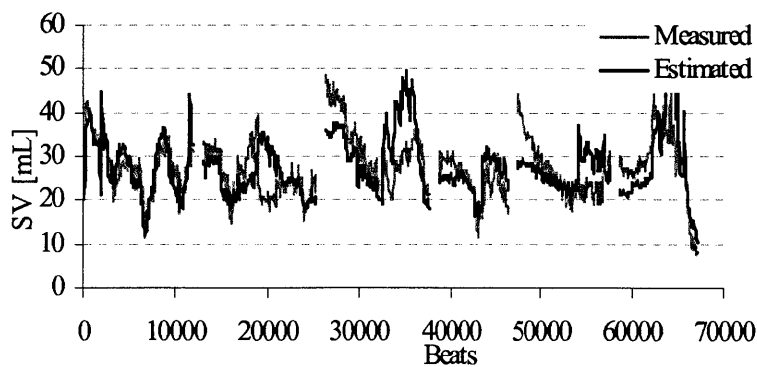
(d) BA Plot, $R^2=0.0024$



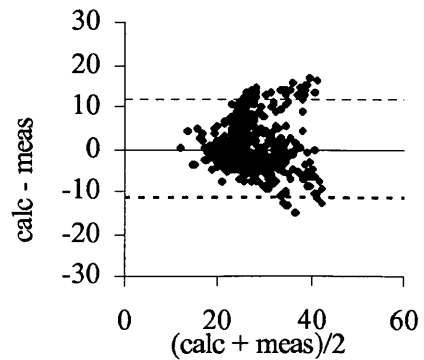
(b) Using FAP



(e) BA Plot, $R^2=0.033$



(c) Using RAP

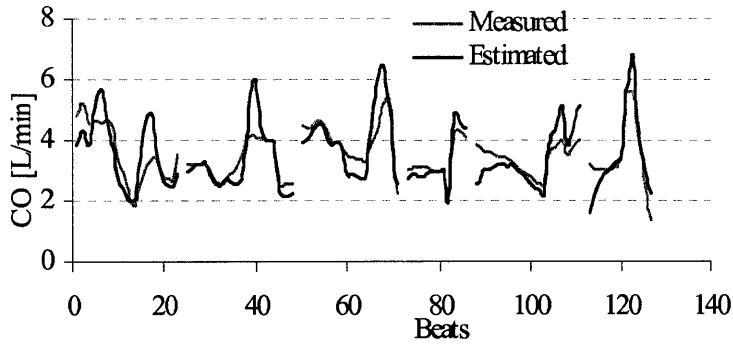


(f) BA Plot, $R^2=0.0016$

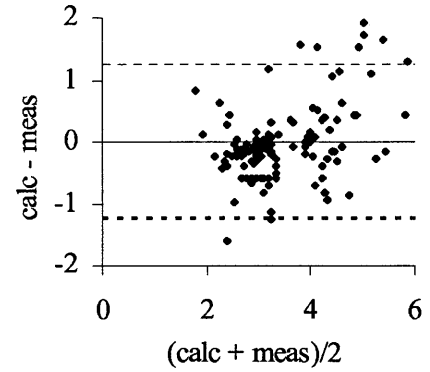
Fig. 6.25. SV estimation by the AC Power method.

Using CAP, FAP, and RAP waveforms, the AC Power method achieved 17.1, 18.1, and 18.8%

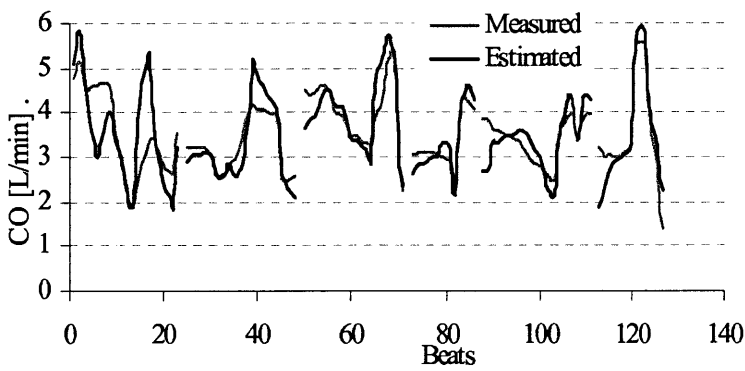
RNMSEs in CO estimation, respectively.



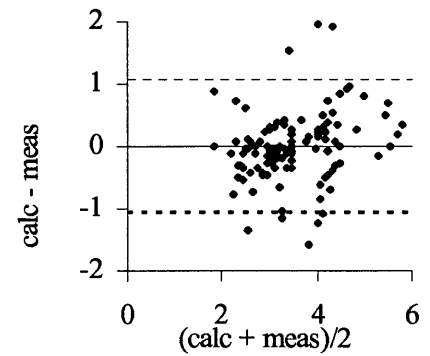
(a) Using CAP



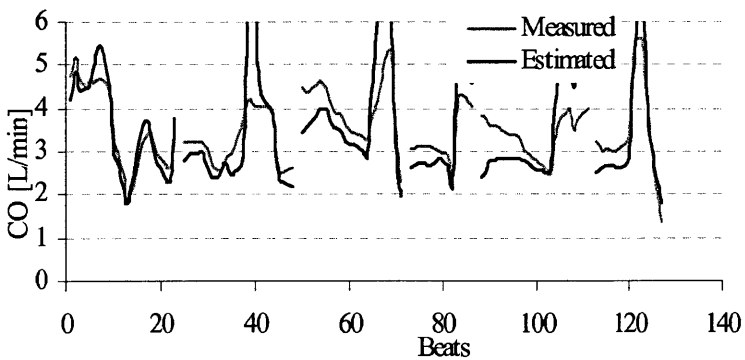
(d) BA Plot, $R^2=0.2213$



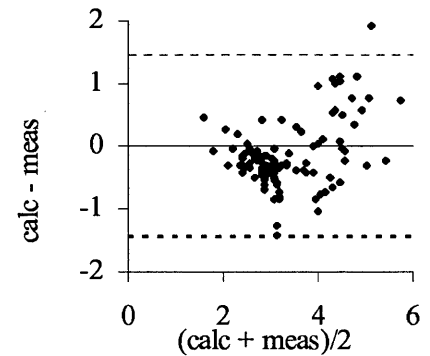
(b) Using FAP



(e) BA Plot, $R^2=0.0669$



(c) Using RAP

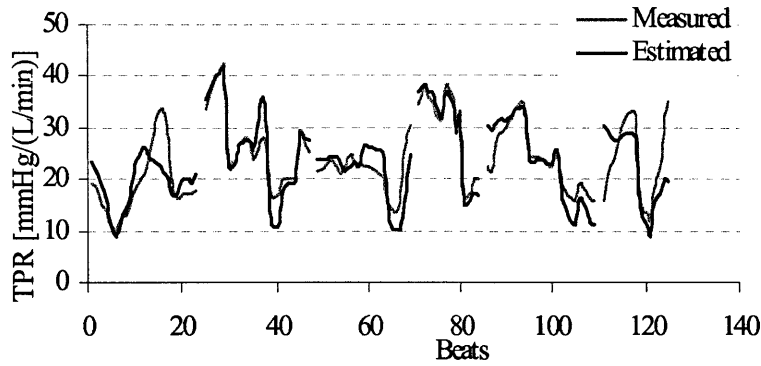


(f) BA Plot, $R^2=0.417$

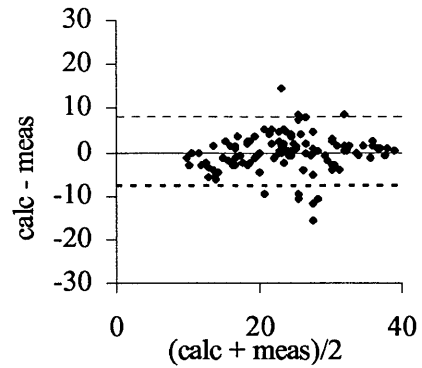
Fig. 6.26. CO estimation by the AC Power method.

Using CAP, FAP, and RAP waveforms, the AC Power method achieved 18.2, 18.2, and 16.2%

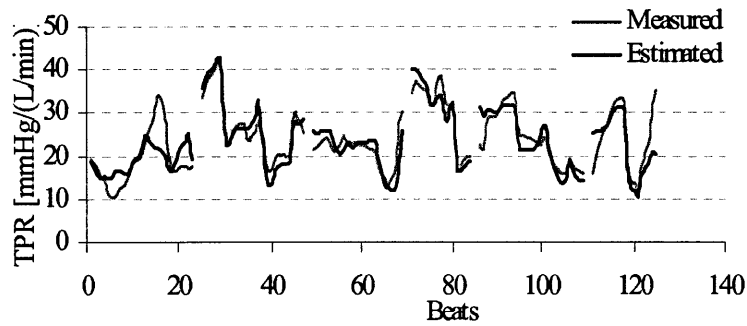
RNMSEs in TPR estimation, respectively.



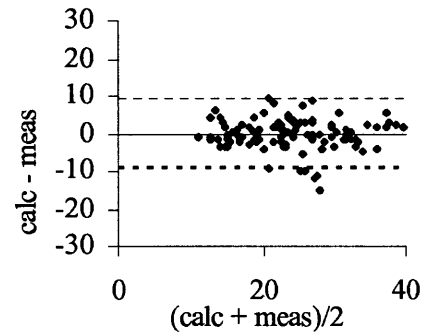
(a) Using CAP



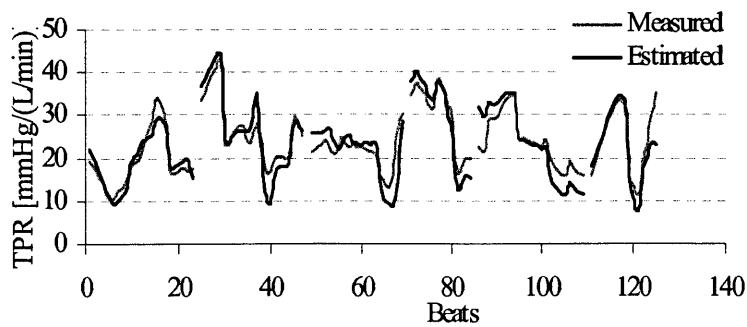
(d) BA Plot, $R^2=0.0065$



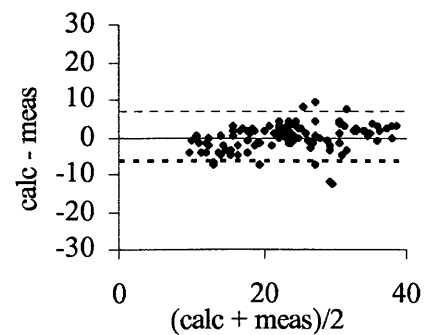
(b) Using FAP



(e) BA Plot, $R^2=0.001$



(c) Using RAP

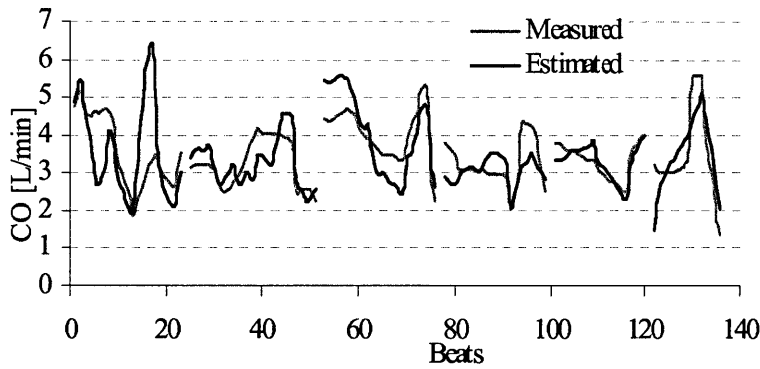


(f) BA Plot, $R^2=0.0751$

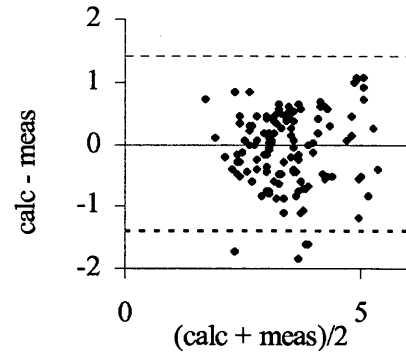
Fig. 6.27. TPR estimation by the AC Power method.

6.2.10. ARMA Model

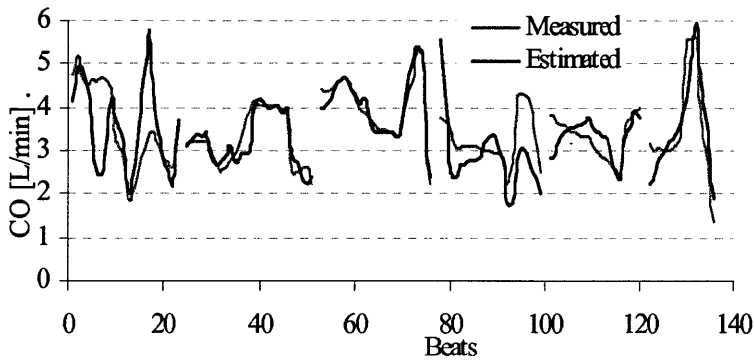
Using CAP, FAP, and RAP waveforms, the ARMA method achieved 20.2, 17.4, and 16.5% RNMSEs in CO estimation, respectively.



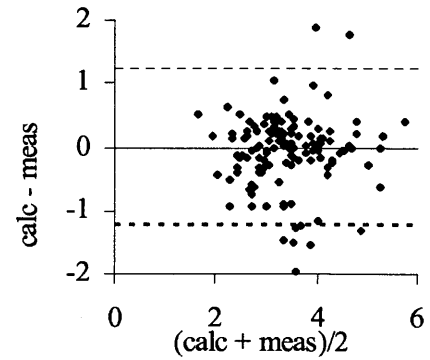
(a) Using CAP



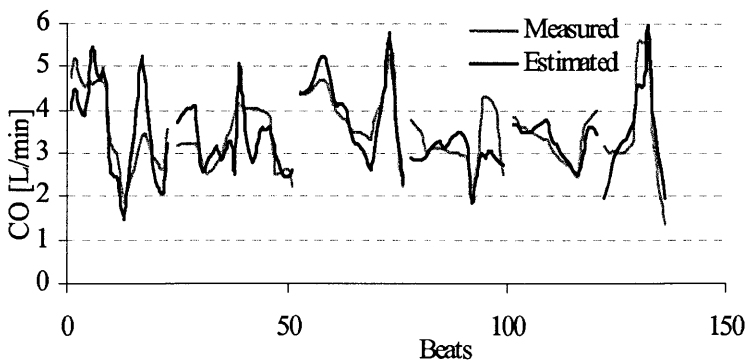
(d) BA Plot, $R^2 = 0.0261$



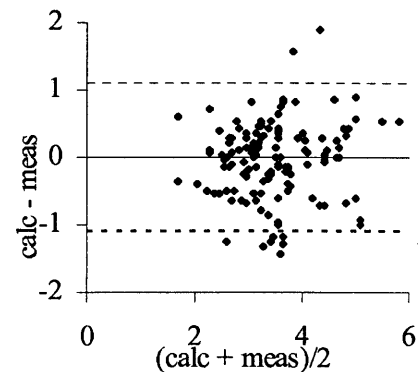
(b) Using FAP



(e) BA Plot, $R^2 = 0.0061$



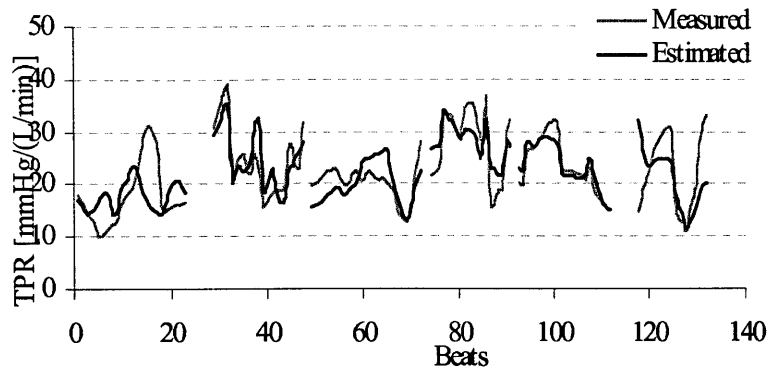
(c) Using FAP



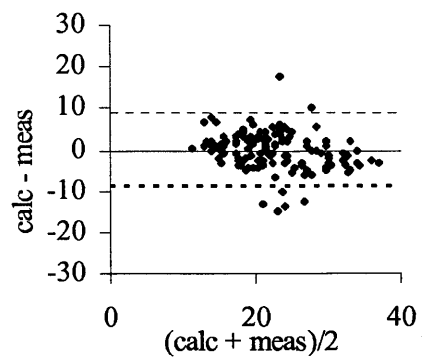
(f) BA Plot, $R^2 = 0.0094$

Fig. 6.28. CO estimation by the ARMA method.

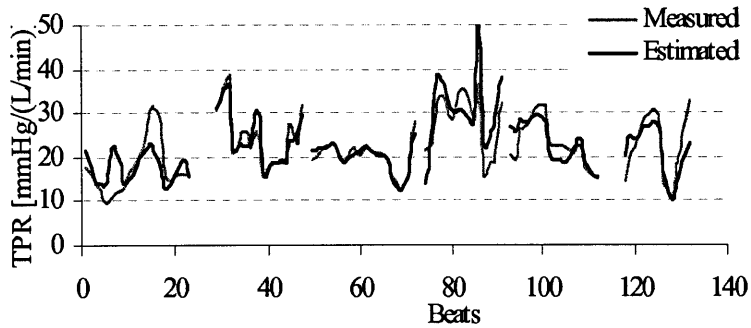
Using CAP, FAP, and RAP waveforms, the ARMA method achieved 16.5, 19.4, and 17.9% RNMSEs in TPR estimation, respectively.



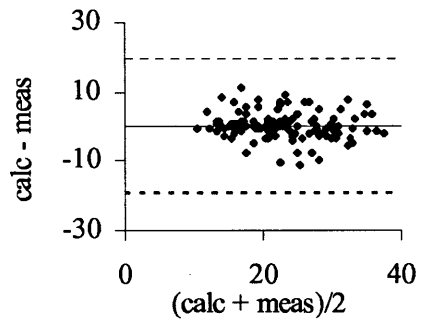
(a) Using CAP



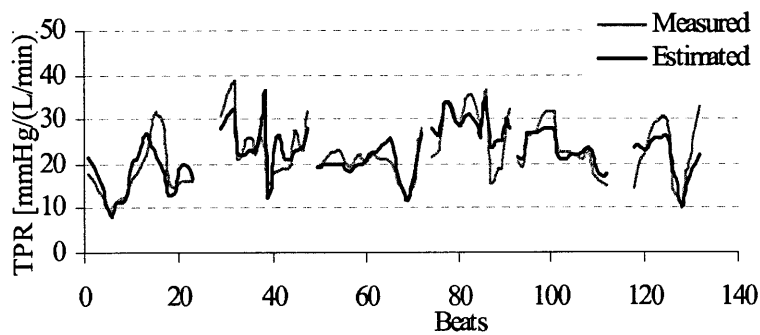
(d) BA Plot, $R^2 = 0.0718$



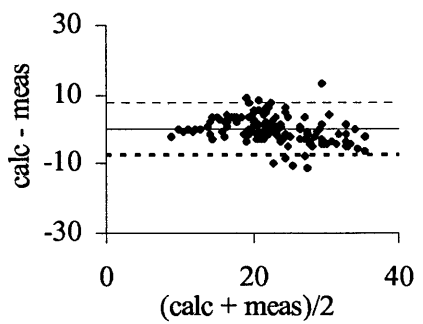
(b) Using FAP



(e) BA Plot, $R^2 = 0.2524$



(c) Using RAP

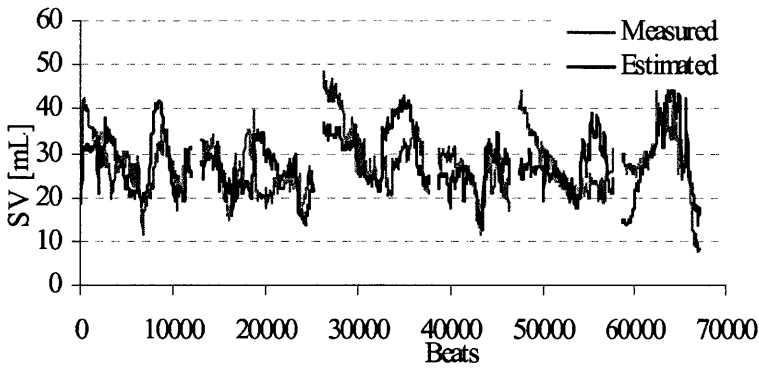


(f) BA Plot, $R^2 = 0.0997$

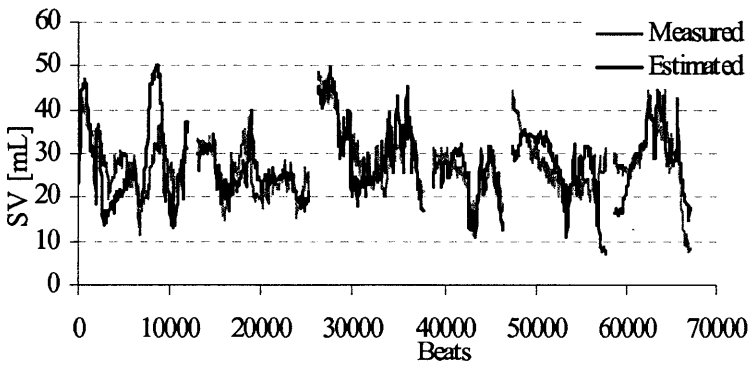
Fig. 6.29. TPR estimation by the ARMA method.

6.2.11. Minimum Variance Method

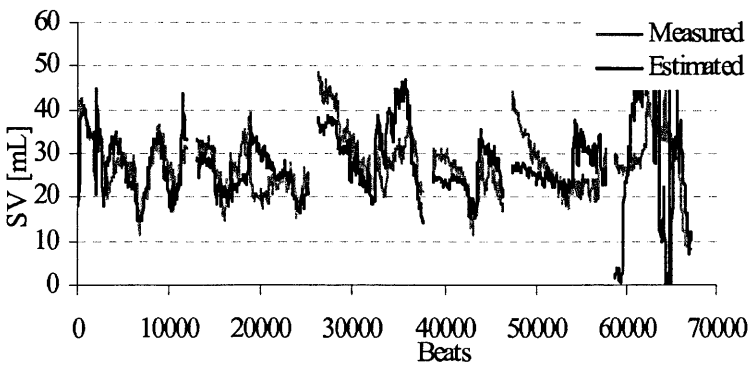
Using CAP, FAP, and RAP waveforms, the Minimum Variance method achieved 21.0, 27.2, and 22.6% RNMSEs in SV estimation, respectively.



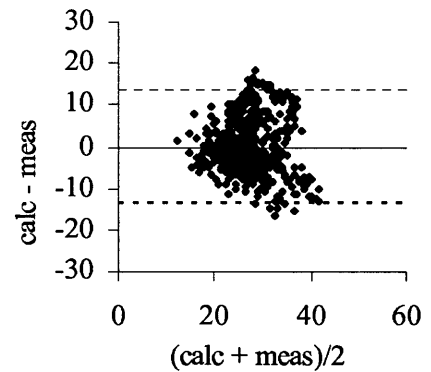
(a) Using CAP



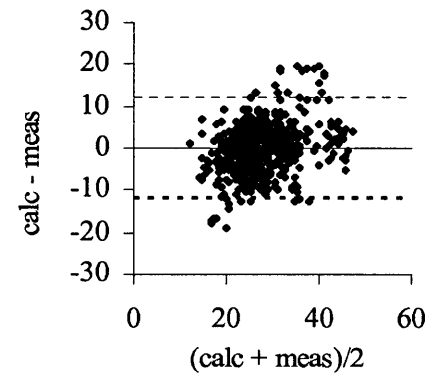
(b) Using FAP



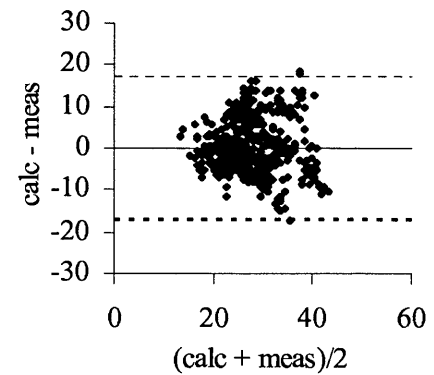
(c) Using RAP



(d) BA Plot, $R^2 = 0.0057$



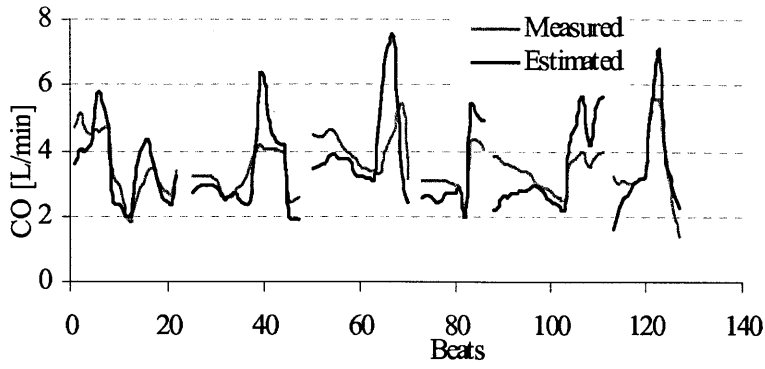
(e) BA Plot, $R^2 = 0.0707$



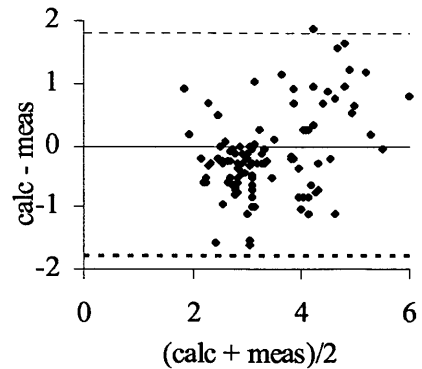
(f) BA Plot, $R^2 = 0.0004$

Fig. 6.30. SV estimation by the Minimum Variance method.

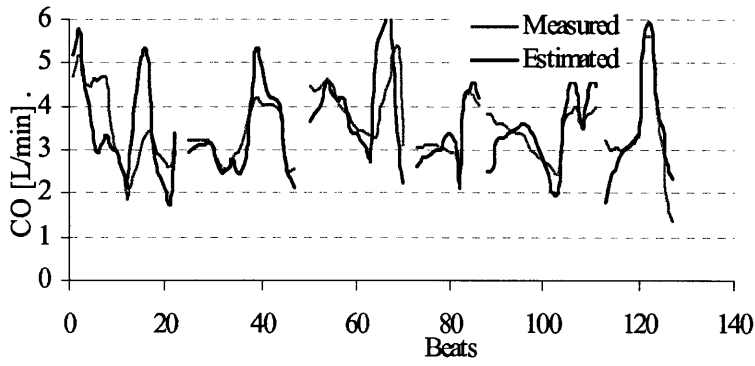
Using CAP, FAP, and RAP waveforms, the Minimum Variance method achieved 15.5, 23.6, and 19.8% RNMSEs in CO estimation, respectively.



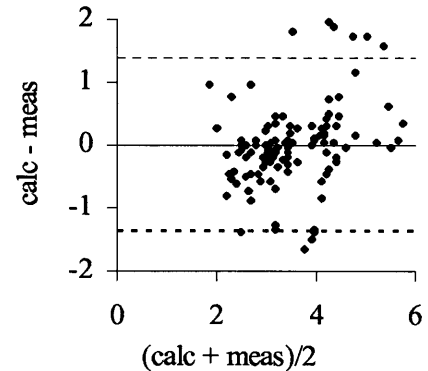
(a) Using CAP



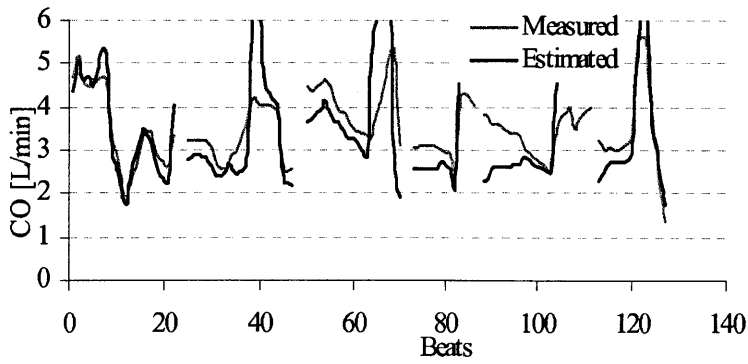
(d) BA Plot, $R^2 = 0.3276$



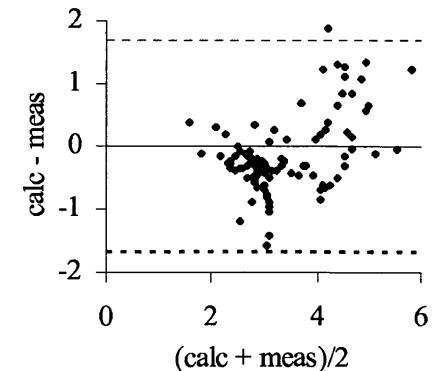
(b) Using FAP



(e) BA Plot, $R^2 = 0.0908$



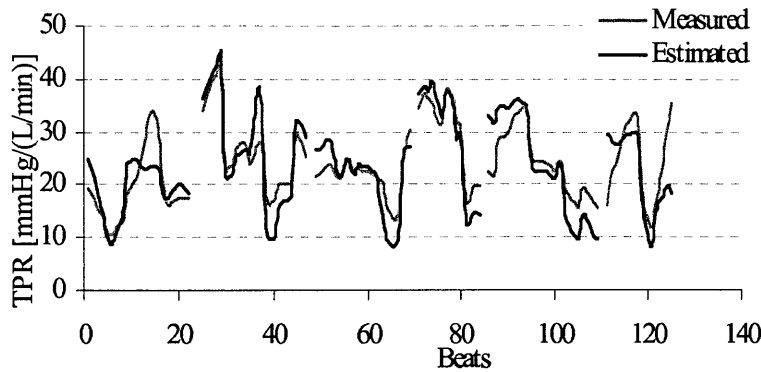
(c) Using RAP



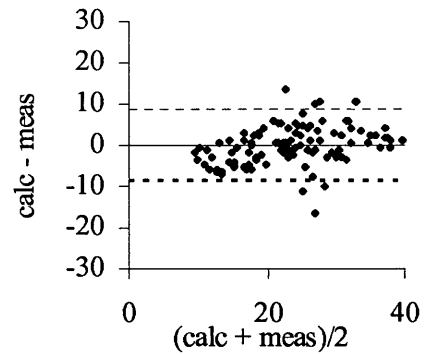
(f) BA Plot, $R^2 = 0.3894$

Fig. 6.31. CO estimation by the Minimum Variance method.

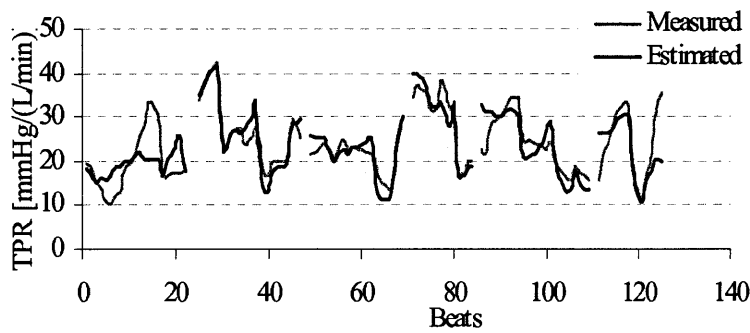
Using CAP, FAP, and RAP waveforms, the Minimum Variance method achieved 23.1, 21.3, and 18.7% RNMSEs in TPR estimation, respectively.



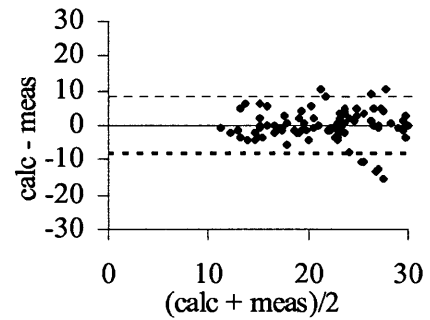
(a) Using CAP



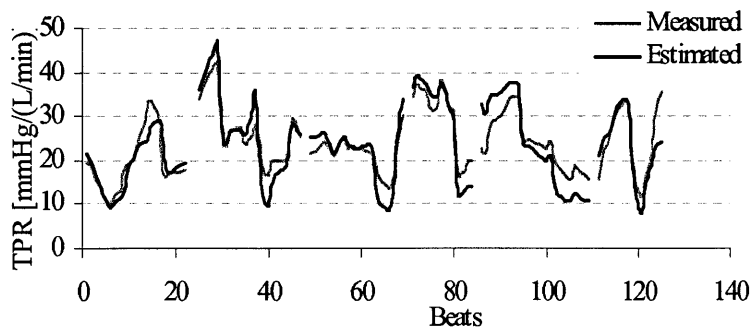
(d) BA Plot, $R^2 = 0.1313$



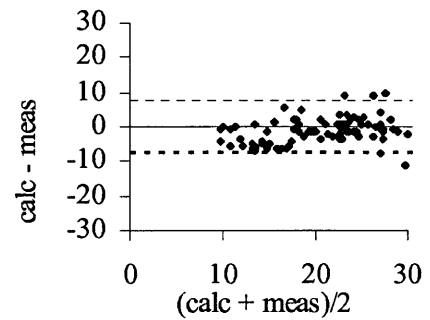
(b) Using FAP



(e) BA Plot, $R^2 = 0.0000$



(c) Using RAP

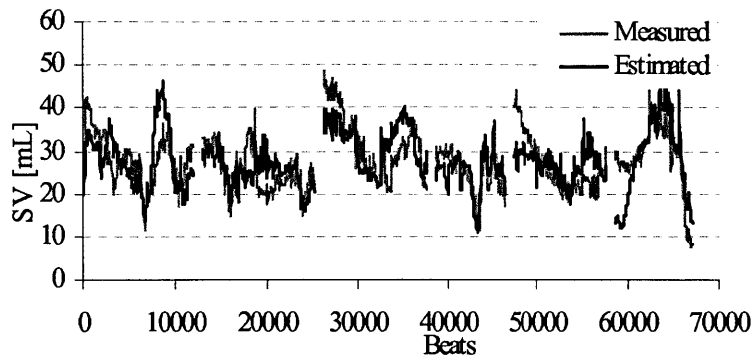


(f) BA Plot, $R^2 = 0.2787$

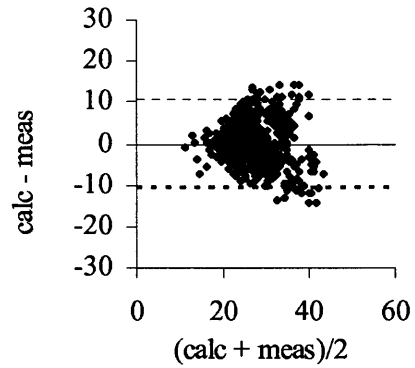
Fig. 6.32. TPR estimation by the Minimum Variance method.

6.2.12. Modified Herd's Method

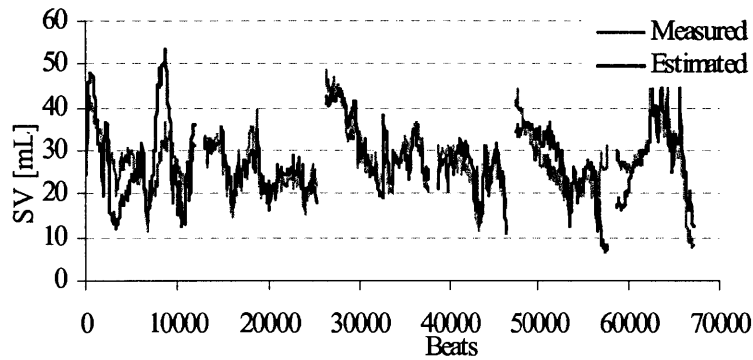
Using CAP, FAP, and RAP waveforms, the Modified Herd's method achieved 14.8% (exponential model for end systole), 18.9% (exponential model for end systole), and 14.8% (exponential model for end systole) RNMSEs in SV estimation, respectively.



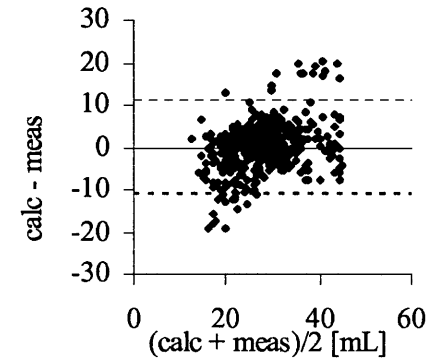
(a) Using CAP



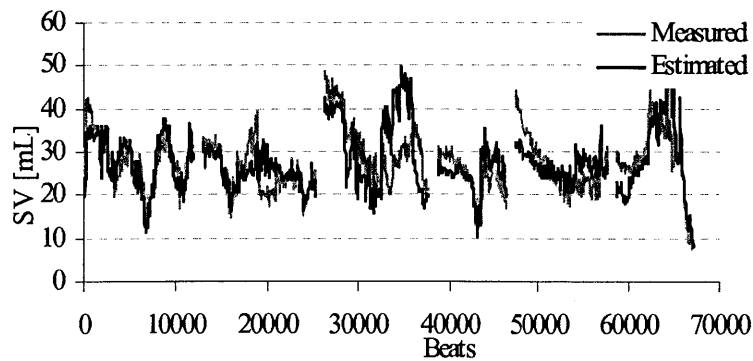
(d) BA Plot, $R^2 = 0.0205$



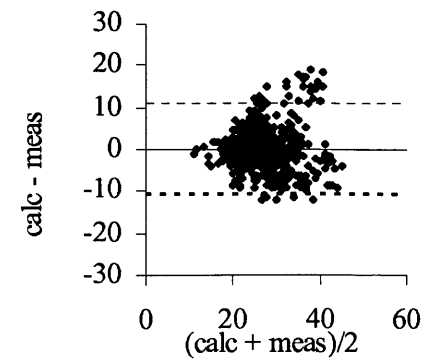
(b) Using FAP



(e) BA Plot, $R^2 = 0.0936$



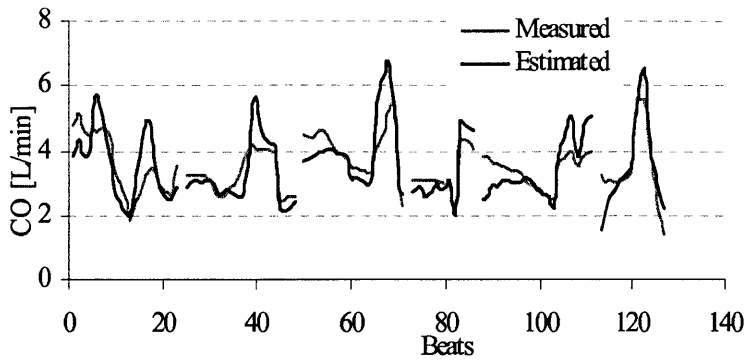
(c) Using RAP



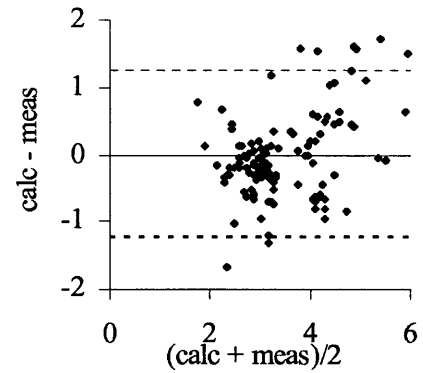
(f) BA Plot, $R^2 = 0.0002$

Fig. 6.33. SV estimation by the Modified Herd's method.

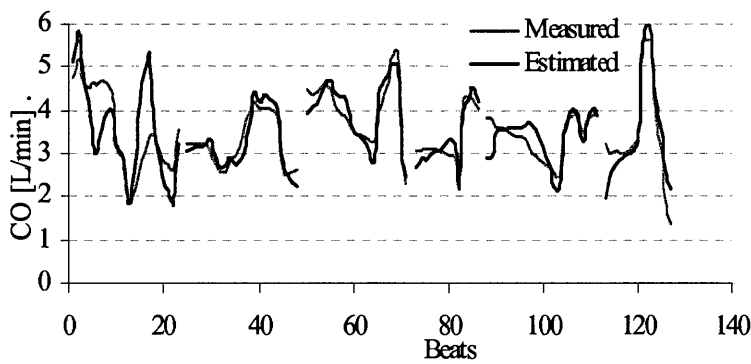
Using CAP, FAP, and RAP waveforms, the Modified Herd's method achieved 12.7% (exponential model for end systole), 17.1% (exponential model for end systole), and 13.0% (exponential model for end systole) RNMSEs in CO estimation, respectively.



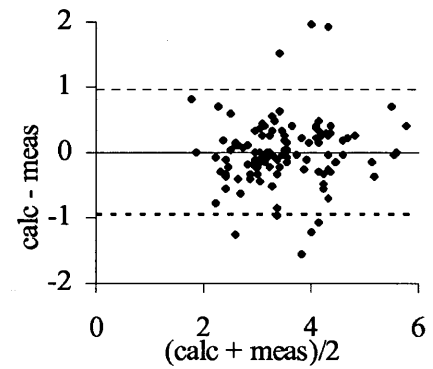
(a) Using CAP



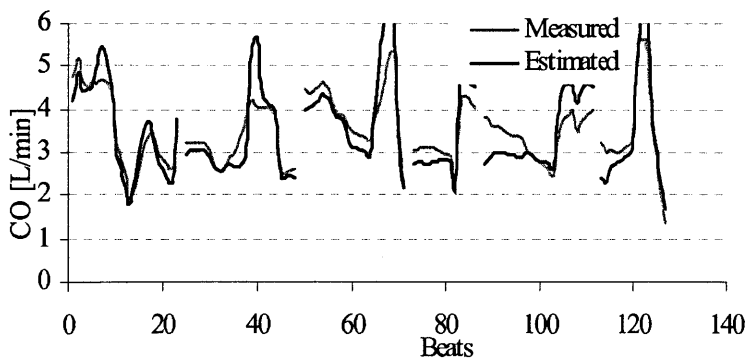
(d) BA Plot, $R^2 = 0.1952$



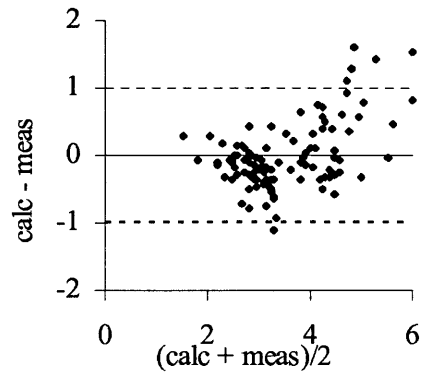
(b) Using FAP



(e) BA Plot, $R^2 = 0.015$



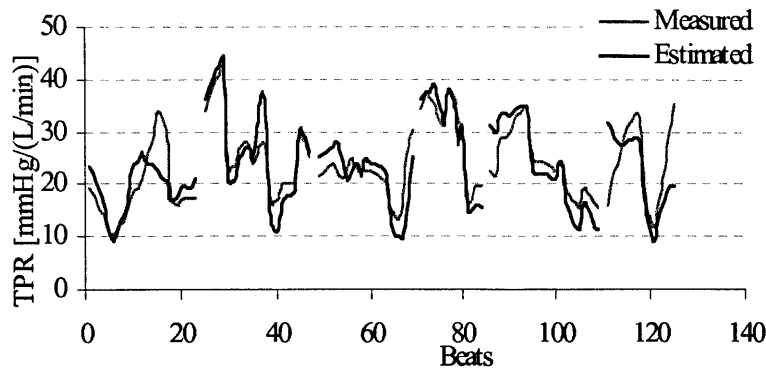
(c) Using RAP



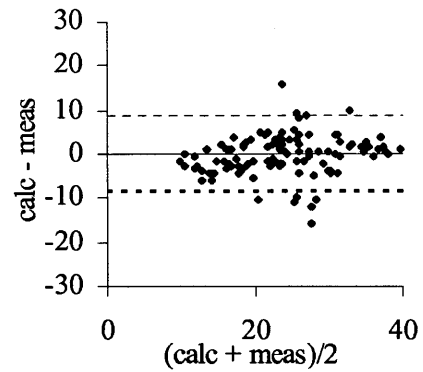
(f) BA Plot, $R^2 = 0.3263$

Fig. 6.34. CO estimation by the Modified Herd method.

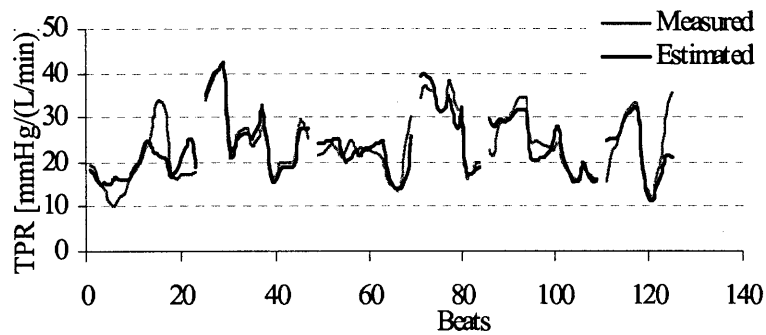
Using CAP, FAP, and RAP waveforms, the Modified Herd's method achieved 16.1% (exponential model for end systole), 17.1% (exponential model for end systole), and 13.7% (exponential model for end systole) RNMSEs in TPR estimation, respectively.



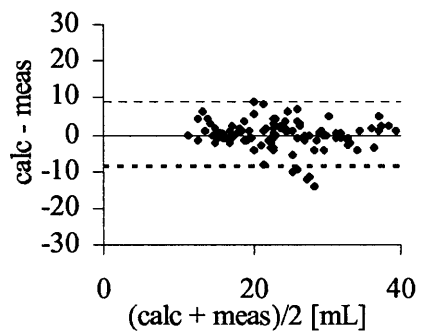
(a) Using CAP



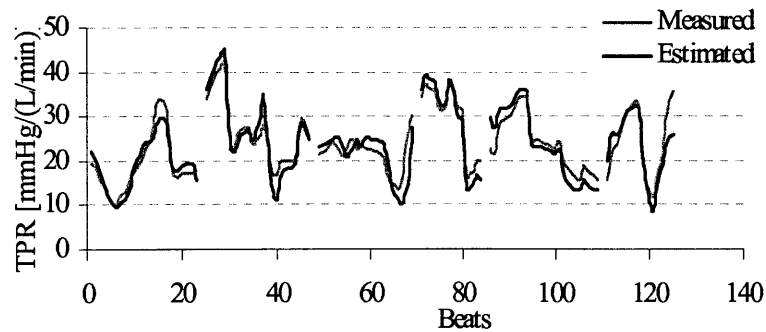
(d) BA Plot, $R^2 = 0.0502$



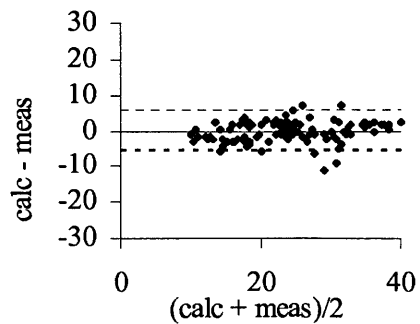
(b) Using FAP



(e) BA Plot, $R^2 = 0.0000$



(c) Using RAP

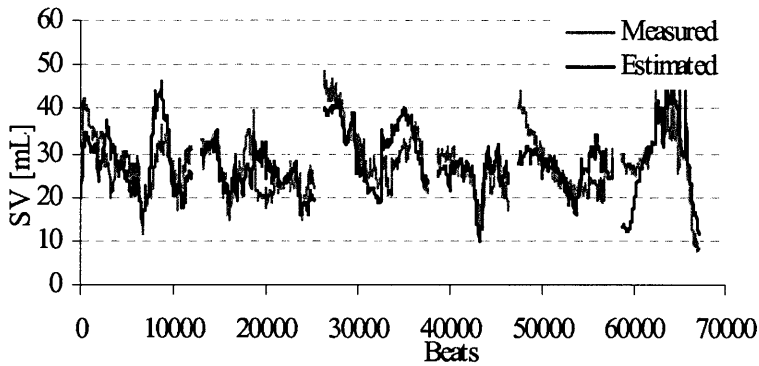


(f) BA Plot, $R^2 = 0.0678$

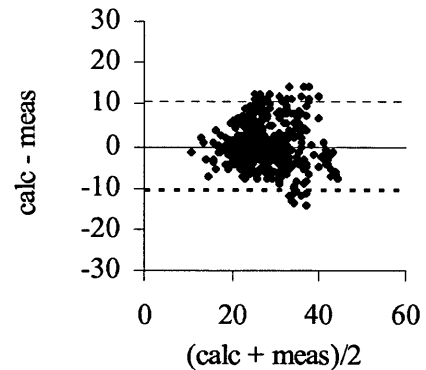
Fig. 6.35. TPR estimation by the Modified Herd method.

6.2.13. Parabolic ABF Model

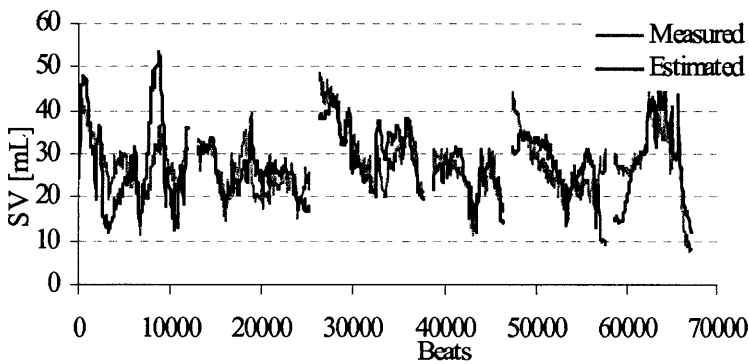
Using CAP, FAP, and RAP waveforms, the Parabolic ABF method achieved 18.3% (50% PP for end systole), 19.9% (40% PP for end systole), and 19.1% (100% PP for end systole) RNMSEs in SV estimation, respectively.



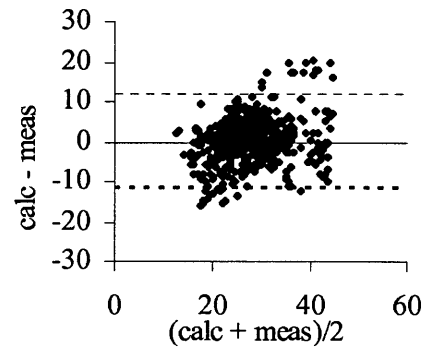
(a) Using CAP



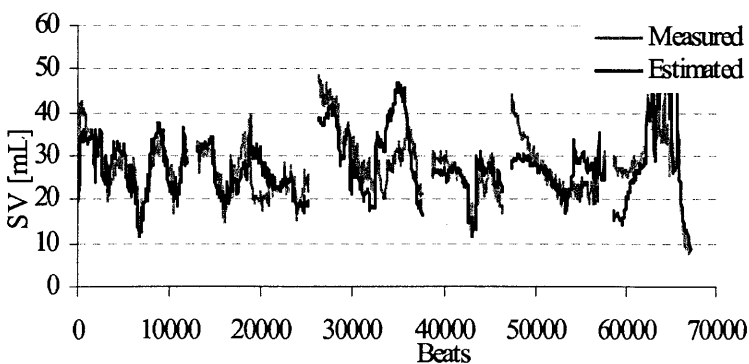
(d) BA Plot, $R^2 = 0.0026$



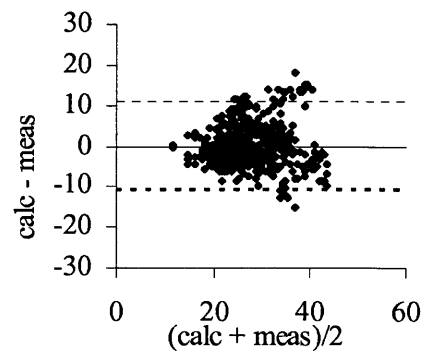
(b) Using FAP



(e) BA Plot, $R^2 = 0.0554$



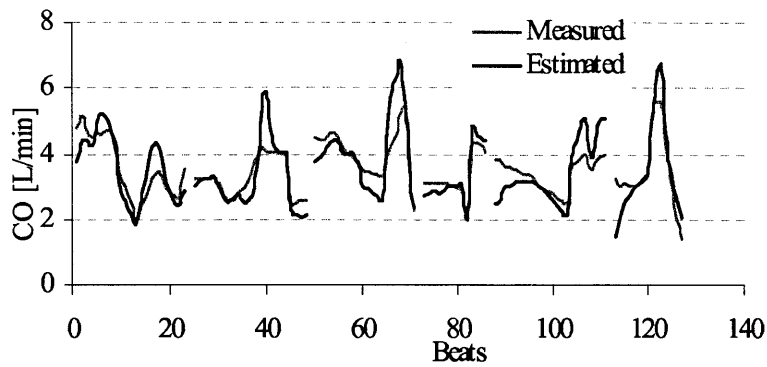
(c) Using RAP



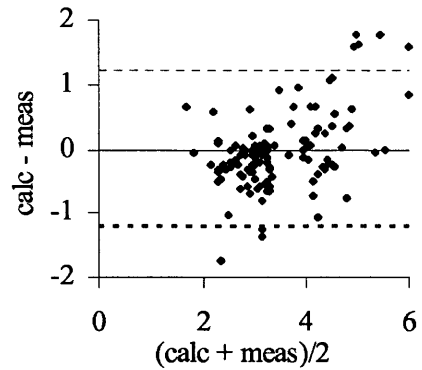
(f) BA Plot, $R^2 = 0.000$

Fig. 6.36. SV estimation by the Parabolic ABF method.

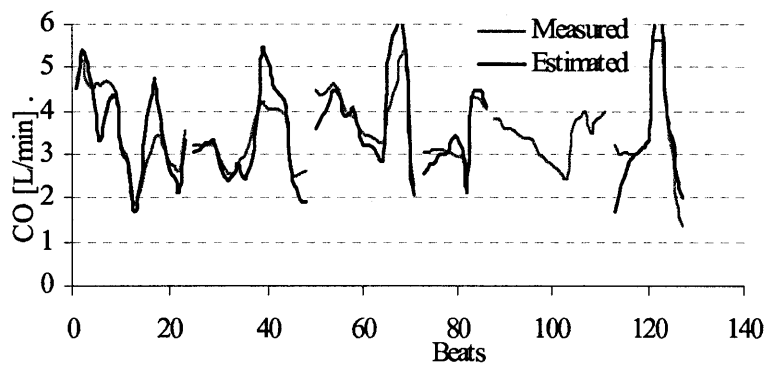
Using CAP, FAP, and RAP waveforms, the Parabolic ABF method achieved 13.5% (40% PP for end systole), 15.7% (40% PP for end systole), and 15.0% (70% PP for end systole) RNMSEs in SV estimation, respectively.



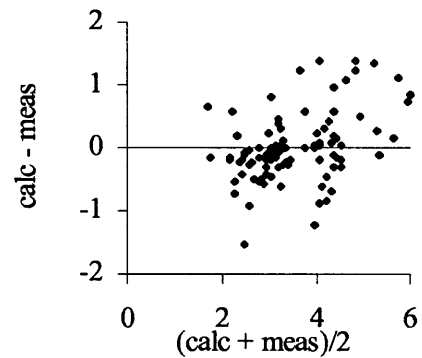
(a) Using CAP



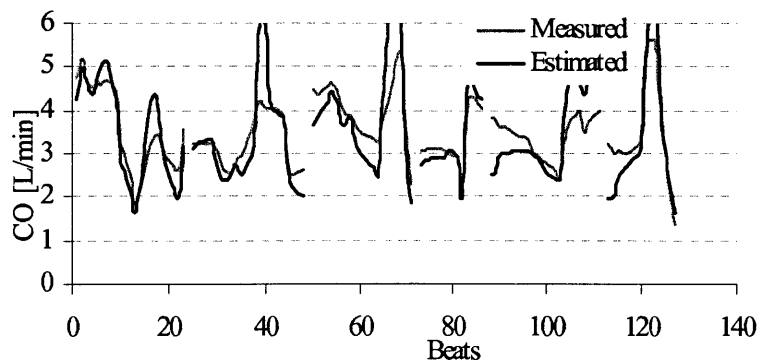
(d) BA Plot, $R^2 = 0.2706$



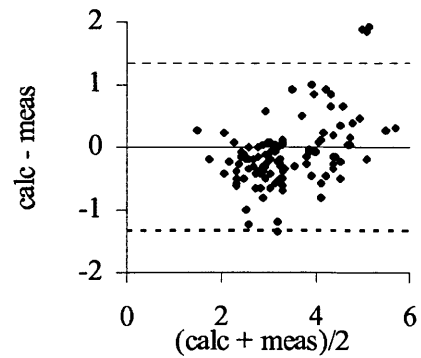
(b) Using FAP



(e) BA Plot, $R^2 = 0.00$



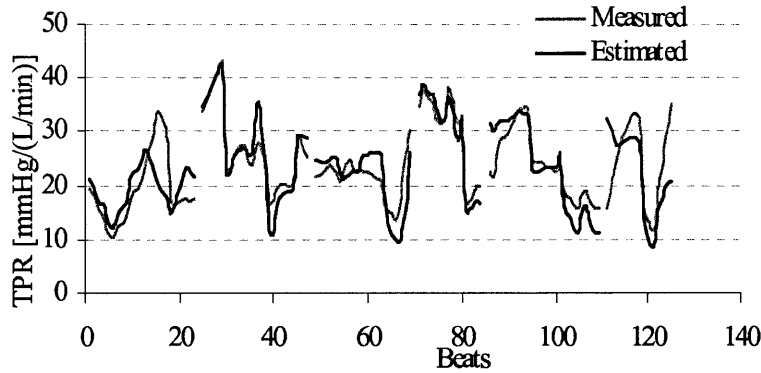
(c) Using RAP



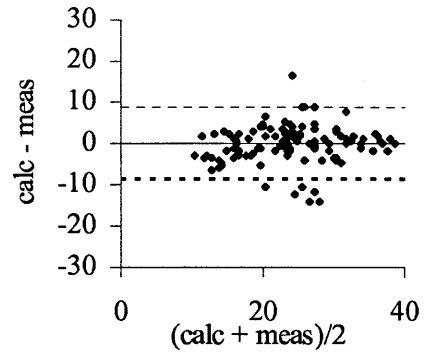
(f) BA Plot, $R^2 = 0.4194$

Fig. 6.37. CO estimation by the Parabolic ABF method.

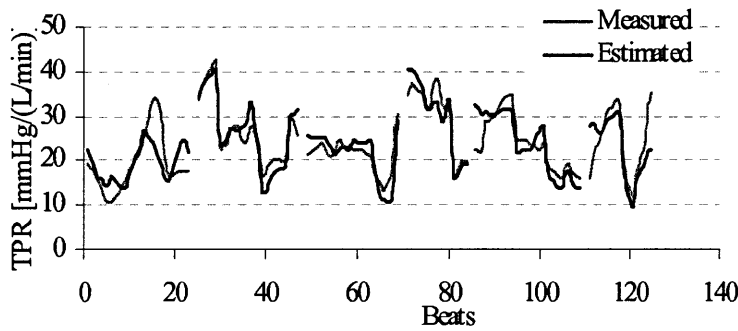
Using CAP, FAP, and RAP waveforms, the Parabolic ABF method achieved 16.2% (80% PP for end systole), 16.4% (40% PP for end systole), and 13.9% (100% PP for end systole) RNMSEs in TPR estimation, respectively.



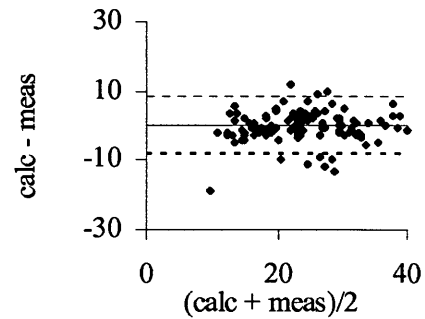
(a) Using CAP



(d) BA Plot, $R^2 = 0.0062$



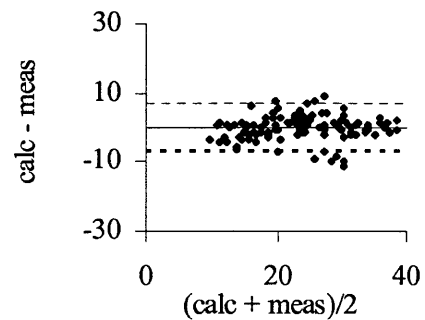
(b) Using FAP



(e) BA Plot, $R^2 = 0.0015$



(c) Using RAP

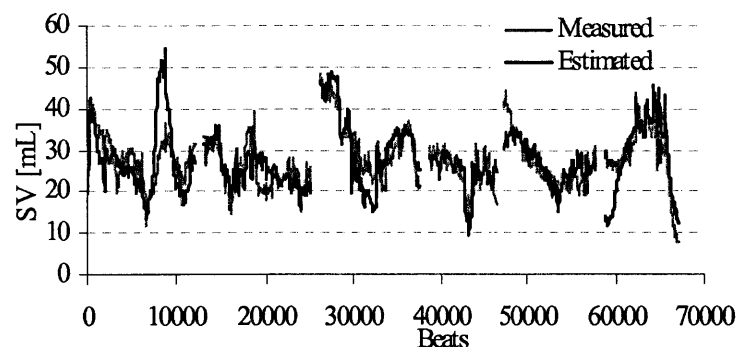


(f) BA Plot, $R^2 = 0.0008$

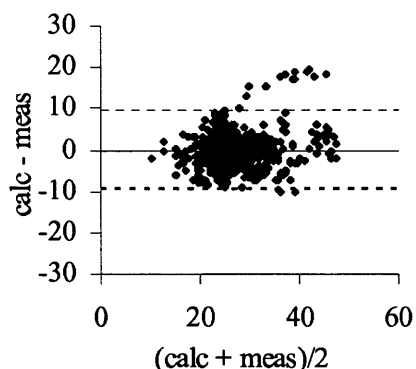
Fig. 6.38. TPR estimation by the Parabolic ABF method.

6.2.14. Pressure Ratio Method

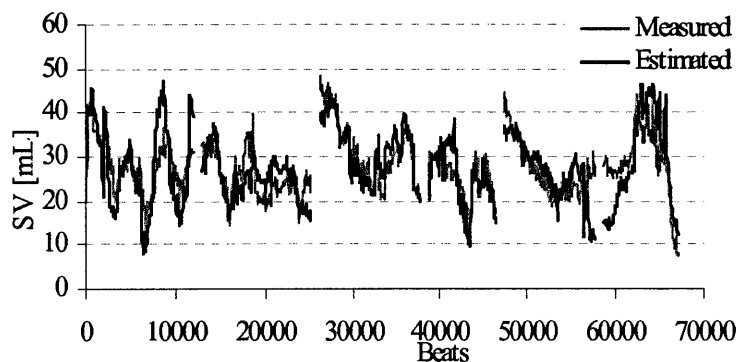
Using CAP, FAP, and RAP waveforms, the Parabolic ABF method achieved 17.4% (90% PP for end systole), 19.6% (40% PP for end systole), and 21.5% (70% PP for end systole) RNMSEs in SV estimation, respectively.



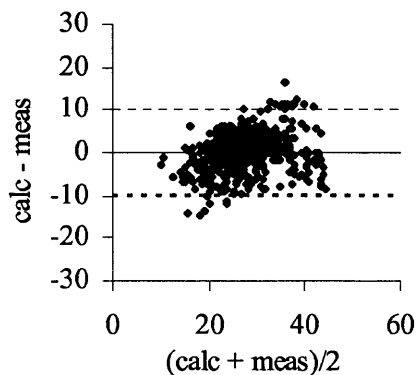
(a) Using CAP



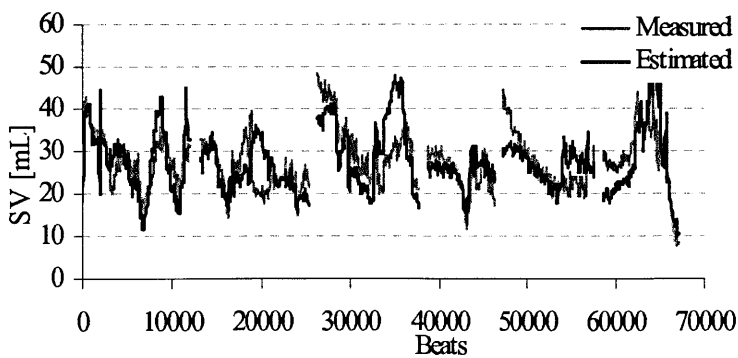
(d) BA Plot, $R^2 = 0.036$



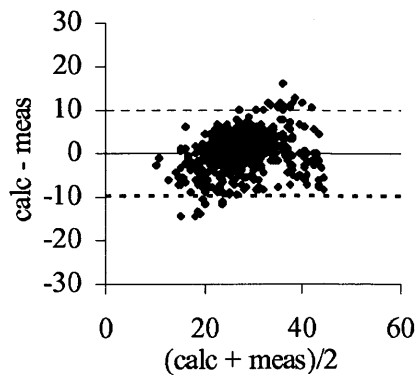
(b) Using FAP



(e) BA Plot, $R^2 = 0.056$



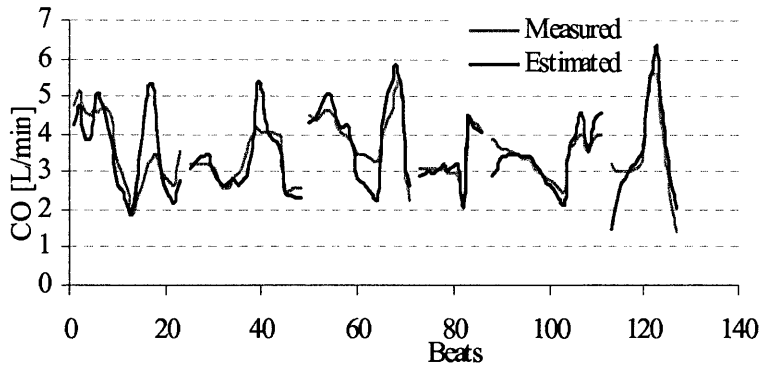
(c) Using RAP



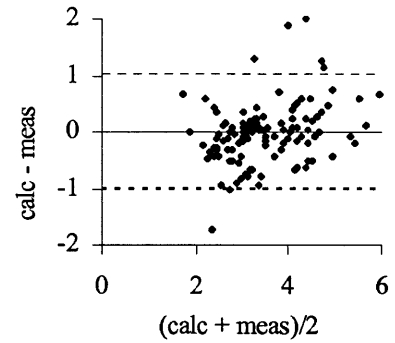
(f) BA Plot, $R^2 = 0.0043$

Fig. 6.39. SV estimation by the Pressure Ratio method.

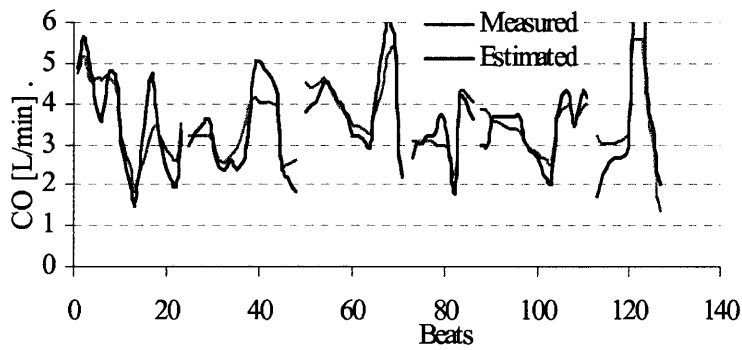
Using CAP, FAP, and RAP waveforms, the Parabolic ABF method achieved 13.9% (90% PP for end systole), 16.1% (40% PP for end systole), and 17.5% (50% PP for end systole) RNMSEs in CO estimation, respectively.



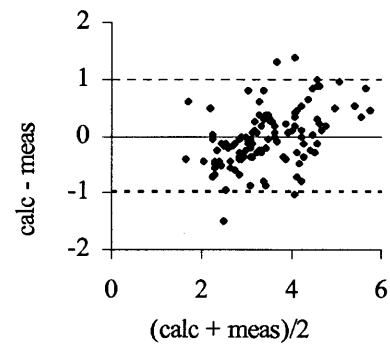
(a) Using CAP



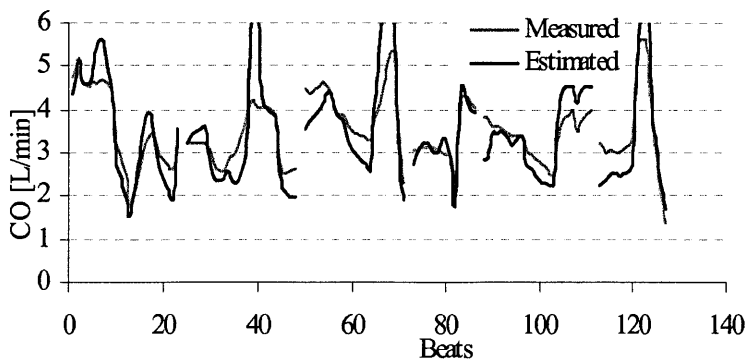
(d) BA Plot, $R^2 = 0.1162$



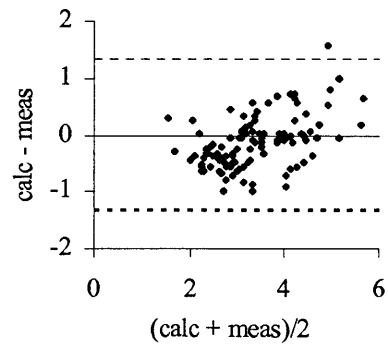
(b) Using FAP



(e) BA Plot, $R^2 = 0.2851$



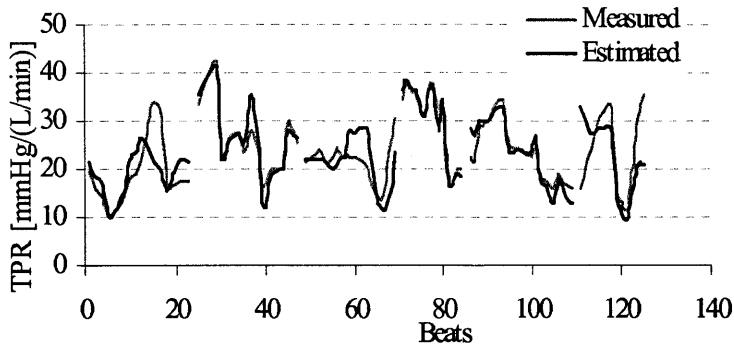
(c) Using RAP



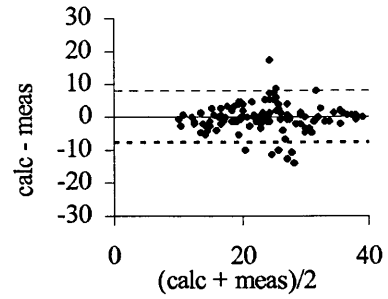
(f) BA Plot, $R^2 = 0.4796$

Fig. 6.40. CO estimation by the Pressure Ratio method.

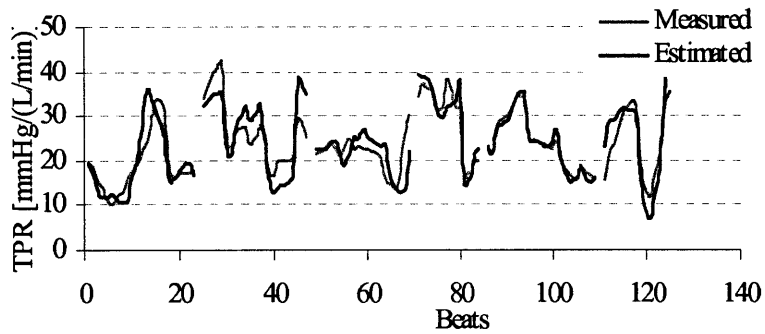
Using CAP, FAP, and RAP waveforms, the Parabolic ABF method achieved 17.9% (80% PP for end systole), 17.0% (exponential model for end systole), and 15.2% (70% PP for end systole) RNMSEs in TPR estimation, respectively.



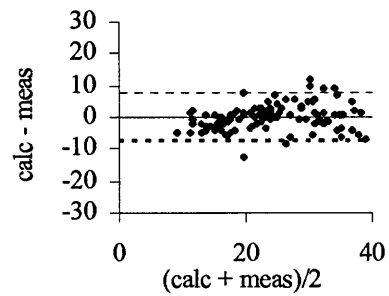
(a) Using CAP



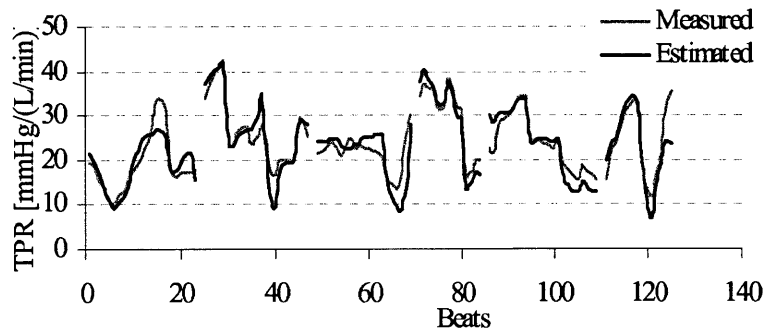
(d) BA Plot, $R^2 = 0.0016$



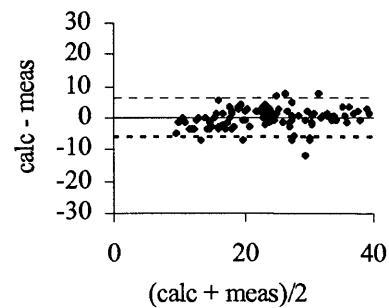
(b) Using FAP



(e) BA Plot, $R^2 = 0.0642$



(c) Using RAP



(f) BA Plot, $R^2 = 0.049$

Fig. 6.41. TPR estimation by the Pressure Ratio method.

6.2.15. Hybrid Method Results

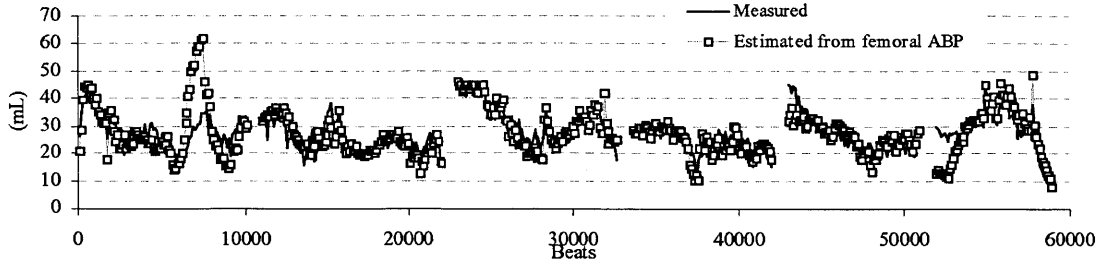
This section describes the results of CO and SV estimation using the Hybrid algorithm.

Using Whole Data as Pilot Data with Common Parameter Sets

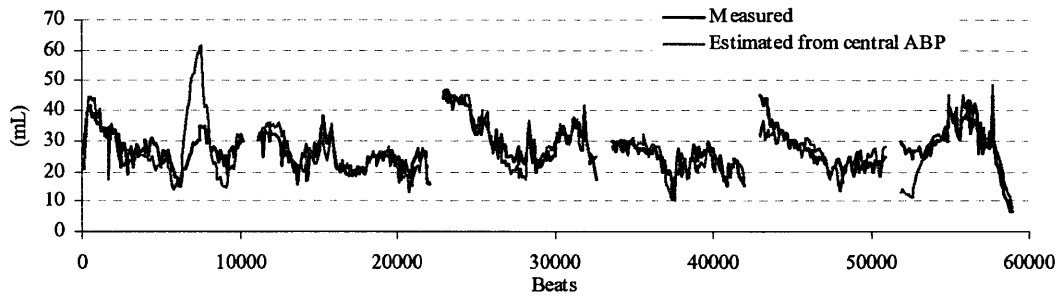
Using the MDL criterion, the order was set to 8 for the analysis of central and femoral ABP, and the order was set to 9 for the analysis of radial ABP. Over a wide physiological range achieved by administering phenylephrine (vasoconstrictor), nitroglycerin (vasodilator), dobutamine (beta agonist), and esmolol (beta blocker), the new method achieved RNMSLEs of 15.6% in CO and 16.3% in SV derived from central ABP; 12.7% in CO and 16.5% in SV derived from femoral ABP; and 10.1% in CO and 14.5% in SV derived from radial ABP.

The overall trend of the measured and estimated CO and SV showed strong agreement (Fig. 6.42). The correlation coefficient (R) between the measured CO (SV) and estimated CO (SV) from femoral ABP was 0.945 (0.914). For CO (SV) derived from radial ABP, the correlation coefficient was 0.970 (0.909).

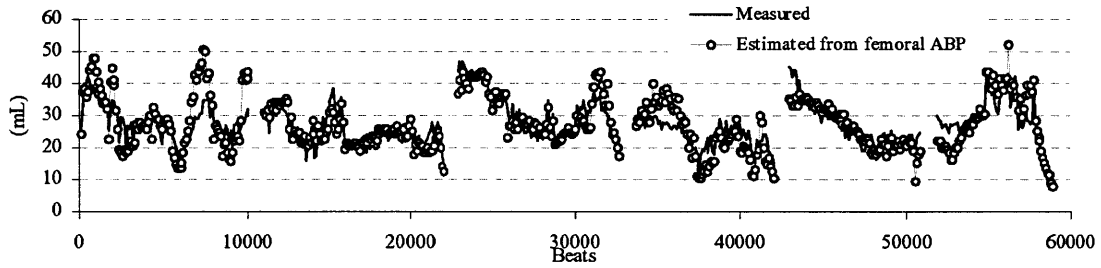
Bland-Altman analysis [34, 35] of the CO and SV estimates was conducted. Bland-Altman analysis involves plotting the estimation errors (difference between estimated and measured values) versus the averages of the estimated and measured values. The analysis showed that 97.6 and 93.8% of the CO and SV estimation errors derived from femoral ABP were within 1.96 SD from the mean ($R = 0.073$ and 0.37 for CO and SV plots, respectively), and 97.6 and 94.3% of the CO and SV estimation errors derived from femoral ABP were within 1.96 SD from the mean ($R^2 = 0.073$ and 0.13 for CO and SV plots, respectively). This indicates that the distributions of the estimation errors have tails of approximately equal weight as for a normal distribution. The low R values indicate that there is no apparent trend (Fig. 6.43) of the estimation errors with the averages.



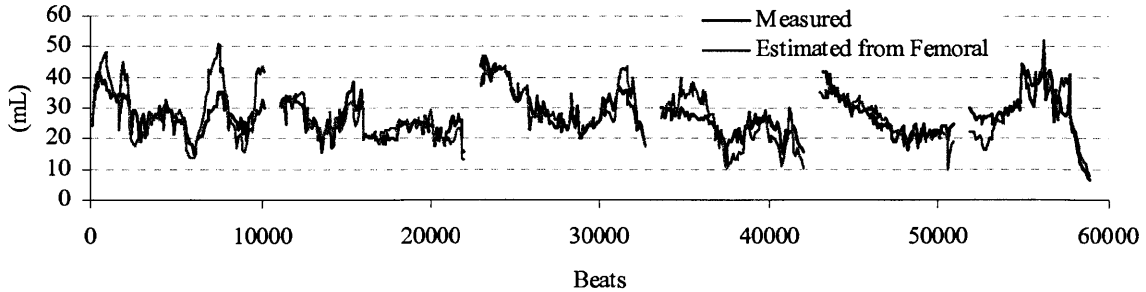
(a) Measured CO (black circles) and estimated CO (white circles) from central ABP ($R = 0.921$).



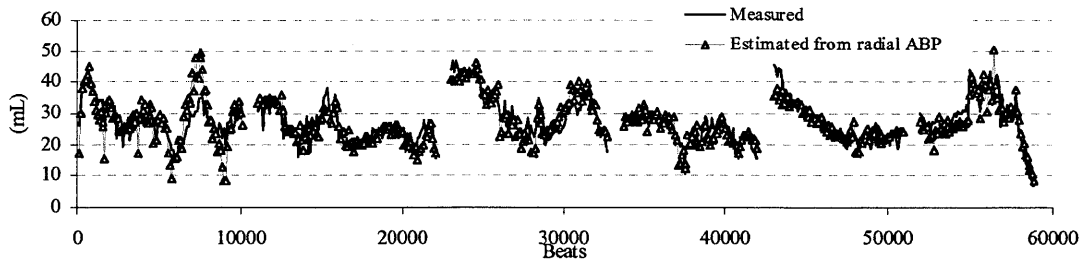
(b) Measured SV (black line) and estimated SV (gray line) from central ABP ($R = 0.889$).



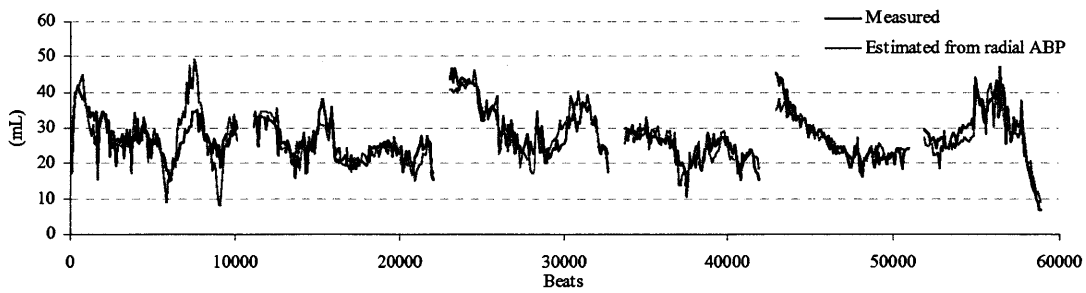
(c) Measured CO (black circles) and estimated CO (white circles) from femoral ABP ($R = 0.945$).



(d) Measured SV (black line) and estimated SV (gray line) from femoral ABP ($R = 0.914$).

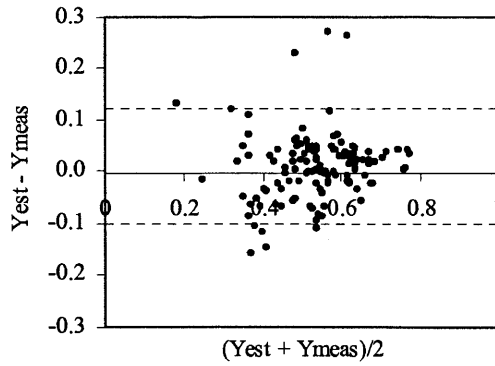


(e) Measured CO (black circles) and estimated CO (white triangles) from radial ABP ($R = 0.970$).

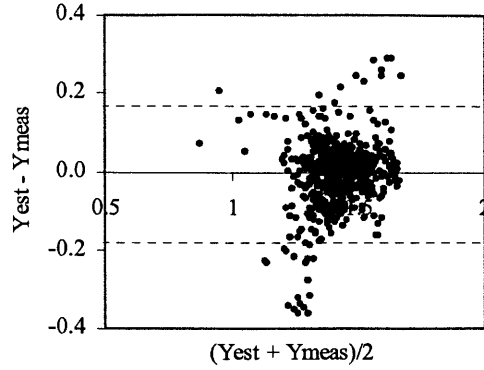


(f) Measured SV (black line) and estimated SV (gray line) from radial ABP ($R = 0.909$).

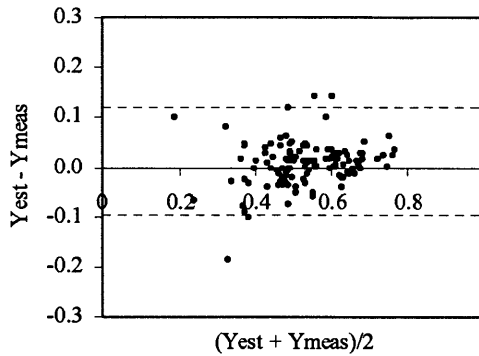
Fig. 6.42. Agreement of the measured and estimated cardiac output and stroke volume. Estimates from central (a-b), femoral (c-d), and radial (e-f) arterial blood pressure in the six Yorkshire swine data sets. The black and gray lines represent measured and estimated values, respectively. A wide physiological range was achieved by administering phenylephrine (vasoconstrictor), nitroglycerin (vasodilator), dobutamine (beta agonist), and esmolol (beta blocker).



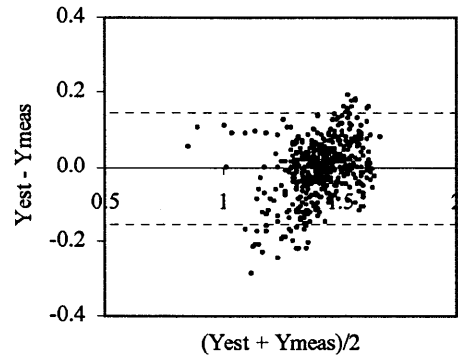
(a) CO estimation from central ABP ($R^2 = 0.149$).



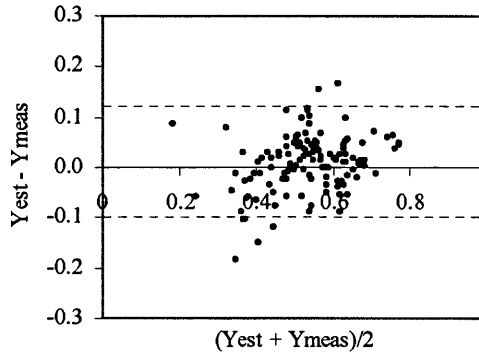
(b) SV estimation from central ABP ($R^2 = 0.260$).



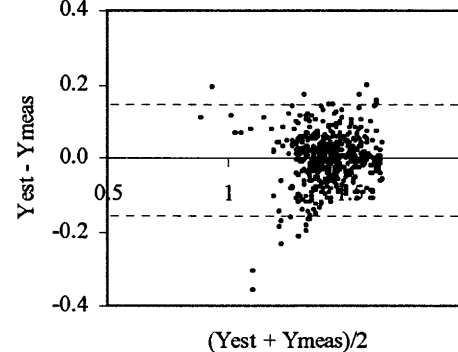
(c) CO estimation from femoral ABP ($R^2 = 0.047$).



(d) SV estimation from femoral ABP ($R^2 = 0.124$).



(e) CO estimation from radial ABP ($R^2 = 0.020$).



(f) SV estimation from radial ABP ($R^2 = 0.009$).

Fig. 6.43. Bland-Altman plots of the CO and SV estimates using the new method.

Over 94% of both CO and SV estimates by the Hybrid method are within 1.96 SD from the mean, respectively. The dotted lines represent 1.96 SD from the mean. Y_{meas} and Y_{est} are natural logarithms of the measured and estimated SV.

Using Half of the Data as Pilot Data with Common Parameter Sets

Using a common parameter set for all the animals, the algorithm achieved SV (CO) errors of 17.3% (16.3%) using central (8th order), 16.5% (12.7%) using femoral (6th order), and 14.5% (10.1%) using radial ABP (5th order).

Using Half of the Data as Pilot Data Applied to the Other Half of the Data

In using (3.55) to obtain the parameters, the first half of each data set was used. The parameters were applied to half of the data sets. The algorithm achieved SV (CO) errors of 20.0% (19.4%) using central (5th order), 18.3% (15.3%) using femoral (6th order), and 17.7% (15.3%) using radial ABP (5th order).

Pilot Data	Common single parameter set selected. Applied to all data.	Common single parameter set obtained by the first half of the data and applied to the latter half of the data.
All	12.6 (10.0) 8th 21.2 (18.7) 8th 13.2 (10.4) 9th	N/A
Half	17.3 (16.3), 7th 16.5 (12.7), 6th 14.5 (10.1), 5th	20.0 (19.4), 5th 18.3 (15.3), 6th 17.7 (15.3), 5th

Table 6.3. RNMSLEs of SV (CO) estimation by the Hybrid algorithm.

6.3. Summary of the SV, CO, and TPR Estimation

The estimation methods that require only one calibration (arterial compliance C_a), as described in the previous chapters, were compared. In the following tables, PR=Pressure Ratio Method (3.34); SM=Modified Herd's Method (Systolic MAP – end DBP, eq.3.19); CI=Corrected Impedance (2.14); Kou=Kouchoukos Correction (2.15); Wind=Windkessel model (2.3); Psa=Area under the curve with end-diastolic ABP value subtracted (2.13); Psa2=Area under the systolic curve (2.12); Par=Parabolic ABF model (3.25); AC=AC Power (2.16); Hyb=Hybrid Method (3.55); MV=Minimum Variance Method (3.2); PP=Pulse Pressure (2.4); PP2=Herd's Pulse Pressure (2.7); BBA=Beat-to-Beat Averaged Model (2.9); ARMA=ARMA model (2.20); Lilj=Liljestrand-Zander's Method (2.6); and Const=CO, SV, and TPR set constant. The single asterisks represent the novel methods developed in this thesis.

The double asterisks (Hybrid Method) signify that the method was calibrated using measured SV. Therefore, it should not be directly compared with the other methods that require only one parameter for calibration (arterial compliance C_a). The details of the Hybrid results are reported in section 6.2.15.

For the ARX model, the ABF waveform estimation results are further reported in section 6.4.

Table 6.4 summarizes the SV estimation results (RNMSEs) using different estimation methods (columns) and end systole detection methods (rows). Using CAP, the Corrected Impedance Method with end systole at 70% PP resulted in the SV RNMSE of 13.9%, as low as the Kouchoukos Correction Method (14.8% with end systoles from the exponential model), the modified Herd's Method (14.8% with end systoles from the exponential model). For FAP, the Corrected Impedance Method with end systole at 40% resulted in the SV RNMSE of 16.4%. For RAP, the Kouchoukos Correction Method with end systole calculated from the preceding RR interval resulted in the SV RNMSE of 13.1%.

Table 6.5 summarizes the CO estimation results (RNMSEs) using different estimation methods (columns) and end systole detection methods (rows). Using CAP, the Parabolic Method with end systoles from 40% PP achieved 13.5% RNMSE, as low as Kouchoukos (12.0% with end systoles by the exponential model), the modified Herd's Method (12.7% with end systoles by the exponential model),

Pressure Ratio Method (13.8% with end systoles of 90% PP), and Kouchoukos (12.0% with end systoles from the exponential model). For FAP, the Parabolic Method with end systoles from 40% PP achieved 15.7% RNMSE, as low as the Corrected Impedance Method (13.6% with end systole at 40%), Pressure Ratio Method (15.9% with end systoles from 40% PP) For RAP, the Kouchoukos Correction Method with true end systole resulted in the CO RNMSE of 11.6%, as low as the Corrected Impedance Method (10.5% with true end systoles), modified Herd's Method (13.1% with end systoles from the exponential model), Area under the curve method (13.6% with true end systoles). The Hybrid Method achieved low RNMSE of 10.1% in CO estimation using RAP. The details of the Hybrid results are reported in section 6.2.15.

Table 6.6 summarizes the TPR estimation results (RNMSEs) using different estimation methods (columns) and end systole detection methods (rows). The TPR values were calculated by the measured MAP and calculated proportional CO using (2.1). Using CAP, the Parabolic Method with end systoles from 90% PP achieved 15.3% RNMSE, as low as Corrected Impedance Method (13.7% with end systole from 70% PP). For FAP, the Corrected Impedance Method with end systole at 40% PP resulted in the lowest TPR RNMSE of 13.8%. For RAP, the Corrected Impedance Method with true end systole resulted in the lowest TPR RNMSE of 10.6%, as low as Kouchoukos (11.3% with end systoles from the exponential model), Pressure Ratio Method (15.4% with end systoles from 70% PP), Area under the curve method (13.4% with true end systoles), and Parabolic Method (13.9% with end systoles from 100% PP).

		PR*	SM*	CI	Kou	Wind	Psa	Psa2	Par*	AC	Hyb**	MV*	PP	PP2	BBA	ARMA	Lilj	Const
End systole detection methods	true	27.0	15.9	14.7	16.8	23.7	16.7	23.3	20.5	20.6	19.1	21.0	20.5	14.9	18.7	N/A	34.9	30.6
	f(RR)	27.0	14.8	15.2	14.8	18.2	16.5	24.0	19.9	N/A	N/A	N/A	N/A	N/A	N/A	N/A	N/A	N/A
	40%PP	19.1	19.6	17.0	37.6	18.7	25.7	35.6	18.6	N/A	N/A	N/A	N/A	N/A	N/A	N/A	N/A	N/A
	50%PP	18.6	19.1	15.8	33.3	18.4	24.4	34.1	18.3	N/A	N/A	N/A	N/A	N/A	N/A	N/A	N/A	N/A
	60%PP	18.4	18.8	14.5	26.6	20.2	21.7	30.4	19.7	N/A	N/A	N/A	N/A	N/A	N/A	N/A	N/A	N/A
	70%PP	18.0	18.8	13.9	22.8	18.8	20.0	28.5	20.6	N/A	N/A	N/A	N/A	N/A	N/A	N/A	N/A	N/A
	80%PP	17.5	18.8	14.5	23.4	18.0	20.6	28.8	21.3	N/A	N/A	N/A	N/A	N/A	N/A	N/A	N/A	N/A
	90%PP	17.4	18.6	16.6	26.8	17.6	23.4	31.2	24.2	N/A	N/A	N/A	N/A	N/A	N/A	N/A	N/A	N/A
	100%PP	17.4	18.3	18.9	29.8	17.6	26.0	33.3	25.2	N/A	N/A	N/A	N/A	N/A	N/A	N/A	N/A	N/A

(a) Using CAP

		PR*	SM*	CI	Kou	Wind	Psa	Psa2	Par*	AC	Hyb**	MV*	PP	PP2	BBA	ARMA	Lilj	Const
End systole detection methods	true	22.1	19.9	17.9	21.6	18.8	22.4	25.4	21.5	20.8	17.4	27.2	20.7	17.2	20.7	N/A	31.2	30.6
	f(RR)	21.7	18.9	18.4	20.6	19.4	22.6	26.3	21.0	N/A	N/A	N/A	N/A	N/A	N/A	N/A	N/A	N/A
	40%PP	19.6	21.6	16.4	21.3	19.4	21.9	24.8	19.9	N/A	N/A	N/A	N/A	N/A	N/A	N/A	N/A	N/A
	50%PP	19.8	21.4	16.6	19.7	20.3	21.6	23.8	20.4	N/A	N/A	N/A	N/A	N/A	N/A	N/A	N/A	N/A
	60%PP	19.8	21.3	17.2	21.4	19.6	22.5	24.9	20.8	N/A	N/A	N/A	N/A	N/A	N/A	N/A	N/A	N/A
	70%PP	19.8	21.4	17.8	23.0	20.2	23.5	25.9	21.0	N/A	N/A	N/A	N/A	N/A	N/A	N/A	N/A	N/A
	80%PP	19.7	21.4	18.3	24.5	20.0	24.6	27.1	21.1	N/A	N/A	N/A	N/A	N/A	N/A	N/A	N/A	N/A
	90%PP	19.6	21.3	18.9	25.9	19.9	25.6	28.3	21.0	N/A	N/A	N/A	N/A	N/A	N/A	N/A	N/A	N/A
	100%PP	19.7	21.2	19.3	26.6	19.9	26.2	28.9	20.8	N/A	N/A	N/A	N/A	N/A	N/A	N/A	N/A	N/A

(b) Using FAP

		PR*	SM*	CI	Kou	Wind	Psa	Psa2	Par*	AC	Hyb**	MV*	PP	PP2	BBA	ARMA	Lilj	Const
End systole detection methods	true	42.5	16.9	16.0	13.6	37.7	14.5	22.1	20.6	22.1	14.6	22.6	22.0	18.6	20.9	N/A	34.2	30.6
	f(RR)	43.0	14.8	16.4	13.1	38.3	14.8	23.3	19.9	N/A	N/A	N/A	N/A	N/A	N/A	N/A	N/A	N/A
	40%PP	20.8	19.0	19.8	33.6	24.5	21.8	33.2	22.3	N/A	N/A	N/A	N/A	N/A	N/A	N/A	N/A	N/A
	50%PP	21.0	18.6	17.9	29.7	24.7	21.1	32.7	20.6	N/A	N/A	N/A	N/A	N/A	N/A	N/A	N/A	N/A
	60%PP	21.7	18.0	15.7	23.0	25.7	19.1	29.7	20.0	N/A	N/A	N/A	N/A	N/A	N/A	N/A	N/A	N/A
	70%PP	21.5	18.0	14.9	25.3	33.6	20.9	31.4	19.6	N/A	N/A	N/A	N/A	N/A	N/A	N/A	N/A	N/A
	80%PP	21.8	17.8	15.4	28.0	32.0	23.2	33.2	19.6	N/A	N/A	N/A	N/A	N/A	N/A	N/A	N/A	N/A
	90%PP	23.0	18.2	17.5	29.5	32.7	25.0	34.7	19.7	N/A	N/A	N/A	N/A	N/A	N/A	N/A	N/A	N/A
	100%PP	22.9	18.3	19.8	32.0	33.1	27.2	36.3	19.1	N/A	N/A	N/A	N/A	N/A	N/A	N/A	N/A	N/A

(c) Using RAP

Table 6.4. RNMSEs in SV estimation using the new and existing estimation methods. Central (a), femoral (b), and radial (c) ABP waveforms were used. f(RR) represents the exponential model of the current systolic duration as a function of the preceding RR interval. N% PP (N=40~100) represents the N% Pulse Pressure method to define an end systole of the beat. PR=Pressure Ratio Method (3.34); SM=Modified Herd's method (Systolic MAP – end DBP, eq.3.19); CI=Corrected Impedance (2.14); Kou=Kouchoukos Correction (2.15); Wind=Windkessel model (2.3); Psa=Area under the curve with end-diastolic ABP value subtracted (2.13); Psa2=Area under the systolic curve (2.12); Par=Parabolic ABF model (3.25); AC=AC Power (2.16); Hyb=Hybrid Method (3.55); MV=Minimum Variance Method (3.2); PP=Pulse Pressure (2.4); PP2=Herd's Pulse Pressure (2.7); BBA=Beat-to-Beat Averaged Model (2.9); ARMA=ARMA model (2.20); Lilj=Liljestrang-Zander's Method (2.6); and Const=CO, SV, and TPR set constant.

End systole detection methods	PR*	SM*	CI	Kou	Wind	Psa	Psa2	Par*	AC	Hyb**	MV*	PP	PP2	BBA	ARMA	Lilj	Const
	true	23.6	13.6	12.8	14.1	17.0	14.7	21.2	15.9	17.2	16.3	15.5	20.1	21.1	17.0	20.2	29.7
f(RR)	23.7	12.7	12.7	12.0	27.2	14.0	21.6	16.4	N/A	N/A	N/A	N/A	N/A	N/A	N/A	N/A	N/A
40%PP	16.1	16.6	14.5	34.2	29.4	23.4	33.2	13.5	N/A	N/A	N/A	N/A	N/A	N/A	N/A	N/A	N/A
50%PP	15.9	16.2	13.8	31.4	32.2	22.7	32.5	14.1	N/A	N/A	N/A	N/A	N/A	N/A	N/A	N/A	N/A
60%PP	15.3	16.0	13.0	25.6	29.1	20.4	29.2	15.0	N/A	N/A	N/A	N/A	N/A	N/A	N/A	N/A	N/A
70%PP	14.6	16.1	12.4	21.5	29.5	18.6	27.1	15.2	N/A	N/A	N/A	N/A	N/A	N/A	N/A	N/A	N/A
80%PP	14.0	16.1	13.0	22.1	27.9	19.2	27.4	15.4	N/A	N/A	N/A	N/A	N/A	N/A	N/A	N/A	N/A
90%PP	13.8	15.9	14.9	25.3	28.1	21.7	29.5	18.1	N/A	N/A	N/A	N/A	N/A	N/A	N/A	N/A	N/A
100%PP	13.9	15.5	16.7	27.8	28.3	24.0	31.4	18.4	N/A	N/A	N/A	N/A	N/A	N/A	N/A	N/A	N/A

(a) Using CAP

End systole detection methods	PR*	SM*	CI	Kou	Wind	Psa	Psa2	Par*	AC	Hyb**	MV*	PP	PP2	BBA	ARMA	Lilj	Const
	true	17.8	17.2	15.1	18.4	16.6	20.1	24.4	16.9	18.0	13.6	23.6	22.7	21.0	16.6	17.4	24.5
f(RR)	16.7	16.3	15.4	18.0	22.4	20.3	25.2	17.4	N/A	N/A	N/A	N/A	N/A	N/A	N/A	N/A	N/A
40%PP	15.9	19.0	13.3	20.3	27.9	20.0	25.0	15.7	N/A	N/A	N/A	N/A	N/A	N/A	N/A	N/A	N/A
50%PP	16.2	18.9	13.5	16.8	28.1	19.1	22.8	16.1	N/A	N/A	N/A	N/A	N/A	N/A	N/A	N/A	N/A
60%PP	16.3	18.8	14.0	18.4	27.9	19.9	23.7	16.5	N/A	N/A	N/A	N/A	N/A	N/A	N/A	N/A	N/A
70%PP	16.4	18.9	14.6	20.0	27.9	20.9	24.8	16.7	N/A	N/A	N/A	N/A	N/A	N/A	N/A	N/A	N/A
80%PP	16.4	18.9	15.2	21.6	26.5	22.0	25.9	16.8	N/A	N/A	N/A	N/A	N/A	N/A	N/A	N/A	N/A
90%PP	16.4	18.9	15.7	23.0	26.4	23.0	27.1	16.9	N/A	N/A	N/A	N/A	N/A	N/A	N/A	N/A	N/A
100%PP	16.4	18.8	15.9	23.6	25.9	23.5	27.7	17.1	N/A	N/A	N/A	N/A	N/A	N/A	N/A	N/A	N/A

(b) Using FAP

End systole detection methods	PR*	SM*	CI	Kou	Wind	Psa	Psa2	Par*	AC	Hyb**	MV*	PP	PP2	BBA	ARMA	Lilj	Const
	true	35.9	14.8	10.5	11.6	44.8	13.6	21.4	16.0	18.9	10.1	19.9	11.5	18.7	13.7	16.5	29.7
f(RR)	36.7	13.1	11.0	11.6	32.8	13.8	22.5	16.4	N/A	N/A	N/A	N/A	N/A	N/A	N/A	N/A	N/A
40%PP	18.0	16.8	12.9	33.3	30.4	21.2	33.5	17.4	N/A	N/A	N/A	N/A	N/A	N/A	N/A	N/A	N/A
50%PP	17.7	16.5	12.3	29.1	29.3	20.6	32.7	15.8	N/A	N/A	N/A	N/A	N/A	N/A	N/A	N/A	N/A
60%PP	18.2	16.0	11.0	22.2	27.2	18.3	29.4	15.1	N/A	N/A	N/A	N/A	N/A	N/A	N/A	N/A	N/A
70%PP	17.9	16.0	12.5	24.7	29.8	20.3	31.4	15.0	N/A	N/A	N/A	N/A	N/A	N/A	N/A	N/A	N/A
80%PP	18.2	15.9	14.8	27.8	27.4	22.8	33.5	15.0	N/A	N/A	N/A	N/A	N/A	N/A	N/A	N/A	N/A
90%PP	19.6	16.2	18.9	29.8	26.4	24.7	35.9	15.6	N/A	N/A	N/A	N/A	N/A	N/A	N/A	N/A	N/A
100%PP	19.7	16.3	21.3	32.7	27.8	27.3	37.9	15.1	N/A	N/A	N/A	N/A	N/A	N/A	N/A	N/A	N/A

(c) Using RAP

Table 6.5. RNMSEs in CO estimation using the new and existing estimation methods.

Central (a), femoral (b), and radial (c) ABP waveforms were used. f(RR) represents the exponential model of the current systolic duration as a function of the preceding RR interval. N% PP (N=40~100) represents the N% Pulse Pressure method to define an end systole of the beat. PR=Pressure Ratio Method (3.34); SM=Modified Herd's method (Systolic MAP – end DBP, eq.3.19); CI=Corrected Impedance (2.14); Kou=Kouchoukos Correction (2.15); Wind=Windkessel model (2.3); Psa=Area under the curve with end-diastolic ABP value subtracted (2.13); Psa2=Area under the systolic curve (2.12); Par=Parabolic ABF model (3.25); AC=AC Power (2.16); Hyb=Hybrid Method (3.55); MV=Minimum Variance Method (3.2); PP=Pulse Pressure (2.4); PP2=Herd's Pulse Pressure (2.7); BBA=Beat-to-Beat Averaged Model (2.9); ARMA=ARMA model (2.20); Lilj=Liljestrang-Zander's Method (2.6); and Const=CO, SV, and TPR set constant.

End systole detection methods	PR*	SM*	CI	Kou	Wind	Psa	Psa2	Par*	AC	Hyb**	MV*	PP	PP2	BBA	ARMA	Lilj	Const
	true	37.6	16.8	13.7	15.0	21.3	16.2	23.3	17.8	18.1	32.8	23.3	44.4	23.0	16.5	22.5	29.9
f(RR)	39.1	16.0	14.7	14.8	28.7	16.4	23.1	18.7	N/A	N/A	N/A	N/A	N/A	N/A	N/A	N/A	N/A
40%PP	23.7	17.2	18.6	45.1	36.6	28.0	41.1	20.0	N/A	N/A	N/A	N/A	N/A	N/A	N/A	N/A	N/A
50%PP	21.5	17.3	17.3	37.1	35.9	26.2	38.2	19.2	N/A	N/A	N/A	N/A	N/A	N/A	N/A	N/A	N/A
60%PP	18.8	17.4	14.7	28.4	33.2	22.6	33.8	17.7	N/A	N/A	N/A	N/A	N/A	N/A	N/A	N/A	N/A
70%PP	17.9	17.4	13.4	24.7	32.0	20.8	32.8	17.0	N/A	N/A	N/A	N/A	N/A	N/A	N/A	N/A	N/A
80%PP	17.6	17.4	13.6	26.0	32.0	21.7	34.7	16.2	N/A	N/A	N/A	N/A	N/A	N/A	N/A	N/A	N/A
90%PP	17.8	17.3	15.8	31.3	32.6	25.6	39.0	17.9	N/A	N/A	N/A	N/A	N/A	N/A	N/A	N/A	N/A
100%PP	18.2	17.1	18.7	35.9	32.7	29.2	42.5	18.2	N/A	N/A	N/A	N/A	N/A	N/A	N/A	N/A	N/A

(a) Using CAP

End systole detection methods	PR*	SM*	CI	Kou	Wind	Psa	Psa2	Par*	AC	Hyb**	MV*	PP	PP2	BBA	ARMA	Lilj	Const
	true	17.0	17.9	14.6	18.2	17.3	20.6	25.0	17.3	18.0	30.4	21.2	38.4	22.7	16.5	19.4	26.7
f(RR)	16.9	16.8	15.5	18.3	23.0	21.3	25.2	17.9	N/A	N/A	N/A	N/A	N/A	N/A	N/A	N/A	N/A
40%PP	16.8	19.1	13.6	19.9	28.9	20.9	25.1	16.4	N/A	N/A	N/A	N/A	N/A	N/A	N/A	N/A	N/A
50%PP	17.0	19.0	13.5	18.8	27.8	20.6	24.8	17.0	N/A	N/A	N/A	N/A	N/A	N/A	N/A	N/A	N/A
60%PP	17.0	19.0	14.0	20.8	27.8	21.6	26.4	17.0	N/A	N/A	N/A	N/A	N/A	N/A	N/A	N/A	N/A
70%PP	17.0	19.1	14.5	22.9	27.9	22.8	28.1	17.1	N/A	N/A	N/A	N/A	N/A	N/A	N/A	N/A	N/A
80%PP	17.0	19.1	15.2	25.3	27.7	24.2	30.0	17.1	N/A	N/A	N/A	N/A	N/A	N/A	N/A	N/A	N/A
90%PP	16.9	19.1	15.9	27.7	27.4	26.0	32.2	17.1	N/A	N/A	N/A	N/A	N/A	N/A	N/A	N/A	N/A
100%PP	16.9	19.1	16.4	28.8	27.3	26.9	33.3	17.4	N/A	N/A	N/A	N/A	N/A	N/A	N/A	N/A	N/A

(b) Using FAP

End systole detection methods	PR*	SM*	CI	Kou	Wind	Psa	Psa2	Par*	AC	Hyb**	MV*	PP	PP2	BBA	ARMA	Lilj	Const
	true	66.8	15.1	10.6	11.4	36.4	13.4	21.7	16.1	16.3	30.7	18.9	22.0	21.5	16.0	17.9	31.1
f(RR)	56.5	13.8	11.2	11.3	32.7	13.7	22.5	16.6	N/A	N/A	N/A	N/A	N/A	N/A	N/A	N/A	N/A
40%PP	16.9	15.6	13.1	35.3	33.9	22.0	35.7	17.5	N/A	N/A	N/A	N/A	N/A	N/A	N/A	N/A	N/A
50%PP	15.9	15.3	12.4	30.8	31.4	21.2	34.8	15.3	N/A	N/A	N/A	N/A	N/A	N/A	N/A	N/A	N/A
60%PP	15.9	14.9	10.8	23.6	28.9	18.8	31.5	14.7	N/A	N/A	N/A	N/A	N/A	N/A	N/A	N/A	N/A
70%PP	15.4	14.9	12.1	26.2	28.7	20.8	33.6	14.6	N/A	N/A	N/A	N/A	N/A	N/A	N/A	N/A	N/A
80%PP	15.4	14.8	14.3	29.0	28.7	23.2	35.7	14.4	N/A	N/A	N/A	N/A	N/A	N/A	N/A	N/A	N/A
90%PP	16.6	15.0	18.4	31.1	27.1	25.4	37.1	14.2	N/A	N/A	N/A	N/A	N/A	N/A	N/A	N/A	N/A
100%PP	16.8	15.0	21.6	34.0	27.0	28.0	38.5	13.9	N/A	N/A	N/A	N/A	N/A	N/A	N/A	N/A	N/A

(c) Using RAP

Table 6.6. RNMSEs in TPR estimation using the new and existing estimation methods.

Central (a), femoral (b), and radial (c) ABP waveforms were used. f(RR) represents the exponential model of the current systolic duration as a function of the preceding RR interval. N% PP (N=40~100) represents the N% Pulse Pressure method to define an end systole of the beat. PR=Pressure Ratio Method (3.34); SM=Modified Herd's method (Systolic MAP – end DBP, eq.3.19); CI=Corrected Impedance (2.14); Kou=Kouchoukos Correction (2.15); Wind=Windkessel model (2.3); Psa=Area under the curve with end-diastolic ABP value subtracted (2.13); Psa2=Area under the systolic curve (2.12); Par=Parabolic ABF model (3.25); AC=AC Power (2.16); Hyb=Hybrid Method (3.55); MV=Minimum Variance Method (3.2); PP=Pulse Pressure (2.4); PP2=Herd's Pulse Pressure (2.7); BBA=Beat-to-Beat Averaged Model (2.9); ARMA=ARMA model (2.20); Lilj=Liljstrand-Zander's Method (2.6); and Const=CO, SV, and TPR set constant.

6.4. ABF Estimation

6.4.1. Comparison with the Windkessel model

Over 68,000 beats were processed and analyzed for ABF and SV, and over 110 six-minute windows were analyzed for CO. Fig. 6.44a-b shows examples of the estimated ABF waveforms from CAP waveforms (Fig. 6.44c). The estimated ABF follows the trend of the measured as well as the beat-to-beat systolic waveforms, compared to the ABF estimated by the Windkessel model (Fig. 6.44d). Fig. 6.45 and Fig. 6.46 show the similar results using FAP and RAP, respectively.

For the quantitative comparison, Table 6.7 summarizes the correlation between the skewness (kurtosis) of the measured and estimated ABF. Using the central, femoral, and radial ABP, the skewness (kurtosis) of the ABF estimated by the algorithm achieved correlation coefficients of 0.78 (0.72), 0.67 (0.63), and 0.69 (0.71). The ABF waveforms estimated by the algorithm had smaller errors in SD, skewness, and kurtosis than the results of the Windkessel model with the exception of kurtosis in FAP and RAP utilization (Fig. 6.48(b), Fig. 6.49). With constant C_a in each animal, the algorithm achieved errors of 15.3% (12.7%) in SV (CO) derived from CAP, 19.6% (15.2%) from FAP, and 21.8% (15.8%) from RAP (Table 6.8, Fig. 6.50). For TPR estimation, the algorithm achieved 14.3, 20.9, and 19.4% RNMSEs using CAP, FAP, and RAP, respectively. For determining AR parameter length L , $\Sigma a[j]$ was found to provide the best results (Table 6.9).

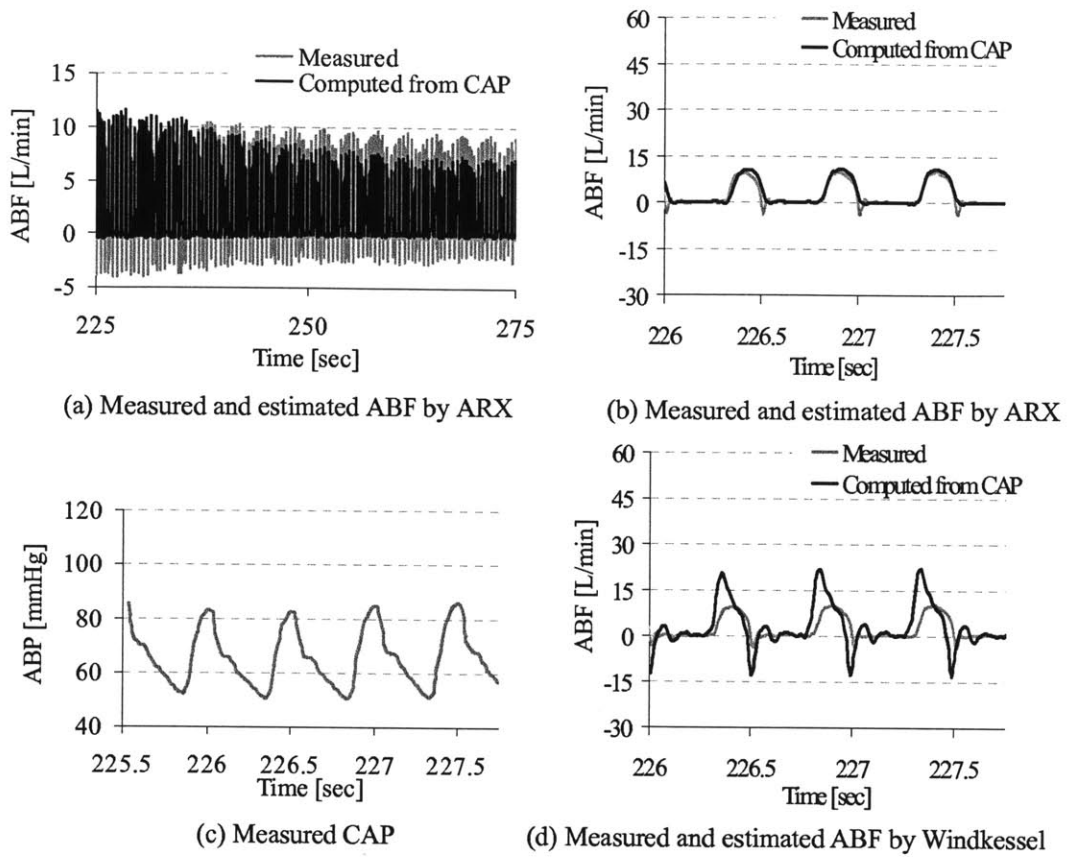
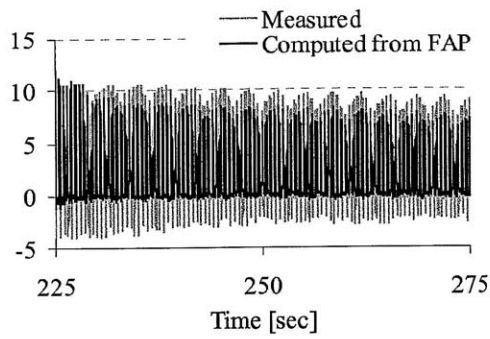
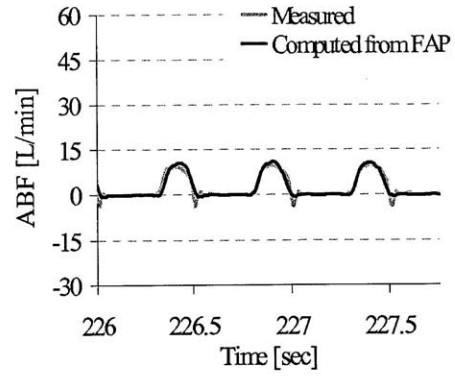


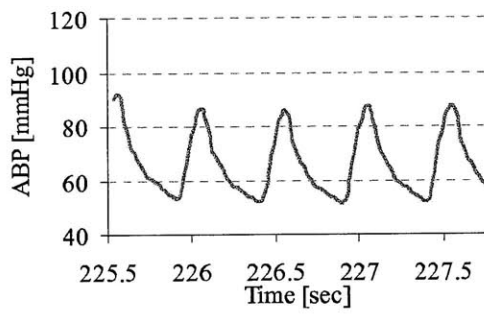
Fig. 6.44. Measured ABF and estimated ABF by the Windkessel model using CAP (applied to Swine #8 data). The computed (black) ABF follows the trend of the measured (gray) ABF. The beat-to-beat ABF waveforms present similar skewness and kurtosis to the measured ABF (b) as opposed to the ABF estimated by the Windkessel model (d).



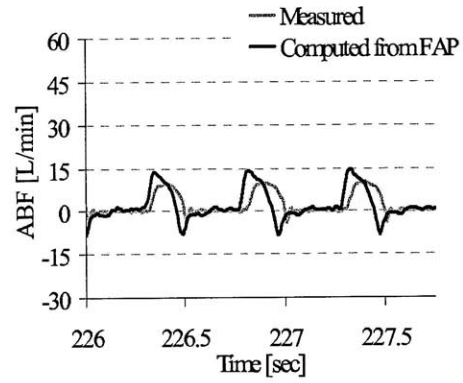
(a) Measured and estimated ABF by ARX



(b) Measured and estimated ABF by ARX



(c) Measured FAP



(d) Measured and estimated ABF by Windkessel

Fig. 6.45. Measured ABF and estimated ABF by the Windkessel model using FAP (applied to Swine #8 data). The computed ABF (black) follows the trend of the measured (gray) ABF. The beat-to-beat ABF waveforms present similar skewness and kurtosis to the measured ABF (b) as opposed to the ABF estimated by the Windkessel model (d).

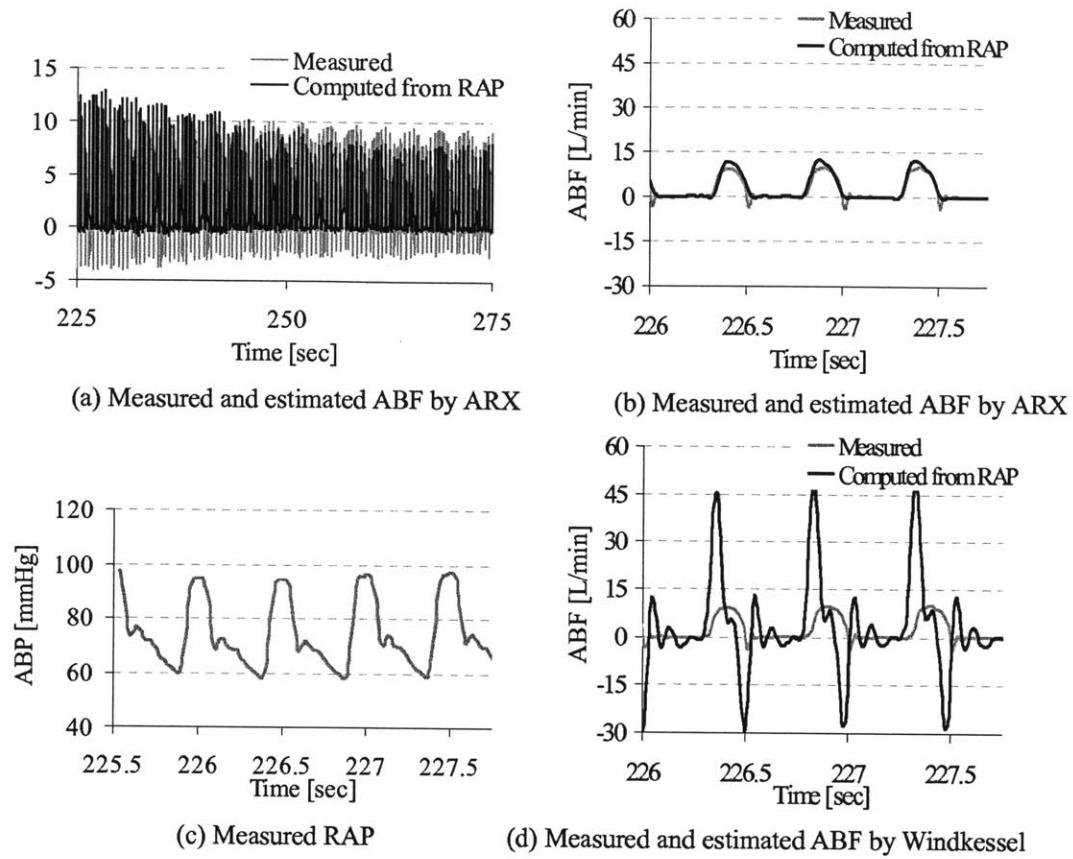


Fig. 6.46. Measured ABF and estimated ABF by the Windkessel model using RAP (applied to Swine #8 data). The computed ABF (black) follows the trend of the measured ABF (gray). The beat-to-beat ABF waveforms present similar skewness and kurtosis to the measured ABF (b) as opposed to the ABF estimated by the Windkessel model (d).

ANIMAL	Skewness			Kurtosis		
	Central	Femoral	Radial	Central	Femoral	Radial
4	0.59	0.75	0.08	0.67	0.70	0.42
5	0.87	0.55	0.83	0.75	0.34	0.59
6	0.82	0.73	0.74	0.85	0.81	0.82
7	0.70	0.81	0.93	0.55	0.36	0.64
8	0.95	0.79	0.93	0.93	0.81	0.93
9	0.88	0.76	0.38	0.76	0.27	0.09
All	0.78	0.67	0.69	0.72	0.63	0.71

Table 6.7. Correlation coefficients of skewness and kurtosis of measured and estimated ABF. The algorithm achieved RNMSEs of approximately 20% in SV and 16% in six-minute CO with constant compliance C_a in each animal.

	Central	Femoral	Radial
SV	15.3	19.6	21.8
CO	12.7	15.2	17.6
TPR	14.3	20.9	19.4

Table 6.8. SV, CO, and TPR estimation results by the ARX method. The arterial compliances C_a were assumed to be constant within each animal.

	Central	Femoral	Radial
$a[j]$	15.3	19.6	21.8
Negative Area	31.0	20.9	32.3
Smoothness	18.9	20.0	19.4

Table 6.9. Results of SV estimations using different evaluation functions to determine L .

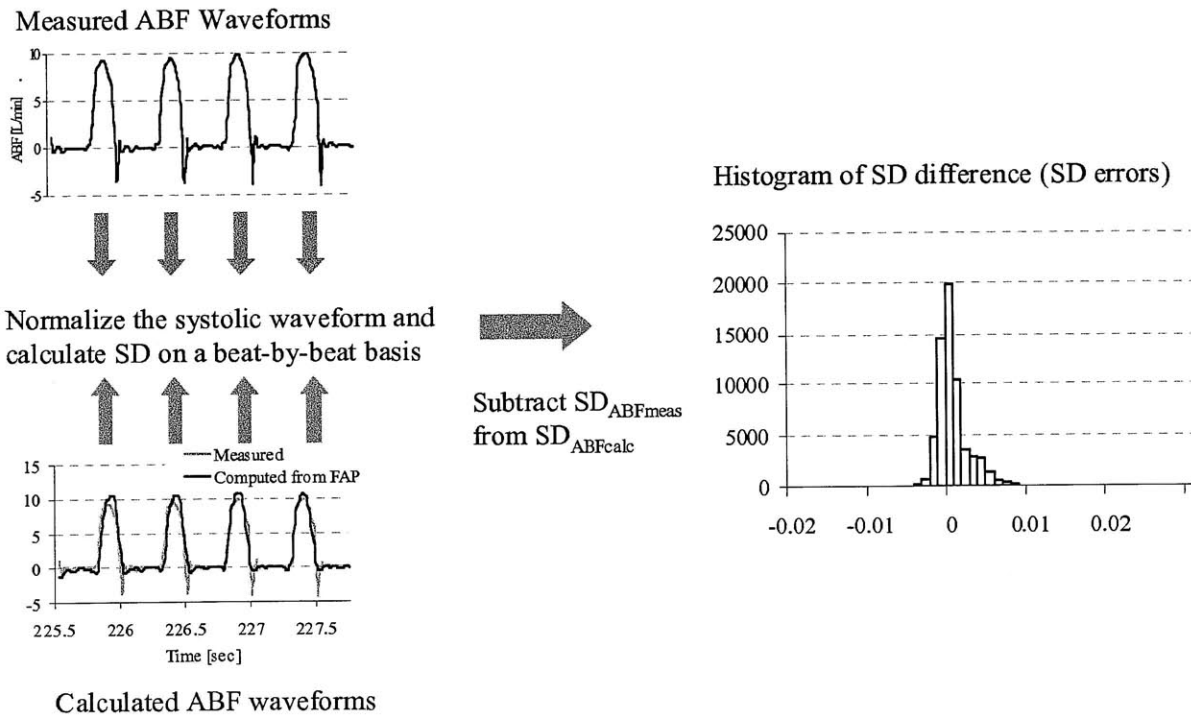
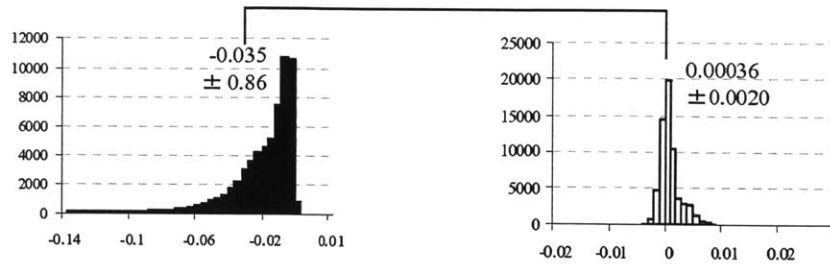
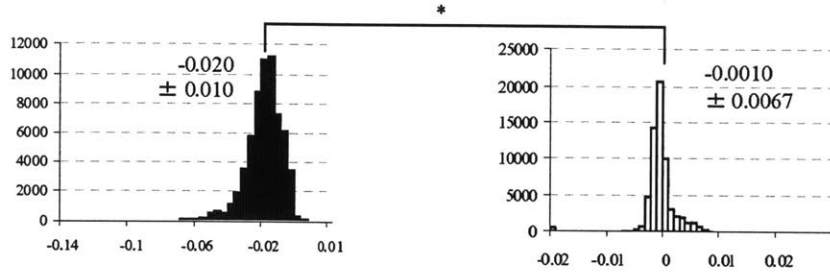


Fig. 6.47. Calculation process of SD differences



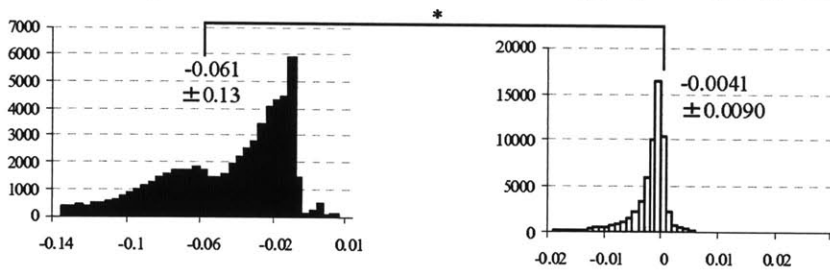
(a) By Windkessel, using CAP

(d) By ARX, using CAP



(b) By Windkessel, using FAP

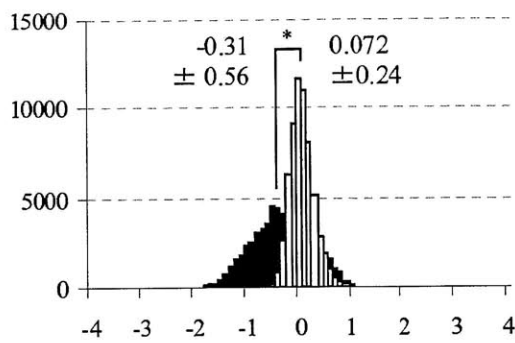
(e) By ARX, using FAP



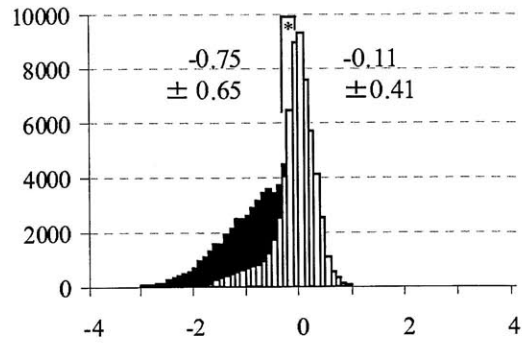
(c) By Windkessel, using RAP

(f) By ARX, using RAP

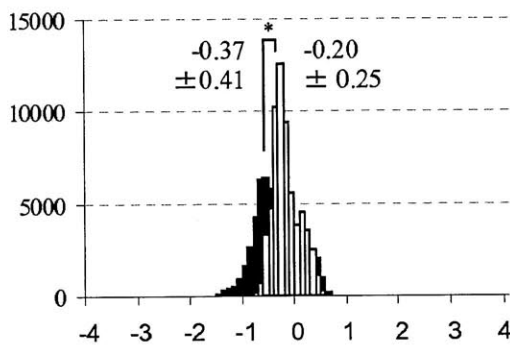
Fig. 6.48. Histograms of the SD errors by the ARX algorithm and the Windkessel model. The value above each histogram indicates the mean of the histogram. The algorithm had smaller SD errors than the Windkessel model (* $P < 0.05$). The true duration of diastole in each beat is given.



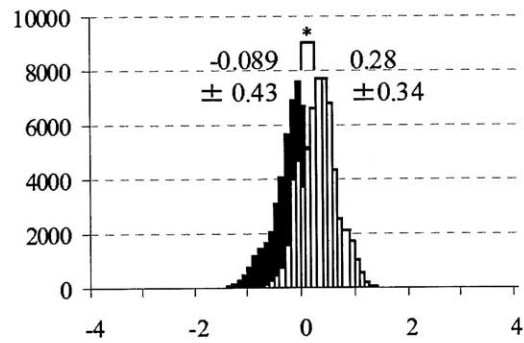
(a) Skewness error, using CAP



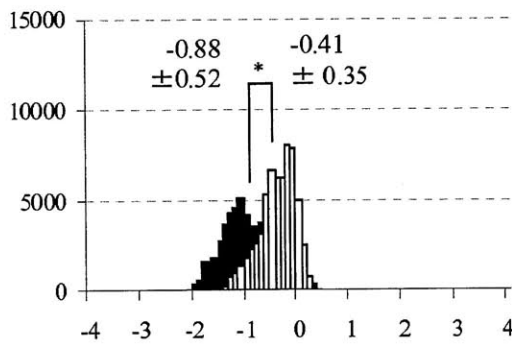
(d) Kurtosis error, using CAP



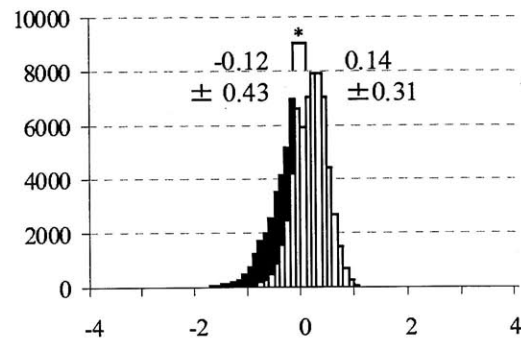
(b) Skewness error, using FAP



(e) Kurtosis error, using FAP



(c) Skewness error, using RAP



(f) Kurtosis error, using RAP

Fig. 6.49. Histograms of the skewness and kurtosis errors by the ARX algorithm and the Windkessel model. The value above each histogram indicates the mean of the histogram. The ARX algorithm (white) had smaller errors than the Windkessel (black) model (* $P < 0.05$). The true duration of diastole in each beat was used in the algorithm.

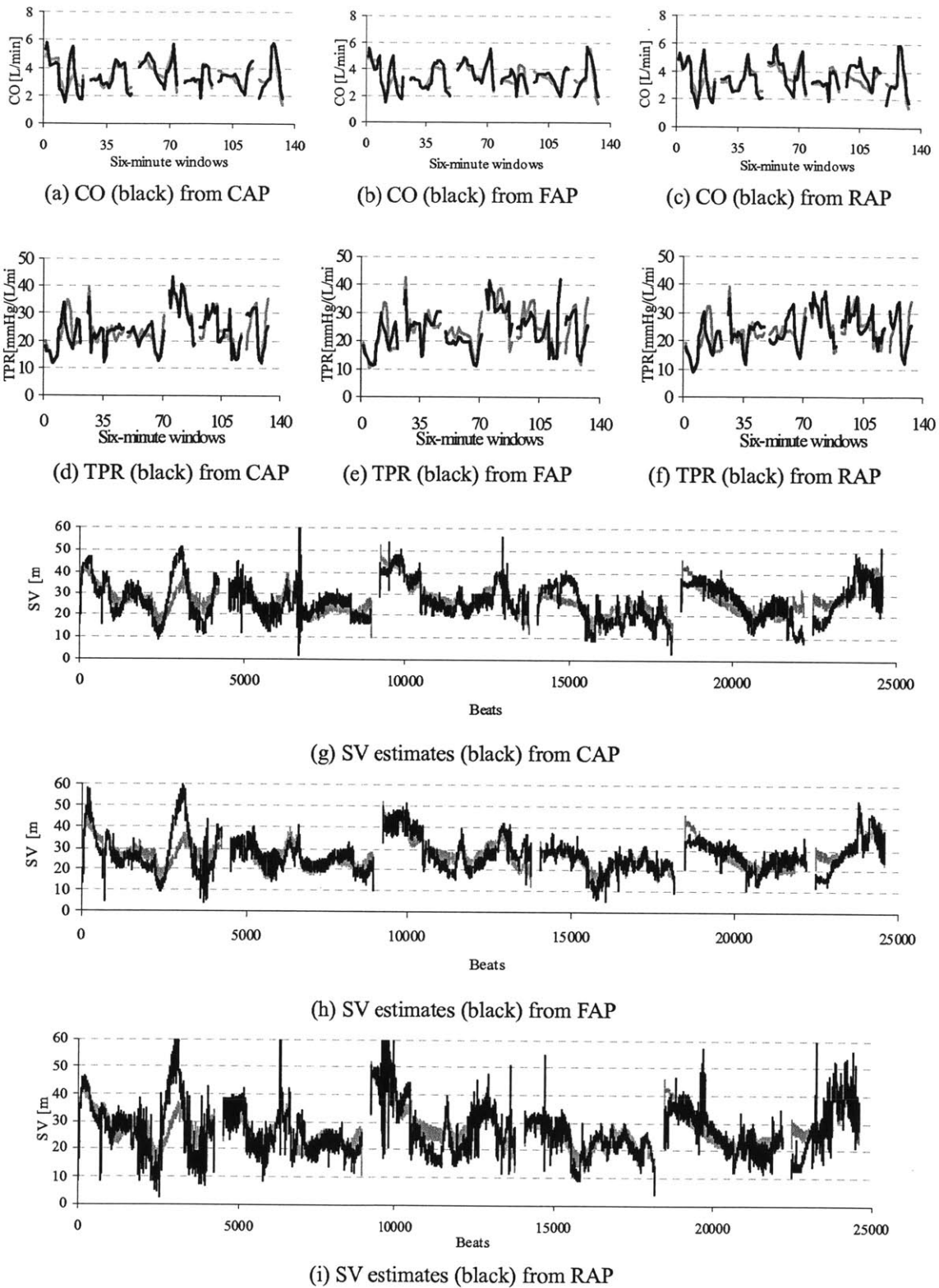


Fig. 6.50. Agreement of the measured and estimated stroke volume and cardiac output from central, femoral, and radial arterial blood pressure using the ARX method.

Ca was set at a constant in each animal. The gray and black lines represent measured and estimated values, respectively.

6.4.2. Comparison with Standard Waveforms

The previous section demonstrated that the ARX method could reconstruct ABF waveforms more accurately than the traditional Windkessel model.

To further validate the ARX method in the ability to track beat-to-beat changes in the ABF waveforms, this section compares the results of the ARX method with cases where the ABF waveforms are assumed to be uniform. Suppose you analyze the first beat of each swine experiment and obtain the ABF waveform (first beat waveform). Then assume the rest of the ABF waveforms do not basically change. One can calculate the SD, skewness, and kurtosis errors of the ABF waveforms by comparing them with the measured ABF waveforms. If the errors of the ARX method are smaller than those of the first beat waveform, it proves that the ARX method tracks beat-to-beat changes in the ABF morphology.

In addition to the first beat ABF waveforms (Fig. 6.51a-f), a median waveform of the ABF recorded all the six swine experiments (Fig. 6.51g) is also compared. In calculating the median waveform, the magnitude and width of each systolic ABF were normalized before taking the median of all the systolic ABF waveform.

Note that the first beat ABF waveforms and the median ABF waveforms are horizontally scaled in each beat so that they have the true systolic durations for fair comparisons of SD, skewness, and kurtosis.

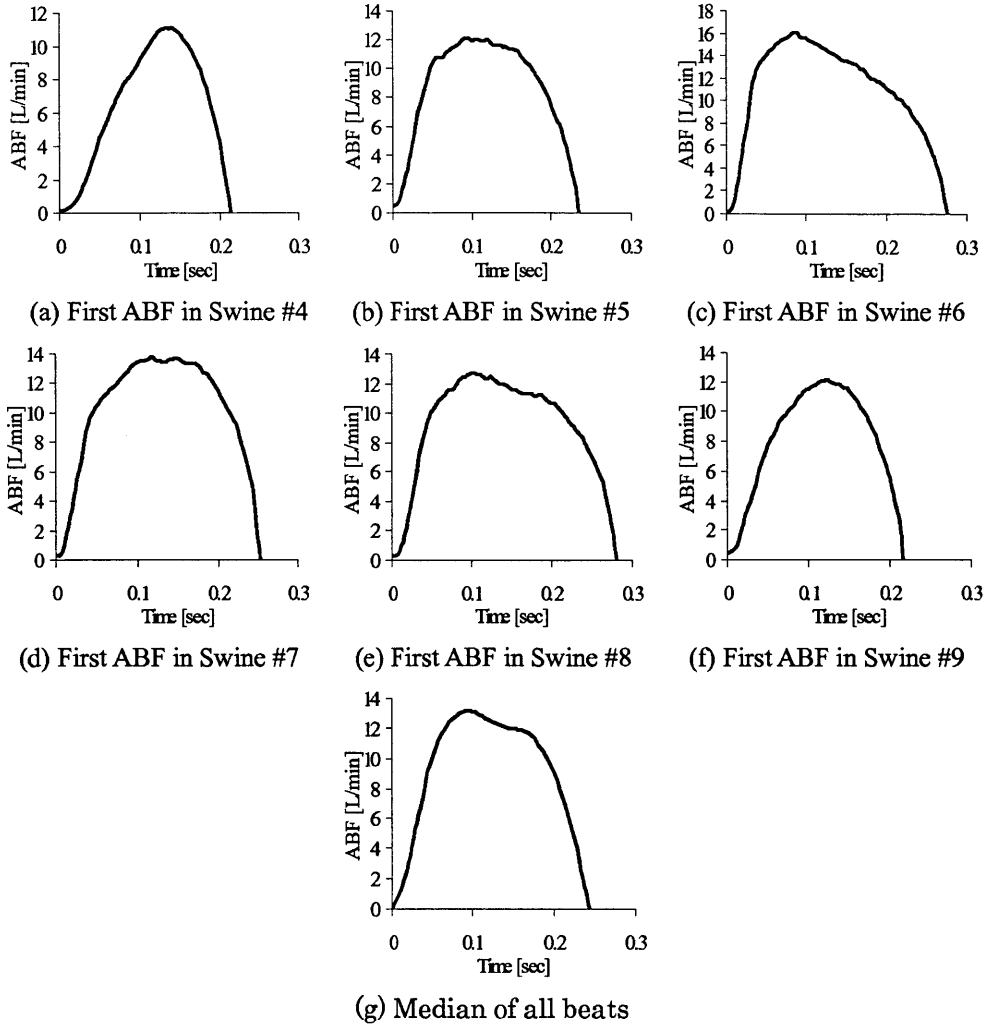
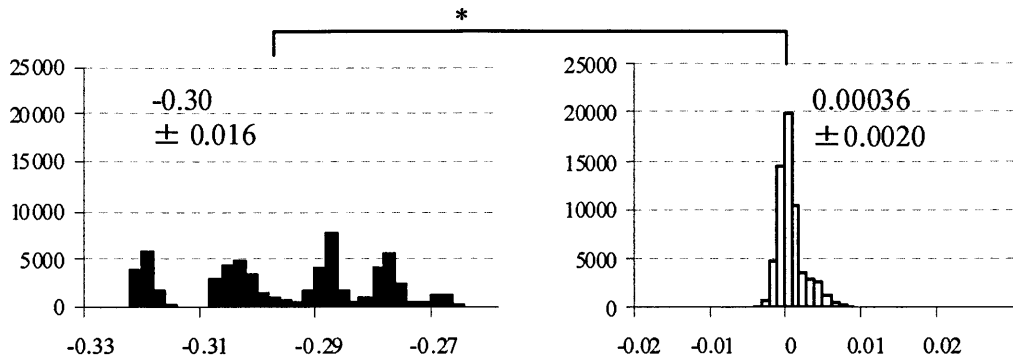
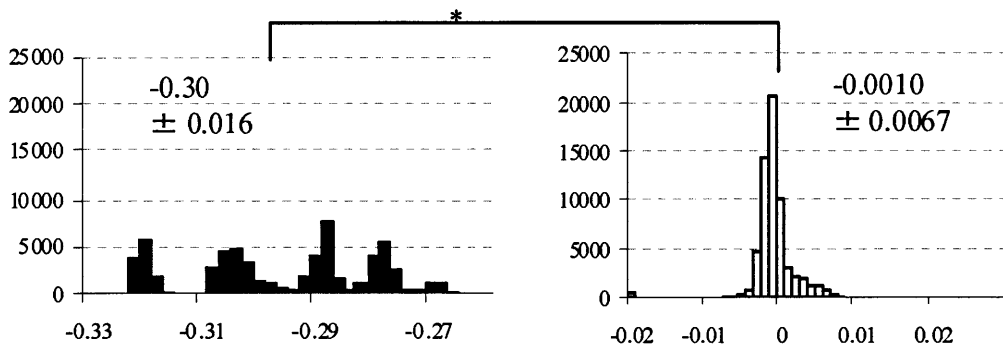


Fig. 6.51. Standard systolic ABF waveforms.

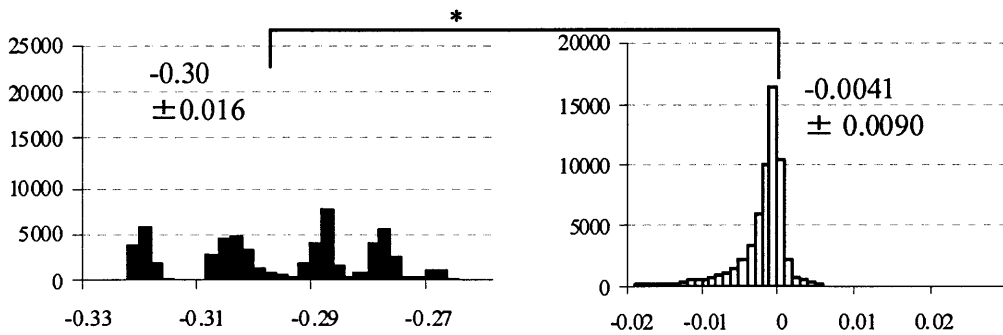
Fig. 6.52 and Fig. 6.53 show the histogram of SD, skewness and kurtosis errors of ABF waveforms by the ARX method and the standard waveforms (first beat in each animal). The ARX method achieved significantly smaller errors and variances than the standard waveform method. Fig. 6.54 and Fig. 6.55 show the case of standard waveforms obtained by all of the beats. Also in this case, the ARX method achieved significantly smaller errors and variances except the skewness of ABF waveforms using RAP. These results demonstrate that the ARX method is able to track beat-to-beat changes in the ABF waveforms better than fixed standard waveforms.



(a) SD difference of the first-beat ABF (black) and estimated ABF (white) by the ARX model using CAP.

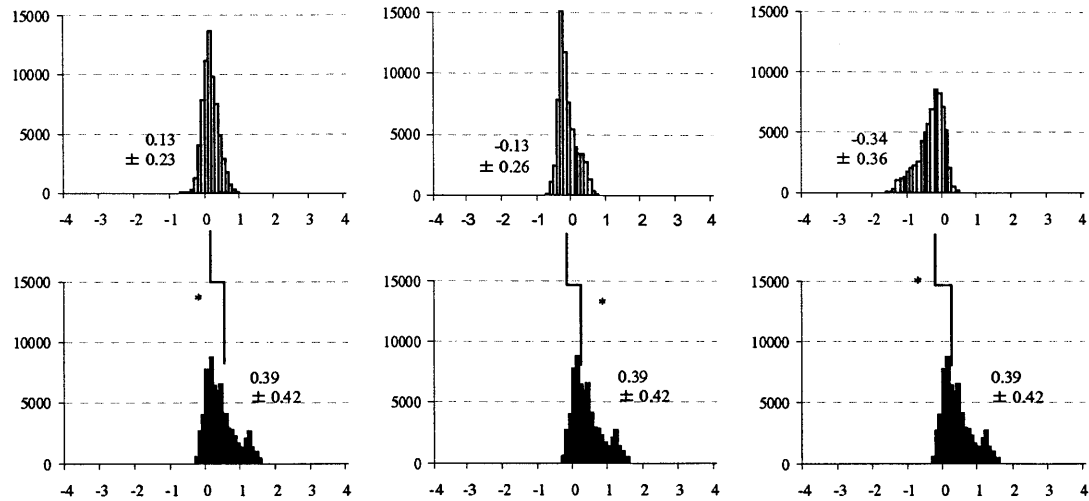


(b) SD difference of the first-beat ABF (black) and estimated ABF (white) by the ARX model using FAP.



(c) SD difference of the first-beat ABF (black) and estimated ABF (white) by the ARX model using RAP.

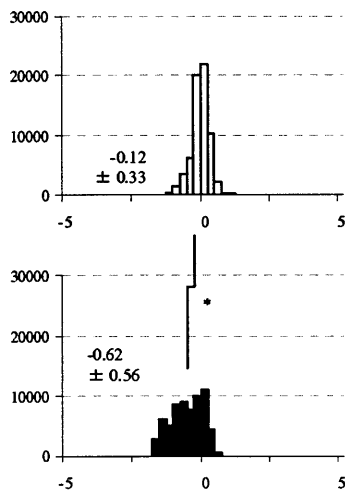
Fig. 6.52. Histograms of the SD errors by the ARX algorithm and the first beat in each animal. The value above each histogram indicates the mean \pm standard deviation (SD). The ARX algorithm (white) had smaller errors and SD than the fixed ABF (black) (* $P < 0.05$).



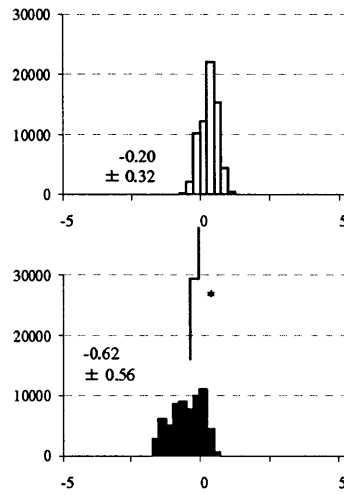
(a) Skewness error, using CAP

(b) Skewness error, using FAP

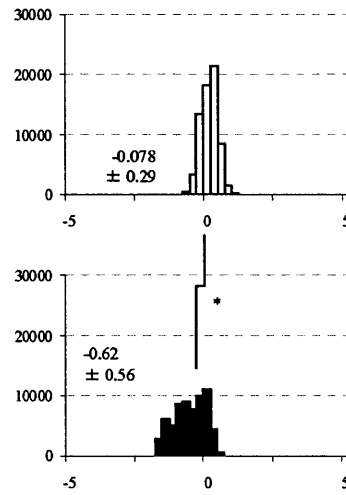
(c) Skewness error, using RAP



(d) Kurtosis error, using CAP

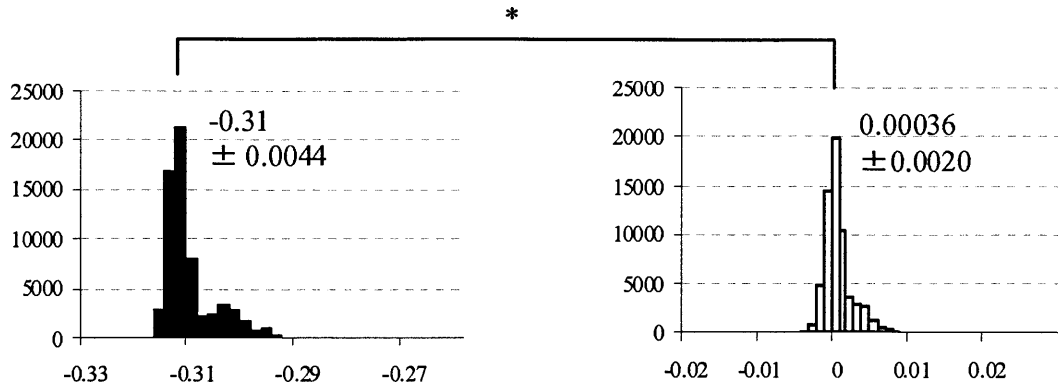


(e) Kurtosis error, using FAP

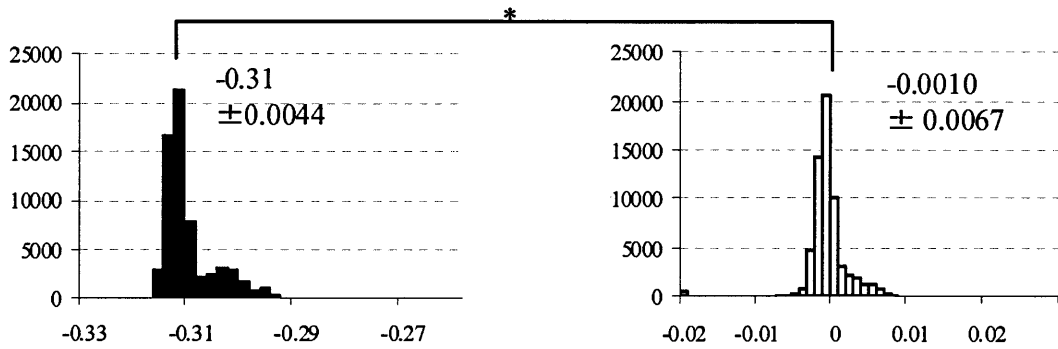


(f) Kurtosis error, using RP

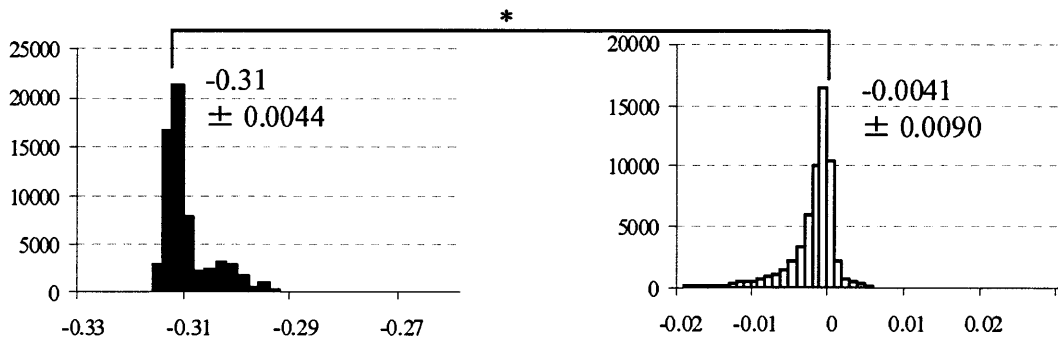
Fig. 6.53. Histograms of the skewness and kurtosis errors by the ARX algorithm and the first beat in each animal. The value above each histogram indicates the mean \pm standard deviation (SD). The ARX algorithm (white) had smaller errors in SD than the fixed ABF (black) (* $P < 0.05$).



(a) SD difference of standard ABF (black) and ARX ABF (white) from the measured ABF, using CAP.



(b) SD difference of standard ABF (black) and ARX ABF (white) from the measured ABF, using FAP.



(c) SD difference of standard ABF (black) and ARX ABF (white) from the measured ABF, using RAP.

Fig. 6.54. Histograms of the SD errors by the ARX algorithm and the median of all the true ABF waveforms. The value above each histogram indicates the mean \pm standard deviation (SD). The ARX algorithm (white) had smaller errors than those of the Windkessel model (* $P < 0.05$).

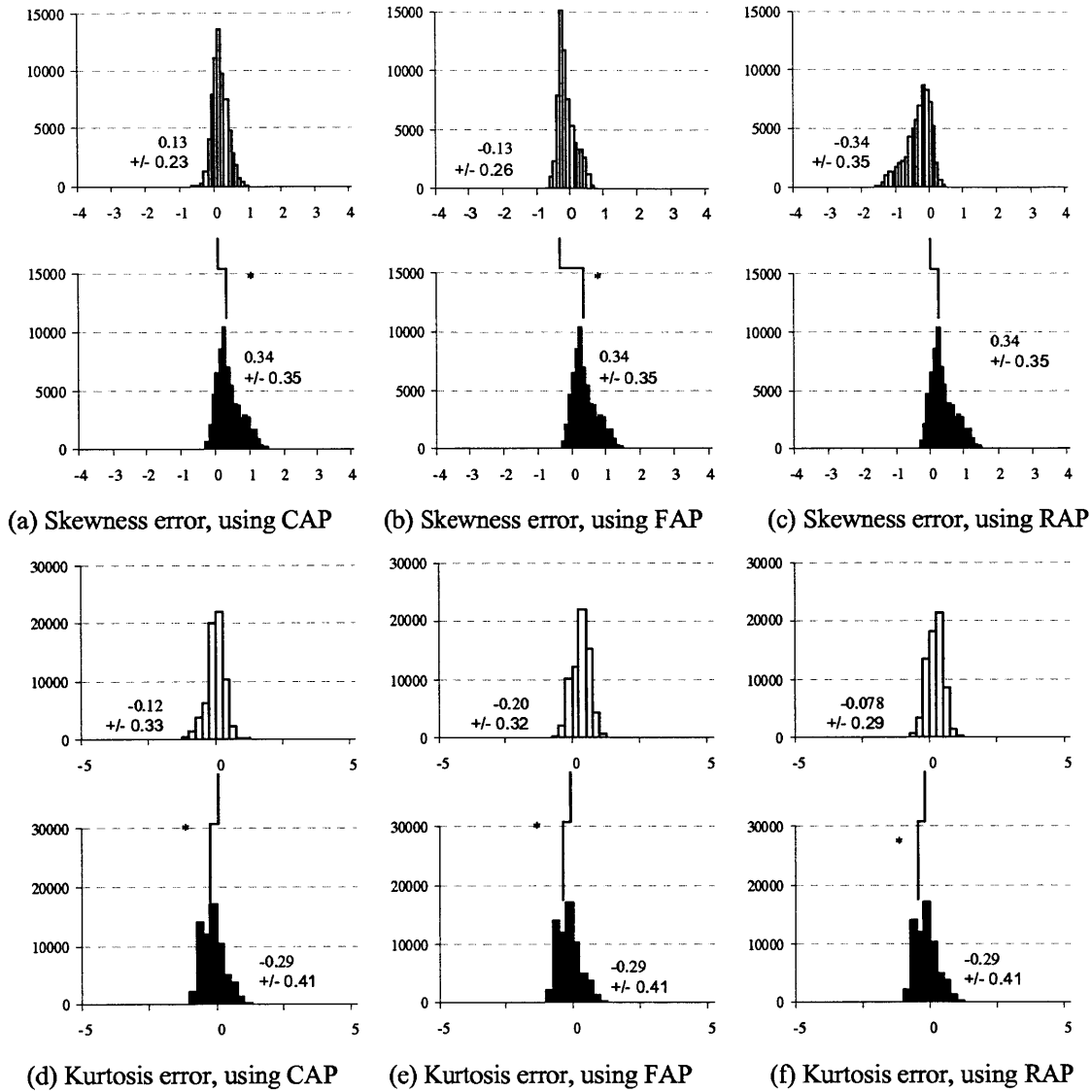


Fig. 6.55. Histograms of the skewness and kurtosis errors of the ARX algorithm and the median of all the true ABF waveforms. The value above each histogram indicates the mean \pm standard deviation. The ARX algorithm (white) had smaller errors than those of the Windkessel model (* P<0.05).

6.4.3. Exponential Model for End Systole Detection

This section reports the result of the ARX method using the exponential model (section 5.4.1) to identify end-systoles on a beat-to-beat basis.

	Central	Femoral	Radial
SV	20.0	22.9	25.9
CO	18.5	25.1	22.7
TPR	14.1	14.8	16.7

Table 6.10. SV and CO estimation results by the ARX method with the estimated diastolic intervals. The Ca in each animal was assumed to be constant.

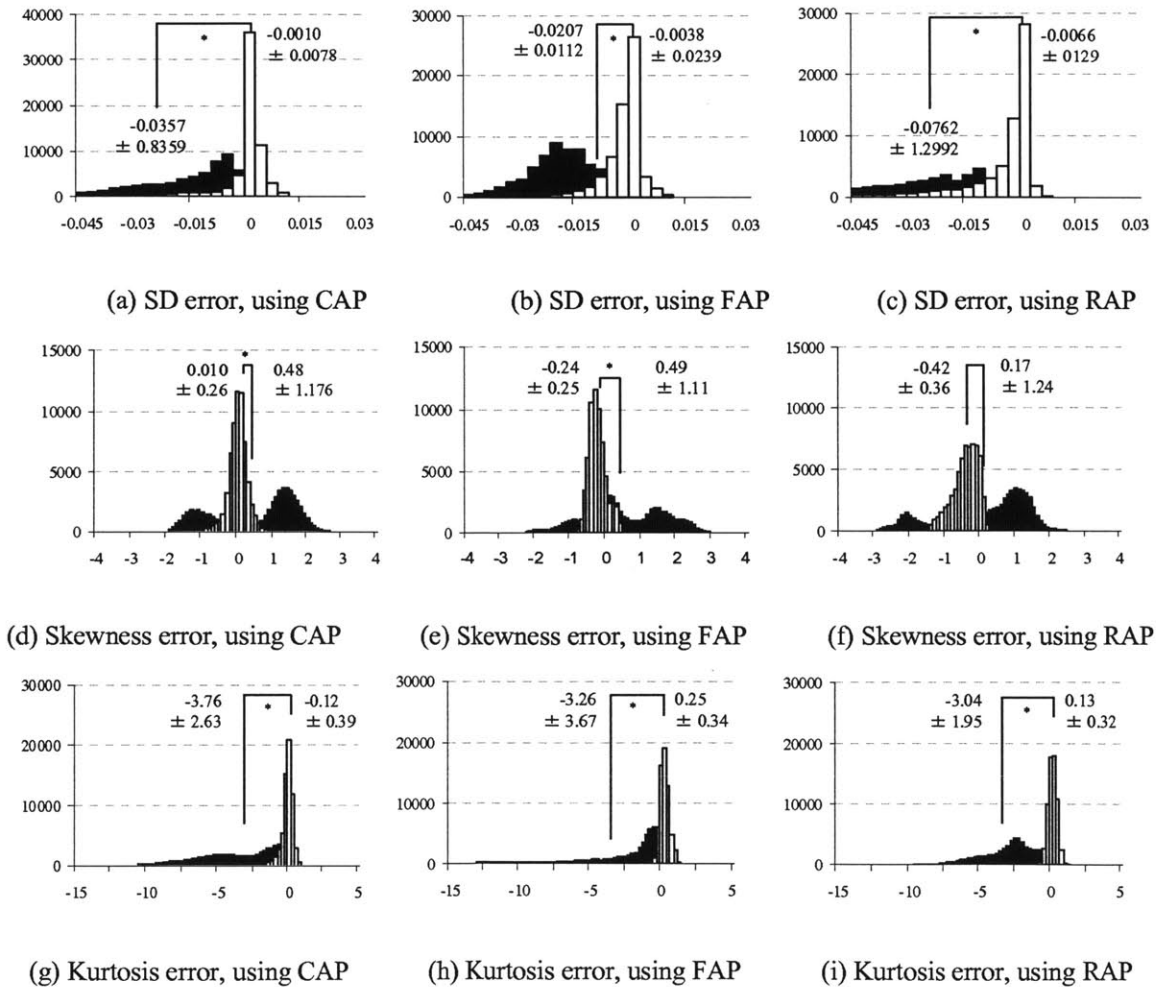


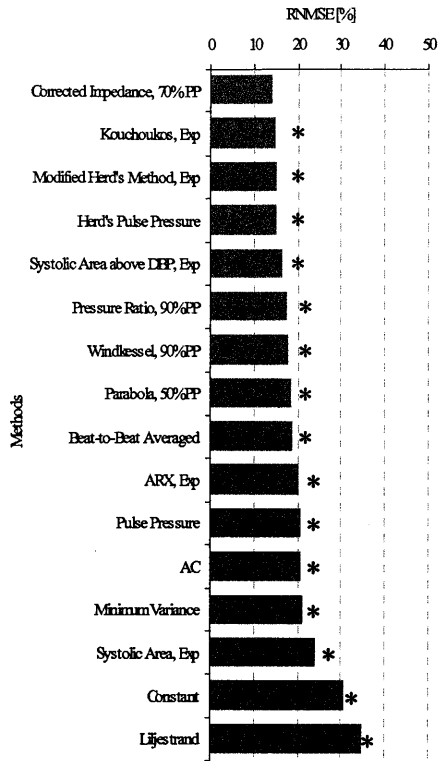
Fig. 6.56. Histograms of the waveform errors using ARX with true and estimated intervals. The ARX model (white) resulted in statistically lower errors (* P<0.05) than the Windkessel model (black).

The ARX method, with the estimated diastolic interval determined by (5.4), resulted in 20.0, 22.9, and 26.0% SV estimation errors using CAP, FAP, and RAP, respectively - increased errors from those with the true end systoles. The SD, skewness, and kurtosis of the calculated ABF waveforms were statistically closer to the measured ABF waveforms than the Windkessel model, as shown in Fig. 6.56.

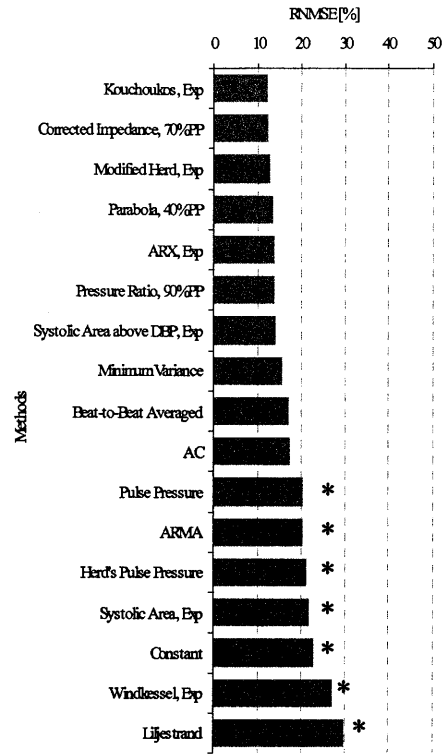
As previously mentioned, the error of diastolic interval estimation was 6.56%. In this thesis, the possible inaccuracy of determining diastolic intervals in practical settings was assumed to be within a 10% envelope. In the following Chapter, further sensitivity analyses are conducted for prolonged and shortened diastolic intervals by 10% from the true diastolic intervals.

6.5. Summary

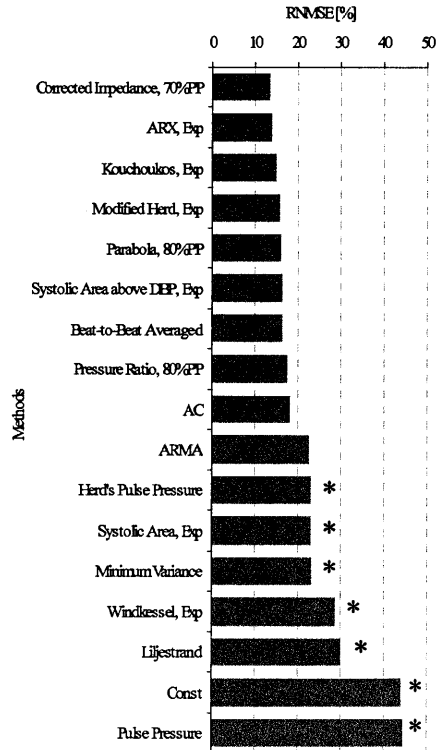
Fig. 6.57a shows the summary of the SV estimation results by the methods with the end systole identification methods. CAP signal was used. For each SV estimation method, the best end systole identification method is reported. One-way ANOVA test showed statistical significance among the methods, and the adjusted pair-wise comparison (Scheffé's test) was conducted. Asterisks show the significant difference ($p < 0.05$) from the lowest error of each comparison. The Corrected Impedance Method with 70% Partial Pulse Pressure as an indicator of end systole resulted in the smallest error among the other methods. In a similar manner, Fig. 6.57b and Fig. 6.57c show the summary of CO and TPR estimation, respectively. The errors of the best methods (Kouchoukos with Exponential model for CO and Corrected Impedance with 70 % PP for TPR) were not statistically significant from the other top nine methods. Similar results were seen in using FAP (Fig. 6.58) and RAP (Fig. 6.59).



(a) SV estimation using CAP

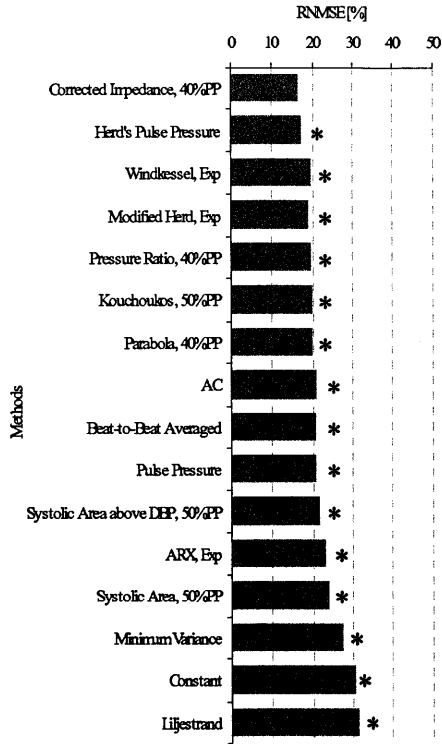


(b) CO estimation using CAP

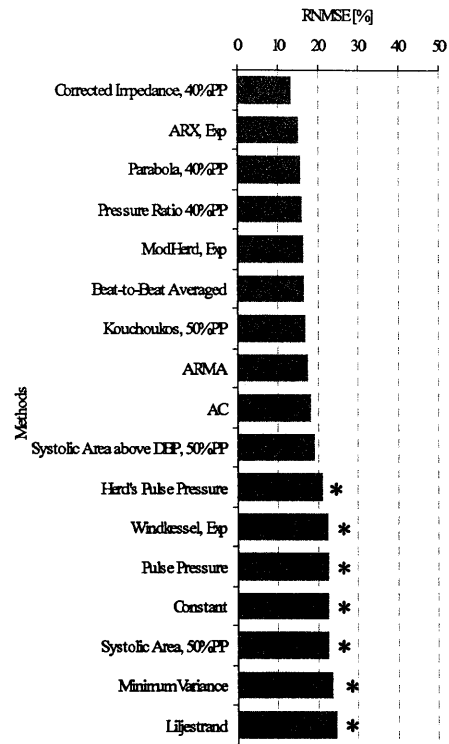


(c) TPR estimation using CAP

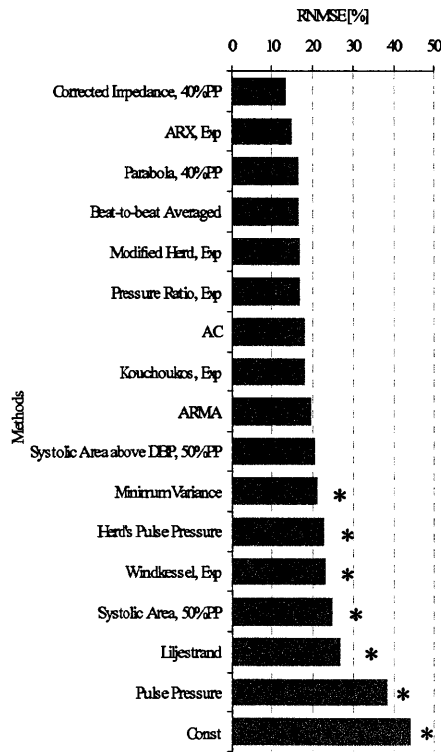
Fig. 6.57. Summary of SV, CO, and TPR estimation using CAP.



(a) SV estimation using FAP

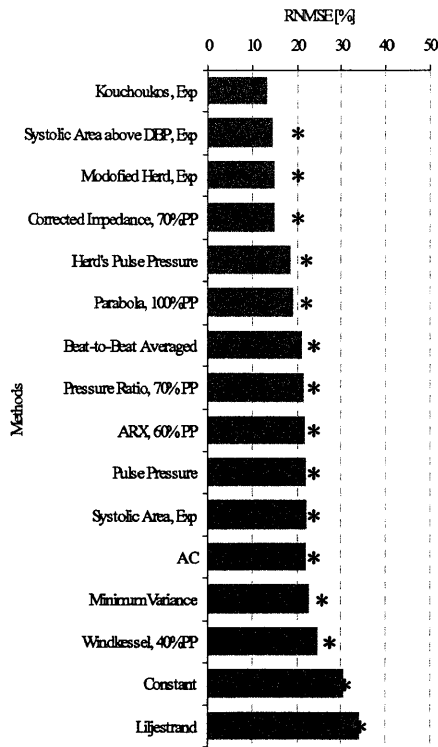


(b) CO estimation using FAP

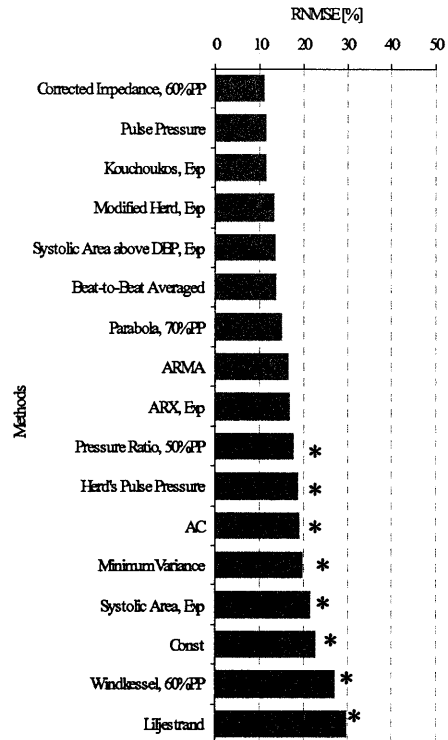


(c) TPR estimation using FAP

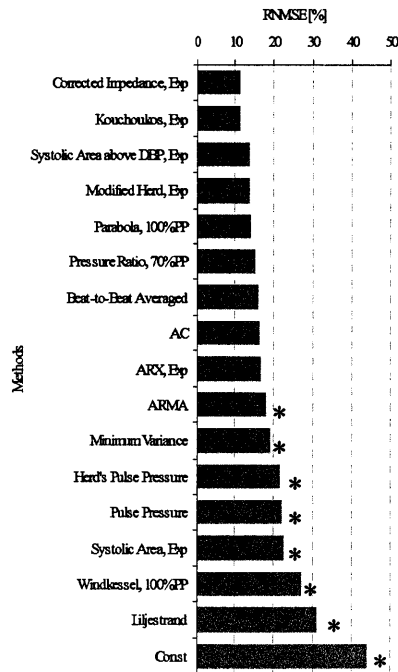
Fig. 6.58. Summary of SV, CO, and TPR estimation using FAP.



(a) SV estimation using RAP



(b) CO estimation using RAP



(c) TPR estimation using RAP

Fig. 6.59. Summary of SV, CO, and TPR estimation using RAP.

7. Discussion

7.1. CO, SV, and TPR estimation

In this thesis, new SV, CO, and TPR estimation methods based on cardiovascular physiology were introduced and validated. In addition, estimation methods for end-systole were also introduced and validated. Furthermore, a thorough comparison of the new methods with the existing estimation methods was conducted by processing the Yorkshire swine data sets. The end-systole identification method advanced the new and existing SV, CO, and TPR estimation methods that utilizes end systole information (Fig. 6.57 – Fig. 6.59). Overall, the Bland-Altman plots showed that the methods reported in this thesis did not show strong trends (i.e., the estimation performance does not change as the true CO, SV, or TPR values change). The following methods showed 0.25+ correlation coefficients (i.e., the estimation performance changes as the true CO, SV, or TPR values change):

- Windkessel model for SV and CO
- Liljestrand-Zander's method for CO and TPR
- Herd's method for TPR
- Systolic Area method for SV
- Kouchoukos Correction for SV using FAP
- AC Power method for CO using RAP
- Minimum Variance method for CO
- Modified Herd's method for CO using RAP
- Parabolic method for CO using CAP and RAP
- Pressure Ratio method for CO using FAP and RAP
- Hybrid method for SV using CAP

As shown in Fig. 6.57 – Fig. 6.59, the Modified Herd’s Method, Corrected Impedance Method, Kouchoukos’s Correction Method, and Parabolic Method achieved low RNMSEs by using the Exponential or Partial Pulse Pressure Model as indicators of end systole. The end systole identification algorithm turned the existing algorithms into new methods that achieved lower RNMSEs than the original methods.

Wesseling’s Corrected Impedance Method is a highly empirical model. The systolic area under the ABP curve above DBP was scaled by an empirically-found scaling factor that is a function of HR and MAP. Although they obtained the scaling factor formula from healthy male subjects in their twenties, the method achieved low RNMSEs, which may indicate the similarity of the human and swine cardiovascular systems in terms of applicability of the Windkessel model.

Kouchoukos Correction Method includes a simple correction factor (T_s/T_D) to model run-off blood flow during systole that escapes into the arterial tree without contributing to the ABP signal. Although the correction factor is empirical, it achieved lower RNMSEs than several theoretical model-based methods.

It should be noted that this empirical method would not work so well on the given data sets when applied to the monitoring of de-conditioned hearts.

Liljestrand-Zander’s method, although it was reported to have the highest agreement with the thermodilution CO in the ICU patient data sets [53], did not result in the best method. This could be attributed to the nature of the ICU data sets. Because ABP is maintained during surgeries, one cannot expect as much cardiovascular perturbation in the ABP signals as animal experiments in which vaso-active drugs are used to provide a wide range of cardiovascular indices. Liljestrand-Zander’s method divides the PP by the mean of SBP and DBP, which is approximately proportional to MAP. Thus, Liljestrand-Zander’s method averages PP by MAP to provide relatively normalized estimates and results in high agreement with the stable ICU thermodilution CO measurements.

Among the methods compared, the Hybrid method is unique in that it requires high-order parameter calibration. Therefore, it should not be directly compared with the other methods that require only one parameter calibration (arterial compliance C_a). The Hybrid algorithm uses beat-MAP and end-DBP, rather

than SBP, values because beat-MAP and end-DBP values are relatively insensitive to distortion of the ABP waveform.

The key feature of the new method is that the three dimensionless variables (T_i^S/T_i , P_i^D/MAP_i , and P_{i+1}^D/MAP_i) used to calculate SV were converted into three proportional SV estimates (SV_{prop1} , SV_{prop2} , and SV_{prop3}) using three variants of the Windkessel model (3.40 – 3.42). The logarithm of the three SV estimates were weighted by parameters obtained from linear regression and least mean square error analysis, and integrated into a single SV value by (3.43).

The new method achieved a RNMSLE of 12.7% in CO and 16.5% in SV derived from femoral ABP, and 10.1% in CO and 14.5% in SV derived from radial ABP (Fig. 6.42).

The Bland-Altman test, which was employed to compare CO (SV) values calculated using our new methods and measured by the ultrasonic blood flow probe, demonstrated that the estimated CO and SV were within 1.96 standard deviations of the direct measurements of these quantities (Fig. 6.43). The high correlation between the measured and calculated CO and SV demonstrates agreement of the new method with the invasive ultrasonic flow probe measurement method.

The analysis demonstrates that our new method for estimating SV and CO performs favorably compared to other PCMs. The algorithm presented in this paper analyzes the shape of individual beats as does all of the other PCMs except for the ARMA [20] method, which analyzes beat-to-beat variability in ABP waveforms.

A limitation of the current methods, along with all PCMs, is that SV and CO are all estimated only to within a proportionality constant. An independent calibration is required if absolute measures are needed.

7.2. ABF Estimation

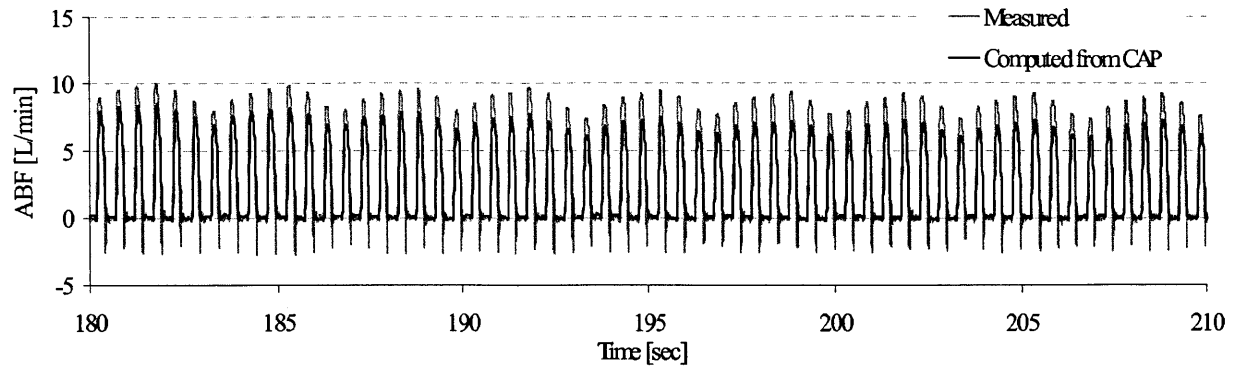
7.2.1. Overview

A novel algorithm using the ARX model to continuously estimate ABF by the analysis of peripheral

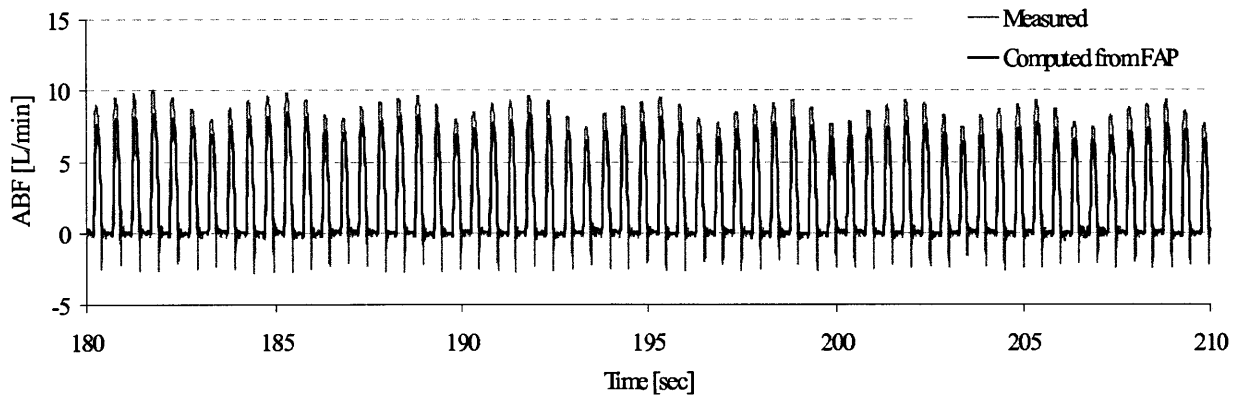
ABP waveforms was developed and validated. As opposed to the existing PCMs that also analyze ABP to calculate CO and SV, the ARX method reconstructs more fundamental information, i.e., instantaneous ABF, that is used to calculate CO and SV. The method estimates ABF within a proportionality constant of C_a and does not require demographical data, as opposed to the existing methods.

The algorithm utilizes the notion that the input to the arterial system is zero during diastole [57]. In the ABF estimation routine, 17 diastolic ABP waveforms were used in the left-hand item of (4.4) to obtain the AR parameters. The AR parameters were integrated into the ARX model (Fig. 4.1) and applied to the entire ABP waveform to obtain the ABF waveform. Note that the AR parameters were also used to obtain the characteristic time constant τ (Fig. 4.2b) as well as the scaling factor α (4.5) to properly scale the estimated ABF (4.10).

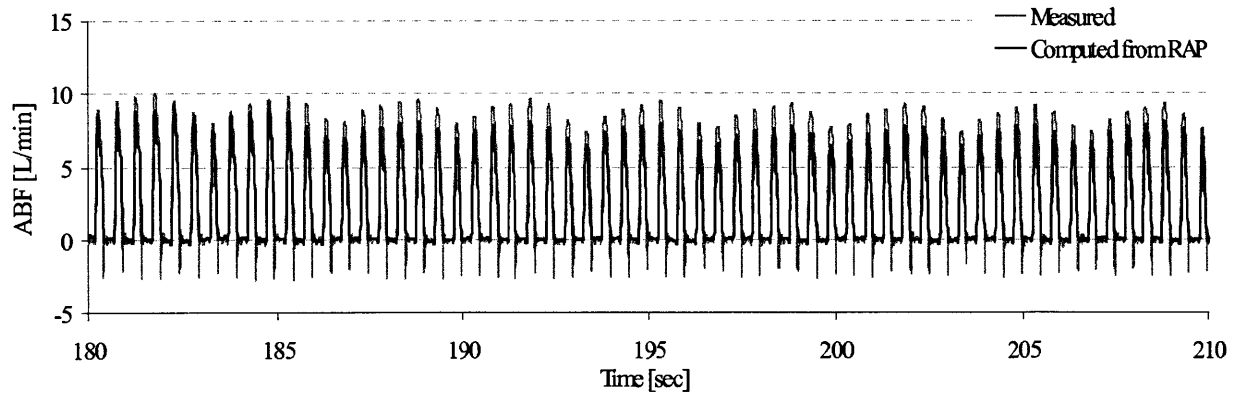
The conditioning of the data to synthesize the systolic and diastolic ABP within the moving window was a key necessary process. Without conditioning, divergences in the impulse responses were observed, and the estimated ABF resulted in high errors in SD, skewness, and kurtosis. The cause of the estimated impulse response instability was varying ABP data that incur computational challenges in obtaining the AR parameters. For example, if beat-to-beat MAP values are rapidly changing on a beat-to-beat basis due to respiration or a physiological feedback system in response to vasoactive drugs, a range of diastolic ABP values vary from one beat to another within a window. Such data force the algorithm (4.4) to find a compromised single set of AR parameters that can reduce multiple diastolic ABP signal amplitudes down to approximately zero. Also, if the length of the RR interval and diastolic duration vary among 17 beats in the window, it is difficult to find a single AR parameter length L that satisfies all beats. Thus, the data-conditioning was conducted to relax the computational challenge in AR parameter acquisition. Although the beats in the moving window are rescaled horizontally (resampling) and vertically (rescaling) for the aforementioned purpose, this procedure was only used to obtain an AR parameter set. The AR parameters were applied to the original ABP waveforms to obtain ABF. Therefore, the physiological changes occurring in a shorter interval than the window size (e.g., respiration) can be seen in the estimated ABF (Fig. 7.1).



(a) Using CAP



(b) Using FAP



(c) Using RAP

Fig. 7.1. Cyclic patterns of the measured and estimated ABF signals.

The cyclic magnitude change due to respiration (~17 breaths per minute) observed in the measured ABF (gray) is also apparent in the estimated ABF waveform (black).

The 17-beat moving window size was empirically chosen; if the window is too short, one cannot excite enough modes to identify the system. On the other hand, if the window is too long, one cannot assume time-invariance of the pertinent cardiovascular system (e.g., baroreflex feedback that changes TPR, characteristic time constant, and impulse response).

For determining AR parameter length L , the minimum $\Sigma a[j]$ was selected as an evaluation function because it gave $a[j]$ that converged to an impulse response $h[n]$. The search space for L was limited to $RR\text{-interval} > L > 20$ samples (at a 250 Hz-sampling frequency), empirically found by authors that provides reasonable ABF waveforms. In cases where there were multiple local minima of $\Sigma a[j]$ in the search space, the minimum with the shortest L was adopted.

The algorithm achieved 15.2-21.8% SV, 12.7-15.8% CO, and 14.3-20.9% TPR RNMSEs (Table 6.8, Fig. 6.50), respectively. Furthermore, the measured ABF and the estimated ABF by the algorithm showed small errors and reasonable correlations in skewness and kurtosis. In particular, the algorithm applied to animals #6 and #8 resulted in an overall high correlation (Table 6.7). The low correlation of skewness (animal #4, radial) and kurtosis (animal #9, femoral and radial) are partially due to the small ranges of the variables. The ABF estimated by the algorithm provided matching SD, skewness and kurtosis with the measured ABF waveforms, as shown in Fig. 6.48 and Fig. 6.49. Regarding the Windkessel results, the left shift of the skewness error histogram (Fig. 6.49a-c) represents an earlier peak of the estimated ABF waveforms than the measured ABF waveforms, and the left shift of the kurtosis histogram (Fig. 6.49 d-f) means that pointier waveforms (leptokurtic) were achieved than the measured ABF waveforms. Both of the characteristics are present in the Windkessel ABF waveforms shown in Fig. 6.44d, Fig. 6.45d, and Fig. 6.46d.

The classical Windkessel model assumes exponential decay during diastole. That model can be described as a low-order (first-order) AR model. The present algorithm, on the other hand, obtains higher-order AR parameters (Fig. 4.2(a)) from diastolic ABP waveforms. The advantage of the present algorithm is that it may take into account the possible distortion involved in the diastolic ABP waveforms. Therefore, when applied to the systolic ABP, the filter created by the algorithm may compensate for the

distortion and could reconstruct systolic ABF waveforms. The distortion property varies from artery to artery, as well as from subject to subject. The algorithm could obtain individual parameters unique to each arterial line of each subject on a beat-to-beat basis.

The algorithm is easy to implement in the existing continuous ABP measuring medical systems. The ABF waveform, CO, and SV estimated by the analysis of ABP waveforms will improve the ABP-only monitoring and enable multi-modal evaluation in clinical and surgical settings.

7.2.2. Sensitivity Analysis Regarding the Onset of Diastole

In the results of the ABF estimation, the diastolic interval in each beat was given by the measured ABF waveforms. In practical settings, a possible method to detect the onsets of diastole would be the use of the dicrotic notch in ABP waveforms. However, the dicrotic notch does not always exist in ABP waveforms. Furthermore, due to the ABP waveform distortion, a systolic interval in an ABF signal does not necessarily match the time interval from systolic onset to the dicrotic notch in an ABP signal.

In this section, the sensitivity analyses of the ARX method on the onset of diastole is conducted over the Yorkshire swine data sets. Each scenario adopts a different formula for identifying the onset of diastole. The first two methods introduced in this section are empirical models. Secondly, a method to identify onsets of diastoles by using heart sounds is addressed to conclude that the heart sound could identify the onset of diastole with an accuracy of 10%. Thirdly, the true diastolic duration was lengthened/shortened by 10% to further investigate the impact of the errors in identifying the onset of diastoles.

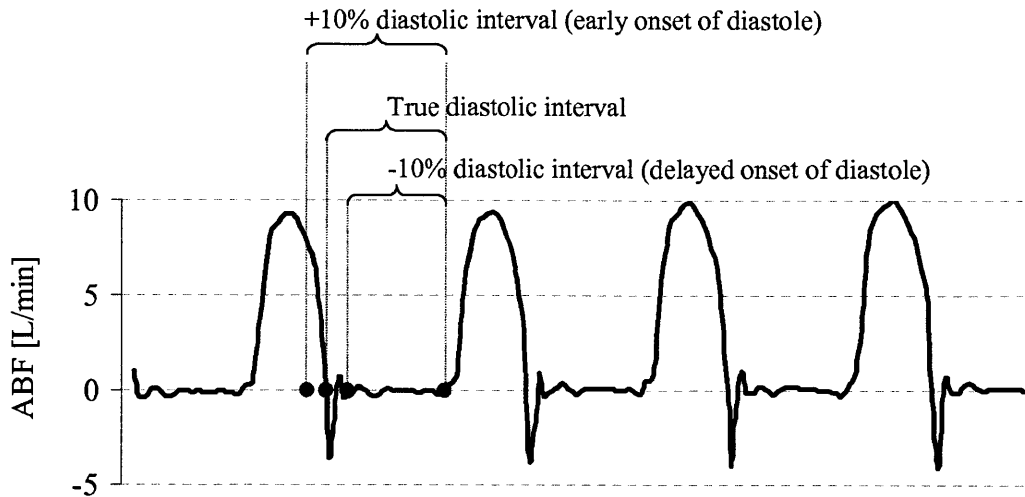


Fig. 7.2. Increased and decreased diastolic interval.

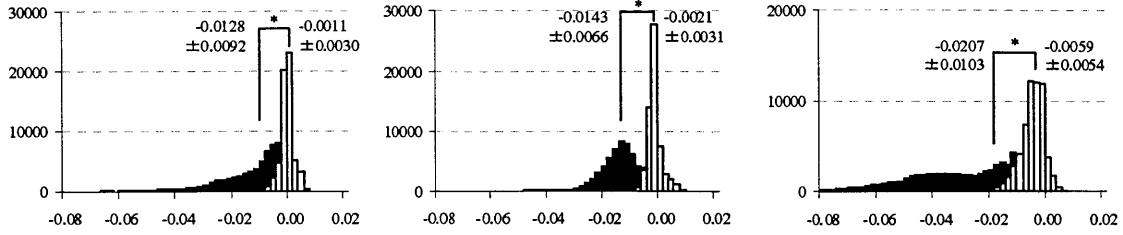
Based on the discussion of the use of heart sounds, further sensitivity analysis is conducted here. Fixing the end-diastolic point, the true diastolic intervals were increased and decreased by 10% (Fig. 7.2). With these offsets of diastolic onset, the ARX method was tested, and CO, SV, ABF skewness, and kurtosis were obtained.

Increased diastolic interval

Table 7.1 shows the RNMSEs in the case of an increased diastolic interval; i.e., the onsets of diastoles were identified earlier than the actual onsets. Portions of the ABP waveforms at the ends of systoles were regarded as the beginning of diastole, causing higher errors (Table 7.1). The ABF waveforms still resulted in smaller errors of skewness and kurtosis than the Windkessel model.

Calibration Methods	Central	Femoral	Radial
SV with Constant Ca	19.2	25.7	23.4
CO with Constant Ca	13.2	19.2	19.5

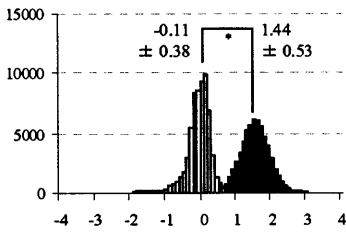
Table 7.1. SV and CO estimation results with the identified diastolic intervals increased by 10%. The Ca in each animal was assumed to be constant.



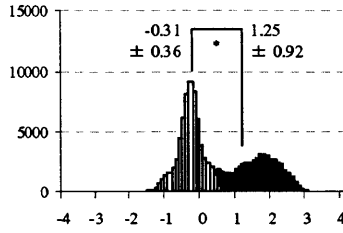
(a) SD error, using CAP

(b) SD error, using FAP

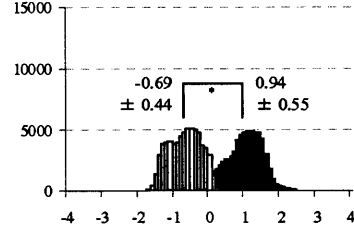
(c) SD error, using RAP



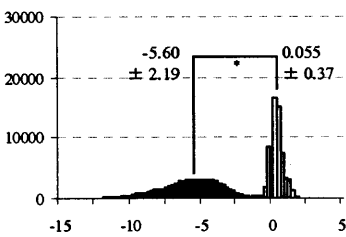
(d) Skewness error, using CAP



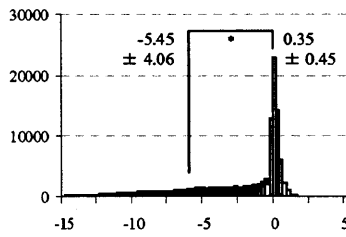
(e) Skewness error, using FAP



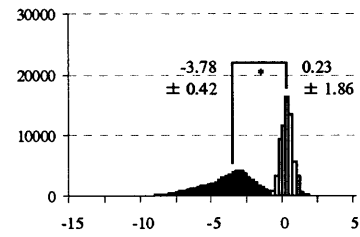
(f) Skewness error, using RAP



(g) Kurtosis error, using CAP



(h) Kurtosis error, using FAP



(i) Kurtosis error, using RAP

Fig. 7.3. Histograms of the standard deviation, skewness, and kurtosis errors of ABF waveforms with a +10% diastolic interval offset.

The duration of diastole in each beat was increased by 10% so that the onset of diastole comes earlier than the actual onset. The value above each histogram indicates the mean of the histogram. The ARX algorithm (white) had smaller errors than the Windkessel (black) model (* P<0.05).

Decreased diastolic interval

Table 7.2 and Fig. 7.4 show the RNMSEs in the case of a decreased diastolic interval; i.e., the onsets of diastoles were identified later than the actual onsets. Higher RNMSEs yet better ABF waveforms are common with increased diastolic interval results.

Calibration Methods	Central	Femoral	Radial
SV with Constant Ca	25.8	24.3	27.3
CO with Constant Ca	16.1	19.6	23.6

Table 7.2. SV and CO estimation results with the identified diastolic interval decreased by 10%. The Ca in each animal was assumed to be constant.

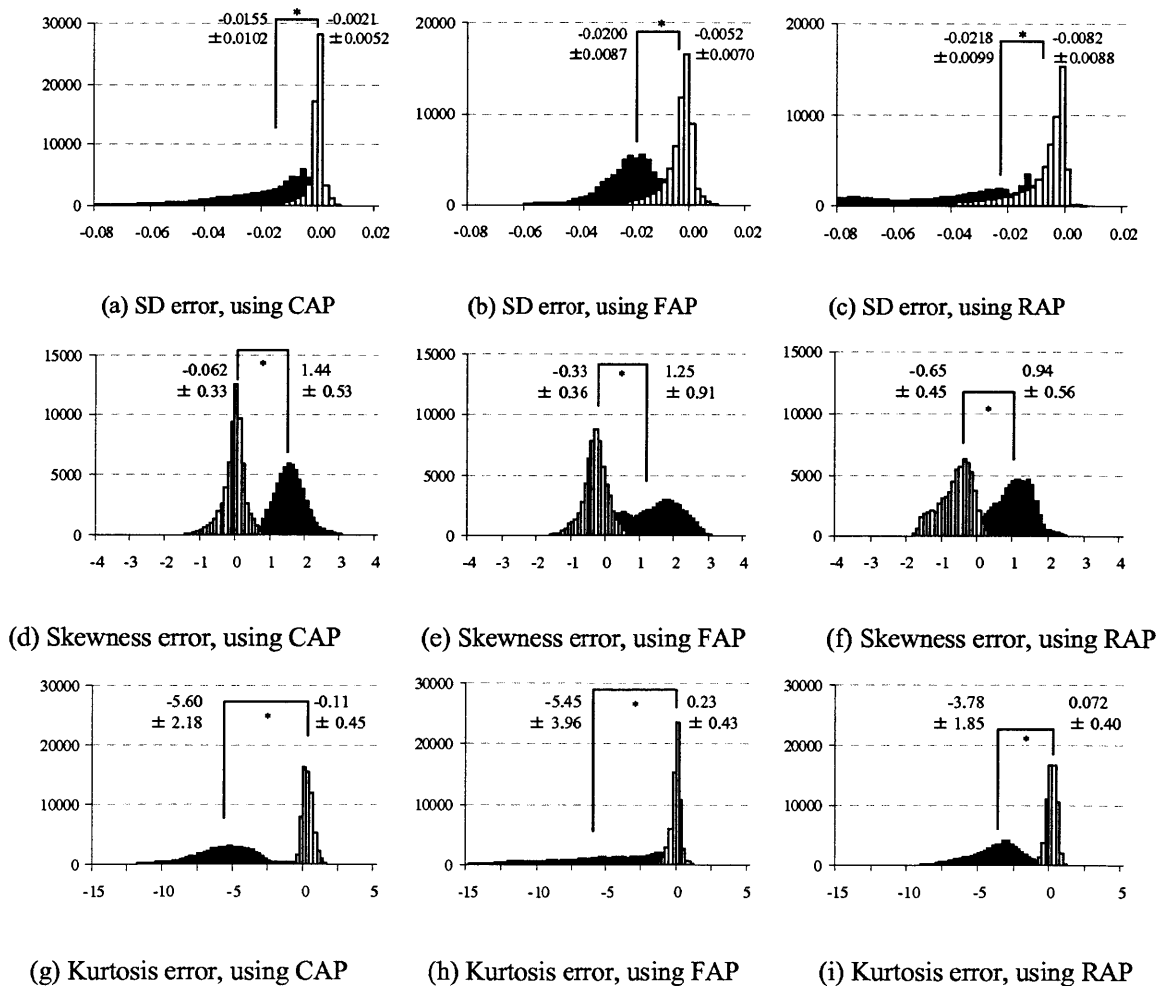


Fig. 7.4. Histograms of the standard deviation, skewness, and kurtosis errors of ABF waveforms with a -10% diastolic interval offset.

The duration of diastole in each beat was decreased by 10% so that the onset of diastole comes earlier than the actual onset. The value above each histogram indicates the mean of the histogram. The ARX algorithm (white) had smaller errors than the Windkessel (black) model (* P<0.05).

7.2.3. Summary

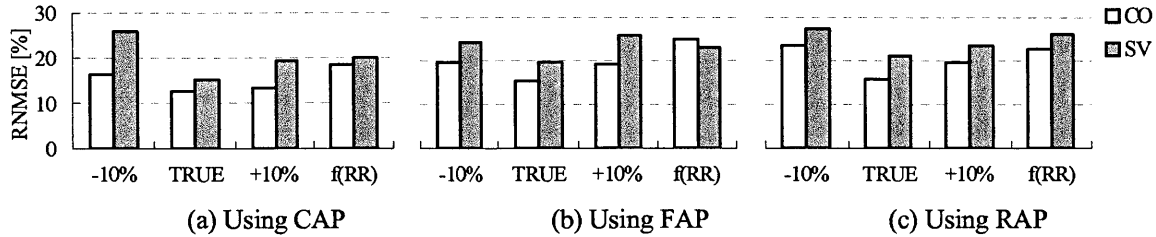


Fig. 7.5. Sensitivity of the new algorithm to the error of the identified diastolic interval.

In using the ARX method, the true diastolic onset provides the lowest CO and SV errors among the estimated diastolic onset as a function of preceding RR intervals, 10% prolonged, and 10% shortened diastolic intervals.

To test the sensitivity of the algorithm to the offset of diastolic onset, the time stamp of the onset of diastole was offset from the actual location so that the diastolic interval was $\pm 10\%$ of the actual interval. With the diastolic intervals increased by 10%, the SV (CO) estimation errors increased by 20.3 (3.9)%, 23.7 (26.3)%, and 9.8 (23.4)% using CAP, FAP, and RAP, respectively. With diastolic intervals decreased by 10%, the errors increased by 68.8 (26.9)%, 23.9 (29.2)%, and 29.5 (7.8)%, respectively (Fig. 7.5). For both the $\pm 10\%$ cases, skewness and kurtosis errors remained as small as the reported errors in Fig. 6.49. The increases in SV errors were larger for the -10% diastolic intervals. This could be attributed to the loss of information-rich, varying ABP signals at the beginning of diastole. Especially when the diastolic ABP is relatively flat, a decaying curve at the beginning of diastole is particularly useful in obtaining correct AR parameters.

The classical Windkessel model assumes exponential decay during diastole. That model can be described as a low-order (first-order) AR model. The Windkessel model resulted in an earlier systolic peak (also indicated by the right shift of the skewness histogram, Fig. 6.49a-c in black) and a pointy peak (also indicated by the left shift of the kurtosis histogram, Fig. 6.49d-f in black) of the estimated ABF waveforms. The ARX algorithm, on the other hand, obtains higher-order AR parameters (Fig. 4.2a) from diastolic ABP waveforms. The advantage of the ARX algorithm is that it may take into account the possible distortion involved in the diastolic ABP waveforms as a result of propagation through the arterial

tree. Therefore, when applied to the systolic ABP, the filter created by the algorithm may compensate for the distortion and could reconstruct systolic ABF waveforms. The distortion property varies from artery to artery, as well as from subject to subject. The algorithm might be able to obtain individual parameters unique to each arterial line of each subject on a beat-to-beat basis.

8. Conclusions and Future Work

8.1. Summary

In Chapter 1, an overview of cardiovascular monitoring and the need for minimally- or non-invasive SV, CO, and TPR monitoring by the analysis of ABP were introduced. Chapter 2 introduced a comprehensive list of existing algorithms that estimate proportional SV, CO, and TPR. The new algorithms were introduced in Chapter 3. The algorithms were developed by taking cardiovascular physiology into consideration. Furthermore, new algorithms to identify end systole were developed and validated (Section 5.4). The end systole identification algorithms advanced the performance of the previous SV, CO, and TPR estimation algorithms as well as the new algorithms. The SV, CO, and TPR estimation algorithms in conjunction with the end systole identification methods were validated (Chapter 6) by using the previously recorded Yorkshire swine data sets (Table 6.1). These algorithms involve the use of instantaneous ABF recorded directly from the aorta, CAP, FAP, and RAP. As summarized in Table 6.4 – Table 6.6, the Pressure Ratio method, modified Herd's method, Corrected Impedance method, Kouchoukos Correction method, and Parabolic method achieved low RNMSEs. The end systole identification algorithms turned existing algorithms into new algorithms, to achieve low RNMSEs. These methods should be tested on cardiovascular data sets recorded from human subjects to evaluate their estimation performance in clinical use.

This thesis also introduced a novel algorithm to estimate instantaneous ABF in Chapter 4. The method adopts ARX modeling technique, with the instantaneous ABF as the exogenous input to be estimated by the algorithm. Because the exogenous input to the system is zero during diastole, the ARX model becomes the AR model during diastole. By the analysis of diastolic ABP, the AR parameters were acquired, and the system impulse responses were calculated. The impulse response and AR parameters were used to develop a filter to process ABF to reconstruct and scale instantaneous ABF. The ARX

algorithm achieved RNMSEs of 15.3, 19.6, and 21.8% in SV estimation; 12.7, 15.2, and 15.8% in CO estimation; and 14.3, 20.9, and 19.4% in TPR estimation derived from CAP, FAP, and RAP, respectively (Table 6.8, Fig. 6.50 in Chapter 6). The results demonstrated that the algorithm can reconstruct ABF waveforms from ABP waveforms more accurately than the Windkessel model.

8.2. Contributions

The contributions of this thesis are four-fold:

- Development and validation of new SV, CO, TPR estimation methods:

A series of novel algorithms for proportional SV, CO, and TPR estimation were introduced and validated. The implementation of cardiovascular physiology in a mathematical form was described. The algorithms have the potential to accurately estimate the cardiovascular indices for de-conditioned cardiovascular systems.

- Development of end systole identification methods:

Using the exponential model and partial pulse pressure model, new identification methods for end systole were developed. The methods could advance the newly developed and existing SV, CO, and TPR estimation methods.

- Comprehensive comparison of the existing and new methods:

The new and existing estimation methods for SV, CO, and TPR were combined with the newly developed methods to identify end systoles and applied to common data sets (Yorkshire swine). This is the first comprehensive comparison of the methods reported in [23] and [53]. Among the methods, the newly developed Parabolic ABF model, Pressure Ratio method, modified Herd's method as well as existing Corrected Impedance Kouchoukos Correction methods with the end systole identification methods were reported to achieve low errors for the swine data sets recorded from the nominal cardiovascular system with perturbations given by vasoactive drugs.

- Development and validation of the new ABF estimation method:

Using the ARX model, a novel algorithm to reconstruct instantaneous ABF on a beat-to-beat basis by analysis of the ABP signal was developed and validated. The quantitative analyses of the reconstructed waveforms demonstrated that the ARX model reliably estimates instantaneous ABF waveforms as well as SV, CO, and TPR.

8.3. Suggestions for Further Research

Building on the contributions listed above, suggestions for future research directions are outlined below.

The use of heart sounds for the identification of diastole onset

In this thesis, sensitivity analyses were conducted to investigate the impact of errors in identifying end systole. Also, an exponential model using the preceding RR interval and Partial Pressure model were also introduced as end-systole determination methods. An alternative method for identifying end systoles would be the S1 and S2 heart sounds that indicate the opening and closing of the aortic valve, respectively. By analyzing the heart sounds, it would be possible to map systolic/diastolic intervals from the heart sound record to corresponding ABP.

Heart failure models

The algorithm was validated using Yorkshire swine data sets whose wide physiological range was achieved by the use of vasoactive drugs. The next step would be to apply and validate the algorithm with abnormal beats, such as premature beats, and heart failure models. The algorithms should be tested to estimate CO and SV, as well as to reconstruct abnormal ABF and evaluate contractility of the left ventricle. While the empirical methods (Corrected Impedance, for example) would not work for these abnormal heart conditions, some of the model-based (cardiovascular physiology-based) methods would

work better than empirical methods.

Animal heart failure models have been developed and used for the validation of heart transplantation, left ventricular assist devices, artificial hearts, and so forth [59]. Major methods to induce heart failure are: (1) pacing-induced (chronic, easy to control [60]), (2) ischemia-induced or coronary ligation/occlusion (could be fatal and difficult to control [61]), and (3) pharmacological [61-63].

Bi-ventricular pacing study

For patients with a severe myocardial infarction, bi-ventricular pacing that stimulates both left and right ventricles is an option to maintain CO (Fig. 8.1). Currently, central ABP analysis (maximizing dP/dt) and/or short-term echocardiography in the ICU are used to optimize the atrioventricular (A-V) and left and right ventricular pacing delays [64, 65]. However, the optimum delay changes and real-time adaptive cardiac resynchronization are needed. The ARX algorithm can be used to process peripheral ABP waveforms to reconstruct ABF, and such instantaneous ABF waveform information can be used to optimize A-V delay and maximize CO and SV in real time.

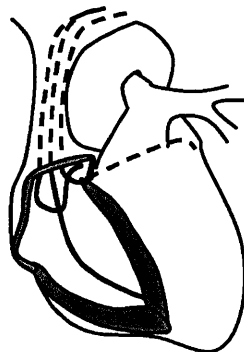


Fig. 8.1. Bi-ventricular pacing.

Long-term monitoring of cardiovascular indices in space

Cardiovascular alterations in space are a major concern. The techniques presented in this thesis to monitor changes in SV, CO, and TPR can be used for health monitoring in aerospace missions to detect deconditioning of the cardiovascular system, predict the magnitude of orthostatic stress upon return to Earth [50], and evaluate countermeasures against such deconditioning. The algorithms developed in this thesis could be implemented into the existing blood pressure monitoring system in clinical, research, and spaceflight settings including the Integrated Cardiovascular Investigation onboard the International Space Station (Fig. 8.2).

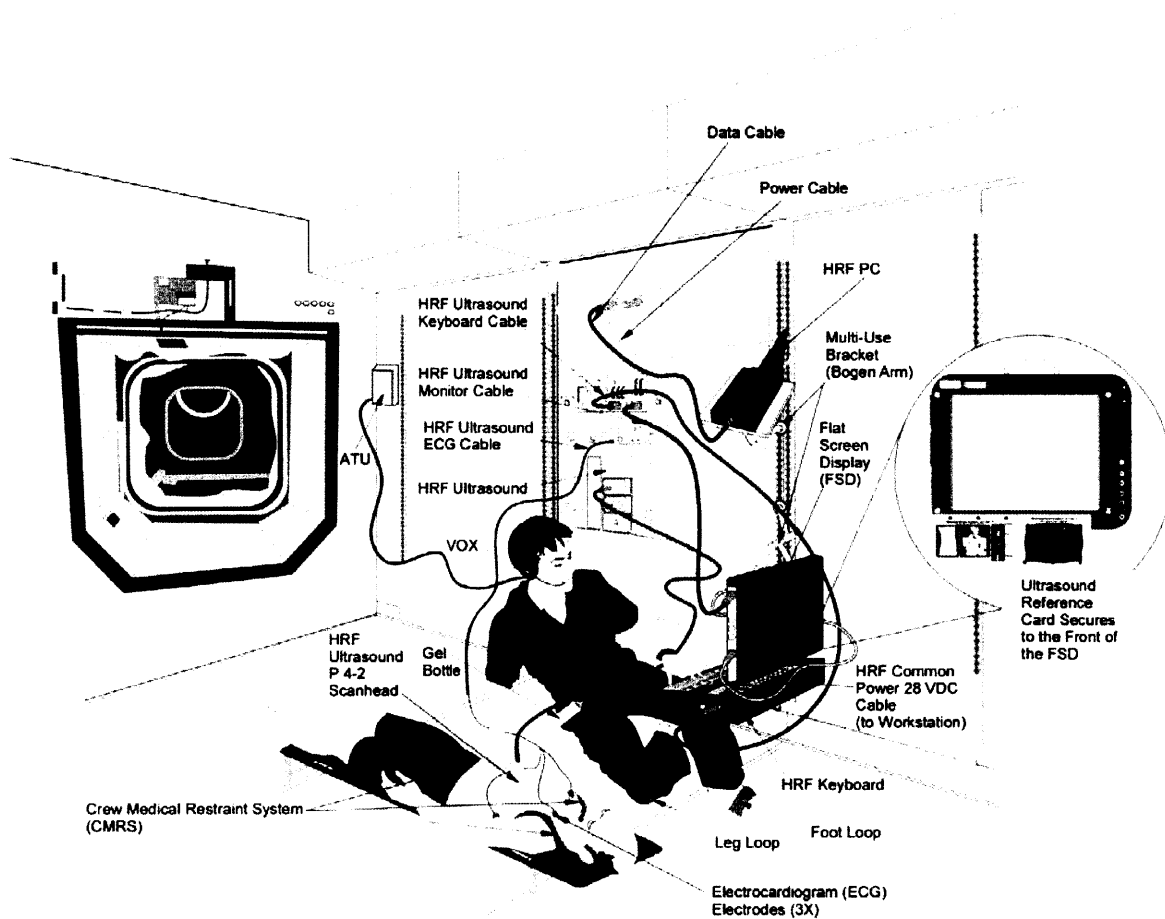


Fig. 8.2. Schematic drawing of the Integrated Cardiovascular Investigation in the Columbus Laboratory onboard the International Space Station. Image obtained from http://www.nasa.gov/mission_pages/station/research/experiments/Integrated_Cardiovascular.html on April 26, 2011. © NASA.

Appendix A: Derivation of High-Order Hybrid Model

A.1. Quadratic Model

A quadratic model

$$y(i, j) = D(j) + y_0(i, j) + a_1 X_1(i, j) + a_2 X_2(i, j) + b_{11} X_1^2(i, j) + 2b_{12} X_1 X_2(i, j) + b_{22} X_2^2(i, j) \quad (\text{A.1})$$

can be described by redefining $y - y_0$ as Y :

$$Y(i, j) = D(j) + a_1 X_1(i, j) + a_2 X_2(i, j) + b_{11} X_1^2(i, j) + 2b_{12} X_1 X_2(i, j) + b_{22} X_2^2(i, j) \quad (\text{A.2})$$

Define the error as

$$E(i, j) \equiv Y(i, j) - D(j) - a_1 X_1(i, j) - a_2 X_2(i, j) - b_{11} X_1^2(i, j) - 2b_{12} X_1 X_2(i, j) - b_{22} X_2^2(i, j) \quad (\text{A.3})$$

and the total error as

$$E \equiv \sum_{j=1}^L \sum_{i=1}^{N(j)} \{Y(i, j) - D(j) - a_1 X_1(i, j) - a_2 X_2(i, j) - b_{11} X_1^2(i, j) - 2b_{12} X_1 X_2(i, j) - b_{22} X_2^2(i, j)\}^2 \quad (\text{A.4})$$

To minimize E with a 's,

$$\begin{aligned} \frac{\partial E}{\partial a_m} &= 2 \sum_{j=1}^L \sum_{i=1}^{N(j)} \{Y(i, j) - D(j) - a_1 X_1(i, j) - a_2 X_2(i, j) - b_{11} X_1^2(i, j) - 2b_{12} X_1 X_2(i, j) - b_{22} X_2^2(i, j)\} \\ &\quad \cdot (-X_m(i, j)) \\ &= 0 \end{aligned} \quad (\text{A.5})$$

$$\begin{aligned} \Rightarrow \sum_{j=1}^L \sum_{i=1}^{N(j)} Y(i, j) X_m(i, j) &= \sum_{j=1}^L \sum_{i=1}^{N(j)} D(j) X_m(i, j) + \sum_{k=1}^2 a_k \sum_{j=1}^L \sum_{i=1}^{N(j)} X_k(i, j) X_m(i, j) \\ &\quad + \sum_{k=1}^2 \sum_{l=1}^2 b_{kl} \sum_{k=1}^2 a_k \sum_{j=1}^L \sum_{i=1}^{N(j)} X_k(i, j) X_l(i, j) X_m(i, j) \end{aligned} \quad (\text{A.6})$$

i.e.,

$$\begin{aligned}
\sum_{j=1}^L \sum_{i=1}^{N(j)} Y(i, j) X_1(i, j) &= \sum_{j=1}^L D(j) \sum_{i=1}^{N(j)} X_1(i, j) + a_1 \sum_{j=1}^L \sum_{i=1}^{N(j)} X_1(i, j) X_1(i, j) + a_2 \sum_{j=1}^L \sum_{i=1}^{N(j)} X_2(i, j) X_1(i, j) \\
&+ b_{11} \sum_{j=1}^L \sum_{i=1}^{N(j)} X_1^3(i, j) + 2b_{12} \sum_{j=1}^L \sum_{i=1}^{N(j)} X_1^2(i, j) X_2(i, j) + b_{22} \sum_{j=1}^L \sum_{i=1}^{N(j)} X_1(i, j) X_1^2(i, j)
\end{aligned} \tag{A.7}$$

and

$$\begin{aligned}
\sum_{j=1}^L \sum_{i=1}^{N(j)} Y(i, j) X_2(i, j) &= \sum_{j=1}^L D(j) \sum_{i=1}^{N(j)} X_2(i, j) + a_1 \sum_{j=1}^L \sum_{i=1}^{N(j)} X_1(i, j) X_2(i, j) + a_2 \sum_{j=1}^L \sum_{i=1}^{N(j)} X_2^2(i, j) \\
&+ b_{11} \sum_{j=1}^L \sum_{i=1}^{N(j)} X_1(i, j) X_2^2(i, j) + 2b_{12} \sum_{j=1}^L \sum_{i=1}^{N(j)} X_1(i, j) X_2^2(i, j) + b_{22} \sum_{j=1}^L \sum_{i=1}^{N(j)} X_1^3(i, j)
\end{aligned} \tag{A.8}$$

To minimize E with b's,

$$\begin{aligned}
\frac{\partial E}{\partial b_{kl}} &= 2 \sum_{j=1}^L \sum_{i=1}^{N(j)} \left\{ Y(i, j) - D(j) - a_1 X_1(i, j) - a_2 X_2(i, j) - b_{11} X_1^2(i, j) - 2b_{12} X_1 X_2(i, j) - b_{22} X_2^2(i, j) \right\} \\
&\quad \cdot (-X_k(i, j) X_l(i, j)) \\
&= 0
\end{aligned} \tag{A.9}$$

$$\begin{aligned}
\sum_{j=1}^L \sum_{i=1}^{N(j)} Y(i, j) X_k(i, j) X_l(i, j) &= \sum_{j=1}^L \sum_{i=1}^{N(j)} D(j) X_k(i, j) X_l(i, j) + a_1 \sum_{j=1}^L \sum_{i=1}^{N(j)} X_1(i, j) X_k(i, j) X_l(i, j) \\
&+ a_2 \sum_{j=1}^L \sum_{i=1}^{N(j)} X_2(i, j) X_k(i, j) X_l(i, j) \\
&+ b_{11} \sum_{j=1}^L \sum_{i=1}^{N(j)} X_1^2(i, j) X_k(i, j) X_l(i, j) \\
&+ b_{12} \sum_{j=1}^L \sum_{i=1}^{N(j)} X_1(i, j) X_2(i, j) X_k(i, j) X_l(i, j) + b_{22} \sum_{j=1}^L \sum_{i=1}^{N(j)} X_2^2(i, j) X_k(i, j) X_l(i, j)
\end{aligned} \tag{A.10}$$

i.e., for $k = 1, 2$ and $l = 1, 2$,

$$\begin{aligned}
\sum_{j=1}^L \sum_{i=1}^{N(j)} Y(i,j) X_1(i,j) X_1(i,j) &= \sum_{j=1}^L \sum_{i=1}^{N(j)} D(j) X_1(i,j) X_1(i,j) + a_1 \sum_{j=1}^L \sum_{i=1}^{N(j)} X_1(i,j) X_1(i,j) X_1(i,j) \\
&+ a_2 \sum_{j=1}^L \sum_{i=1}^{N(j)} X_2(i,j) X_1(i,j) X_1(i,j) + b_{11} \sum_{j=1}^L \sum_{i=1}^{N(j)} X_1^2(i,j) X_1(i,j) X_1(i,j) \\
&+ b_{12} \sum_{j=1}^L \sum_{i=1}^{N(j)} X_1(i,j) X_2(i,j) X_1(i,j) X_1(i,j) + b_{22} \sum_{j=1}^L \sum_{i=1}^{N(j)} X_2^2(i,j) X_1(i,j) X_1(i,j)
\end{aligned} \tag{A.11}$$

$$\begin{aligned}
\sum_{j=1}^L \sum_{i=1}^{N(j)} Y(i,j) X_1(i,j) X_2(i,j) &= \sum_{j=1}^L \sum_{i=1}^{N(j)} D(j) X_1(i,j) X_2(i,j) + a_1 \sum_{j=1}^L \sum_{i=1}^{N(j)} X_1(i,j) X_1(i,j) X_2(i,j) \\
&+ a_2 \sum_{j=1}^L \sum_{i=1}^{N(j)} X_2(i,j) X_1(i,j) X_2(i,j) + b_{11} \sum_{j=1}^L \sum_{i=1}^{N(j)} X_1^2(i,j) X_1(i,j) X_2(i,j) \\
&+ b_{12} \sum_{j=1}^L \sum_{i=1}^{N(j)} X_1(i,j) X_2(i,j) X_1(i,j) X_2(i,j) + b_{22} \sum_{j=1}^L \sum_{i=1}^{N(j)} X_2^2(i,j) X_1(i,j) X_2(i,j)
\end{aligned} \tag{A.12}$$

$$\begin{aligned}
\sum_{j=1}^L \sum_{i=1}^{N(j)} Y(i,j) X_2(i,j) X_2(i,j) &= \sum_{j=1}^L \sum_{i=1}^{N(j)} D(j) X_2(i,j) X_2(i,j) + a_1 \sum_{j=1}^L \sum_{i=1}^{N(j)} X_1(i,j) X_2(i,j) X_2(i,j) \\
&+ a_2 \sum_{j=1}^L \sum_{i=1}^{N(j)} X_2(i,j) X_2(i,j) X_2(i,j) + b_{11} \sum_{j=1}^L \sum_{i=1}^{N(j)} X_1^2(i,j) X_2(i,j) X_2(i,j) \\
&+ b_{12} \sum_{j=1}^L \sum_{i=1}^{N(j)} X_1(i,j) X_2(i,j) X_2(i,j) X_2(i,j) + b_{22} \sum_{j=1}^L \sum_{i=1}^{N(j)} X_2^2(i,j) X_2(i,j) X_2(i,j)
\end{aligned} \tag{A.13}$$

Also, change D's to minimize E

$$\begin{aligned}
\frac{\partial E}{\partial D_n} &= \sum_{i=1}^{N(n)} Y(i,n) + a_1 \sum_{i=1}^{N(n)} X_1(i,n) + a_2 \sum_{i=1}^{N(n)} X_2(i,n) \\
&+ b_{11} \sum_{i=1}^{N(n)} X_1^2(i,n) + 2b_{12} \sum_{i=1}^{N(n)} X_1(i,n) X_2(i,n) + b_{22} \sum_{i=1}^{N(n)} X_2^2(i,n) \\
&= 0
\end{aligned} \tag{A.14}$$

$$\begin{aligned}
\sum_{i=1}^{N(n)} Y(i, n) &= \sum_{i=1}^{N(n)} Y(i, n) + a_1 \sum_{i=1}^{N(n)} X_1(i, n) + a_2 \sum_{i=1}^{N(n)} X_2(i, n) \\
&\quad + b_{11} \sum_{i=1}^{N(n)} X_1^2(i, n) + 2b_{12} \sum_{i=1}^{N(n)} X_1(i, n)X_2(i, n) + b_{22} \sum_{i=1}^{N(n)} X_2^2(i, n)
\end{aligned} \tag{A.15}$$

Therefore,

$$\begin{aligned}
\sum_{i=1}^{N(1)} Y(i, 1) &= \sum_{i=1}^{N(1)} Y(i, 1) + a_1 \sum_{i=1}^{N(1)} X_1(i, 1) + a_2 \sum_{i=1}^{N(1)} X_2(i, 1) \\
&\quad + b_{11} \sum_{i=1}^{N(1)} X_1^2(i, 1) + 2b_{12} \sum_{i=1}^{N(1)} X_1(i, 1)X_2(i, 1) + b_{22} \sum_{i=1}^{N(1)} X_2^2(i, 1) \\
&\quad \vdots \\
\sum_{i=1}^{N(L)} Y(i, L) &= \sum_{i=1}^{N(L)} Y(i, L) + a_1 \sum_{i=1}^{N(L)} X_1(i, L) \\
&\quad + a_2 \sum_{i=1}^{N(L)} X_2(i, L) + b_{11} \sum_{i=1}^{N(L)} X_1^2(i, L) + 2b_{12} \sum_{i=1}^{N(L)} X_1(i, L)X_2(i, L) + b_{22} \sum_{i=1}^{N(L)} X_2^2(i, L)
\end{aligned} \tag{A.16}$$

Combining the equations in (A.16),

$$\begin{pmatrix} \sum_{i=1}^{N(1)} Y(i,1) \\ \vdots \\ \sum_{i=1}^{N(L)} Y(i,L) \\ \sum_{j=1}^L \sum_{i=1}^{N(j)} Y(i,j)X_1(i,j) \\ \sum_{j=1}^L \sum_{i=1}^{N(j)} Y(i,j)X_2(i,j) \\ \sum_{j=1}^L \sum_{i=1}^{N(j)} Y(i,j)X_1^2(i,j) \\ \sum_{j=1}^L \sum_{i=1}^{N(j)} Y(i,j)X_1(i,j)X_2(i,j) \\ \sum_{j=1}^L \sum_{i=1}^{N(j)} Y(i,j)X_2^2(i,j) \end{pmatrix} = \begin{pmatrix} N_1 & \dots & 0 & \sum_{i=1}^{N(1)} X_1(i,1) & \sum_{i=1}^{N(1)} X_2(i,1) & \sum_{i=1}^{N(1)} X_1^2(i,1) & \sum_{i=1}^{N(1)} X_1(i,1)X_2(i,1) & \sum_{i=1}^{N(1)} X_2^2(i,1) \\ \vdots & \ddots & \vdots & \vdots & \vdots & \vdots & \vdots & \vdots \\ 0 & 0 & N_L & \sum_{i=1}^{N(L)} X_1(i,L) & \sum_{i=1}^{N(L)} X_2(i,L) & \sum_{i=1}^{N(L)} X_1^2(i,L) & \sum_{i=1}^{N(L)} X_1(i,L)X_2(i,L) & \sum_{i=1}^{N(L)} X_2^2(i,L) \\ \sum_{i=1}^{N(1)} X_1(i,1) & \dots & \sum_{i=1}^{N(L)} X_1(i,L) & \sum_{j=1}^L \sum_{i=1}^{N(j)} X_1^2 & \sum_{j=1}^L \sum_{i=1}^{N(j)} X_2 X_1 & \sum_{j=1}^L \sum_{i=1}^{N(j)} X_1^3 & \sum_{j=1}^L \sum_{i=1}^{N(j)} X_1^2 X_2 & \sum_{j=1}^L \sum_{i=1}^{N(j)} X_1 X_2^2 \\ \sum_{i=1}^{N(1)} X_2(i,1) & \dots & \sum_{i=1}^{N(L)} X_2(i,L) & \sum_{j=1}^L \sum_{i=1}^{N(j)} X_1 X_2 & \sum_{j=1}^L \sum_{i=1}^{N(j)} X_2^2 & \sum_{j=1}^L \sum_{i=1}^{N(j)} X_1^2 X_2 & \sum_{j=1}^L \sum_{i=1}^{N(j)} X_1 X_2^2 & \sum_{j=1}^L \sum_{i=1}^{N(j)} X_2^3 \\ \sum_{i=1}^{N(1)} X_1^2(i,1) & \dots & \sum_{i=1}^{N(L)} X_1^2(i,L) & \sum_{j=1}^L \sum_{i=1}^{N(j)} X_1^3 & \sum_{j=1}^L \sum_{i=1}^{N(j)} X_1^2 X_2 & \sum_{j=1}^L \sum_{i=1}^{N(j)} X_1^4 & \sum_{j=1}^L \sum_{i=1}^{N(j)} X_1^3 X_2 & \sum_{j=1}^L \sum_{i=1}^{N(j)} X_1^2 X_2^2 \\ \sum_{i=1}^{N(1)} X_1(i,1)X_2(i,1) & \dots & \sum_{i=1}^{N(L)} X_1(i,1)X_2(i,L) & \sum_{j=1}^L \sum_{i=1}^{N(j)} X_1^2 X_2 & \sum_{j=1}^L \sum_{i=1}^{N(j)} X_1 X_2^2 & \sum_{j=1}^L \sum_{i=1}^{N(j)} X_1^3 X_2 & \sum_{j=1}^L \sum_{i=1}^{N(j)} X_1^2 X_2^2 & \sum_{j=1}^L \sum_{i=1}^{N(j)} X_1 X_2^3 \\ \sum_{i=1}^{N(1)} X_2^2(i,1) & \dots & \sum_{i=1}^{N(L)} X_2^2(i,L) & \sum_{j=1}^L \sum_{i=1}^{N(j)} X_1 X_2^2 & \sum_{j=1}^L \sum_{i=1}^{N(j)} X_2^3 & \sum_{j=1}^L \sum_{i=1}^{N(j)} X_1^2 X_2^2 & \sum_{j=1}^L \sum_{i=1}^{N(j)} X_1 X_2^3 & \sum_{j=1}^L \sum_{i=1}^{N(j)} X_2^4 \end{pmatrix} \begin{pmatrix} D_1 \\ \vdots \\ D_L \\ a_1 \\ a_2 \\ b_{11} \\ 2b_{12} \\ b_{22} \end{pmatrix}$$

$$y(i, j) = D(j) + y_0(i, j) + \sum_{M=1}^{M \max} \sum_{q=0}^M {}_M C_q \cdot a_{Mq} \cdot (X_1(i, j))^{M-q} (X_2(i, j))^q \quad (\text{A.17})$$

A.2. General Model

In the same manner as the quadratic (second-order) model, the matrix equation for the general M_{\max}^{th} order hybrid model

$$y(i, j) = D(j) + y_0(i, j) + \sum_{M=1}^{M \max} \sum_{q=0}^M {}_M C_q \cdot a_{Mq} \cdot (X_1(i, j))^{M-q} (X_2(i, j))^q \quad (\text{A.18})$$

can be derived by considering the patterns in the matrix elements:

$$\begin{pmatrix} [Y]_{\text{vector}} \\ [YX^2]_{\text{vector}} \\ \vdots \\ [YX^{pp}]_{\text{vector}} \end{pmatrix} = \begin{pmatrix} [L \times L]_{\text{matrix}} & [L \times 2]_{\text{matrix}} & \cdots & [L \times qq]_{\text{matrix}} \\ & [2 \times 2]_{\text{matrix}} & \cdots & [2 \times qq]_{\text{matrix}} \\ & & \ddots & \vdots \\ \text{syn} & & & [pp \times qq]_{\text{matrix}} \end{pmatrix} \begin{pmatrix} [D]_{\text{vector}} \\ [C_1]_{\text{vector}} \\ \vdots \\ [C_{pp-1}]_{\text{vector}} \end{pmatrix} \quad (\text{A.19})$$

where *syn* represents symmetric elements, and the $[L \times L]_{\text{matrix}}$ block element in (A.19) is defined as

$$\begin{pmatrix} N_1 & 0 & \cdots & 0 \\ 0 & N_2 & & \vdots \\ \vdots & & \ddots & 0 \\ 0 & \cdots & 0 & N_L \end{pmatrix} \quad (\text{A.20})$$

The $[L \times qq]_{\text{matrix}}$ block in (A.19) is

$$\begin{pmatrix} \sum_{i=1}^{N(1)} X_1^{qq-1}(i,1)X_2^0(i,1) & \sum_{i=1}^{N(1)} X_1^{qq-2}(i,1)X_2^1(i,1) & \cdots & \sum_{i=1}^{N(1)} X_1^0(i,1)X_2^{qq-1}(i,1) \\ \vdots & \vdots & \vdots & \vdots \\ \sum_{i=1}^{N(L)} X_1^{qq-1}(i,L)X_2^0(i,L) & \sum_{i=1}^{N(L)} X_1^{qq-2}(i,L)X_2^1(i,L) & \cdots & \sum_{i=1}^{N(L)} X_1^0(i,L)X_2^{qq-1}(i,L) \end{pmatrix} \quad (\text{A.21})$$

where each p-q element is generalized as

$$\sum_{i=1}^{N(p)} X_1^{qq-q}(i,p)X_2^{q-1}(i,p) \quad (\text{A.22})$$

The $pp \times qq$ block in (A.19) is

$$\begin{pmatrix} \sum_{j=1}^L \sum_{i=1}^{N(j)} X_1^{pp+qq-2}(i,j)X_2^0(i,j) & \sum_{j=1}^L \sum_{i=1}^{N(j)} X_1^{pp+qq-3}(i,j)X_2^1(i,j) & \cdots & \sum_{j=1}^L \sum_{i=1}^{N(j)} X_1^{pp+qq-(qq+1)}(i,j)X_2^{qq-1}(i,j) \\ \sum_{j=1}^L \sum_{i=1}^{N(j)} X_1^{pp+qq-3}(i,j)X_2^1(i,j) & \sum_{j=1}^L \sum_{i=1}^{N(j)} X_1^{pp+qq-4}(i,j)X_2^2(i,j) & \cdots & \sum_{j=1}^L \sum_{i=1}^{N(j)} X_1^{pp+qq-(qq+2)}(i,j)X_2^{qq}(i,j) \\ \vdots & \vdots & \ddots & \vdots \\ \sum_{j=1}^L \sum_{i=1}^{N(j)} X_1^{pp+qq-(pp+1)}(i,j)X_2^{pp-1}(i,j) & \sum_{j=1}^L \sum_{i=1}^{N(j)} X_1^{pp+qq-(pp+2)}(i,j)X_2^{pp}(i,j) & \cdots & \sum_{j=1}^L \sum_{i=1}^{N(j)} X_1^{pp+qq-(qq+pp)}(i,j)X_2^{qq+(pp-2)}(i,j) \end{pmatrix} \quad (\text{A.23})$$

where each p-q element is generalized as

$$\sum_{i=1}^{N(j)} \sum_{j=1}^L X_1^{pp+qq-(p+q)}(i,j)X_2^{p+q-2}(i,j) \quad (\text{A.24})$$

The YX^{pp} vector of the left item of (A.19) is

$$\begin{pmatrix} \sum_{j=1}^L \sum_{i=1}^{N(j)} Y(i, j) X_1^{pp-1}(i, j) X_2^0(i, j) \\ \sum_{j=1}^L \sum_{i=1}^{N(j)} Y(i, j) X_1^{pp-2}(i, j) X_2^1(i, j) \\ \vdots \\ \sum_{j=1}^L \sum_{i=1}^{N(j)} Y(i, j) X_1^0(i, j) X_2^{pp-1}(i, j) \end{pmatrix} \quad (\text{A.25})$$

and finally, the p th element of the YX^{pp} vector is

$$\sum_{j=1}^L \sum_{i=1}^{N(j)} Y(i, j) X_1^{pp-p}(i, j) X_2^{p-1}(i, j) \quad (\text{A.26})$$

Appendix B: Conference Posters

B.1. The 59th International Astronautical Congress

September 29 – October 3, 2008 in Glasgow, Scotland. Supported by the Japan Aerospace Exploration Agency (JAXA) Student Program.

A NOVEL ALGORITHM TO CONTINUOUSLY MONITOR CHANGE OF TOTAL PERIPHERAL RESISTANCE USING PERIPHERAL ARTERIAL BLOOD PRESSURE VALUES FOR PREDICTION OF ORTHOSTATIC INTOLERANCE

Tatsuya Arai¹, Kichang Lee² and Richard J. Cohen²
¹Aeronautics and Astronautics, ²Harvard-MIT Division of Health Sciences and Technology
 Massachusetts Institute of Technology, Cambridge, MA, USA

ABP: Arterial Blood Pressure [mmHg] AC: Aortic Compliance [sec x L/min / mmHg] CO: Cardiac Output [L/min]
 HR: Heart Rate [beat per minute] PP: Pulse Pressure [mmHg] SV: Stroke Volume [mL] TPR: Total Peripheral Resistance [mmHg/(L/min)]

Post-flight Orthostatic Hypotension and Vascular Resistance

1-G μ-G Fluid Shift (Re-distribution) Adaptation to μ-G Low vascular resistance High vascular resistance 1-G

Presyncope Non-presyncope

Estimation of Total Peripheral Resistance (TPR)

Windkessel Circuit
(widely accepted lumped model)

Voltage (V) = Blood Pressure (BP)
 Current (i) = Cardiac Output (CO)
 Charge (Q) = Blood Volume (Q, SV)

Resistance (R) = Total Peripheral Resistance (TPR)
 Capacitor (C) = Aortic Compliance (AC)

$$SV = PP \times AC$$

$$CO = SV \times HR$$

$$MAP = CO \times TPR$$

$$TPR = \frac{MAP}{AC \times PP \times HR}$$

Problem in TPR Estimation from Blood Pressure

ABP Waveform propagates from a central to peripheral tapered arterial tree

↓

Waveform distortion, especially in systole

Hypothesis

End diastolic pressure, beat duration, time from the onset to the peak of systole, and mean arterial pressure are relatively insensitive to distortion.

TPR estimation can be improved by using this information.

Algorithm

Time Constant $\tau = TPR \times AC$

$$P(t) = P_i^D e^{-t/T_i^D} \tau_i$$

$$P(t) = (P_i^D e^{-T_i^D/t} + \Delta Q_i / AC) e^{-t/T_i^D} \tau_i$$

Curve-fitting

Equal mean arterial pressure of measured and Windkessel BP

$$MAP = \frac{1}{T_i} \int_0^{T_i} P_i(t) dt = \frac{\tau_i}{T_i} (P_i^D + \frac{\Delta Q_i}{AC} - P_{i+1}^D)$$

Stroke volume and pulse pressure:

$$\Delta Q_i = P_{i+1}^D e^{(T_i - T_i^S)/\tau_i} - P_i^D e^{-T_i^S/\tau_i}$$

Numerically solve:

$$MAP_i = \frac{\tau_i}{T_i} \{ P_{i+1}^D (e^{(T_i - T_i^S)/\tau_i} - 1) + P_i^D (1 - e^{-T_i^S/\tau_i}) \}$$

for time constant τ of the beat.

Proportional TPR (within a scaling factor of AC) is obtained to monitor the change of TPR.

Method and Results

Yorkshire Swine Ultrasonic flow probe Heart Aortic Flow Femoral Artery External pressure transducer MAP

Method	Error [%]
PP1	17.9%
PP2	19.7%
New	14.0%

* PP2 defines pulse pressure as MAP - Diastolic ABP

Conclusion and Future Work

The new method had statistically lower error in TPR estimation than other methods.


The new method has the potential for clinical applications.

Future work includes CO and SV estimation analysis and application to prediction of post-flight orthostatic hypotension using pre-flight ABP waveform.

B.2. The 18th IAA Humans in Space Symposium

April 11–15, 2011 in Houston, Texas. Supported by the MIT Graduate Student Council (GSC) Travel


Fund Grant.



Estimation of Aortic Blood Flow by Analysis of Peripheral Arterial Blood Pressure

T. Arai¹, K. Lee², and R. J. Cohen²

¹Department of Aeronautics and Astronautics and ²Harvard-MIT Division of Health Sciences and Technology
Massachusetts Institute of Technology 45 Carleton Street, Rm. E25-335, Cambridge MA 02142



Background

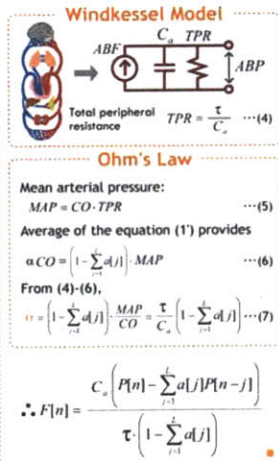
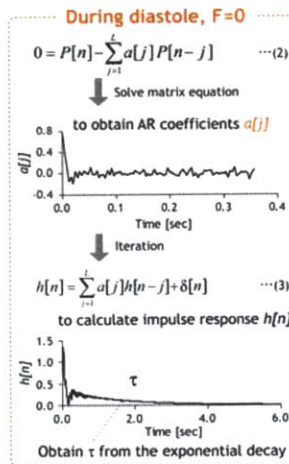
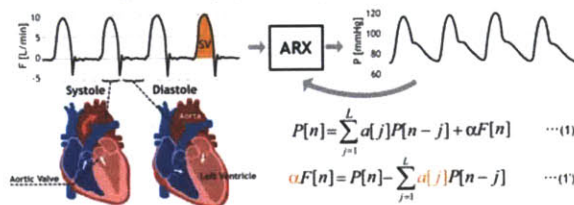
Continuous monitoring of cardiovascular parameters is needed to study the effect of space flight on cardiovascular function and to develop improved methods of monitoring the health of astronauts. In particular, **aortic blood flow (ABF)**, the instantaneous blood flow in the aorta, is one of the most essential cardiovascular parameters; by analyzing the ABF waveforms, one can calculate cardiac output (CO) and stroke volume (SV).

In spite of its importance, **ABF is not available clinically** except during short-term echocardiographic recordings because of the difficulty in acquiring the ABF signal in an accurate and continuous manner. In contrast, **arterial blood pressure (ABP)** can be readily obtained invasively or noninvasively.

The purpose of this research was to develop and validate a novel algorithm to **reconstruct ABF waveforms from ABP waveforms**. Availability of continuous ABF would enable multi-modal assessment of cardiovascular function.

Algorithm Auto-Regressive with Exogenous Input (ARX) Model

We have developed and validated a novel time-domain algorithm to reconstruct the continuous ABF signal from the peripheral ABP signal.

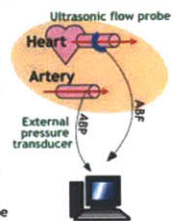


Validation Method Yorkshire swine data sets

• Perturbation

Vaso-active drugs (e.g. phenylephrine) administered to achieve a wide physiological range:

ANIMAL	Length (cm)	CO (L/min)	SV (mL)	Femoral MAP (mmHg)	Radial MAP (mmHg)	HR (bpm)
1	113	3.6 +/- 1.0	28.4 +/- 5.8	63 +/- 19	61 +/- 19	129 +/- 29
2	97	3.2 +/- 0.6	25.0 +/- 5.0	83 +/- 21	73 +/- 20	135 +/- 38
3	88	4.0 +/- 0.7	31.7 +/- 7.1	83 +/- 16	87 +/- 15	133 +/- 32
4	106	3.2 +/- 0.6	25.2 +/- 4.3	89 +/- 19	79 +/- 18	129 +/- 34
5	90	3.3 +/- 0.5	26.7 +/- 6.4	80 +/- 21	85 +/- 19	130 +/- 32
6	68	3.4 +/- 1.2	28.3 +/- 8.1	72 +/- 19	75 +/- 20	130 +/- 34
MEAN	94	3.5 +/- 0.8	27.5 +/- 6.7	79 +/- 21	76 +/- 21	131 +/- 32



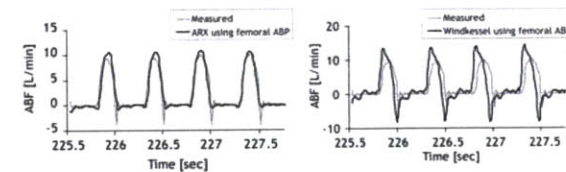
• Measurement

Reference ABF measured by a surgically implanted aortic flow probe (T206 with A-series probes, Transonic Systems, Ithaca, NY)

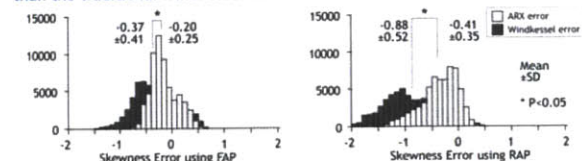
Peripheral ABP measured by a 23- or 25-gauge angio-catheter placed into the femoral and radial artery, attached to an external pressure transducer (TSD104A, Biopac Systems, Santa Barbara, CA)

Results

• First successful reconstruction of ABF waveforms from peripheral ABP



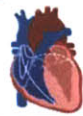
• Smaller waveform error (standard deviation, skewness, and kurtosis) than the traditional Windkessel model



- Stroke volume error: 19.6% using femoral ABP, 21.8% using radial ABP
- Cardiac output error: 15.2% using femoral ABP, 17.6% using radial ABP

Future Work

- Application to non-invasive ABP data recorded from astronauts
Long-term monitoring of the cardiovascular function
Easy to implement in cardiovascular monitoring systems
- Adaptive cardiac resynchronization therapy (CRT)
Reconstruction of ABF waveforms in premature beats as well as optimization of pacing parameters during bi-ventricular pacing for patients with advanced heart failure



Supported by the MIT Graduate Student Council Travel Fund Grant

Bibliography

- [1] M. F. O'Rourke, *et al.*, *The Arterial Pulse*: Lea & Febiger, 1992.
- [2] T. Heldt, *et al.*, "Computational modeling of cardiovascular response to orthostatic stress," *J Appl Physiol*, vol. 92, pp. 1239-54, Mar 2002.
- [3] R. Mukkamala, "A forward model-based analysis of cardiovascular system identification methods," Ph.D., Electrical Engineering and Computer Science, Massachusetts Institute of Technology, Cambridge, 2000.
- [4] R. Mukkamala and R. J. Cohen, "A forward model-based validation of cardiovascular system identification," *Am J Physiol Heart Circ Physiol*, vol. 281, pp. H2714-30, Dec 2001.
- [5] T. J. Mullen, *et al.*, "System identification of closed-loop cardiovascular control: effects of posture and autonomic blockade," *Am J Physiol*, vol. 272, pp. H448-61, Jan 1997.
- [6] X. Xiao, *et al.*, "Effects of simulated microgravity on closed-loop cardiovascular regulation and orthostatic intolerance: analysis by means of system identification," *J Appl Physiol*, vol. 96, pp. 489-97, Feb 2004.
- [7] G. Antonutto, *et al.*, "Noninvasive assessment of cardiac output from arterial pressure profiles during exercise," *Eur J Appl Physiol Occup Physiol*, vol. 72, pp. 18-24, 1995.
- [8] T. Arai, *et al.*, "A novel algorithm to continuously monitor change of total peripheral resistance using peripheral arterial blood pressure values for prediction of orthostatic intolerance," presented at the International Astronautical Congress, Glasgow, Scotland, 2008.
- [9] M. J. Bourgeois, *et al.*, "Continuous determination of beat to beat stroke volume from aortic pressure pulses in the dog," *Circ Res*, vol. 39, pp. 15-24, Jul 1976.
- [10] D. Burkhoff, *et al.*, "Assessment of Windkessel as a model of aortic input impedance," *Am J Physiol*, vol. 255, pp. H742-53, Oct 1988.
- [11] C. Cerutti, *et al.*, "Beat-to-beat stroke volume estimation from aortic pressure waveform in conscious rats: comparison of models," *Am J Physiol Heart Circ Physiol*, vol. 281, pp. H1148-55, Sep 2001.
- [12] J. Erlanger and D. R. Hooker, "An experimental study of blood-pressure and of pulse-pressure in man," Johns Hopkins Hospital, Baltimore, MD 1904.
- [13] W. F. Hamilton and J. W. Remington, "The measurement of the stroke volume from the pressure pulse," *Am J Physiol*, vol. 148, pp. 14-24, 1946.
- [14] J. A. Herd, *et al.*, "Arterial pressure pulse contours during hemorrhage in anesthetized dogs," *J Appl Physiol*, vol. 21, pp. 1864-8, Nov 1966.
- [15] N. T. Kouchoukos, *et al.*, "Estimation of stroke volume in the dog by a pulse contour method," *Circ Res*, vol. 26, pp. 611-23, May 1970.
- [16] G. J. Langewouters, *et al.*, "Pressure-diameter relationships of segments of human finger arteries," *Clin Phys Physiol Meas*, vol. 7, pp. 43-56, Feb 1986.
- [17] G. Liljestrand and E. Zander, "Vergleichende Bestimmung des Minutenvolumens des Herzens beim Menschen mittels der Stickoxydulmethode und durch Blutdruckmessung.," *Zeitschrift fur die gesamte experimentelle Medizin*, vol. 59, pp. 105-122, 1928.
- [18] N. W. Linton and R. A. Linton, "Estimation of changes in cardiac output from the arterial blood pressure waveform in the upper limb," *Br J Anaesth*, vol. 86, pp. 486-96, Apr 2001.
- [19] P. Molino, *et al.*, "Beat-to-beat estimation of windkessel model parameters in conscious rats," *Am J Physiol*, vol. 274, pp. H171-7, Jan 1998.
- [20] R. Mukkamala, *et al.*, "Continuous cardiac output monitoring by peripheral blood pressure waveform analysis," *IEEE Trans Biomed Eng*, vol. 53, pp. 459-67, Mar 2006.
- [21] T. Nieminen, *et al.*, "Can stroke volume and cardiac output be determined reliably in a tilt-table test using the pulse contour method?," *Clin Physiol*, vol. 20, pp. 488-95, Nov 2000.
- [22] T. Parlikar, *et al.*, "Cycle-Averaged Models of Cardiovascular Dynamics," *IEEE Trans Circuit and Systems*, vol. 53, pp. 2459-2468, Nov. 2006 2006.
- [23] T. A. Parlikar, "Modeling and Monitoring of Cardiovascular Dynamics for Patients in Critical Care," Ph.D. , Department of Electrical Engineering and Computer Science, Massachusetts Institute of Technology, Cambridge, 2007.
- [24] J. D. Redling and M. Akay, "Noninvasive cardiac output estimation: a preliminary study," *Biol Cybern*, vol. 77, pp. 111-22, Aug 1997.

- [25] W. J. Stok, *et al.*, "Noninvasive cardiac output measurement in orthostasis: pulse contour analysis compared with acetylene rebreathing," *J Appl Physiol*, vol. 87, pp. 2266-73, Dec 1999.
- [26] G. P. Toorop, *et al.*, "Beat-to-beat estimation of peripheral resistance and arterial compliance during pressure transients," *Am J Physiol*, vol. 252, pp. H1275-83, Jun 1987.
- [27] P. D. Verdouw, *et al.*, "Stroke volume from central aortic pressure? A critical assessment of the various formulae as to their clinical value," *Basic Res Cardiol*, vol. 70, pp. 377-89, Jul-Aug 1975.
- [28] H. R. Warner, *et al.*, "Quantitation of beat-to-beat changes in stroke volume from the aortic pulse contour in man," *J Appl Physiol*, vol. 5, pp. 495-507, Mar 1953.
- [29] K. H. Wesseling, *et al.*, "A simple device for the continuous measurement of cardiac output. Its model basis and experimental verification.," *Adv Cardiovasc Phys*, vol. 5, pp. 16-52, 1983.
- [30] K. H. Wesseling, *et al.*, "Computation of aortic flow from pressure in humans using a nonlinear, three-element model," *J Appl Physiol*, vol. 74, pp. 2566-73, May 1993.
- [31] R. Mukkamala, *et al.*, "System identification of closed-loop cardiovascular control mechanisms: diabetic autonomic neuropathy," *Am J Physiol*, vol. 276, pp. R905-12, Mar 1999.
- [32] T. Heldt, *et al.*, "Model-based parameter estimation using cardiovascular response to orthostatic stress," *Comput Cardiol*, vol. 28, pp. 337-40, 2001.
- [33] A. C. Guyton, *et al.*, "Circulation: overall regulation," *Annu Rev Physiol*, vol. 34, pp. 13-46, 1972.
- [34] A. C. Guyton and J. E. Hall, *Textbook of medical physiology*, 10th ed. Philadelphia: Saunders, 2000.
- [35] H. Barcroft, *et al.*, "Posthaemorrhagic fainting. Study by cardiac output and forearm flow," *Lancet*, pp. 489-491, 1944.
- [36] W. Ganz, *et al.*, "A new technique for measurement of cardiac output by thermodilution in man," *Am J Cardiol*, vol. 27, pp. 392-6, Apr 1971.
- [37] R. D. Yoder and E. A. Swan, "Cardiac output: comparison of Stewart-Hamilton and gamma-function techniques," *J Appl Physiol*, vol. 31, pp. 318-21, Aug 1971.
- [38] G. R. Manecke, Jr., *et al.*, "An unusual case of pulmonary artery catheter malfunction," *Anesth Analg*, vol. 95, pp. 302-4, table of contents, Aug 2002.
- [39] J. S. Vender and H. C. Gilbert, *Monitoring the anesthetized patient*, 3 ed. Philadelphia: Lippincott-Raven Publishers, 1997.
- [40] M. Botero, *et al.*, "Measurement of cardiac output before and after cardiopulmonary bypass: Comparison among aortic transit-time ultrasound, thermodilution, and noninvasive partial CO₂ rebreathing," *J Cardiothorac Vasc Anesth*, vol. 18, pp. 563-72, Oct 2004.
- [41] A. Noordergraaf, *Circulatory System Dynamics*. New York: Academic Press, 1978.
- [42] R. P. Patterson, "Fundamentals of impedance cardiography," *IEEE Eng Med Biol Mag*, vol. 8, pp. 35-8, 1989.
- [43] D. G. Newman and R. Callister, "The non-invasive assessment of stroke volume and cardiac output by impedance cardiography: a review," *Aviat Space Environ Med*, vol. 70, pp. 780-9, Aug 1999.
- [44] L. A. Critchley, "Impedance cardiography. The impact of new technology," *Anaesthesia*, vol. 53, pp. 677-84, Jul 1998.
- [45] D. G. Haryadi, *et al.*, "Partial CO₂ rebreathing indirect Fick technique for non-invasive measurement of cardiac output," *J Clin Monit Comput*, vol. 16, pp. 361-74, 2000.
- [46] L. Nilsson, *et al.*, "Lack of agreement between thermodilution and carbon dioxide-rebreathing cardiac output," *Acta Anaesthesiol Scand*, vol. 45, pp. 680-685, 2001
- [47] J. M. Bland and D. G. Altman, "Statistical methods for assessing agreement between two methods of clinical measurement," *Lancet*, vol. 1, pp. 307-10, Feb 8 1986.
- [48] O. Frank, "Die Grundform des Arteriellen Pulses," *Zeitschrift für Biologie*, vol. 37, pp. 483-526, 1899.
- [49] T. Arai, *et al.*, "Cardiac output and stroke volume estimation using a hybrid of three Windkessel models," presented at the Conf Proc IEEE Eng Med Biol Soc, Buenos Aires, Argentina 2010.
- [50] T. Arai, *et al.*, "Preliminary application of a novel algorithm to monitor changes in pre-flight total peripheral resistance for prediction of post-flight orthostatic intolerance in astronauts " *Acta Astronaut*, vol. 68, pp. 770-777, 2011.
- [51] M. J. Bourgeois, *et al.*, "Characteristics of aortic diastolic pressure decay with application to the continuous monitoring of changes in peripheral vascular resistance," *Circ Res*, vol. 35, pp. 56-66, Jul 1974.
- [52] Z. Lu and R. Mukkamala, "Continuous cardiac output monitoring in humans by invasive and noninvasive peripheral blood pressure waveform analysis," *J Appl Physiol*, vol. 101, pp. 598-608, Aug 2006.
- [53] J. X. Sun, *et al.*, "The cardiac output from blood pressure algorithms trial," *Crit Care Med*, vol. 37, pp. 72-80, Jan 2009.

- [54] M. H. Perrott and R. J. Cohen, "An efficient approach to ARMA modeling of biological systems with multiple inputs and delays," *IEEE Trans Biomed Eng*, vol. 43, pp. 1-14, Jan 1996.
- [55] M. W. Mohiuddin, *et al.*, "Increase in pulse wavelength causes the systemic arterial tree to degenerate into a classical windkessel," *Am J Physiol Heart Circ Physiol*, vol. 293, pp. H1164-71, Aug 2007.
- [56] J. Rissanen, "Modeling by shortest data description," *Automatica*, vol. 14, pp. 465-471, 1978.
- [57] R. J. Cohen, "Flow estimation," USA Patent.
- [58] A. M. Weissler, *et al.*, "Left Ventricular Ejection Time Index in Man," *J Appl Physiol*, vol. 18, pp. 919-23, Sep 1963.
- [59] E. Monnet and J. C. Chachques, "Animal models of heart failure: what is new?," *Ann Thorac Surg*, vol. 79, pp. 1445-53, Apr 2005.
- [60] G. W. Moe and P. Armstrong, "Pacing-induced heart failure: a model to study the mechanism of disease progression and novel therapy in heart failure," *Cardiovasc Res*, vol. 42, pp. 591-9, Jun 1999.
- [61] R. Einstein and N. Abdul-Hussein, "Animal models of heart failure for pharmacological studies," *Clin Exp Pharmacol Physiol*, vol. 22, pp. 864-8, Nov 1995.
- [62] J. A. Dixon and F. G. Spinale, "Large animal models of heart failure: a critical link in the translation of basic science to clinical practice," *Circ Heart Fail*, vol. 2, pp. 262-71, May 2009.
- [63] J. M. Power and A. M. Tonkin, "Large animal models of heart failure," *Aust N Z J Med*, vol. 29, pp. 395-402, Jun 1999.
- [64] T. Ishikawa, *et al.*, "Optimization of atrioventricular delay and follow-up in a patient with congestive heart failure and with bi-ventricular pacing," *Jpn Heart J*, vol. 42, pp. 781-7, Nov 2001.
- [65] A. H. Jansen, *et al.*, "Correlation of echo-Doppler optimization of atrioventricular delay in cardiac resynchronization therapy with invasive hemodynamics in patients with heart failure secondary to ischemic or idiopathic dilated cardiomyopathy," *Am J Cardiol*, vol. 97, pp. 552-7, Feb 15 2006.